

Contents

INDEX	5
FINITELY-ELEMENT MODELLING OF ELECTRON-OPTICAL PROCESSES IN THE LOW-VOLTAGE CATHODOLUMINESCENT INDICATOR ON AN ACTIVE SUBSTRATE <i>Abanshin N.P., Yakunin A.N., Gorfinkel B.I.</i>	7
BASIC PHYSICS OF FORMATION OF AN ELECTRON FLOW IN FLAT GRAPHIC INDICATORS ON THE BASIS OF PLANAR-EDGE AUTO-EMISSIVE STRUCTURES <i>Abanshin⁴⁵ N.P., Yakunin A.N., Gorfinkel B.I.</i>	11
QUESTIONS OF DEVELOPMENT OF DURABLE FLAT GRAPHIC INDICATORS ON THE BASIS OF PLANAR-EDGE AUTO-EMISSIVE STRUCTURES <i>Abanshin N.P., Yakunin A.N., Gorfinkel B.I.</i>	16
SPECTRAL-POLARIZING PROPERTIES AND LIGHT STABILITY OF FILM POLARIZERS WITH AZODYES <i>V. Agabekov, N. Ariko, L. Filippovich</i>	20
PRETRANSITIONAL CHMRAL LC PHASE: OPTICAL CHARACTERISTICS AND LASING <i>A. Chanishvili, D. Chilaia, G. Chilaya, G Petriashvili, R. Barberi, R. Bartolino, M.P. De Santo, M.A. Matranga, F. Ciuchi</i>	27
THE ANALYSIS OF PRINCIPLES OF DISPLAY READABILITY IMPROVEMENT FOR DISPLAY SYSTEM FOR MOBILE APPLICATION. <i>M. V. Dyatlov</i>	35
GENERAL PRINCIPLES OF RUGGEDIZATION OF COMMERCIALY AVAILABLE LIQUID CRYSTAL DISPLAYS FOR DISPLAYS FOR MOBILE APPLICATION ANALYSIS. <i>Dyatlov V.M., Dyatlov M.V., Semash A.A., Savina E.V., Seliverstov V.I.</i>	42

LIGHT TRANSMISSION POLARIMETRY OF CHOLESTERIC CELLS IN PLANAR AND WEDGE GEOMETRIES: ANALYSIS OF POLARIZATION PARAMETER FIELDS	
<i>Roman I. Egorov, Roman G. Vovk, Alexei D. Kiselev, and Marat S. Soskin.</i>	<i>49</i>
ELUCIDATION OF ENERGY TRANSFER MECHANISM FROM FLUORENE POLYMER TO IR COMPLEXES AIMING FOR HIGH EFFICIENCY OLEDs	
<i>Larysa Fenenko, Chihaya Adachia, V.E. Lashkaryov</i>	<i>54</i>
POROUS ANODIC ALUMINA AND SOL-GEL PRODUCTS FOR OPTOELECTRONIC APPLICATIONS	
<i>G.K. Maliarevich, I.S. Molchan, N.V. Gaponenko, S.V. Gaponenko, A.A. Lutich, G.E. Thompson</i>	<i>58</i>
SECOND HARMONIC GENERATION IN ZNS PHOSPHORS UNDER THE STRONG IR IRRADIATION	
<i>L.V. Grigoryev, E.V. Komarov, V.V. Rychgorskyi, M.M. Sychov</i>	<i>62</i>
TESTING OF P-N JUNCTION ON SILICON SURFACE IN NEMATIC CELL	
<i>Gritsenko M.I., Kucheev S.I., Litvin P.M., Tkach V.M., Yelshansky V.B.</i>	<i>66</i>
THE RESEARCH ON PLASMA DISPLAY PANELS IN KYIV NATIONAL TARAS SHEVCHENKO UNIVERSITY: HISTORY AND POSSIBLE MODERN APPLICATION	
<i>O.I. Kelynyk, T.E. Lisitchenko</i>	<i>73</i>
INDEX MATCHING COATINGS FOR LCD	
<i>E. Khokhlov, S. Fetisenkov, K. Krivetski</i>	<i>77</i>
ION BEAM SPUTTERING TECHNOLOGY FOR DEPOSITION OF THIN FILMS FOR FPD.	
<i>Shiripov V., Khokhlov A., Maryshev S., Leuchuk N., Khisamov A.</i>	<i>82</i>
LIQUID CRYSTAL LIGHT MODULATORS CREATED FROM GLASS CERAMIC MATERIALS WITH ULTRA LOW THERMAL EXPANSION COEFFICIENT	
<i>Kolomzarov Yu. V., Maslov V.P.</i>	<i>88</i>
NANO- AND MICRO-RELIEF OF HIGH RELIABILITY FOR OPTICAL SYSTEMS	
<i>Yu. Timoshkov, T. Orekhovskaya, V. Timoshkov, V. Kurmashev</i>	<i>96</i>
NEW PATHS TO HIGH TWISTING CHIRAL COMPONENTS FOR SHORT-PITCH CHOLESTERIC LIQUID CRYSTALS	
<i>T.G. Drushlyak, V.V. Abakumov, L.A. Kutulya, I.M. Gella, S.V. Shishkina, N.S. Pivnenko, N.I. Shkolnikova, O.V. Shishkin</i>	<i>103</i>
ELLIPSOMETRICAL PARAMETERS OF THE POLYMER DISPERSED LIQUID-CRYSTAL FILM WITH NANOSIZED NEMATIC DROPLETS	
<i>V.A. Loiko, A.V. Konkolovich, A.A. Miskevich, P.G. Maksimenko</i>	<i>113</i>
VFD MODULES FOR WIDE APPLICATION	
<i>Malyayeva N.A., Neudakhin A.V., Zhukov N.D., Frolov V.L., Zotov N.A., Zhidkikh V.V.</i>	<i>118</i>

POLYACRYLONITRILE XEROGEL – NEMATIC LIQUID CRYSTAL. STRUCTURE AND PROPERTIES	
<i>V.I. Mashchenko, S.A. Udra, L.A. Kazarin, V.V. Sorokin, V.I. Gerasimov, V.V. Belyaev</i>	<i>123</i>
CHARGE TRANSPORT PROCESSES IN THE SENSOR MATERIALS BASED ON CONJUGATED POLYAMINOARENES	
<i>O. Aksimentyeva, P. Stakhira, Z. Mykytyuk, V. Cherpak, A. Fechan, V. Gurali</i>	<i>128</i>
OPTICAL CHARACTERISTICS OF POLYANILINE IN MEDIUM WITH DIFFERENT PH VALUE	
<i>Mykytyuk Z.M., Stakhira P.Y., Aksimentyeva O.I., Hlushyk I.P., Sushynskyy O.J., Fechan A.V., Cherpak V.V.</i>	<i>135</i>
LYOTROPIC CHROMONIC LIQUID CRYSTALS WITH NEGATIVE BIREFRINGENCE FOR DISPLAY APPLICATIONS	
<i>O. Boiko, Yu.A. Nastishin, R. Vasyuta and V. Nazarenko</i>	<i>140</i>
LATEST MULTI-USER 3D DISPLAY DEVELOPMENTS	
<i>Phil Surman, Ian Sexton, Richard Bates, Wing Kai Lee, Triantafillos Koukoulas</i>	<i>148</i>
OPERATION STEADINESS AND MANUFACTURING PROSPECTS OF PASSIVELY ADDRESSED FLC DISPLAYS POSSESSING AN INHERENT GRAY SCALE	
<i>E.P. Pozhidaev, V.G. Chigrinov, Yu.P. Bobilev, V.M. Shoshin, A.A. Zhukov, A.L. Andreev, I.N. Kompanets, Li Xihua, E.E. Gukasjan, P.S. Komarov, O.A. Shadura, H.S. Kwok</i>	<i>157</i>
APPROXIMATION OF DYNAMIC HYSTERESIS CHARACTERISTICS OF A CHLC	
<i>A. Rybalochka, M. Chumachkova, M. Minyaylo, V. Sorokin.....</i>	<i>165</i>
SILICON BASED INTEGRATED LED MICRODISPLAY	
<i>A. Smirnov, V. Labunov, S. Lazarouk</i>	<i>182</i>
LCOS BACKPLANE LAYOUT VERIFICATION METHOD THAT USES COMPUTATIONAL MODELS OF LITHOGRAPHY PROCESSES	
<i>S.N. Koukharenko, S.V. Volk, A.M. Zayats, A.G. Smirnov</i>	<i>189</i>
PERSPECTIVES OF PASSIVE MATRIX LCD IMPROVEMENTS	
<i>Studentsov S.A., Brezhnev V.A., Gorfinkel B.I., Zhukov N.D.,</i>	<i>196</i>
INTERACTIVE DISPLAYS	
<i>Trofimov Yu., Posedko V., Sivenkov V., Lishik S., Tsvirko V., Posedko A.</i>	<i>201</i>
Aλ VFD MODULE ON SILICON SUBSTRATE	
<i>Usova T.V., Loginov A.P., Zhukov N.D., Gorfinkel B.I., Frolov V.L., Neudakhin A.V., Zotov N.A.</i>	<i>210</i>
THE PHOTSENSITIVE POLYMERIC COMPOSITES FROM INORGANIC AND ORGANIC SEMICONDUCTORS AND PROSPECTS OF THEIR USE	
<i>James G. Grote, Yaroslav I. Vertsimakha,</i>	<i>216</i>

INFLUENCE OF PREPARATION AND EXCITATION CONDITIONS OF ZNS:ER,F TFELS ON RADIATIVE CHARACTERISTICS IN VISIBLE AND NEAR-INFRARED SPECTRAL REGIONS.	
<i>N.A. Vlasenko, L.I. Veligura, Z.L. Denisova, M.A. Mukhlyo, Yu.A. Tsytkunov, F. Zinchenko, A.V. Bagazky.....</i>	<i>225</i>
THE METHOD TO SUPPRESS OFF-AXIS HAZE OF PDLC	
<i>L.O. Dolgov, O.V. Yaroshchuk,</i>	<i>233</i>
LIQUID CRYSTAL ALIGNMENT ON THE FILMS DEPOSITED BY SPUTTERING: DEPENDENCE ON TARGET MATERIAL AND GASEOUS FEED	
<i>O. Yaroshchuk, R. Kravchuk, L. Dolgov, E. Telesh, A. Khokhlov, J. Brill, N. Fruehauf, M.A Reijme,</i>	<i>240</i>
CHOLESTERIC LCD FOR CREATION OF ACOUSTOOPTICAL HOLOGRAPHIC IMAGE.	
<i>P. Oleksenko, V. Sorokin, P. Tytarenko, R. Zelinskyy.....</i>	<i>248</i>
PASSIVE-MATRIX ADDRESSING OF THE DISPLAY BASED ON BISTABLE PDCHLC FILM	
<i>A.V. Barannik, V.F. Shabanov, V.Ya. Zyryanov, V.M. Sorokin</i>	<i>257</i>
FORMATION CONDITIONS OF POLARIZING STRUCTURE OF H- AND L-TYPE POLARIZERS IN VIEW OF OPTICAL ANISOTROPY	
<i>N. Ivanova, V. Agabekov, S. Shahab, A. Tsaruk , V. Dlugunovich</i>	<i>263</i>
DISPLAYS FOR GREEN EARTH	
<i>Shigeo Mikoshiba.....</i>	<i>268</i>

Index

A

Abakumov, V.V. 106
Abanshin N.P. 10, 14, 19
Adachi, C. 57
Agabekov, V. 23, 266
Aksimentyeva, O. 131, 138
Andreev, A.L. 160
Ariko, N. 23

B

Bagazky, A.V. 228
Barannik, A.V. 260
Barberi, R. 30
Bartolino, R. 30
Bates, R. 151
Belyaev, V.V. 126
Bobilev, Yu.P. 160
Boiko, O. 143
Brezhnev V.A. 199
Brill, J. 243

C

Chanishvili, A. 30
Cherpak, V. 131, 138
Chigrinov, V.G. 160
Chilaia, D. 30
Chilaya, G. 30
Chumachkova, M. 168
Ciuchi, F. 30

D

De Santo, M.P. 30
Denisova, Z.L. 228
Dlugunovich, V. 266
Dolgov, L. 243, 236
Drushlyak, T.G. 106
Dyatlov M.V. 45, 38
Dyatlov V.M. 45

E

Egorov, R.I. 52

F

Fechan, A. 131, 138
Fenenko, L. 57
Fetisenkov, S. 80
Filippovich, L. 23
Frolov V.L. 121, 213
Fruehauf, N. 243

G

Gaponenko, N.V. 61
Gaponenko, S.V. 61
Gella, I.M. 106
Gerasimov, V.I. 126
Gorfinkel B.I. 10, 14, 19, 199, 213
Grigoryev, L.V. 65
Gritsenko M.I. 69
Grote, J.G. 219
Gukasjan, E.E. 160
Gural, V. 131

H

Hlushyk I.P. 138

I

Ivanova, N. 266

K

Kazarin, L.A. 126
Kelnyk, O.I. 76
Khisamov A. 85
Khokhlov A. 85, 243
Khokhlov, E. 80
Kiselev, A.D. 52
Kolomzarov Yu.V. 91
Komarov, E.V. 65
Komarov, P.S. 160
Kompanets, I.N. 160
Konkolovich, A.V. 116
Koukharenko, S.N. 192
Koukoulas, T. 151
Kravchuk, R. 243
Krivetski, K. 80
Kucheev S.I., 69
Kurmashev, V. 99
Kutulya, L.A. 106
Kwok, H.S. 160

L

Labunov, V. 185
Lashkaryov, V.E. 57
Lazarouk, S. 185
Lee, Wing Kai 151
Leuchuk N. 85
Lishik S. 204
Lisitchenko, T.E. 76
Litvin P.M. 69

Loginov A.P. 213
Loiko, V.A. 116
Lutich, A.A. 61

M

Maksimenko, P.G. 116
Maliarevich, G.K. 61
Malyayeva N.A. 121
Maryshev S 85
Mashchenko, V.I. 126
Maslov V.P. 91
Matranga, M.A. 30
Mikoshiya, Shigeo 271
Minyaylo, M. 168
Miskevich, A.A. 116
Molchan, I.S. 61
Mukhlyo, M.A. 228
Mykytyuk, Z. 131, 138

N

Nastishin, Yu.A. 143
Nazarenko, V. 143
Neudakhin A.V. 121, 213

O

Oleksenko, P. 251
Orekhovskaya, T. 99

P

Petriashvili, G 30
Pivnenko, N.S. 106
Posedko A. 204
Posedko V. 204
Pozhidaev, E.P. 160

R

Reijme, M.A 243
Rybalochka, A. 168
Rychgorskyi, V.V. 65

S

Savina E.V. 45
Seliverstov V.I. 45
Semash A.A. 45
Sexton, I. 151
Shabanov, V.F. 260
Shadura, O.A. 160
Shahab, S. 266
Shiripov V. 85
Shishkin, O.V. 106
Shishkina, S.V. 106
Shkolnikova, N.I. 106
Shoshin, V.M. 160

Sivenkov V. 204
Smirnov, A. 185, 192
Sorokin, V.M. 168, 251, 260
Sorokin, V.V. 126
Soskin, M.S. 52
Stakhira, P. 131
Stakhira P.Y. 138
Studentsov S.A. 199
Surman, P. 151
Sushynskyy O.J 138
Sychoy, M.M. 65

T

Telesh, E. 243
Thompson, G.E. 61
Timoshkov, V. 99
Timoshkov, Yu. 99
Tkach V.M. 69
Trofimov Yu. 204
Tsaruk, A. 266
Tsvirko V. 204
Tsyrkunov, Yu.A. 228
Tytarenko, P. 251

U

Udra, S.A. 126
Usova T.V. 213

V

Vasyuta, R. 143
Veligura, L.I. 228
Vertsimakha, Y.I. 219
Vlasenko, N.A. 228
Volk, S.V. 192
Vovk, R.G. 52

X

Xihua, Li 160

Y

Yakunin A.N. 10, 14, 19
Yaroshchuk, O. 243, 236
Yelshansky V.B. 69

Z

Zayats, A.M. 192
Zelinskyy, R. 251
Zhidkikh V.V. 121
Zhukov, A.A. 160
Zhukov N.D. 121, 199, 213
Zinchenko, V.F. 228
Zotov N.A. 121, 213
Zyryanov, V.Ya. 260

Finitely-element modelling of electron-optical processes in the low-voltage cathodoluminescent indicator on an active substrate

Abanshin N.P., Yakunin A.N., Gorfinkel B.I.

Research & Development Institute “Volga”, Saratov, Russia

The basic problem having fundamental importance at development of a perspective design of the competitive long-lived flat cathodoluminescent indicator on active substrate, is providing of high current loading onto light-emitting elements – pixels of an anode matrix. This current loading must be sufficient for keeping of a necessary level of a low-voltage phosphor luminescence at activation energy not higher than 30 eV.

Emissive structures (thermo-emissive or auto-emissive) with high intensity of an electron flow have, as a rule, accelerating working voltages at a level of 200 V and more. It essentially complicates application of low-voltage phosphors, because owing to appearance of sizeable areas with a decelerating electrostatic field, level of a reverse current becomes inadmissible high. Bombardment of emissive structure electrodes by a reverse current reduces longevity of the device and its power efficiency (technical efficiency factor).

It is offered, for elimination of the specified lacks, to enter of an electron flow recuperation system which operates selectively in relation to a direct and reverse electron flow:

- passes a maximum of a direct flow towards the anode matrix;
- catch a maximum of the reverse flow reflected towards the emissive structure.

Structure of this device can be represented by the scheme on Fig. 1.

Thus the recuperation system electrodes potential should be low, on approximately order, than the accelerating potential, for reduction of losses level, and, accordingly, of level of thermal loading of decelerating grid.

The decelerating grid in such design play a role of a recuperator for catching of the undesirable reverse electron flow directed from the anode to the cathode grid. The potential of cathode grid U_{KP} is essentially higher than control potentials of anode structure pixels (U_A). The potential of decelerating grid U_{TP} also is much lower than U_{KP} and is close by level to the anode potential.

In a space “emitter - cathode grid”, the electrostatic field accelerates an electron flow in direction to the anode structure. The electron flow is focused on the cathode grid electrodes, therefore an “electron-optical” transparency of the grid is always low than classical optical one.

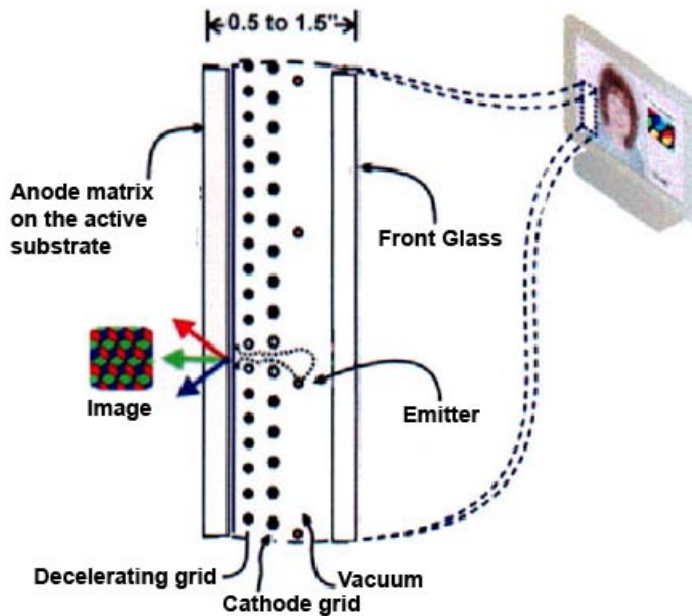


Fig. 1. Design of the cathodoluminescent indicator with the decelerating grid

In a space «cathode grid - decelerating grid», an electric field intensity vector has an opposite direction, and the field is decelerating in relation to a direct electron flow. For the reverse electron flow, this field is focusing. In the space “decelerating grid – anode”, the field changes both on value and on direction. This changes depends on the separate pixel state: “is open” or “is closed”.

Set of inconsistent criteria for design synthesis can be formulated as follows. It is necessary:

- to maximize current-passing to “open” pixels of anode structure;
- to minimize current-catch by the cathode grid (this current-catch is find as the sum of deposition of both the direct and reflected electron flows);
- to minimize the direct electron flow deposition to decelerating grid;
- to maximize current-catch of a reverse flow by the decelerating grid.

The important feature of systems with electron flow decelerating is the increased sensitivity to quadrature axiz speed of emitted electrons (in this case, longitudinal one is the speed vector component to direction from the emitter to the anode structure). Thus, the allowable trajectories obliquity describing a ratio of quadrature-axis and direct-axis components of velocity vector, depends on value both accelerating, and decelerating potential. Typical dependence is shown on Fig. 2.

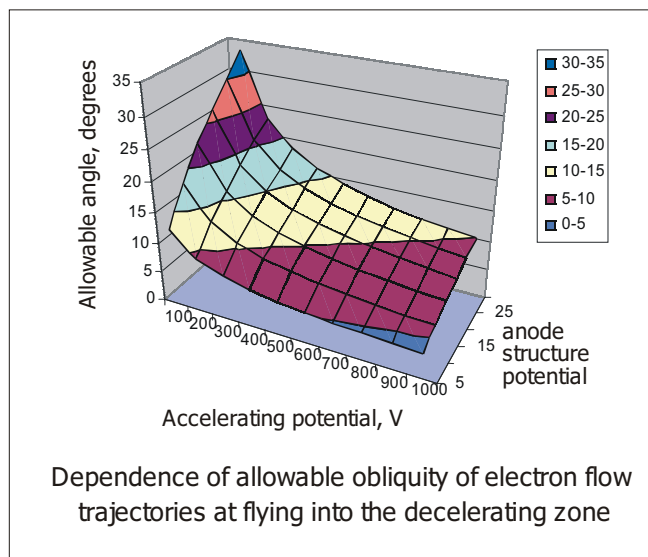


Fig.2

Results of finite-element model construction and the calculations carried out on its basis prove serviceability and existence of the optimum constructive decision. Influence of “open” pixels portion and “cathode grid – decelerating grid” distances to numerical values of the normalized currents of electrodes is estimated.

Then, the results of the numerical analysis of an opportunity of construction of indicator with anode structure pixels pitch of 50 microns are quoted. For reduction of current-catch by the cathode grid, its electrodes pitch has been accepted multiple to a pitch of a decelerating grid and anode structure, and amounts 150 microns. In connection with existence of transmitting symmetry, the fragment of indicator structure by 150x150 micron section and the height equal to “cathode-anode” distance was examined at calculation.

All calculations are carried out at the following values of parameters:

- cathode potential $U_k=0$ V
- cathode grid potential $U_{kc}=200$ V
- decelerating grid potential $U_{tc}=30$ V
- “open” pixel potential $U_{A1}=30$ V
- “closed” pixel potential $U_{A2}=30$ V
- “emitter-cathode grid” space $X_{\ominus-KP} = 800$ μm
- “decelerating grid – anode” space $X_{TC-A} = 200$ μm
- “cathode grid – decelerating grid” space X_{KC-TC} was varied
- the width of grids crosspieces is 10 microns, thickness is 20 microns.

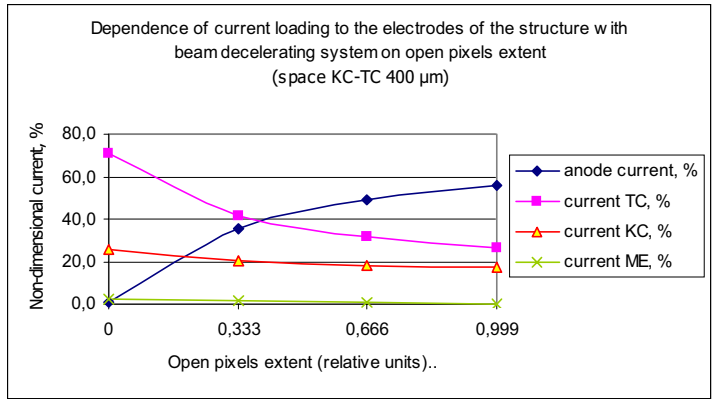


Fig. 3

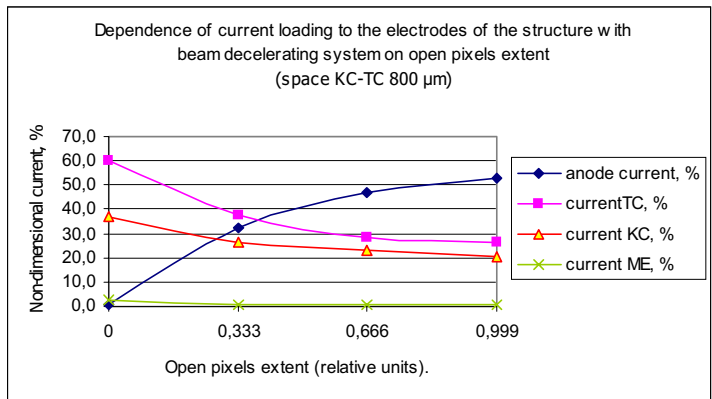


Fig.4

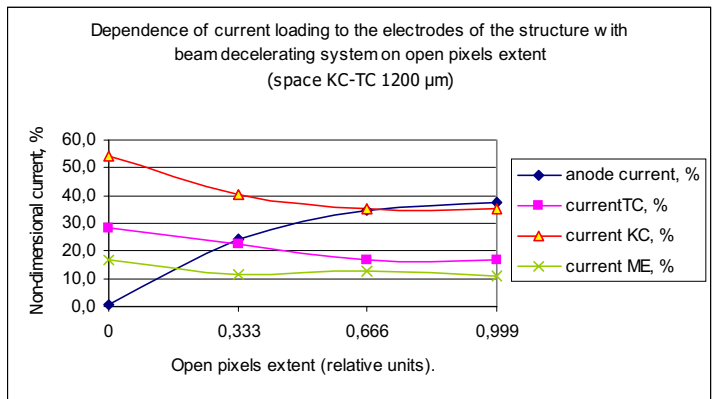


Fig.5

This work is executed by support of RFBR grant 05 02 - 17490

Basic Physics of formation of an electron flow in flat graphic indicators on the basis of planar-edge auto-emissive structures


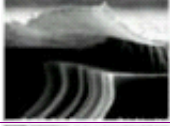


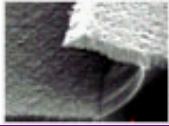
Abanshin N.P., Yakunin A.N., Gorfinkel B.I.

Research & Development Institute "Volga", Saratov, Russia

Research of influence of small disorders of planar-edge auto-emissive structures topology is important in the view of understanding of possible electron flow channeling mechanisms to an anode. It has experimentally been found that, depending on structure layers etching modes parameters, the obtained structures have differing electron-optical properties which are determined by their topological features.

Classification of auto-emissive structures by geometrical attributes is resulted in the Table 1. Difference in values of current-voltage characteristics obliquity tangent, at practically significant currents, reaches 1.6 times.

Table 1

Classification of auto-emissive structures by features of carbon film "cap peak" length, its orientation, and also molybdenum layer edge shape			
1	"Classical"	carbon "cap peak" of 0.3 μm length is oriented parallel to the "gate"-electrode plane	
2	"Peak up"	edge of carbon "cap peak" of 0.3 μm length is lifted to 0.1 μm	
3	"Peak down"	Edge of carbon "cap peak" of 0.3 μm length is pulled down to 0.1 μm to the "gate" side	
4	"Shorted carbon"	Carbon "cap peak" have diminished length of 0.03 μm	
5	"Sharp molybdenum"	Carbon "cap peak" of 0.03 μm length, molybdenum "fang" have profile with 45° obliquity	

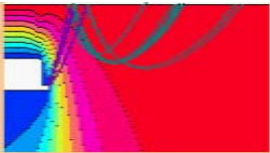
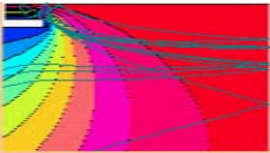
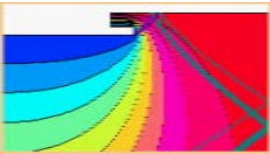
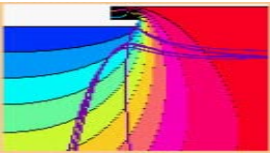
Analysis of results of electro-physical processes numerical modelling in auto-emissive structures, in view of secondary emission phenomena, allows

to choose four variants of typical trajectories of electron flow movement (see table 2):

1. The primary electron flow reaches a control electrode surface. The secondary electrons generated at its interaction with “gate” cannot overcome an existing potential barrier in near-electrode area of “gate” and are blocked on it. This type of movement is unproductive for auto-emissive structure because does not provide transportation of a secondary electron flow to the anode.

2. Secondary-emissive electrons have an energy and an eject direction from the “gate” surface, providing an opportunity of overcoming of a potential barrier in near-electrode areas. After reflection from the next cathode, the flow of secondary-emissive electrons moves aside the anode. This type of trajectories provides the channeling of a secondary-electron flow to the anode. It is necessary to note criticality of this type of trajectories in relation to parameters of generated secondary electrons – reflection in near-cathode area can occur both aside the anode, and aside “gate” (these electrons are blocked on the control electrode).

Table 2

Standard trajectories of electrons movement in auto-emissive structures	
1	 <p>All secondary electrons are “locked” on the “gate”</p>
2	 <p>A portion of secondary electrons arrive at the anode, the other ones are locked on the “gate”</p>
3	 <p>100% of secondary electrons arrive at the anode</p>
4	 <p>(Primary) auto-electrons trajectories</p>

1. The primary flow has a significant hade to the control electrode surface, accordingly secondary emissive electrons also have a significant eject angle from the “gate” surface. When secondary-emissive electrons energy is

higher than some value, the secondary electrons flow injects into area of anode attraction through the channel with the minimal caving in the potential. This channel is located in a plane of symmetry between the neighbour emitters. Allure of this type of trajectories is reliability of secondary-electron flow transportation to the anode

2. Auto-electrons will start from the emitter with positive (aside the anode) eject angles β and after reflection from near-cathode area of the neighbour emitter move aside the anode. Advantage of this type of movement is, first, exception of secondary emission mechanism from process of channeling of electron flow to the anode (only primary electrons fall to the anode) and, second, accordingly influences of a significant amount of additional factors.

Theoretical research of auto-emissive edge-type composite structures allowed to reveal also the features connected with that presence of small-structure heterogeneities on a dielectric layer surface promotes additional field concentration. The key moment for understanding of the mechanism of electric field intensity “strengthening” in edge-type auto-emissive structures with application of a dielectric layer as the emitter is fundamental expression for normal component of intensity on interface of two environments with various values of permittivity.

For case of a boundary surface “vacuum-dielectric” it is as following:

$$E_0 = \varepsilon_1 * E_1,$$

where E_0 and E_1 – normal component of electric field intensity in vacuum and in dielectric on their interface border, accordingly; ε_1 - permittivity of a material.

Mechanism of occurrence of area with the increased field intensity near to dielectric edge can be evidently illustrated with the results of calculation of electrostatic field equipotentials distribution in such structure. Fig. 1 shows the topogram of the found electrostatic field distribution at solving of a modelling task for an edge with the typical sizes of experimentally observable micro-heterogeneities. The equipotentials condensation near to edge top testifies to increase of electric field intensity in the noted area.

The degree of field concentration can be expressed through factor of strengthening of field intensity K_e (relation of field intensity in vacuum near to edge of dielectric microheterogeneity to value of field intensity in the same area in case of dielectric inclusion absence).

As a result of carrying out of numerical experiment, the existence of conditions when presence of a dielectric layer on the metal basis can play a role of amplifier of electric field intensity and stimulate occurrence of auto-emission from the dielectric microheterogeneities (a-P), is proved.

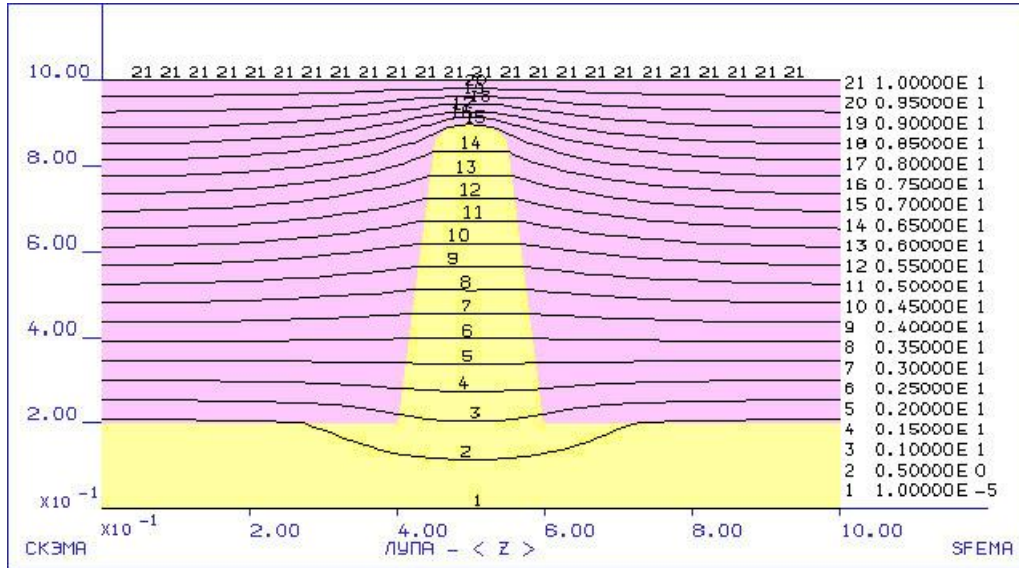


Fig. 1. Potentials field in dielectric edge

To estimate of possible K_e values, a series of finite-element calculations of electric field potential distribution in a flat space, at presence of microheterogeneities as sequence of edges with height a and thickness b , was carried out. Edges are oriented in direction perpendicular to the planes bounding the flat space. The edge curvature radius was considered equal to half of its thickness. The period of microheterogeneities sequence is indicated as L .

In this modelling task, the impedance boundary conditions chosen so that an electric field in the space were set, on topology and amplitude values, to field near to the emitter of the real auto-emissive structure, shown in table 2, was specified on planes.

Results of calculation of K_e , at variation of parameters a , b and L are shown on Fig. 2. All the dimensions on fig. 2 are normalized in relation to dielectric layer thickness $h=0.06$ micron. It is visible that, at the accepted microheterogeneities scales, the field gain factor can vary from 1.4 up to 2.6. Thus, gain factor K_e increase is connected to height increase, thickness decrease and increase of the microheterogeneities sequence period. At the identical sequence periods and heights, thinner microheterogeneities provide higher values field gain factor K_e (profit is approximately 20% at thickness twice decrease).

Influence of edge top radius of curvature to K_e is not significant: replacement of a rounded edge with flat top results in K_e decrease no more than to 5%. Transition to model axisymmetric tip microheterogeneities, instead of

edge ones, results in K_e increase to 20%. As a result, the maximal gain factor value reaches 3.14.

Influence of geometrical parameters of microheterogeneities located on the dielectric layer, to level field intensity gain factor K_e is investigated. It is shown, that, at allowable from the practical point of view assumptions, K_e is not low than 1.4, and at some sets of parameters can exceed 3.0. Results of calculation are shown on Fig. 2.

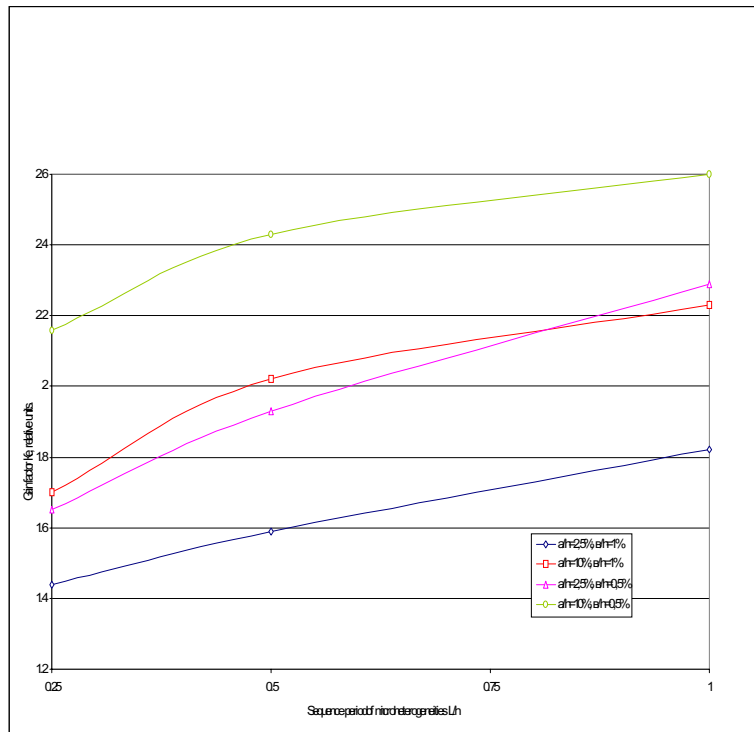


Fig. 2. Dependence of field strength gain factor K_e on parameters of dielectric coating microheterogeneities

It is found that strengthening of electric field intensity, by the dielectric microheterogeneities located near to open “metal-dielectric” contact surface, essentially depends on topology of cross-section of the dielectric layer and the metal substrate.

This work is executed by support of RFBR grant 05 02 - 17490

Questions of development of durable flat graphic indicators on the basis of planar-edge auto-emissive structures

Abanshin N.P., Yakunin A.N., Gorfinkel B.I.

Research & Development Institute “Volga”, Saratov, Russia

Structures of planar-edge auto-emissive emitters (see fig. 1) on the basis of diamond-like carbon thin films (on the accepted classification, such auto-emissive structures refers to “edge”), developed in last years by the experts of Research & Development Institute “Volga”, initiated the further development of perspective direction of creation of flat screens on field emission. Research of laws of electron flows formation in auto-emissive structures allows to obtain an information are in fundamental importance for revelation of ways of quality improvement of both electron-optical systems, and devices as a whole.

With that end in view, a mathematical models have been constructed, and a software complex was developed. The functionalities of the software complex include:

- solution of bidimensional and three-dimensional field tasks of electrophysics;
- trajectory analysis of auto-emissive electron flows;
- trajectory analysis of ionic streams;
- modelling of secondary emission effects;
- calculation of current-deposition and thermal loadings onto elements of auto-emissive structures;
- graphic interpretation of results of numerical calculation;
- use of methods of numerical models adaptation for numerical solution errors control.

The comparative analysis of results of the carried out numerical modelling has allowed to reveal the basic differences of processes of formation of electronic and ionic flows in auto-emissive massif on the basis of planar-edge (PE) emitters and Spindt’s cathodes. Due to them, the high longevity of flat graphic indicators on PE auto-emissive structures basis is provided.

Equipotentials character in classical auto-emissive structure as “Spindt’s cathode” shown on fig. 2, testifies to existence defocusing, for an electron flow, lens in the aperture of a control electrode (“gate”). For ionic stream, such electric field distribution is focusing on the contrary.

The results of modelling of ionic bombardment of auto-emissive structure are of largest interest. Character of trajectories in near-cathode areas and far from the “gate” plane is various as it is seen on Fig. 3 and Fig. 4. Practically in whole calculated area, ions trajectories are rectilinear and directed from the anode to the opposite plane. But near to the cathode and

“gate”, the contortion of the trajectories aside the cathode edges is observed. This effect is typical for ions with small kinetic energy (those from them, whose velocity is not enough for overcoming a potential barrier of control electrode).

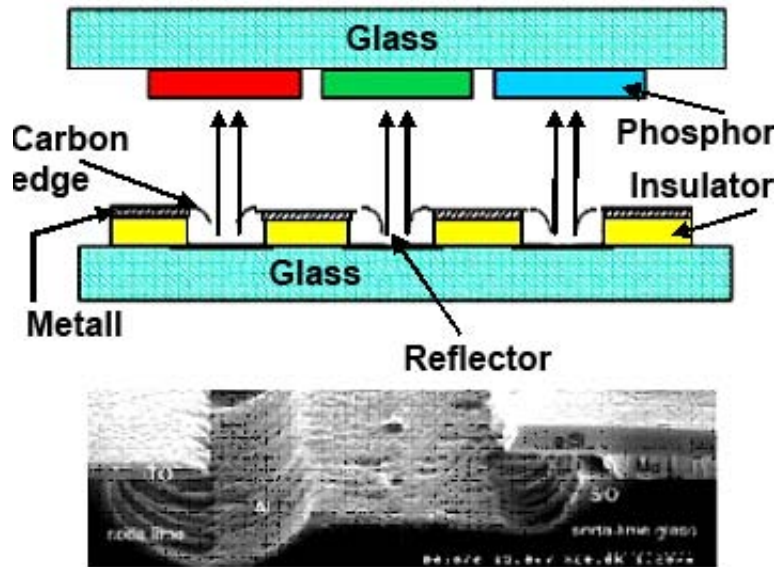


Fig.1 Topological features of planar auto-emissive structures

Developing of the generated electric field focusing action to ions becomes the reason of increased thermo-loading of the cathode due to ionic current deposition. As a result, a power density of edge loading can exceed power density of the “gate” loading on 5 orders.



Fig. 2. A field of potentials in near-cathode areas of Spindt's cathode.

The basic difference of edge PE design is the different structure of electric field (see Fig. 5): the equipotentials direction in near-cathode area is changed

approximately to 90° . Thus, some tilt of the equipotentials aside the “gate” is observed. Absence of full-blown maximum of field intensity is very important. As a result, emission current from the cathode is approximately regularly distributed in a significant angular segment.

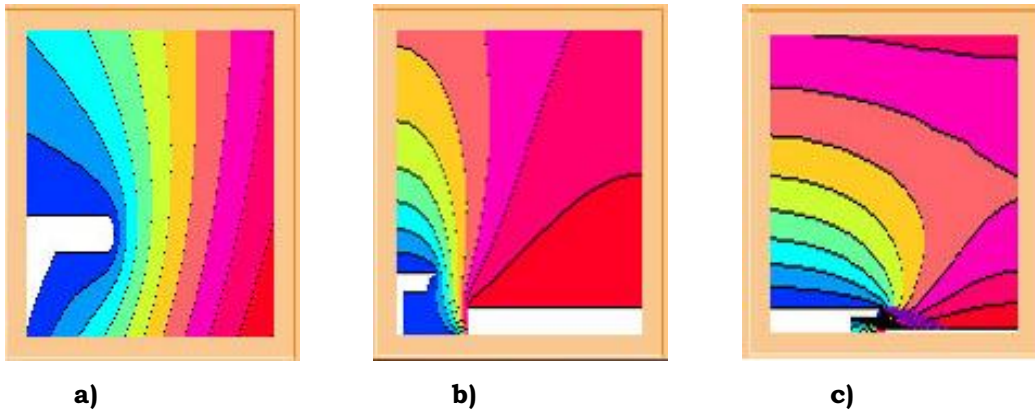


Fig. 5. Electric field equipotentials distribution: a – in near-cathode area; b – in “cathode-gate” area (extended scale); c – in “cathode-gate” area (reduced scale)

Between the “gate” and anode, in whole width of calculated area, there is a potential barrier as shown on Fig. 6. Its presence, on the one hand, complicates an opportunity of direct hit of electron macro-particles from the cathode to the anode, and on the other hand, results in evident complication of ions movement trajectories. It shows itself in occurrence of significant number of the trajectories directed along the cathode plane. First of all it touches ions with small energy, generated in neighbourhood of area «cathode – gate». Ions, being generated on distance from this area (closer to the anode), have classical trajectories of movement which were observed and in Spindt’s cathode structure (see fig. 7).



Fig. 6. (left) Potentials field and electron macro-particles movement trajectories in the “cathode-gate” area.

Fig. 7. (right) Potentials field and electron macro-particles movement trajectories in the near-cathode area.

Only 3.66% of the ion current common capacity falls to the emitter region; 97.6% of the ion current common capacity falls to cathode massif and space “cathode - sweeping electrode”; relation of the maximal specific load onto the emitter to the maximal specific load onto the cathode massif is 0.45. It is possible to note also the increased level of ion bombardment of the central part of the cathode electrode, but this part of the electrode has a reliable heat-conducting path on whole area to the substrate. It allows to predict good stability of the structure in relation to negative influence of factor of ionic bombardment to serviceability and longevity of the device.

Comparison of both structures from the point of view of their thermo-load will be correct when the integrated auto-emission current recalculated to separate pixel will be identical for them. Hence, and using of results of electron-optical calculation of auto-emissive structures, it is possible to obtain the following estimation (see the Table).

Table

#	Parameter name	Spindt's cathode	Edge structure	Relation of edge structure parameters to the ones of Spindt cathode	Inverse relation
1	Area of elementary emitting segment of the tip (spot with angle segment 40°, μm^2)	$2.3 \cdot 10^{-4}$	-----	-----	-----
2	Emitting area for one pixel, μm^2	1.15	791.65	690	$1.45 \cdot 10^{-3}$
3	Emission current density required for providing of the same pixel integral current, relative units	690	1	$1.45 \cdot 10^{-3}$	690
4	Power density of emitter thermo-load by ion current at emission of unit current density, rel. un	$1.2 \cdot 10^{-12}$	$5.0 \cdot 10^{-15}$	$4.16 \cdot 10^{-3}$	240
5	Power density of emitter thermo-load by ion current at emission of the same current, rel. un	$8.28 \cdot 10^{-10}$	$5.0 \cdot 10^{-15}$	$6.04 \cdot 10^{-6}$	$1.66 \cdot 10^5$
6	Power density of emitter thermo-load by ion current at emission of the same current (case of 200 emitting segment), rel. un	$3.31 \cdot 10^{-9}$	$1.0 \cdot 10^{-14}$	$3.02 \cdot 10^{-6}$	$3.31 \cdot 10^5$

The obtained estimation of indisputable advantages of PE auto-emissive structures finds also experimental confirmation: the developed sample of the graphic indicator on the base of planar-edge emitters kept good emission ability at tests within 1 year.

This work is executed by support of RFBR grant 05 02 - 17490

SPECTRAL-POLARIZING PROPERTIES AND LIGHT STABILITY OF FILM POLARIZERS WITH AZODYES

V. Agabekov, N. Ariko, L. Filippovich

Institute of Chemistry of New Materials of the National Academy of Sciences of Belarus, st.F.Skarini 36, 220141, Minsk-141, Belarus

Abstract

Linear film polarizers are made by introducing iodine or organic dyes into a stretched polyvinyl alcohol film. It is known that dyes are susceptible to UV radiation that causes their photodestruction and reduces the polarizing efficiency of a film as a result. Experimental investigations testify that velocity of photoreaction depends on different factors such as dye and polymer structure, dye concentration, film production conditions [1,2]. The earlier produced polarizers with azobenzeneazonaphtalene dyes [3] are characterized by high polarizing efficiency. However, in order to use them in practice it is necessary to examine their light stability and to find ways for its increasing.

The present paper contains the results on the study of UV photostability of uniaxial oriented PVA-films containing azobenzeneazonaphtalene dyes and their correlation with spectral-polarizing performance. The aim is to develop the technology of manufacturing of a light stable film polarizers.

Experiment

Water-soluble azobenzeneazonaphtalene dyes were synthesized in accordance with a known procedure usually used for synthesis of azocompounds but improved in terms of azocoupling reaction which allows to avoid formation of trisazenes and products of their transformation [4].

Films of 60-70 mm thick were cast from 10% PVA solutions (Moviol 28-99) with concentrations of dye, gelling and plasticizing agents as described in [5]. Uniaxial orientation were carried out in water, in 10-15 w. % MgSO_4 solution or in 4% boron hydroxide (boric acid, H_3BO_3) solution. Then the films were dried in air at different temperature. The stretch ration of all samples was 4.

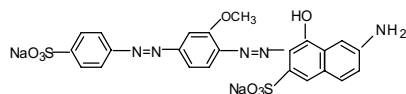
UV photostability of polarizing films was studied using unfiltered radiation of high-pressure Hg-lamp DRSH-1000 with power at 0,12 W. At exposure temperature of sample was 20-22 °C.

Spectral measurements of film examples were made with spectrometer Specord UV VIS in unpolarized light with correction to protection TAC films.

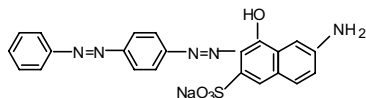
Results and discussions

The examined dyes are secondary azo dyes of azobenzeneazonaphtalene group. Dye M_1 is structurally similar to dye M_3 with the difference that the former has $-\text{OCH}_3$ and $-\text{OSO}_3\text{H}$ groups in phenyl rings additionally.

M₁



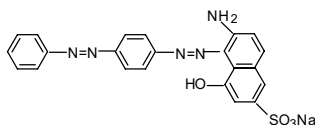
M₂



As a result they have similar absorption spectra with two wide bands: 505-510 and 595-600 nm in film with M₁; 435-490 and 575-580 nm in film with M₃. In these molecules there are the conjugated double bond chain connecting their auxochromes and another conjugate electronic system of naphthalene nucleus and its substitutes. The systems are crossed that leads to widening of absorption bands.

Spectrum of M₂ has one absorption band with maximum at 555-565 nm which is narrower than bands in spectra of M₁ and M₃.

M₂



As is apparent from structure of M₂ in its molecule it is possible the formation of single conjugate system (NH₂- group is included in this system and OH-group being in *peri* position to azo group is connected with last by hydrogen bond).

On exposure to UV light in spectra of colored films the intensity of longwave absorption maximum continuously decreases and a band at 658-659 nm appears in films with M₂ that testifies to photo destruction process of azo dyes.

The investigation results of photo destruction kinetics of M₁, M₂ and M₃ shown that a form of kinetic curve of film fading depends on a dye concentration. At low dye concentration (< 0,1 w %) photo reaction proceeds as first order reaction (for example results for M₁, fig.1.). Increasing in dye concentration changes photo reaction kinetics (fig.2). For films with M₂ the reaction order become equal to 0 (curve 2) whereas in case of films with M₁ and M₃ kinetics become more complex and plateau or maximum appeared on kinetic curves.

The increasing of dye concentration also reduces a photo reaction velocity.

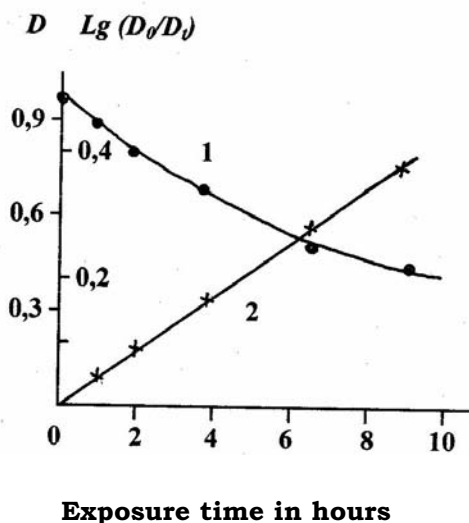


Figure 1 Kinetic curve of M_1 photodestruction in PVA-film (1) and its semi-logarithmic anamorphoza (2). $[M_1] = 0,05$ w.%. Stretching of film in $MgSO_4$ or H_3BO_3 solutions.

These effects are well explained by aggregation of dye molecules in polymeric matrix. According to papers [6, 7] aggregation is one of the factors determining a degree of film color fading.

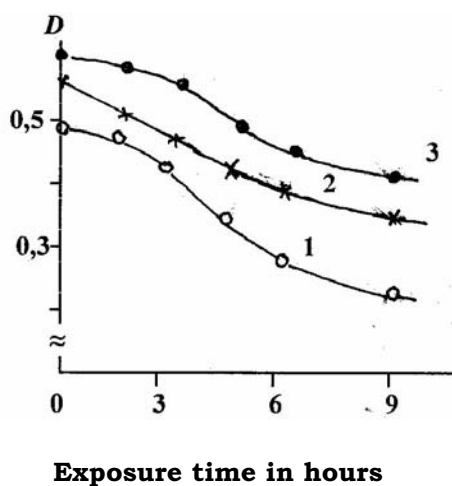
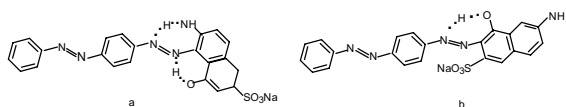


Figure 2 Kinetic curves of fading of PVA-films colored by M_1 (1), M_2 (2), M_3 (3). Dye concentration in films is 0,4 w. %. Stretching in H_3BO_3 solution.

Zero-order reaction for M_2 and complex character of kinetic curves for M_1 and M_3 indicate that dyes are in polydisperse state and M_1 and M_3 form bigger aggregates than M_2 . Lower aggregation of M_2 is connected with the possibility to form two intramolecular hydrogen bonds between electron-donor substitutes and azo group (a) whereas M_1 and M_3 molecules are able to form only one H-bond (b) which is weakened by steric hindrances: a repul-

sion between the sulfonic group and unshared electrons of N results in twist C-N bond.



It is known that uniaxial orientation of PVA-films is carried out in different salt and boron-containing solutions [8, 9]. Such film treatment must influence on structure of polymer matrix in which dye molecules are incorporated. In order to clarify this question a study on spectral-polarizing and light stability properties of films stretched in water, in solutions of magnesium sulfate and boric acid has been fulfilled. The effect of film drying temperature ranged from 20 to 105°C has also been examined. The influence of the above-mentioned factors on polymeric matrix structure has been tested by X-ray diffraction analysis by Dron-3.

It is established that nature of solution affecting on a film makes low influence on optical and polarizing properties but changes a lot film light stability. As fig. 3 shows boric acid-treated films are most resistant to UV radiation.

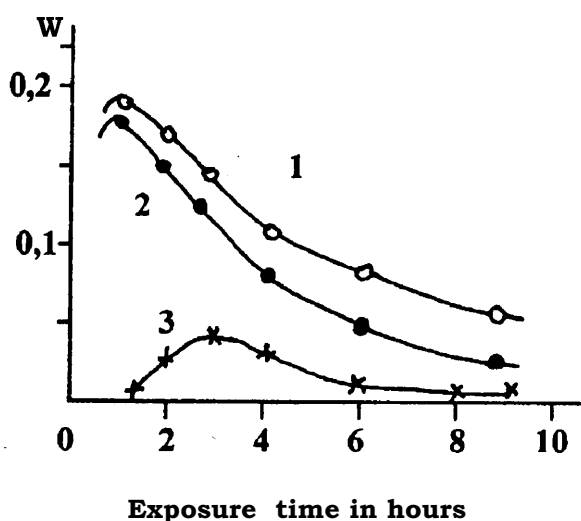


Figure 3 Velocity d of photodestruction of M_1 in PVA-films orientated in water (1), $MgSO_4$ (2) and H_3BO_3 . $[M_1] = 0,1$ w.%.

Light stability of films orientated in water or in $MgSO_4$ solution appeared to be susceptible to drying temperature (fig.4). It is seen that films heated at temperature $>60^\circ C$ lose their color faster than those heated at temperature $<60^\circ C$.

Similar influence of drying temperature on photodestruction velocity of films treated by boric acid was not observed (fig.4).

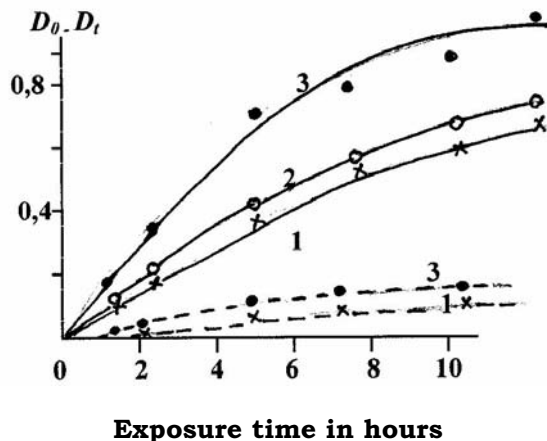


Figure 4 Kinetic curves of dye photodestruction in PVA-films dried at 20-37°C (1), 60°C (2) and 90-105°C (3) [M_1] = 0,2 w %. Stretching in $MgSO_4$ (—) and H_3BO_3 (---) solutions.

It is quite probable that these results are explained by influence of orientation and drying conditions on polymeric structure and matrix-dye interaction.

It is known that PVA-film structure is heterogeneous and includes both crystalline and amorphous segments [10]. It is proved now that dye molecules are incorporated not only in amorphous regions (as it was earlier thought) but also in film crystalline phase.

Bonds between dye and polymer chains are stronger in more compact crystalline regions than in disorder amorphous phase.

The X-ray phase analysis indicates that a peak of crystalline phase observed in all films is broadening after H_3BO_3 -treatment of films as a result of the formation of cross-linked structure due to formation of ether bridges.

Such structure facilitates both film dye orientation and interaction between dye molecules and PVA-chains.

Figure 5 demonstrates the influence of drying temperature on quantity of crystal phase in film. At temperature $>60^\circ C$ considerable increasing of crystalline phase in films treated in water or in $MgSO_4$ solution is observed. But the ratio between amorphous and crystalline phases is less sensitive to heating temperature in films treated by boric acid.

Probably cross-linked polymer structure has a higher temperature of transition to glassiness state (for usual PVA it is equal to $85-90^\circ C$).

During of film drying process water molecules unbounded with polymer matrix are removing first of all. The removing of bound water takes place at higher temperature and this process is accelerated after polymer transition

in glassiness state. As a result quantity of crystalline phase increases in films treated by MgSO_4 solution (fig. 5).

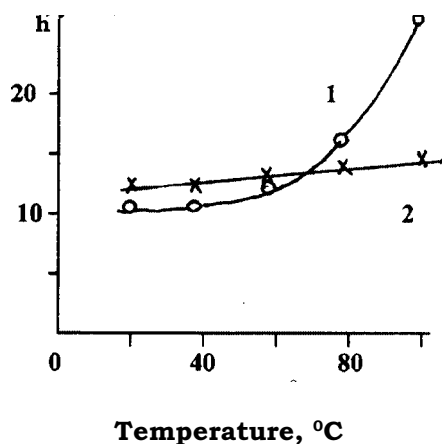


Figure 5 Influence of drying temperature on height of peak determining quantity of crystalline phase in PVA-film. Stretching of films in MgSO_4 (1) and H_3BO_3 (2) solutions. $[M_1] = 0,4 \text{ w \%}$.

In case of films treated by boric acid solution the removing of bound water insignificantly depends on drying temperature because polymer matrix does not essentially change itself structure at 20-105°C.

It is very interesting that films containing more water are subjected to photodestruction far less than films with little water content. Probably this fact is connected with solvation processes playing a significant role in proceeding of photoreaction: the formation of solvates prevents dye fading and on the contrary the destruction of solvates accelerates this process.

Thus, the conditions of chemical treatment of colored PVA-films and following drying allow to affect on light stability of dyes incorporated in PVA matrix. It was designed a method of film treatment by boric acid solution containing special additives which promote the formation of more stable polymer structure.

On base of the investigation results the optimum ration of dye and polymer, the conditions of chemical treatment and following drying of films have been offered for technological process of fabrication of film polarizers with azobenzene-azonaphthalene dyes.

Literature

1. I.D.S. Kliger et.al. Polarized Light in Optics and Spectroscopy. Acad. Press, San Diego. 1990.
2. W. A. Shurkliff. Polarized Light. M, 1965.
3. V. Agabekov, S. Shahab, N. Ariko, T. Kosmacheva, N. Ivanova. Proc. 10th Symposium SID «Advanced Display Technologies». P.148 (september 2001, Minsk).

4. P. Malashko, V. Tarasevich, V. Agabekov. Vesti NAN Belarus, ser. chem. nauk. 2003, #4, p.105.
5. N. Ariko, L. Filippovich, V. Agabekov, S. Shahab, P. Malashko. Vesti NAN Belarus, ser. chem. nauk. 2002, #3, p.71.
6. C. Giles, R. Haslam. Text. Res. J. 1978, v.48, p. 490.
7. C. Giles, J. de Bernat. Text. Res. J. 1976, v. 46, p. 673.
8. Patent USA 4 514 559.
9. Patent USA 5 310 509.
10. A. Vogeve, L. Margulies, Y. Mazur. J. Amer. Chem. Soc. 1970, v. 92, p.6059.

Pretransitional chiral LC phase: optical characteristics and lasing

A. Chanishvili, D. Chilaia, G. Chilaya, G. Petriashvili

Institute of Cybernetics of Georgian Academy of Sciences, Euli str. 5, 0186, Tbilisi, Georgia

R. Barberi, R. Bartolino, M.P. De Santo, M.A. Matranga, F. Ciuchi

Licryl Laboratory, c/o Physics Department, University of Calabria, via Pietro Bucci, 87036 Rende (CS), Italy

The pretransitional phase was observed in three component chiral systems, consisted of two nematogenic liquid crystals (LC) with different phase sequences (one with smectic A phase and another with smectic C phase) and optically active nonmesomorphic dopant. In the temperature interval, corresponding to the intermediate phase, between cholesteric and smectic phases an unusually low intensity of transmitted light ($\sim 20\%$) was observed. The investigation of circularly polarized light shows that this structure transmitted both the right and left handed circularly polarized light. We doped to this 3-component mixture the luminescent dye. We investigated the luminescent characteristics for the case when the wavelength of selective reflection band coincides with luminescence wavelengths in cholesteric and the intermediate phases. The suppression of luminescence was greater in the intermediate phase than in the cholesteric phase. To obtain laser emission in intermediate phase the samples were pumped by nitrogen laser. The lasing was observed at the long wavelength edge of the photonic band gap. Regarding the structure of this intermediate phase an alternative model of twist grain boundary (TGB) phase is proposed. The model represents a layered structure where between cholesteric layers the smectic A layers oriented normally to the cell surfaces, and thus with director parallel to the surfaces are formed.

The cholesteric liquid crystals (CLC) possess selective reflection properties: the maximum of Bragg selective reflection occurs at the wavelength $\lambda_B = Pn$ with a bandwidth $\Delta\lambda = P\Delta n$, where n is the average refractive index, Δn is the optical anisotropy of the material and P is the helical pitch accordingly. The reflected light is circularly polarized; the reflected and transmitted beams have opposite handedness [1]. In an induced cholesteric system which represents the mixture of nematic LC and chiral nonmesomorphic or mesomorphic dopant [2-4], if a smectogenic substance is used as a nematic host, the typical picture of pre-transitional phenomena is observed: due to the effect of helix divergence near the cholesteric smectic A phase transition, the pitch increases with decreasing temperature [5]. In spirit of de Gennes theory, near the phase transition from the cholesteric to smectic A phase, an intermediate phase, called "Twist Grain Boundary" (TGB), was predicted in [6]. This complex "defect" phase represents the frustrated phase derived from chiral molecules and stabilized by screw dislocation [7]. The term frustration describes any type of competing interactions for a different type of ordered state. And TGB phase arises as a competition between helical structure of the cholesteric phase (appeared at higher temperatures) and layered struc-

ture of the smectic phase (appeared at lower temperatures). This competition revealed in the case of low pitch (high chirality).

The pretransitional phase was observed in three component chiral systems, consisted of two nematogenic liquid crystals with different phase sequences (one with smectic A phase and another with smectic C phase) and optically active nonmesomorphic dopant [8-10]. This ternary system consisted of two nematics: 4-cyano-4'-n-octylbiphenyl (8CB, Merck) and 4-n-octyloxybenzoate (HOPOOB, NIOPIK, Moscow). As a chiral dopant, tigogenin caprate (TC) [5] was used, TC was synthesized from natural product tigogenin (Institute of PharmacoChemistry, Academy of Sciences of Georgia).

The mixture - 82% (80% 8CB + 20% HOPOOB) + 18% TC - possess the cholesteric phase in temperature range 43.8-47.4°C and the intermediate phase between cholesteric and smectic A phase in the range 41.6-43.8°C. Fig 1 shows the temperature dependence on the wavelength of the Bragg peak λ_B .

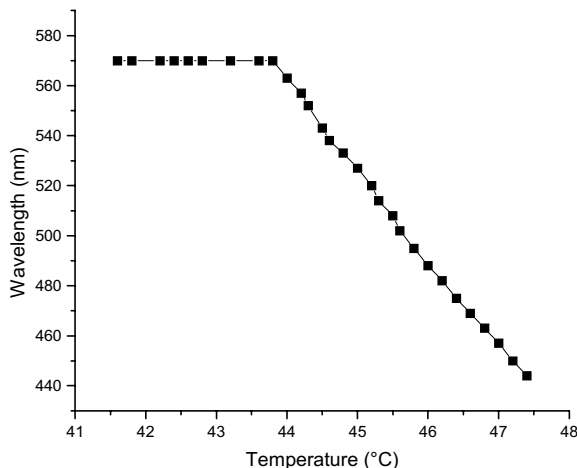


Fig.1. Temperature dependence of the transmission peak wavelength λ_B .

Spectroscopic measurements for nonpolarized light show that in the cholesteric phase the output intensity is equal approximately to 50% with respect to the input intensity. But in the temperature interval, corresponding to the intermediate phase, λ_B ceases changing with temperature and an unusually low intensity of transmitted light (~20%) is observed [8]. The investigation of circularly polarized light shows that this structure transmitted both the right and left handed circularly polarized light [8]. Calorimetric investigations gave evidence that the intermediate state is a separated twisted mesophase. X-ray investigations pointed out that this phase has a layered structure and the layer spacing of 33 Å corresponds to that in the S_A phase [9]. This result allowed us to identify this pretransitional phase as the TGB

phase. However, besides of the anomalous selective reflection, the texture, the pitch dependence on temperature and the behaviour in an electric field obtained in pretransitional phase [8-11] differed from those observed in conventional TGB phase.

The explanation of both the right and left circularly polarized light reflection can be found in the biological structures. The wings of rare kind of beetles *Plusiothis resplendens* have layered structure: between layers with cholesteric like structure, possessing the same handedness, a layer with unidirectional orientation of fibrils, owning half-wave ($\lambda/2$) plate properties, is arranged [12]. This type of structure reflects both right and left circularly polarized light. Recently a look-alike structure was proposed in [13].

If a small amount of dichroic dye (“guest”), possessing linear dichroic absorption, is dissolved in nematic LC (“host”), the dye molecules align across the preferable orientation of the LC molecules (director) [1]. The obtained mixture possesses dichroic absorption. The same effect is observed for a cholesteric liquid crystal (CLC) host: if a small amount of dye, possessing linear dichroic absorption, is dissolved in the CLC, the elongated dye molecules follow the helical director orientation and the helical arrangement transforms linear dichroism into circular dichroism. The induced circular dichroism is given by $D = (I_l - I_r) / (I_l + I_r)$, where I_l and I_r are the light transmission coefficients for left-handed and right-handed circularly polarized light, respectively. Induced circular dichroism was studied by several authors [14-19]. It was investigated even for a dye possessing simultaneously both positive and negative dichroism [19]. With the sign inversion of the linear dichroism, the sign of circular dichroism is changed, as well. The data given in [14-19] were obtained for structures where the pitch was greater than the absorption wavelength of the dye. However, the absorption is suppressed when the wavelengths of absorption and selective reflection coincide. Since the arrangement of the molecules is helical, the absorption of light with the diffracted polarization undergoes an abrupt change near the region of selective reflection. On the short wavelength side of Bragg reflection, the electric vector is perpendicular to the long axis of the molecules, i. e. to the absorbing effective oscillators in dyes with positive dichroism. This effect is analogous in many respects to the anomalous absorption of X-rays (Borrmann effect) that occurs as a result of diffraction in ordinary crystals. Some measurements and the corresponding theoretical works show a quantitative agreement between the theory and the experiment 20-23].

If we now add a dichroic luminescent dye to a CLC, the LC structure acquires a property of polarizing luminescence. Investigation of the polarized irradiation in the luminescent dye doped nematics for orientational order parameter estimation was carried out in [24,25]. The polarizing characteristics of luminescence when the selective reflection spectral region (“stop band”) of cholesteric LC was far away from emission wavelengths was studied in [26] and when stop band overlapped the embedded dye emission were investigated in [27-35]. The helical structure suppress the photoluminescence of one sense of circular polarization and emission is circularly polar-

ized. The degree of circular polarization luminescence is quantified by dissymmetry factor g_c : $g_c = 2 (I_L - I_R / I_L + I_R)$, where I_L and I_R are emission intensities of left-handed and right-handed circularly polarized light, respectively.

Consideration of selective reflection band as a photonic band gap [36] stimulated the observation and investigation of lasing in thermotropic [37-40] and lyotropic [41] CLCs, blue phases [42], chiral smectic C liquid crystals [43], network polymers [44], elastomers [45] and glass forming CLCs [46]. Though the lasing in cholesterics was obtained long time ago [47]; Tunability of lasing in these systems was achieved changing the chiral dopant concentration in different cells, varying the temperature, applying a mechanical stress or an electric field. Recently laser emission was demonstrated by using two new strategies: phototransformation of constituent molecules and pitch gradient inside the cell [48-51].

For investigation luminescence characteristics and obtain lasing effect, in the intermediate phase, we doped this 3 component mixture with the luminescent dye 4-dicyanomethylene-2-methyl-6-(*p*-dimethylaminostyryl)-4H-pyran (DCM from Exciton). The concentration of the dye was 0.5% of weight which changed very slightly the selective reflection characteristics. A 40 μm thick cell was made by two glass plates coated with rubbed polyimide in order to obtain the planar alignment of the CLC film. A conventional violet light-emitting diode (LED) with an emission peak at 405 nm was used for fluorescence measurements. For laser emission the samples were pumped by nitrogen laser (Model VSL-337ND-S, Spectra-Physics). The pulse wavelength, width, and repetition rate were 337 nm, 4ns and 1–10 Hz, respectively. The laser beam was focused by a lens ($f = 10$ cm) to reduce the spot size onto the cell to few hundreds of micrometers. The pump beam hits the sample at 45° with respect to the cell normal, a usual experimental geometry for this kind of experiment. The fiberoptic spectrophotometer Avantes Fiberoptics AVS-S2000 was used as detector.

Luminescence spectra obtained by LED illumination were acquired in cooling regime of temperature. On the top of Fig.2 the luminescence spectra in isotropic phase, in cholesteric phase close to intermediate phase transition and in intermediate phase are shown. As the figure shows, the suppression of luminescence is greater in the intermediate phase than in the cholesteric phase. Then the temperature was stabilised in the intermediate phase at 42°C to obtain lasing. The excitation energy was about $1\mu\text{J}$. As seen on the bottom of Fig.2 the lasing was observed at the long wavelength edge of the selective reflection band.

Thus we observed for the first time lasing in the intermediate phase between the cholesteric and smectic A phase. Regarding the structure of this intermediate phase in the first publication [8] we mainly considered the mosaic structure of cholesteric phase, though indicated also the possibility of TGB phase formation. In the second paper [9], where we carried out calorimetric and X-ray measurements, we preferred the TGB phase explanation.

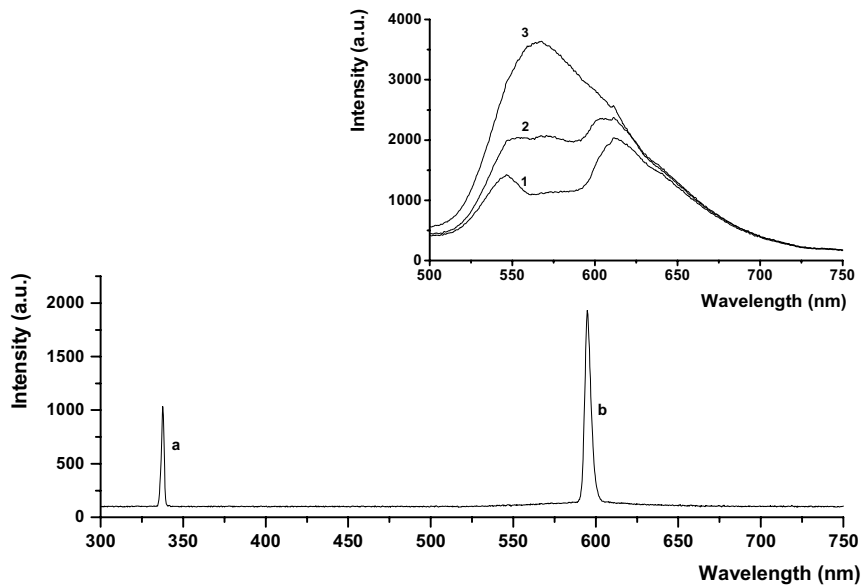


Fig.2. Luminescence spectra in the intermediate (1), cholesteric (2) and isotropic (3) phases at temperatures 42°C, 44°C and 50°C respectively (upper graph). In the lower graph the peaks of laser generation from the intermediate phase (b) and pump beam (a) are shown.

After further considerations we do not exclude that this phase could be similar to structural composition used in [13] where between two cholesteric layers with the same handedness a nematic layer, owning phase retarder properties, is arranged. In our case, instead of nematic layers, smectic A layers oriented normal to the cell surfaces, and thus with director parallel to surfaces, could exist. One or more these three layered structures, consisting in two cholesteric layers with a smectic layer between them, could be packed between the glass plates. (In Fig.3 the proposed structure is demonstrated). Or, instead of cholesteric layers, the helical structure could be the TGB phase itself. The structural properties of this phase are still under investigation.

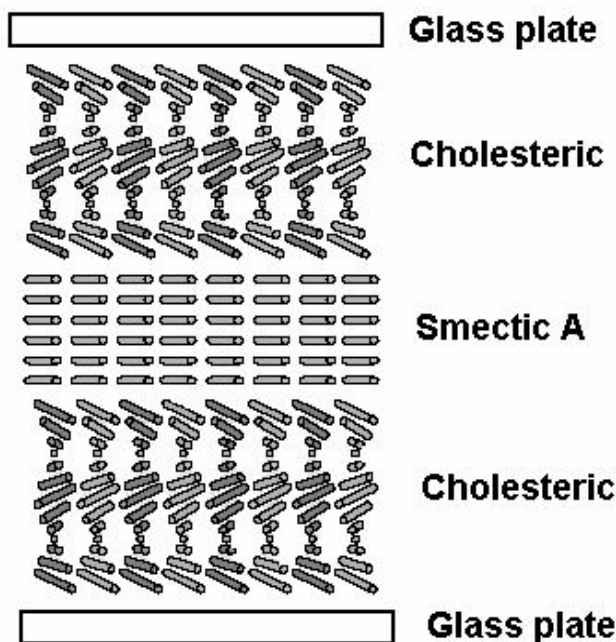


Fig. 3. The model of layered structure

References

1. G. Chilaya, Cholesteric Liquid Crystals: Optics, Electrooptics and Photooptics, chap. 6 in "Chirality in Liquid Crystals", edited by H. Kitzerow and Ch. Bahr, series Partially Ordered Systems, Springer Verlag, NY (2001).
2. G. Chilaya, Rev. Phys.Appliq., **16**, pp.193-208, (1981).
3. G.Chilaya and L.N.Lisetski, Sov.Phys.Usp. **24**, pp.496-510, (1981).
4. G.S.Chilaya and L.N.Lisetski, Mol.Cryst.Liq.Cryst., **140**, pp.243-286, (1986).
5. G.S.Chilaya, Z.M.Elashvili, L.N.Lisetski, T.S.Piliashvili, K.D.Vinokur, Induced cholesteric systems: helix pitch dependence on temperature and concentration, Mol.Cryst.Liq.Cryst., **74**, pp.261-273, (1981).
6. S.R.Renn and T.C.Lubensky, Phys.Rev.A, **38**, pp.2132, (1988).
7. H.-S. Kitzerow, Twist Grain Boundary Phases, chap. 10 in "Chirality in Liquid Crystals", edited by H.-S. Kitzerow and Ch. Bahr, series Partially Ordered Systems, Springer Verlag, NY, (2001).
8. G.Chilaya, A, Chanishvili, G.Petriashvili and D.Sikharulidze, Mol.Cryst.Liq.Cryst., **261**, pp.233-239, (1995).
9. A.Chanishvili, G.Chilaya, M.Neundorf, G.Pelzl, G.Petriashvili, Cryst. Res. Technol., **31**, pp.679-683, (1996).
10. G.Chilaya, G.Petriashvili, A.Chanishvili, D.Sikharulidze, Mol. Materials, **8**, pp.245-255, (1997).
11. G. S. Chilaya, Crystallography Reports, **45**, p.871, (2000).

12. Bouligand, Y., Liquid crystalline order in biological materials. In: Blumstein, A. (Ed.), Liquid crystalline order in polymers. Academic Press, New York, pp.261-297 (1978)
13. M. H. Song, B. Park, K.-C. Shin, T. Ohta, Y. Tsunoda, H. Hoshi, Y. Takanishi, K. Ishikawa, J. Watanabe, S. Nishimura, T. Toyooka, Z. Zhu, T. M. Swager, H. Takezoe, *Adv. Mater.*, **16**, p.779 (2004).
14. F.D.Saeva, J.J.Wysocki, *J. Am. Chem. Soc.* **94**, 135 (1971).
15. I.Chabay, *Chem. Phys. Lett.* **17**, 283 (1972).
16. E.Sackman, J.Voss, *Chem. Phys. Lett.* **14**, 528 (1972).
17. G.Holzwarth, N.A.W. Holzwarth, *J. Opt. Soc. Am.* **63**, 324 (1973).
18. H.J.Krabbe, H.Heggemeier, B.Schrader, E.H.Korte, *Angew. Chem.* **89**, 831 (1977).
19. D.G.Khoshtaria, G.S.Chilaya, A.V.Ivashchenko, V.G.Rumiantsev, 5th International Liquid Crystal Conference of Socialist Countries, Odessa (USSR), 1983, Abstracts,V1,Part 2, P.94.
20. V.A.Beliakov, V.E.Dmitrienko and V.P.Orlov, *Sov. Phys. Uspekhi* **22**,63 (1979).
21. V.A.Beliakov, V.E.Dmitrienko, *Sov. Phys. Solid State* **18**, 1681 (1976).
22. K.A.Suresh,, *Mol. Cryst. Liquid Cryst.* **35**, 267 (1976).
23. S.N.Aronishidze, V.E.Dmitrienko D.G.Khoshtaria and G.S.Chilaya, *JETP Lett.* **32**,17 (1980)
24. E. Sackman, D.Rehm, *Chem. Phys. Lett.* **4**, 537 (1970)
25. V.K.Dolganov and B.M.Bolotin, *Mol. Cryst. Liq. Cryst.*, **47**,179 (1978)
26. P. Pollmann, K.-J. Mainusch, H. Stegemeyer, *Z. Physik. Chem. (NF)* **103**, 295 (1976)
27. B.M. Conger, J.C. Mastrangelo, S.H. Chen, *Macromolecules* **30**, 4049 (1997)
28. H. Shi, B.M. Conger, D. Katsis, S.H. Chen, *Liq. Cryst.* **24**,163 (1998)
29. B.M. Conger, D. Katsis, J.C. Mastrangelo, S.H. Chen, *J.Phys. Chem. A* **102**, 9213 (1998)
30. D. Katsis, A.W. Schmid, S.H. Chen, *Liq. Cryst.* **26**, 181(1999)
31. S.H. Chen, D. Katsis, A.W. Schmid, J.C. Mastrangelo, T.Tsutsui, T.N. Blanton, *Nature* **397**, 506 (1999)
32. M. Voigt, M. Chambers, M. Grell, *Chem. Phys. Lett.* **347**, 173 (2001)
33. J. Schmidtke and W. Stille, *Eur. Phys. J.* **B 31**, 179 (2003)
34. A. Yu. Bobrovsky, N. I. Boiko, V. P. Shibaev, and J. H. Wendorff, *Adv. Mater.* **15**, 282 (2003)
35. K. L. Woon, M. O'Neill, G. J. Richards, M. P. Aldred, S. M. Kelly, and A. M. Fox, *Adv. Mater.* **15**, 1555 (2003)
36. Dowling, M.Scalora, M.J.Bloemer, C.M.Bowden, *J.Appl.Phys.*, **75**, p.1896, (1994).
37. V.I. Kopp, B.Fan, H.K.M. Vithana, A.Z. Genack, *Optics Letters*, **23**, p.1709, (1998).
38. A.Munoz, P.Palfy-Muhoray and B.Taheri, *Opt.Lett*, **26**, p.804, (2001).

39. F.Araoka, K.-C.Shin, Y.Takanishi, K.Ishikawa, H.Takezoe, Z.G.Zhu and T.M.Swager, *J.Appl.Phys.*, **94**, 279, (2003).
40. M.Chambers, M.Fox, M.Grell and J.Hill, *Adv.Funct.Mater.*, **12**, p.808, (2002).
41. P.V.Shibaev, K.Tang, A.Z.Genack, V.Kopp and M.M.Green, *Macromolecules*, **35**, p.3022, (2002).
42. W.Y.Cao, A.Munoz, P.Palffy-Muhoray and B.Taheri, *Nature Mater.*, **1** p.111, (2002).
43. M.Ozaki, M.Kasano, D.Ganzke, W.Haase and K.Yoshino, *Adv.Mater.*, **14**, p.306, (2002).
44. J.Schmidtke, W.Stille, H.Finkelmann and S.T.Kim, *Adv.Mater.*, **14**, p.746, (2002).
45. H.Finkelmann, S.T.Kim, A.Munoz, P.Palffy-Muhoray and B.Taheri, *Adv. Mater.*, **13**, p.1069, (2001).
46. P.V. Shibaev, V. Kopp, A. Genack, E. Hanelt, *Liquid Crystals*, **30**, pp.1391-1400, (2003).
47. I.P.Il'chishin, E.A.Tikhonov, V.G.Tischenko and M.T.Shpak, *JETP Lett.*, **32**, p.27, (1980).
48. A. Chanishvili, G. Chilaya, G. Petriashvili, R. Barberi, R. Bartolino, G. Cipparrone, A. Mazzulla, L. Oriol, *Appl. Phys. Lett.*, V.83, N. 23, pp.5353-5355, (2003).
49. A. Chanishvili, G. Chilaya, G. Petriashvili, R. Barberi, R. Bartolino, G. Cipparrone, A. Mazzulla, L. Oriol, *Adv. Mat.*, **16**, N.9-10, pp. 791-794, (2004).
50. S. Furumi, S. Yokoyama, A. Otomo, and S. Mashiko, *Appl. Phys. Lett.*, **84(14)**, p.2491, (2004).
51. A. Chanishvili, G. Chilaya, G. Petriashvili, R. Barberi, R. Bartolino, G. Cipparrone, A. Mazzulla, R. Gimenez, L. Oriol, M. Pinol, *Appl. Phys. Lett.*, **86**, pp. 051107, (2005).

The Analysis of Principles of display Readability Improvement for display system for mobile application.

M.V. Dyatlov

ZAO "KB Technotronic", 124040, Russia, Moscow, Leningradskiy prospect 24-A,
Tel: +7(095)7481144, Fax: +7(095)7481141
e-mail: kbtdir@mail.ru, www: www.kbtec.ru

Visual information reading performance analysis shows that reading always takes place in some ambient conditions: sometime comfortable for the operator, sometimes not.

The general visual information reading performance criteria's include:

1. Average operator reaction time, when the information appears.
2. Average operators reaction error when the information appears.
3. Visual information search time.
4. Probability of the necessary information correct recognizing.
5. Long time working operator comfortability of the mobile display.

Mobile display information reading improvement principles and performance factors include:

1. System factors. That are defined the firstly in optimal graphical screen design.
2. Human Factors. That includes specific factors of displayed information reading by operator (driver, pilot).
3. Hardware factors, that include certain mobile display design and its optical and ergonomic performance parameters.
4. Psycho – physiological factors that are defined by the requirements to the physical and psychical operators conditions.

The information readability improvements system factors include:

1) Display only and all the necessary data to the user. At any step in the sequence, ensure that whatever data a user needs will be available for display. Tailor the display of the data to user needs, providing only necessary and immediately usable data at any step in the process. The designer of user interface software must employ some method of task analysis to determine a user's detailed information requirements.

2) Display the data in a usable form. Do not require a user to transpose, compute, interpolate, or translate displayed data into other units, or refer to documentation to determine the meaning of displayed data.

3) Display the data consistent with user convention. If no specific user conventions have been established, adopt some consistent data display standards.

4) Maintain a consistent display format from one display to another.

5) Use consistent, familiar wording with a minimal use of abbreviations.

6) Use the simplest display concept commensurate with the information transfer needs of the operator or observer. The more complex the display, the more time it takes to read and interpret the information provided by the display, and the more act the observer or operator is to misinterpret the information or fail to use it correctly. Avoidance of complexity is another way of stating the KISS (Keep It Simple, Stupid) principle that is a cornerstone of applied ergonomics.

7) Use the least precise display format that is commensurate with the readout accuracy actually required and/or the true accuracy that can be generated by the display-generating equipment. Requiring operators to be more precise than necessary only increases their response time, adds to their fatigue or mental stress, and ultimately causes them to make unnecessary errors.

8) Use the most natural or expected display format commensurate with the type of information or interpretive response requirements. Unfamiliar formats require additional time to become accustomed to them, and they encourage errors in reading and interpretation as a result of unfamiliarity and interference with habit patterns. When new and unusual formats seem to be needed, consider experimental tests to determine whether such formats are compatible with basic operator capabilities and limitations and/or whether the new format does in fact result in the required performance level.

9) Use the most effective display technique for the expected viewing environment and operator viewing conditions.

10) Optimize the following display features:

- o Visibility
- o Conspicuousness: Ability to attract attention and distinguishability from background interference and distraction
- o Legibility
- o Interpretability: Meaningfulness to the intended observer within the environment

11) Consistency of data displays. This principle is frequently violated, but it is easy to repair. During the design process, the terminology, formats and so on should all be standardized and controlled.

12) Efficient information assimilation by the user. The format should be familiar to the operator and related to the tasks required to be performed with the data.

13) Minimal memory load on user. Do not require the user to remember information from one screen for use on another screen. Arrange tasks such that completion occurs with few commands, minimizing the chance of forgetting to perform a step.

14) Compatibility of data display with data entry.

15) Flexibility for user control of data display. Users can get the information in the form most convenient for the task they are working on.

In the field of optical and ergonomic parameters the information readability can be estimated by the following quantity parameters:

1) Angle size of the graphical symbol for the operator view point. Correct information recognition probability dependence of the angle size of the information signal symbol is shown on the figure 1. The data were acquired with the white&black text image with contrast ratio CR=1,5:1 and the screen resolution 640x480.

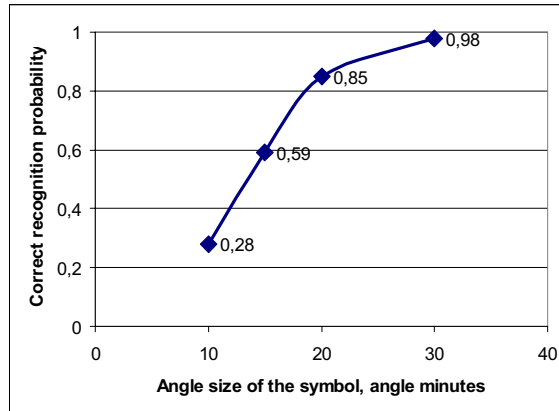


Figure 1. Correct information recognition probability vs angle size of information signal symbol (CR=1,5:1 and 640x480 pixels screen resolution).

2) Image resolution. Correct information recognition probability dependence of the screen resolution and symbol angle size is shown on the figure 2. The data were acquired with the white&black text image with contrast ratio CR=1,5:1.

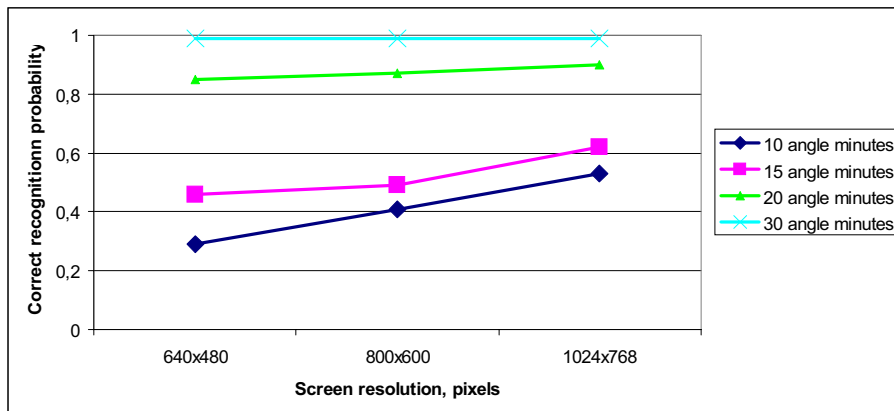


Figure 2. Correct information recognition probability vs screen resolution and symbol angle size (CR=1,5:1 and 640x480 pixels screen resolution).

3) Luminance contrast ratio of the information displayed relative to the background. Correct information recognition probability dependence of the image contrast ratio and screen resolution are shown on the figures 3,4 and 5.

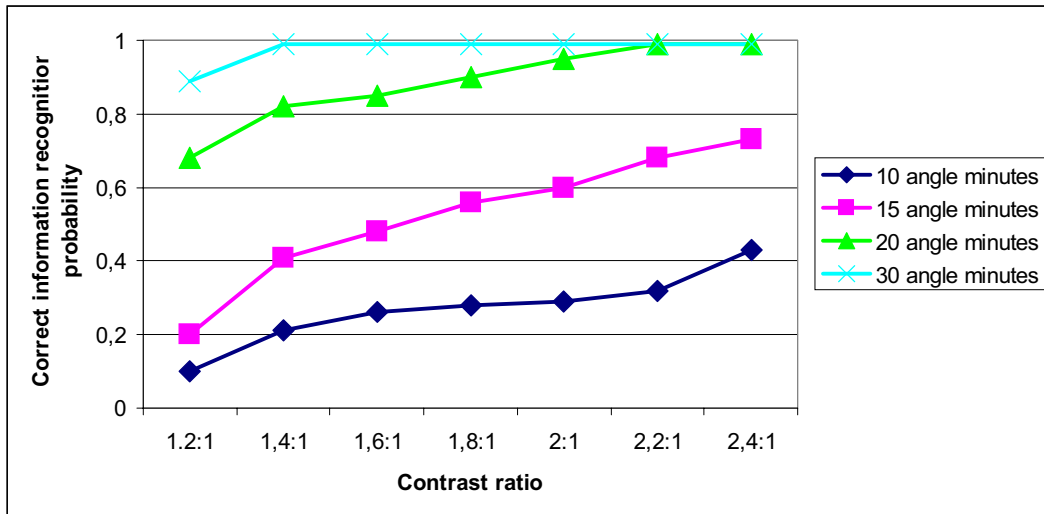


Figure 3. Correct information recognition probability vs contrast ratio for the screen resolution 640x480 pixels.

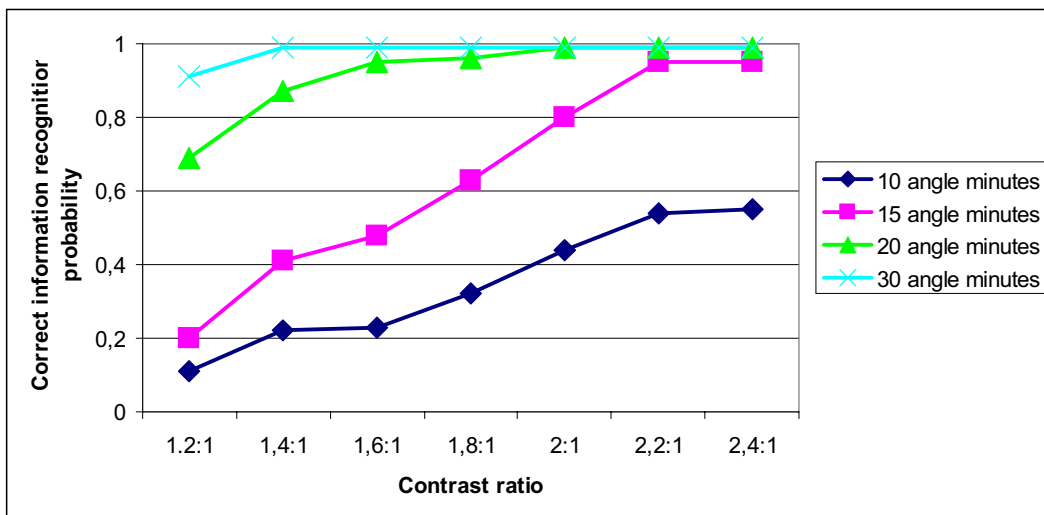


Figure 4. Correct information recognition probability vs contrast ratio for the screen resolution 800x600 pixels.

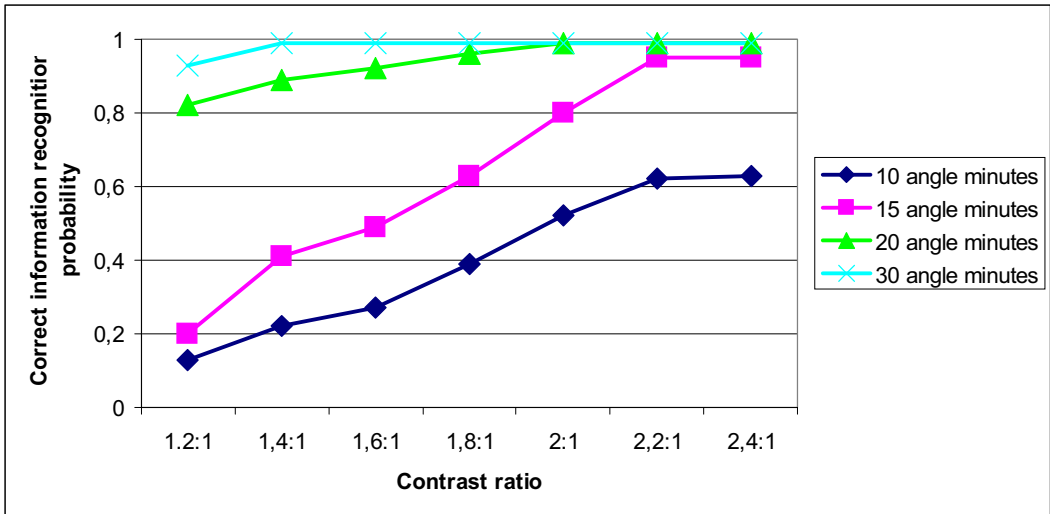


Figure 5. Correct information recognition probability vs contrast ratio for the screen resolution 1024x768 pixels.

4) Color contrast of the information displayed. Correct information recognition probability dependence of the image and background color is shown on the figure 6. The data were acquired with the text image with contrast ratio of the white and black image CR=1,5:1, angle size of the symbol 20 angle minutes, and screen resolution 640x480.

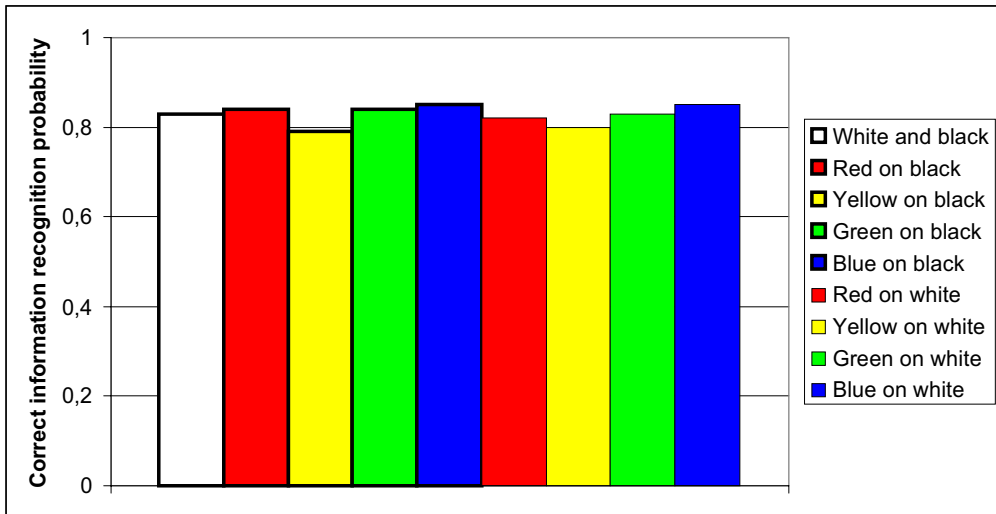


Figure 6. Correct information recognition probability vs colors of the symbol and the background.

Besides the correct information recognition probability, the information search time can be used for characterization of the information readability.

The information search time dependence of contrast ratio and symbol angle size is shown on the figure 7.

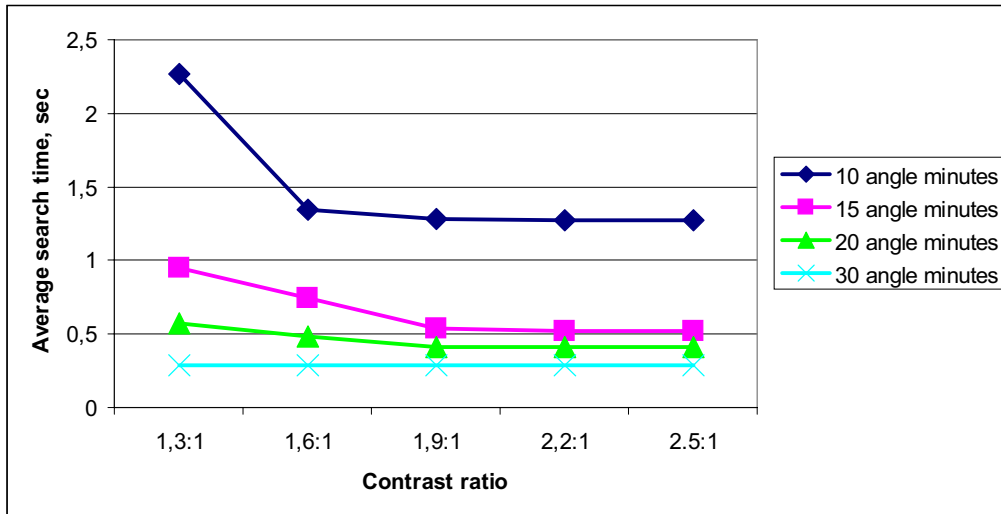


Figure 7. Average search time vs contrast ratio and angle size of the symbol.

This relationships of the energetic, geometric optical parameters and readability show that to obtain a high readability of the text information you have to use a symbol with angle size not less than 20 angle minutes and to supply contrast ratio of the image not less than 2:1 **under the worst viewing conditions** (direct sunlight ambient illumination and angle viewing).

Today our firm ZAO “KB Technotronic” have developed indicators with contrast ratio in high ambient illuminance conditions (more than 100 000 lx) more than 10:1. and more than 5:1 under high illuminance and under high viewing angle ($\pm 70^\circ$ horizontally or vertically). Such high contrast ratio under high ambient illuminance is supplied by high luminance backlight and custom made antireflective coating on the front of the display screen that supply following optical characteristics:

- 1) High luminance (more than 850 cd/m²).
- 2) Low diffuse reflectance (less than 0,1%).
- 3) Low specular reflectance (less than 0,8%).

So, displays developed and manufactured by ZAO “KB Technotronic” are fully readable under any illuminance conditions from full darkness to the direct sunlight.

References

1. ОСТ 1 00345-87 «Система отображения информации в кабинах экипажа. Общие эргономические требования». *(in russian)*

2. ГОСТ Р 50949-96 «Средства отображения информации индивидуального пользования. Методы измерений и оценки эргономических параметров и параметров безопасности». *(in russian)*
2. MIL-STD-1472D «HUMAN ENGINEERING DESIGN CRITERIA STANDARD FOR MILITARY SYSTEMS, EQUIPMENT AND FACILITIES».
3. «FLAT PANEL MEASUREMENTS STANDARD» Version 1, VESA, May 15, 1998
4. M. Helander, T.K. Landauer, P. Prabhu «Handbook of Human-Computer Interaction» 1997, Elsevier Science B.V., ASC-96-1832.
5. MIL-HDBK-87213 «ELECTRONICALLY/OPTICALLY GENERATED AIRBORNE DISPLAYS».
6. ISO 13406-2:2001 «ERGONOMIC REQUIREMENTS FOR WORK WITH VISUAL DISPLAYS BASED ON FLAT PANELS — PART 2: ERGONOMIC REQUIREMENTS FOR FLAT PANEL DISPLAYS».
7. «Энциклопедический справочник по авиационной эргономике и экологии» М., 1997. *(in russian)*
8. «Справочник по инженерной психологии», ред. Б.Ф. Ломова, М. 1982. *(in russian)*

General Principles of Ruggedization of Commercially Available Liquid Crystal Displays for Displays for Mobile Application Analysis.

Dyatlov V.M., Dyatlov M.V., Semash A.A.

ZAO "KB Technotronic", 125040, Russia, Moscow, Leningradskiy prospect, 24A,
tel: +7(095)-7481144, Fax: +7(095)7481141

Savina E.V., Seliverstov V.I.

FNPC RPKB 140103, Russia, Ramenskoye of Moscow region, Guryeva street 2.

Application of flat display units for displays for mobile application is continuously expanding in Russia and in the foreign countries. The main technology of manufacturing such display units became COTS technology (Commercially On The Shelf), that based on ruggedization of liquid crystal displays.

The General requirements to display units for displays for mobile application include:

1. Full information readability under different ambient illumination condition – from direct sunlight to full darkness. To withstand this requirement display information system should form image with such optical parameters:

1.1. White color luminance range from not less than 700 cd/m² to not more than 0,1 cd/m².

1.2. Reflection from image surface not more than 1%.

1.3. Contrast ratio in dark environment (ambient illuminance not more than 3 lx) not less than 200:1.

1.4. Contrast ratio under high ambient illuminance environment (100 000 lx) not less than 10:1.

1.5. Contrast ratio of general colors (red, green, blue) image not less than 2,3:1.

2. Mechanical durability of the information display systems – the immunity to the mechanical shocks, accelerations without image performance reduction, because it can be danger for transport vehicle crew.

3. Climate endurance – immunity to hot and cold environment, high and low moisture ambient air.

4. Availability – there should be models of all desirable sizes for comfortable price at the market, and there should be several manufacturers at the market.

5. Long life time – not less than 30000 hours.

6. Flatness – low depth if compare with image dimensions.

7. Wide viewing angles to allow several crew members to simultaneously read information from one information display.

8. It should have opportunity to display halftone image with not less than 8 halftones of every color.

9. High resolution, not less than 4 pixels/mm.
10. Frame rate not less than 50 frames/sec.

Based on the combination of this parameters the only technology of display units for displays for mobile application is the ruggedized AM TFT LCD (see table 1 for performance parameters of different technologies). The availability of display units based on AM TFT LCD for displays for mobile application is confirmed by its continuously expanding manufacturing up to 2009 (this information was taken from InterLingva Corp. “Flat Panel Display Materials: Trends and Forecasts, 2005 review., see table 2)

From our point of view the general principles of ruggedization are include:

1. Reducing the reflectance ratio from the panel surface to less than 0,5%.
2. Increasing the image brightness up to 700 nits and more.
3. Reducing thermal load on the LCD from the backlight.
4. Reducing the mechanical loads on the glass substrate of the LCD.
5. Reduce mechanical stresses in LCD – chassis (stress free mounting).
6. Temperature gradients elimination in liquid crystal material and in the glass substrate for reducing the effects of “window framing”.
7. Reducing the local overheating of the LCD.
8. Reducing the level of radiation in radio frequency range (EMI noise).

ZAO “KB Technotronic” together with FNPC RBKB manufacture display units with characteristics that listed in table 4.

Table 1.

User oriented performance parameters of general display technologies or displays for mobile application.							
Performance	(TFT LCD)	(CRT)	(LED)	(EL)	(PDP)	(FED)	(OLED)
Dynamical dimming range	1	3	4	5	4	5	4
Reflection ratio	1	3	3	5	3	3	5
Contrast ratio under direct sunlight illumination	2	2	3	4	5	5	5
Color saturation under sunlight illuminance	1	3	5	5	5	5	5
Mechanical durability	1	2	1	1	2	1	1
Climatic durability	2	1	2	1	2	1	3
Commercial accessibility	2	2	1	3	2	5	4
Life time more than 30000 hours	1	5	1	2	2	4	4
Resolution more than 4 pixels/mm	1	5	5	1	5	4	1
Wide viewing angle	2	1	1	1	1	1	1
Video/grayscale	2	1	1	2	1	1	3

Table 2

Type	FY	Unit	Actual		Estimate	Forecast				
			2002	2003	2004	2005	2006	2007	2008	2009
LCD	Volume (1,000 units)		1,571,870	1,904,390	2,053,850	1,957,971	2,111,040	2,189,340	2,260,920	2,335,520
	% change from previous year		-	121.2	107.8	95.3	107.8	103.7	103.3	103.3
	Value (million yen)		3,201,593	4,273,383	5,550,720	6,290,320	7,420,810	8,016,900	8,523,600	9,024,030
	% change from previous year		-	133.5	129.9	113.3	118.0	108.0	106.3	105.9
Color PDP	Volume (1,000 units)		845	2,070	4,360	6,800	9,500	12,500	14,900	17,900
	% change from previous year		-	245.0	210.6	156.0	139.7	131.6	119.2	120.1
	Value (million yen)		189,700	386,900	661,400	886,800	1,083,500	1,288,400	1,459,100	1,679,100
	% change from previous year		-	204.0	170.9	134.1	122.2	118.9	113.2	115.1
Mono Color PDP	Volume (1,000 units)		38	39	38	37	36	35	34	33
	% change from previous year		-	102.6	97.4	97.4	97.3	97.2	97.1	97.1
	Value (million yen)		1,900	1,910	1,830	1,750	1,680	1,610	1,550	1,490
	% change from previous year		-	100.5	95.8	95.6	96.0	95.8	96.3	96.1
Inorganic EL display	Volume (1,000 units)		970	950	880	920	1,000	1,100	1,250	1,450
	% change from previous year		-	97.9	92.6	104.5	108.7	110.0	113.6	116.0
	Value (million yen)		19,500	19,000	17,500	20,300	21,500	22,800	30,000	34,000
	% change from previous year		-	97.4	92.1	116.0	105.9	106.0	131.6	113.3
Organic EL display	Volume (1,000 units)		2,880	19,310	29,910	33,450	49,380	71,250	99,830	131,950
	% change from previous year		-	670.5	154.9	111.8	147.6	144.3	140.1	132.2
	Value (million yen)		8,100	36,420	55,600	66,650	135,890	215,580	315,230	437,700
	% change from previous year		-	449.6	152.7	119.9	203.9	158.6	146.2	138.9
VFD	Volume (1,000 units)		220,000	222,000	224,000	226,000	228,000	230,000	232,000	234,000
	% change from previous year		-	100.9	100.9	100.9	100.9	100.9	100.9	100.9
	Value (million yen)		74,000	74,100	74,150	74,200	74,250	74,300	74,350	74,400
	% change from previous year		-	100.1	100.1	100.1	100.1	100.1	100.1	100.1
FED/SED	Volume (1,000 units)		0	0	0	10	30	100	300	600
	% change from previous year		-	-	-	-	300.0	333.3	300.0	200.0
	Value (million yen)		0	0	0	10,000	27,000	65,000	150,000	250,000
	% change from previous year		-	-	-	-	270.0	240.7	230.8	166.7
CDT	Volume (1,000 units)		75,500	69,480	58,270	49,010	40,960	33,930	27,910	22,980
	% change from previous year		-	92.0	83.9	84.1	83.6	82.8	82.3	82.3
	Value (million yen)		523,000	438,800	337,900	262,200	201,700	155,200	119,500	91,900
	% change from previous year		-	83.9	77.0	77.6	76.9	76.9	77.0	76.9
CPT	Volume (1,000 units)		154,500	158,500	160,200	162,400	158,100	155,100	152,300	148,400
	% change from previous year		-	102.6	101.1	101.4	97.4	98.1	98.2	97.4
	Value (million yen)		1,745,000	1,763,000	1,765,000	1,772,000	1,735,000	1,707,000	1,705,000	1,697,000
	% change from previous year		-	101.0	100.1	100.4	97.9	98.4	99.9	99.5
PRT	Volume (1,000 units)		12,315	13,809	12,903	12,000	9,600	7,200	5,100	3,300
	% change from previous year		-	112.1	93.4	93.0	80.0	75.0	70.8	64.7
	Value (million yen)		47,030	48,450	43,920	39,600	28,800	20,520	13,770	8,580
	% change from previous year		-	103.0	90.7	90.2	72.7	71.3	67.1	62.3
DLP	Volume (1,000 units)		522	930	1,370	2,130	2,785	3,350	3,930	4,430
	% change from previous year		-	178.2	147.3	155.5	130.8	120.3	117.3	112.7
	Value (million yen)		55,050	90,900	131,600	199,800	247,900	274,900	297,850	309,150
	% change from previous year		-	165.1	144.8	151.8	124.1	110.9	108.3	103.8
LCOS (projector)	Volume (1,000 units)		33	53	360	1,180	1,710	2,270	2,760	3,300
	% change from previous year		-	160.6	679.2	327.8	144.9	132.7	121.6	119.6
	Value (million yen)		795	1,190	7,620	16,450	20,340	22,650	24,980	27,500
	% change from previous year		-	149.7	640.3	215.9	123.6	111.4	110.3	110.1
LCOS (direct view)	Volume (1,000 units)		1,300	2,050	3,700	4,500	5,800	6,800	7,700	9,000
	% change from previous year		-	157.7	180.5	121.6	128.9	117.2	113.2	116.9
	Value (million yen)		2,490	3,340	5,600	6,460	7,960	8,970	9,470	10,280
	% change from previous year		-	134.1	167.7	115.4	123.2	112.7	105.6	108.6
Electronic paper	Volume (1,000 units)		0	△	50	800	1,600	2,900	4,300	5,600
	% change from previous year		-	-	-	1,600.0	200.0	181.3	148.3	130.2
	Value (million yen)		0	△	750	8,200	14,400	24,000	33,000	39,000
	% change from previous year		-	-	-	1,093.3	175.6	166.7	137.5	118.2
LED display	Value (million yen)		80,000	81,000	83,500	86,000	88,500	91,000	93,500	96,000
	% change from previous year		-	101.3	103.1	103.0	102.9	102.8	102.7	102.7
	Volume (1,000 units)		2,040,773	2,393,581	2,549,891	2,457,208	2,619,541	2,715,875	2,813,234	2,918,463
	% change from previous year		-	117.3	106.5	96.4	106.6	103.7	103.6	103.7
Display Total	Value (million yen)		5,948,158	7,218,393	8,737,090	9,740,730	11,109,230	11,988,830	12,850,900	13,780,130
	% change from previous year		-	121.4	121.0	111.5	114.0	107.9	107.2	107.2

Table 4

SPECIFICATIONS		Display Unit Model				
Unit	ME-15-1 DHA	ME-16-1 DHA	ME-17-1 DHA	ME-18 DHA	ME-21 DHA	MFD-26
Mechanical Characteristics						
Image Area, mm	211,2x158,4	211,2x158,4	132,5x99,4	304,5x228,4	129,0x96,8	211,2x158,4
Full Color Pixels	640x480	1024x768	640x480	1400x1050	1024x768	640x480
Pixel Pitch, mm	0,330x0,330	0,206x0,206	0,207x0,207	0,218x0,218	0,126x0,126	0,330x0,330
Resolution, px/mm	3,0	4,9	4,8	4,6	7,9	3,0
Display Colors	262144	262144	262144	262144	16194277	262144
Dimensions (WxHxD), mm	248x198x77	248x199x73	195x132x58	345x270x96	166x124x80	258x210x96
Weight, kg	1,7	1,9	1,2	3,8	0,9	3,5
Electrical Specifications						
Video Interfaces						
Graphical format	VGA	XGA	VGA	SXGA+	XGA	VGA
Signal System	1 channel LVDS	1 channel LVDS	1 channel LVDS	2 channel LVDS	1 channel LVDS	RGB- analog; 2 channel CAN
Refresh rate, Hz	50	50	50	50	50	50
Power Supply Voltage						
Power Supply Voltage, V DC	5; 12; 27	5; 12; 27	5; 12; 27	27; 300	5; 300	50
Power Consumption, Wt						
By supplyVoltage	5V DC	0,8	0,6	-	0,8	-
	12V DC	21	30	-	-	-

27V DC	Heater off	0	0	0	50	-	-
	Heater on	180	180	115	50	-	-
50V DC	Heater off	-	-	-	-	20	-
	Heater on	-	-	-	-	220	-
300V DC	Heater off	-	-	-	0	25	-
	Heater on	-	-	-	300	140	-

Optical Characteristics

Luminance maximum, cd/m		1000	850	850	850	850	850	500
Luminance minimum, cd/m		0,15	0,15	0,15	0,15	0,05	0,05	0,5
Luminance Uniformity (RGBW),%		15	15	15	15	15	15	20
Luminance Uniformity Black Large Area,%		30	30	30	30	30	30	35
Dark Contrast Ratio		500 : 1	700 : 1	400:1	400:1	500 : 1	500 : 1	500 : 1
High Ambient Contrast Ratio (110000 lx)		10 : 1	10 : 1	10 : 1	10 : 1	10 : 1	10 : 1	15 : 1 (80000лк)
Response Time, ms	Ton	18	20	20	8	30	6	18
	Toff	16	20	17	17	30	15	16
Chromaticity in day mode	White	x	0,313±0,05	0,313±0,05	0,313±0,05	0,313±0,05	0,323±0,05	0,312±0,05
		y	0,329±0,05	0,325±0,03	0,329±0,05	0,329±0,05	0,340±0,05	0,330±0,05
	Red	x	0,582±0,03	0,612±0,03	0,582±0,03	0,582±0,03	0,594±0,03	0,581±0,03
		y	0,341±0,03	0,341±0,03	0,341±0,03	0,332±0,03	0,349±0,03	0,342±0,03
	Green	x	0,301±0,03	0,294±0,03	0,301±0,03	0,312±0,03	0,339±0,03	0,302±0,03
		y	0,522±0,03	0,568±0,03	0,522±0,03	0,544±0,03	0,521±0,03	0,523±0,03
	Blue	x	0,154±0,03	0,156±0,03	0,154±0,03	0,149±0,03	0,158±0,03	0,153±0,03
		y	0,153±0,03	0,133±0,03	0,153±0,03	0,132±0,03	0,162±0,03	0,154±0,03
Viewing angle with contrast ratio 10:1	Horizontal H	± 85		± 80	± 85	± 60	± 85	
	Vertical V	± 85		+ 80 ; - 60	± 85	+ 45 ; - 60	± 85	
Specular reflectance		0,8 %	0,8 %	0,8 %	0,8 %	0,8 %	1%	

Diffuse reflectance	0,1 %	0,1 %	0,1 %	0,1 %	0,1 %	0,1 %	0,3%
NVIS radiance, NR _B under MIL-STD-3009.	2,2·10 ⁻⁹	2,2·10 ⁻⁹	2,2·10 ⁻⁹	2,2·10 ⁻⁹	2,2·10 ⁻⁹	2,2·10 ⁻⁹	-
Image Retention (CR after 10 hrs)	1,2:1	1,2:1	1,2:1	1,2:1	1,2:1	1,2:1	1,2:1
Display Crosstalk, %	10	10	10	10	10	10	10
Flicker, %	5	5	5	5	5	5	5

Environmental Characteristics

Operating Temperature Range, C	from - 60 up to + 71	from - 60 up to + 71	from - 60 up to + 71	from - 60 up to + 71	from - 60 up to + 71	from - 60 up to + 71	from - 40 up to + 55
Storage Temperature Range, C	from - 60 up to + 85	from - 60 up to + 85	from - 60 up to + 85	from - 60 up to + 85	from - 60 up to + 85	from - 60 up to + 85	from - 60 up to + 85
Humidity	RH 98% @ +35 C	RH 98% @ +35 C	RH 98% @ +35 C	RH 100% @ +35 C	RH 100% @ +35 C	RH 100% @ +35 C	RH 98% @ +35 C
Acceleration, g	10	10	10	10	10	10	-
Vibration Random	10 2000 Hz = 4,3 g	10 2000 Hz = 4,3 g	10 2000 Hz = 4,3 g	10 2000 Hz = 4,3 g	10 2000 Hz = 4,3 g	10 2000 Hz = 4,3 g	0,5 100 Hz 1 g
Vibration Random at Gunfire	10 2000 Hz = 13,6 g	10 2000 Hz = 13,6 g	10 2000 Hz = 13,6 g	10 2000 Hz = 9 g	10 2000 Hz = 9 g	10 2000 Hz = 9 g	-
Shock single	15 g (15 ms)	15 g (15 ms)	15 g (15 ms)	15 g (15 ms)	15 g (15 ms)	15 g (15 ms)	5g, 20 msec
Shock multi	-	-	-	-	-	-	3g, 20 msec
Low pressure, Pa	2500 (18 mm.pt.ct.)	2500 (18 mm.pt.ct.)	2500 (18 mm.pt.ct.)	2500 (18 mm.pt.ct.)	2500 (18 mm.pt.ct.)	2500 (18 mm.pt.ct.)	-
Salt Fog	5% NaCl, pH6,5 48 hours. @ +35 C	5% NaCl, pH6,5 48 hours. @ +35 C	5% NaCl, pH6,5 48 hours. @ +35 C	5% NaCl, pH6,5 48 hours. @ +35 C	5% NaCl, pH6,5 48 hours. @ +35 C	5% NaCl, pH6,5 48 hours. @ +35 C	5% NaCl, pH6,5 48 hours. @ +35 C

Salt Fog	5% NaCl, pH6,5 48 hours. @ +35 C	5% NaCl, pH6,5 48 hours. @ +35 C	5% NaCl, pH6,5 48 hours. @ +35 C	5% NaCl, pH6,5 48 hours. @ +35 C	5% NaCl, pH6,5 48 hours. @ +35 C	5% NaCl, pH6,5 48 hours. @ +35 C
Dust, m/sec	1,0	1,0	1,0	1,0	1,0	1,0
Solar Radiation	1120Wt/m ² 55 C	1120Wt/m ² 55 C	1120Wt/m ² 55 C	1120Wt/m ² 55 C	1120Wt/m ² 55 C	1120Wt/m ² 55 C
Fungus	RH 95 98% @ +29 C	RH 95 98% @ +29 C	RH 95 98% @ +29 C	RH 95 98% @ +29 C	RH 95 98% @ +29 C	RH 95 98% @ +29 C
Vibro-Acoustic	50 10000Hz 130dB	50 10000Hz 130dB	50 10000Hz 130dB	50 10000Hz 130dB	50 10000Hz 130dB	50 10000Hz 130dB
Атмосферные конденсированные осадки (иней, роса)	-30 C, 170 mm of mercury column RH 95% @ +35 C	-30 C, 170 mm of mercury column RH 95% @ +35 C	-30 C, 170 mm of mercury column RH 95% @ +35 C	-30 C, 170 mm of mercury column RH 95% @ +35 C	-30 C, 170 mm of mercury column RH 95% @ +35 C	-30 C, 170 mm of mercury column RH 95% @ +35 C
Icing/Freesing Rain	-30 C, 170 mm of mercury column RH 95% @ +35 C	-30 C, 170 mm of mercury column RH 95% @ +35 C	-30 C, 170 mm of mercury column RH 95% @ +35 C	-30 C, 170 mm of mercury column RH 95% @ +35 C	-30 C, 170 mm of mercury column RH 95% @ +35 C	-30 C, 170 mm of mercury column RH 95% @ +35 C
Warm-up-time at -60 C, minute	5	5	5	5	5	5 (-40 C)
Reliability						
MTBF in Airborne, hrs	20000	20000	20000	20000	20000	20000
Live Time, years	30	30	30	30	30	30
Storage Life, years	10	10	10	10	10	10

References:

1. "Flat Panel Display Materials: Trends and Forecasts", InterLingva Corp., 2005ä.
2. "Cockpit Displays VII-XI", SPIE 2000-2004.

Light transmission polarimetry of cholesteric cells in planar and wedge geometries: Analysis of polarization parameter fields

Roman I. Egorov, Roman G. Vovk, Alexei D. Kiselev, and Marat S. Soskin.

Institute of Physics, National Academy of Sciences of Ukraine, Prospekt Nauki, 03680 Kiev, Ukraine

Abstract

We apply the improved technique of Stokes polarimetry to measure the azimuthal angle and the ellipticity form factor of the transmitted light in cholesteric liquid crystal (CLC) cells of planar and wedge geometries at different polarizations of the incident wave. In the wedge geometry, spatially varying local CLC pitch and the cell thickness are found to complicate the structure of the polarization parameter fields. This structure is interpreted theoretically using a modified version of the de Vries theory. We also observed polarization singularities located on some of disclination strips and arranged in chains of optical dipoles.

I. INTRODUCTION

The optical properties of cholesteric liquid crystal (CLC) cells are known to be of considerable importance for their applications in display devices [1, 2]. Tendency of CLCs to form helical twisting patterns manifests itself in a number of distinctive features such as the presence of a single photonic stop gap for normal incidence of circularly polarized light [3, 4].

This work concerns polarization properties of light transmitted through the CLC layers sandwiched between the substrates imposing the strong homogeneous anchoring conditions. We apply the experimental method of singular Stokes polarimetry [5, 6] which allows to study in detail polarization fields (the distribution of Stokes parameters) of light passed through the CLC film with wedge-shaped boundaries.

In the wedge geometry, the structure of the polarization fields is complicated due to the presence of the Cano-Grandjean disclinations dividing the area of the substrates into Grandjean zones. Within each zone the CLC helical structure is generally distorted and, in the simplest case, can be characterized by spatially varying helical pitch. Such variations of the orientational structure will affect the polarization fields and our goal is to examine the effects of the orientational distortions on the polarization fields. Study of such effects is of importance for the understanding of the properties of photonic defect modes in CLCs [7, 8] and the polarization singularities of light propagating in anisotropic media [9, 10].

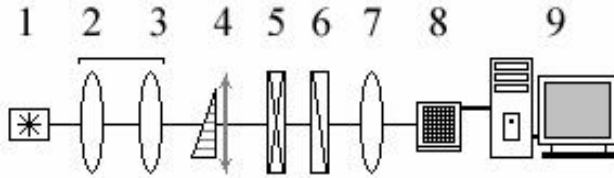


FIG. 1: Experimental setup: (1) He-Ne laser; (2) collimator lenses; (3) CLC wedge cell; (4) quarter-wave plate; (5) polarizer; (6) magnifying lens; (7) charge coupled device (CCD) camera; (8) computer.

II. EXPERIMENT

In our experiments we used the CLC cells filled with chirally doped liquid crystal mixture E7. The equilibrium CLC pitch, P_0 , was about $5 \mu\text{m}$ with the extraordinary and ordinary refractive indices: $n_e \approx 1.74$ and $n_o \approx 1.52$. The cells were wedge-shaped at the wedge angle about 0.12 degrees. Polyimide alignment films (PI255) rubbed along the Grandjean zones was used to align CLC molecules at the substrates.

Figure 1 shows the experimental setup for performing the measurements using the method previously described in our papers [5, 6]. The sample (3) was irradiated with a beam generated by He-Ne laser (1) ($\lambda = 633 \text{ nm}$) and collimated by the lenses (2). The cell was arranged so as to keep its back surface in the focal plane of the projecting system. After passing the cell (3) and the analyzer (4-5), the beam is magnified and projected onto the screen of the CCD camera (7) connected to the computer (8). The computer processing of the obtained data up to building of the azimuth and eccentricity map of the field area under measurement was performed by a special program using the Stokes vector in each point of CCD-matrix.

III. THEORY

We consider a CLC cell of thickness d sandwiched between two parallel plates that are normal to the z axis: $z = -d/2$ and $z = d/2$. We assume that the substrates impose the strong homogeneous anchoring conditions and the CLC helical structure is of the spiral form with the director $\vec{n} = \vec{e}_x \cdot \cos\Phi(z) + \vec{e}_y \sin\Phi(z)$ where $\Phi(z) = qz + \phi_0$, $q = 2\pi/P$ is the twist wave-number, P is the CLC pitch and ϕ_0 is the twist angle of the director in the middle of the cell. The strong anchoring conditions require the ratio $2D/P \equiv \nu$ to be the integer, $\nu \in \mathbb{Z}$, giving the half-turn number of the CLC helix.

It is now our task to relate the polarization vector of the planar wave normally incident on the CLC cell, $\vec{E}_i = E_+^{(i)} \vec{e}_+ + E_-^{(i)} \vec{e}_-$, and the polarization vector of the wave transmitted through the slab, $\vec{E}_t = E_+^{(t)} \vec{e}_+ + E_-^{(t)} \vec{e}_-$, where

$e_{\pm} = \frac{(e_x \pm ie_y)}{\sqrt{2}}$ are the vectors of spherical basis. Clearly, this relation is linear and can generally be written in the matrix form as follows

$$\begin{pmatrix} E_+^{(i)} \\ E_-^{(i)} \end{pmatrix} \equiv E_t = \hat{T} \cdot E_i \quad (1)$$

where carets will indicate 2 x 2 matrices.

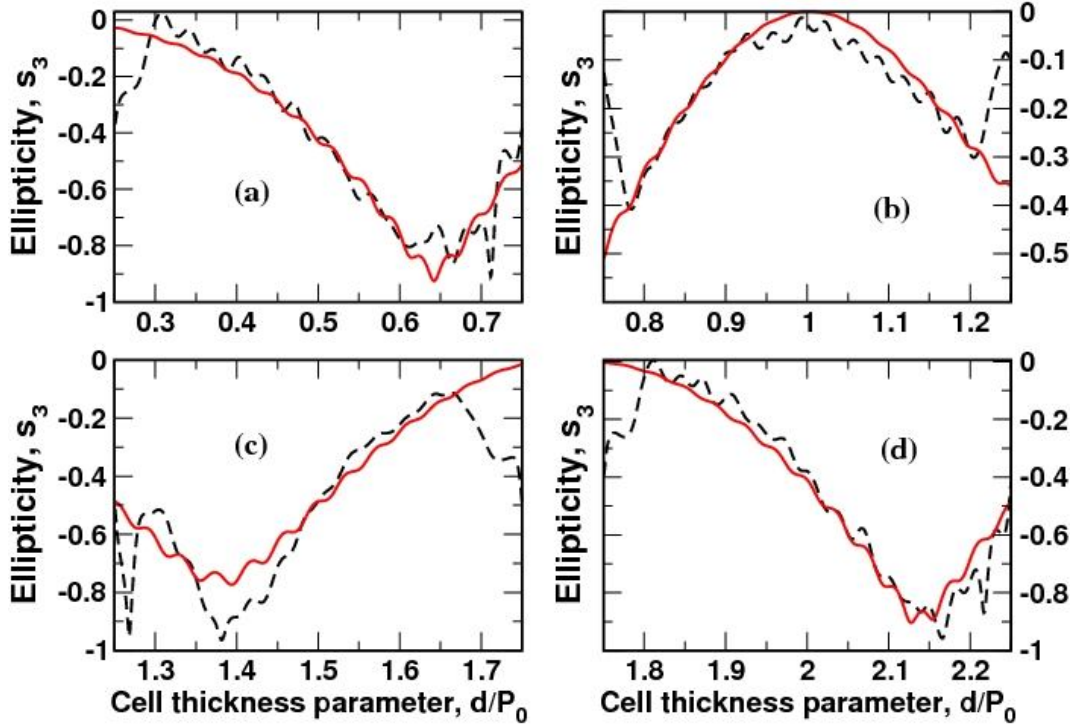


FIG. 2. Ellipticity factor (normalized Stokes parameter s_3) as a function of the dimensionless thickness parameter, d/P_0 . Incident light is linearly polarized along the easy axis. Dashed lines represent the experimental data measured in the first four Grandjean zones (from (a) to (d)) separated by disclinations. Theoretical curves (solid lines) are computed using the formula (4).

For planar waves propagating along the normal to the cell, the matrix \hat{T} can be found in the closed form as the underlying boundary-value problem is exactly solvable. In this case, the electric field inside the CLC cell, $E_c(z)$, is given as a linear combination of the well known eigenmodes [3, 4] and we shall write the result in the matrix form

$$\begin{pmatrix} E_+^{(c)}(z)e^{iqz} \\ E_-^{(c)}(z)e^{iqz} \end{pmatrix} = \hat{Q}(z) \cdot \alpha + \hat{\sigma}_x \cdot \hat{Q}(-z) \cdot \beta \quad (2)$$

$$\hat{Q}(z) = \begin{pmatrix} \gamma_+ \exp\{ik_+z\} & u \cdot \exp\{ik_-z\} \\ u \cdot \exp\{ik_+z\} & \gamma_- \exp\{ik_-z\} \end{pmatrix} \quad (3)$$

where $\hat{\sigma}_x = \begin{pmatrix} 0 & 1 \\ 1 & 0 \end{pmatrix}$, $\gamma_{\pm} \cdot k_c^2 = (k_{\pm} \pm q)^2 - k_c^2$, $k_{\pm}^2 = k_c^2 + q^2 \pm k_c \sqrt{(uk_c)^2 + 4q^2}$, α and β are the columns of constants, $u = \frac{(\varepsilon_{||} - \varepsilon_{\perp})}{(\varepsilon_{||} + \varepsilon_{\perp})}$ is the anisotropy parameter, $k_c = n_c \cdot k_0$ is the wavenumber in the cell with the refractive index $n_c = [(\varepsilon_{||} + \varepsilon_{\perp})/2]^{1/2}$, $k_0 = 2\pi/\lambda$ is the free-space wavenumber. When the optical axis is directed along the CLC director \mathbf{n} , $\sqrt{\varepsilon_{||}}$ and $\sqrt{\varepsilon_{\perp}}$ give the refractive indices of extraordinary and ordinary waves, respectively.

We can now use continuity of the tangential components of the electric and magnetic fields at the boundary surfaces $z = \pm d/2$ and after lengthy algebraic calculations obtain the expression for the matrix \hat{T} in the final form

$$m \cdot \exp\{ikd\} \cdot T^{-1} = \hat{\sigma}_x P_a \{-I + [P_a^{-1}(mI - P_s)]^{\mathbb{P}}\} \quad (4)$$

where $2k_c P_a = \hat{Q}_a \hat{K} \hat{Q}_s^{-1} - \hat{Q}_s \hat{K} \hat{Q}_a^{-1}$, $2k_c P_s = \hat{Q}_s \hat{K} \hat{Q}_s^{-1} - \hat{Q}_s \hat{K} \hat{Q}_a^{-1} - 2q\sigma_z$, $Q_{s,a} = Q(d/2) \pm \sigma_x Q(-d/2)$, $K = \text{diag}(k_+, k_-)$, $\sigma_z = \text{diag}(1, -1)$, \mathbf{I} is the identity matrix and $k = n_m k_0 = mk_c$ is the wavenumber in the ambient medium with the refractive index n_m and $m = n_m/n_c$

IV. RESULTS

We can now apply the theory to interpret the experimental data. For this purpose, we use the simplest model where complications arising from the complexity of director structure near the dislocations [11] and oblique incidence [12, 13] are neglected. In this model, the pitch P is linearly related to the thickness of the cell through the relation, $d = \nu P/2$, so that $d = \nu P/2$ at the center of the Grandjean zone characterized by the half-turn number ν .

So, we can use the formulas (1)-(4) to compute the Stokes parameters as a function of thickness. For the normalized Stokes parameter,

$$S3 = \frac{\left(|E_+^{(t)}| - |E_-^{(t)}| \right)}{\left(|E_+^{(t)}| + |E_-^{(t)}| \right)}, \text{ describing the ellipticity (eccentricity), the re-}$$

sults are shown in figure 2. In this case the incident light is linearly polarized along the direction of preferential orientation of the CLC molecules at the surface (the easy axis).

Figure 2 demonstrates remarkable agreement between the theory and the experiment. For other cases where the incident light is circularly polarized and linearly polarized perpendicular to the easy axis, the theory is also found to give the results that are in good agreement with the experimental data.

Referring to figure 2, it can be seen that, in the immediate vicinity of disclinations, where the director field is strongly distorted, the model becomes inapplicable leading to noticeable differences between the theoretical and experimental curves. In this region we have also observed polarization singularities arranged in chains of optical dipoles. In addition, during the scanning across the Cano-Grandjean zones, a periodical set of Mauguin points where the incident and transmitted waves are both linearly polarized was detected.

- [1] J. W. Doane, in *Liquid Crystals — Application and Uses*, edited by B. Bahadur (World Scientific, Singapore, 1990), vol. 1, p. 361.
- [2] V. G. Chigrinov, *Liquid crystal devices: Physics and Applications* (Artech House, Boston, 1999).
- [3] V. A. Belyakov and V. E. Dmitrienko, *Optics of Chiral Liquid Crystals*, vol. 13 of Soviet scientific reviews (Harwood Academic Pub., Chur, Switzerland, 1989).
- [4] P. Yeh and C. Gu, *Optics of Liquid Crystal Displays* (Wiley, Singapore, 1999).
- [5] M. S. Soskin, V. Denisenko, and I. Freund, *Opt. Lett.* 28, 1475 (2003).
- [6] M. S. Soskin, V. Denisenko, and R. Egorov, *J. Opt. A: Pure Appl. Opt.* 6, S281 (2004).
- [7] J. Schmidtke and W. Stille, *Eur. Phys. J. E* 12, 553 (2003).
- [8] M. Becchi, S. Ponti, J. A. Reyes, and C. Oldano, *Phys. Rev. E* 70, 033103 (2004).
- [9] M. V. Berry and M. R. Dennis, *Proc. R. Soc. Lond. A* 459, 1261 (2003).
- [10] M. V. Berry, *Proc. R. Soc. Lond. A* 461, 2071 (2005).
- [11] T. J. Scheffer, *Phys. Rev. A* 5, 1327 (1972).
- [12] C. Oldano, E. Miraldi, and P. T. Valabrega, *Phys. Rev. A* 27, 3291 (1983).
- [13] C. Oldano, *Phys. Rev. A* 31, 1014 (1985).

Acknowledgments

A.D.K. thanks Dr. Mark R. Dennis (University of Southampton, UK) and Dr. Dmitry A. Yakovlev (Saratov State University, Russia) for stimulating discussions.

Elucidation of energy transfer mechanism from fluorene polymer to Ir complexes aiming for high efficiency OLEDs

Larysa Fenenko^{a,b} and Chihaya Adachi^a, ^bV.E. Lashkaryov

^aChitose Institute of Science and Technology, 758-65 Bibi, Chitose, Hokkaido, 066-8655 Japan

^bInstitute of Semiconductor Physics of NASU, 45 Pr. Nauky, 03028, Kyiv, Ukraine

ABSTRACT

Red phosphorescence from Btp₂Ir(acac) in a PDOFO-TFB host polymer was investigated. Relatively high photoluminescence efficiency of $\eta_{PL} = 41\%$ in the thin films (50-100nm) was observed. The imperfect energy transfer and energy loss mechanism that limit the PL efficiency were studied.

Keywords: phosphorescence, polyfluorene, Ir complex, energy transfer

1. INTRODUCTION

The promising candidates for dopants in high efficiency organic light emitting diodes (OLEDs) are the phosphorescent emitters having heavy metals such as Ir complexes. They can emit light with very high efficiency from the triplet metal-to-ligand charge transfer (³MLCT) state [1-3]. The excited states generated by electron-hole recombination are trapped by the phosphors where the strong spin-orbit coupling leads to singlet-triplet state mixing, leading to efficient phosphorescent emission even at room temperature. OLEDs using heavy metal complexes showed internal quantum efficiency higher than 25% and external efficiency higher than 15% [1] since the singlet-triplet branching ratio is 1:3.

The use of fluorescent polymers doped with phosphorescent dopants can also provide a new type of efficient OLEDs. Excellent mechanical properties, flexibility, simple and low-cost fabrication technology in the polymer based devices have great advantage compared with the small molecular OLEDs. Here, we demonstrate the efficient red phosphorescence using energy transfer from blue polyfluorene, poly[9,9-dioctylfluorenyl-2,7-diyl)-co-(4,4'-(N-(4-sec-butylphenyl)diphenyl-amine))] (PDOFO-TFB), into the red emitting iridium complex: bis[2-(2'-benzothienyl)pyridinato-N,C^{3'}](acetylacetonato)iridium(III) [Btp₂Ir(acac)].

2. EXPERIMENT

Various Btp₂Ir(acac) concentrations (0 ~ 20 wt%) in a PDOFO-TFB host were prepared. After filtration using a 0.45 mm pore-size filter, the organic films were spin-coated on a silicon (for transient photoluminescence (PL) measurement), quartz (for absolute PL efficiency measurement) and glass (for absorption and PL measurements) substrates, respectively. Before the film formation, all substrates were pre-cleaned and exposed to UV-ozone. The films were spin-coated at 2000 rpm for 60 s and dried in a vacuum oven at T = 45°C for 20 min. The film thicknesses were 50-100 nm.

The absolute PL efficiency (η_{PL}) of the films was measured under nitrogen flow using an integrating sphere [4] with 325 nm He-Cd laser as the excitation source and multi-channel spectrometer (Hamamatsu PMA-11) as the optical detector. The transient photoluminescence was measured using a streak camera (Hamamatsu C4334) with a nitrogen gas laser ($\lambda = 337$ nm, pulse width ~ 300 ps, repetition rate = 20 Hz) as the excitation source. The measurements were done under a low pressure ($\sim 10^{-1}$ Pa) in a cryostat.

3. RESULTS AND DISCUSSION

The η_{PL} of $Btp_2Ir(acac)$ in PDOFO-TFB as a function of doping concentration is shown in Fig. 1. The doping concentration was varied from 0 (undoped) to 20wt%. The maximum η_{PL} reached 41% at dopant concentration of 6 wt%. A further increase of the dopant concentration leads to PL quenching possibly due to the dopant aggregation. With an increase of the dopant concentration, the distance between guest molecules became smaller, leading to the strong deactivation interaction. Comparing with the η_{PL} decrease in $Btp_2Ir(acac)$ in CBP, the decrease of η_{PL} in the PDOFO-TFB host is significant, indicating that the PDOFO-TFB polymer host accelerates the dopant aggregation.

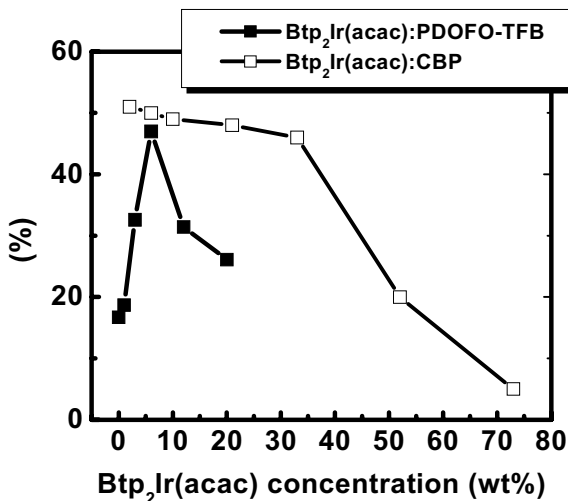


Fig. 1. η_{PL} vs dopant concentration in $Btp_2Ir(acac)$: PDOFO-TFB.

An increase of the dopant concentration leads to change of the PL spectra of the doped films (Fig. 2a). With an increase of the dopant concentration, energy transfer from the host to guest increases, leading to change in ratio of the polymer and dopant PL intensities (Fig. 2b). The ratio of PL peak intensity of $Btp_2Ir(acac)$ to PDOFO-TFB reached 12.5 at 6wt%.

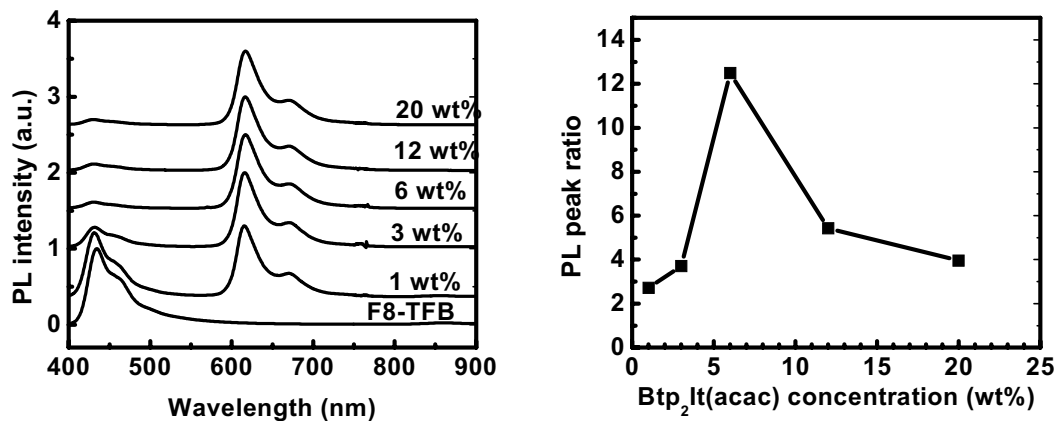


Fig. 2. (a) PL spectra of Xwt%-Btp₂Ir(acac) : PDOFO-TFB layers with the dopant concentration of 1 ~ 20 wt%; (b) PL peak ratio between dopant and polymer PL intensities.

Even at higher concentration (> 12 wt%) of Btp₂Ir(acac) in PDOFO-TFB, the weak polymer emission was observed, indicating that the energy transfer from host to guest is imperfect. This would be due to the imperfect dopant distribution in the polymer matrix, probably caused by the characteristic polymer morphology, although the perfect energy transfer takes place in Btp₂Ir(acac) : CBP system [3].

Figure 3 shows temperature dependence of η_{PL} in 6wt%-Btp₂Ir(acac) : PDOFO-TFB. We obtained the monotonic increase of the PL intensity with temperature decrease, and maximum η_{PL} at the lowest temperature of 5K was observed. This concludes that nonradiative decay from the triplet level of Btp₂Ir(acac) competes with radiative decay at room temperature and is well suppressed at low temperature.

Fig. 3 (below) The PL spectra of 6wt% Btp₂Ir(acac) : PDOFO-TFB. The PL intensities of both polymer and dopant monotonically increased with a decrease of the temperature.

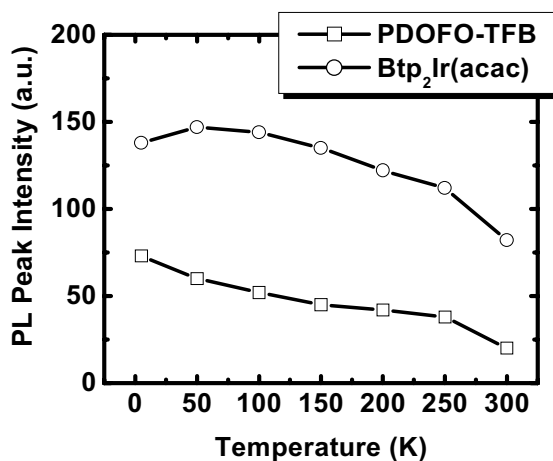


Figure 4 summarizes energy levels of Btp₂Ir(acac) : PDOFO-TFB system. In the polymer films doped with Btp₂Ir(acac), imperfect energy transfer takes place from PDOFO-TFB into Btp₂Ir(acac). A part of excitation energy in the singlet level of PDOFO-TFB (2.5 eV) was transferred into the singlet level of Btp₂Ir(acac), while a part of the energy decays radiatively and nonradiatively to the ground state from the singlet level of PDOFO-TFB (Fig. 4). The excitation energy transfer from the singlet excited state of Btp₂Ir(acac) into the triplet level is perfect and the phosphorescent emission competes with the nonradiative decay.

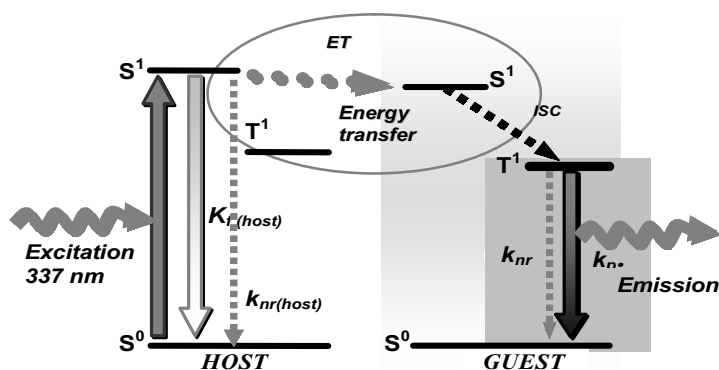


Fig. 4. Energy levels and energy transfer schemes for PDOFO-TFB and Btp₂Ir(acac).

CONCLUSION

The new phosphorescent polymer system based on a blue polyfluorene (PDOFO-TFB) doped with red emitting iridium complex Btp₂Ir(acac) was investigated. The maximum PL efficiency of $\eta_{PL} = 41\%$ at optimal dopant concentration of 6 wt% was obtained. The limitation of PL efficiency due to the energy losses processes was discussed.

REFERENCES

1. S. Lamansky, P. Djurovich, D. Murphy, F. Abdel-Razzaq, H.-E. Lee, C. Adachi, P. E. Burrows, S. R. Forrest, and M. E. Thompson, "Highly phosphorescent bis-cyclometalated iridium complexes: synthesis, photophysical characterization, and use in organic light emitting diodes", *J. Am. Chem. Soc.* 123, pp. 4304-4312, 2001.
2. M. A. Baldo, C. Adachi, and S. R. Forrest, "Transient analysis of organic electrophosphorescence. II. Transient analysis of triplet-triplet annihilation", *Phys. Rev. B* 62, pp. 10967-10977, 2000.
3. Y. Kawamura, K. Goushi, J. Brooks, J. Brown, H. Sasabe and C. Adachi, "100% phosphorescence quantum efficiency of Ir(III) complexes in organic semiconductor films", *Appl. Phys. Lett.* 86, pp. 071104, 2005.
4. Y. Kawamura, H. Sasabe, and C. Adachi, "Simple accurate system for measuring absolute photoluminescence quantum efficiency in organic solid-state thin films" *Jpn. J. Appl. Phys. Part 1* 43, pp. 7729-7730, 2004.

Porous anodic alumina and sol-gel products for optoelectronic applications

G.K. Maliarevich, I.S. Molchan, N.V. Gaponenko*,
(*corresponding author, email nik@nano.bsuir.edu.by)

Belarusian State University of Informatics and Radioelectronics, P. Browki St. 6,
220013 Minsk, Belarus.

S.V. Gaponenko, A.A. Lutich,

Institute of Molecular and Atomic Physics, Prospekt Nezavisimosti 70, Minsk
220072 Belarus.

G.E. Thompson

Corrosion and Protection Centre, School of Materials, The University of
Manchester, PO Box 88, Manchester, M60 1QD, UK

Introduction

Progress in the display industry has stimulated development of novel, highly-efficient luminescent materials. One approach, based on the combination of sol-gel synthesis and anodizing of aluminium, allows fabrication of phosphors capable of intense emission over all optical ranges, from UV, through the visible range, to IR [1]. The strong enhancement of lanthanide photoluminescence, confined in the porous anodic alumina matrix, is described from the viewpoint of multiple scattering of exciting light by the porous matrix [2]. Such structures may exhibit predominant emission in the pore directions [3] and electroluminescence [4-6]. In this work, it is demonstrated that the porous anodic alumina and xerogel structures, doped with both europium and terbium, show change of the emission wavelength, from red to green, with variation of the excitation wavelength. Erbium-related luminescence in a yttrium-aluminium garnet xerogel/porous anodic alumina structure is also demonstrated.

Experimental

Membranes of porous anodic alumina were fabricated by anodizing of pure (99.99 %) aluminium foils in tartaric acid or a mixture of sulphuric and oxalic acids. The films formed in tartaric acid were subsequently etched in phosphoric acid solution for pore widening. The anodic film was released from the substrate by dissolution of the aluminium in an aqueous solution of hydrochloric acid and copper chloride. Several films of porous anodic alumina were also fabricated on silicon wafer, with Ref. [6] providing further details.

The europium-, terbium- and europium/terbium-doped titania xerogel films were formed in the membranes generated in the mixture of sulphuric and oxalic acids; erbium-doped yttrium-aluminium-garnet films were fabricated in the pores of anodic film fabricated in tartaric acid. The method, described in [6], was used for preparation of titania sols, containing both Tb and Eu. In order to prepare the sol for fabrication of erbium-doped garnet films, the nitrates of Y, Al and Er, with molar concentrations of 0.2°M, were

dissolved in water in the ratio corresponding to the chemical formula of the xerogel $\text{Er}_{0,15}\text{Y}_{2,85}\text{A}_{15}\text{O}_{12}$. Subsequently, this solution was mixed with citric acid and ethylene glycol and stirred for 30 min. The sols were deposited onto the porous anodic alumina membranes by spinning at 3000 rpm for 30 s, followed by annealing at 200 and 900°C for europium/terbium- and erbium-doped samples respectively.

Results and Discussion

Figure 1 shows the micrographs of the anodic alumina film formed in tartaric acid, demonstrating significant widening of the pore diameters after post-anodic treatment. Moreover, the pore diameters and interpore distance are the largest for anodic films obtained in tartaric acid because anodizing is possible at relatively high voltages (above 200 V) without additional cooling of electrolyte.

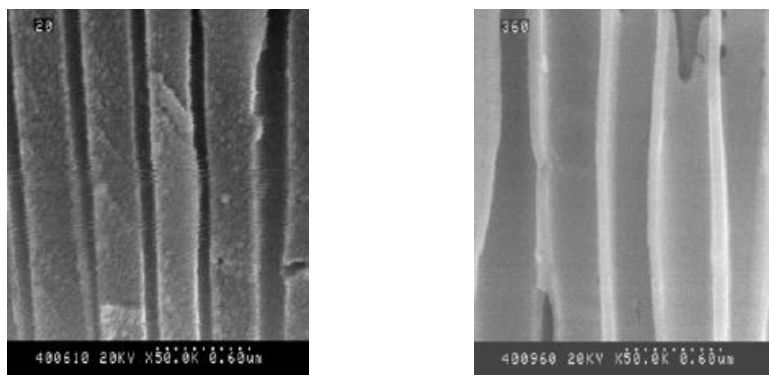


Figure 1. Scanning electron micrographs of porous anodic alumina membranes formed by anodizing high purity aluminium in tartaric acid: (a-left) as-anodized; (b-right) after etching in phosphoric acid solution for 180 min.

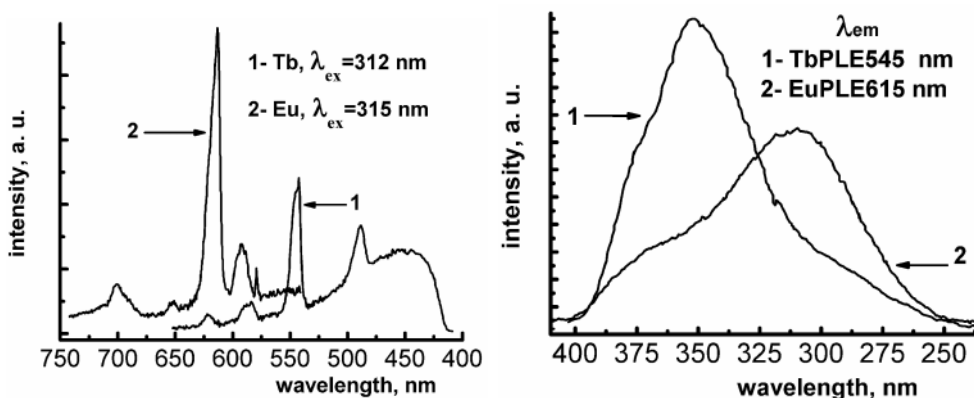


Figure 2. The photoluminescence (a-left) and photoluminescence excitation (b-right) spectra of Eu- and Tb-doped titania xerogel films fabricated in porous anodic alumina.

The specimens, doped with europium or terbium, demonstrate intense photoluminescence in the red or green range respectively, that results from $^5D_0 \rightarrow ^7F_2$ (614 nm) electron transitions of europium ions and $^5D_4 \rightarrow ^7F_5$ (543 nm) transitions of terbium ions (Fig. 2 a). Photoluminescence excitation spectra of these specimens (Fig. 2 b) show that the excitation maximum wavelengths differ for europium- and terbium-doped specimens, recorded for the most intense bands at 613 and 543 nm respectively.

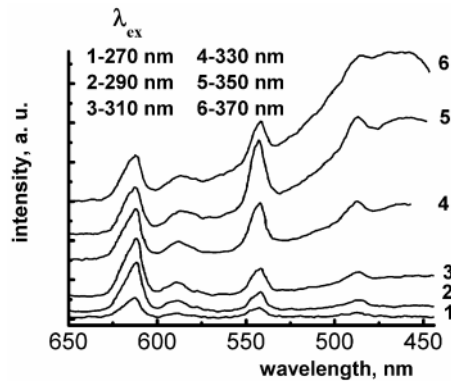


Figure 3. The photoluminescence spectra of titania xerogel, doped with both Eu and Tb, fabricated in porous anodic alumina.

Further, the increase of excitation wavelength of the specimens, co-doped with both europium and terbium, leads to redistribution of emission intensities of the predominant bands of europium and terbium ions, with increased contribution of terbium-related luminescence. In particular, the increase of excitation wavelength from 270 to 370 nm results in a 2.5 fold increase of the integral intensity of the $^5D_4 \rightarrow ^7F_5$ band of terbium ions compared with the $^5D_0 \rightarrow ^7F_2$ band of europium ions (Fig. 3). The images of this sample, co-doped with both europium and terbium, taken at excitation wavelength of 300 and 365 nm, show a distinct changing the emission colour from red to green (Fig. 4).



Figure 4. Photoluminescence recorded from the titania xerogel, doped with both Eu and Tb, confined in porous anodic alumina. A change in the emission colour with excitation wavelength is revealed: (a-left) red emission at $\lambda_{ex}=300$ nm; (b-right) green emission at $\lambda_{ex}=365$ nm.

Er-doped structures reveal a narrow photoluminescence band at 1.53 μm , corresponding to the ${}^4\text{I}_{13/2} \rightarrow {}^4\text{I}_{15/2}$ transition of Er^{3+} in yttrium-aluminium garnets, with strong Stark splitting evident at room temperature (Fig. 5).

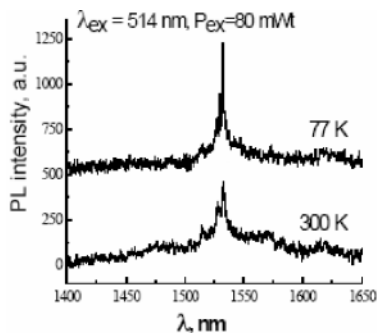


Figure 5. Photoluminescence spectra at 77 and 300 K of Er-doped yttrium-aluminium garnet, fabricated in porous anodic alumina.

In conclusion, the xerogel films, doped with both terbium and europium and confined in the porous anodic alumina matrix, allow change of colour of emission that can be used for creation of multi-colour image displays. The structures based on erbium-doped yttrium-aluminium garnet are of potential for laser applications.

This work was supported by the grant INTAS (project # 03-51-6484) and ISTC (project B-276.2).

Acknowledgements

We wish to thank Professor A.G. Smirnov, M. V. Stepikhova and A.V. Mudryi for stimulating discussions.

References

1. N. V. Gaponenko, Synthetic Metals 124 (2001) 125; J. Appl. Spectrosc. 69 (2002) 1,
2. N. V. Gaponenko, I. S. Molchan, S. V. Gaponenko, A. V. Mudryi, A. A. Lyutich, J. Misiewicz, R. Kudrawiec, J. Appl. Spectroscopy 70 (2003) 57.
3. A. A. Lutich, S. V. Gaponenko, N. V. Gaponenko, I. S. Molchan, V. A. Sokol, V. Parkhutik, Nano Lett. 4 (2004) 1755.
4. I.S. Molchan, PhD. Thesis. Belarusian State University of Informatics and Radioelectronics. Minsk (2003).
5. I. S. Molchan, N. V. Gaponenko, G. E. Thompson, J. Soc. Inf. Disp. 13/4 (2005) 295.
6. N.V. Gaponenko, I. S. Molchan, D. A. Tsyrukunov, G. K. Maliarevich, M. Aegerter, J. Puetz, N. Al-Dahoudi, J. Misiewicz, R. Kudrawiec, V. Lambertini, N. Li Pira, P. Repetto. Microelectronic Engineering 81 (2005) 255.
7. I. S. Molchan, N. V. Gaponenko, R. Kudrawiec, J. Misiewicz, G. E. Thompson, P. Skeldon, J. Electrochem. Soc. 151 (2004) H16.

SECOND HARMONIC GENERATION IN ZnS PHOSPHORS UNDER THE STRONG IR IRRADIATION

L.V. Grigoryev¹, E.V. Komarov², V.V. Rychgorskyi³, M.M. Sychov²

¹ Physical Research Institute of St.Petersburg University, Old Petergof, Ulianovskaya 1, Russia; lvgrigoryev@mail.ru

² St.Petersburg Institute of Technology, Russia; msychov@yahoo.com

³ Russian State Pedagogical University, St. Petersburg, Russia

Abstract

We report second harmonic generation in the ZnS-based materials. Self-activated ZnS, ZnS:Cu,Br and ZnS:Cu,Al were studied. Phosphor powders were subjected to the 30mJ pulses of YAG infrared laser. Wavelength of the generated green emission was 532 nm, exactly one half of that of incident laser light (1064 nm). It is shown that high copper content in the phosphor is crucial for the non-linear properties.

1 Introduction

Materials with non-linear properties are very promising for optoelectronics applications. One kind of such materials is ferroelectrics based on lithium niobate, however they are difficult to process and deposit onto the substrate. Thus development of new materials with advanced properties and more suitable for the fabrication and utilization in the optoelectronics devices is very important. Recently there were several reports on second harmonic generation (SHG) in electron beam deposited ZnS thin films and nanometer-sized thin layers of ZnS:A (A=Al, In,Sn) [1,2]. We report second harmonic generation in the ZnS-based powder materials.

2 Sample Preparation

To fabricate phosphors high-purity zinc sulfide was mixed with the flux containing copper and (if needed) aluminum compounds and sintered. Sintering was performed in closed quartz crucibles in slightly reducing atmosphere. Charge flux contained sulfur in order to prevent zinc sulfide oxidation and formation of sulfur vacancies. Halogen-containing substance was also added to the flux to facilitate gas-phase process of grain growth. After sintering and consequent annealing, excess of copper sulfide phase was washed out from the surface of the powders.

Three samples were studied: self-activated zinc sulfide (ZnS-SA) as well as ZnS:Cu,Br and ZnS:Cu,Al where copper is activator and aluminum or bromine are co-activators. At the photoexcitation with UV light samples emit blue, blue-green and green light correspondingly due to the presence of Cl_S-V_{Zn} ; Cu_i-Cu_{Zn} and Cl_S-Cu_{Zn} ; Cu_i-Cu_{Zn} and $Al_{Zn}-Cu_{Zn}$ associates in the ZnS-SA, ZnS:Cu,Br ZnS:Cu,Al correspondingly [3].

3 Excitation Method

At the room temperature ZnS-SA, ZnS:Cu,Br and ZnS:Cu,Al powders were irradiated with strong pulses of infrared (IR) laser – fig.1.

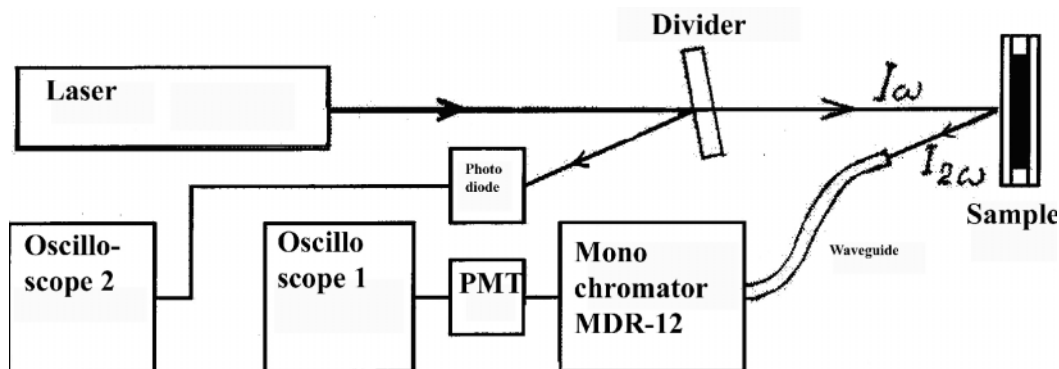


Fig. 1. Experiment setup

Yttrium aluminum garnet laser with wavelength of 1.064 μ was used, pulse length in a Q-switched regime was 15 ns, repetition rate 18Hz, pulse energy 30 mJ, averaged power density 0.25MW/cm².

Laser beam firstly was directed through the red filter (KS-17 glass) to cut off green emission of optical pumping flash-lamp and transmit laser IR-emission. Part of the beam was reflected from the filter-divider and used for the measurement of the intensity of first harmonic with the use of silicon photodiode and first oscilloscope. Then filtered beam excited phosphor sample placed in a quartz cuvette with layer thickness app. 1 mm. Generated second harmonic was waveguided to the monochromator and its intensity measured with photo-multiplying tube (PMT) FEU-100 and second oscilloscope. Start of oscilloscopes' time base was provided by the ignition impulse of laser pump lamp. Intensity of laser beam was controlled by discharge voltage of lamp's power supply.

4 Second Harmonic Generation

Typical luminescence spectra and SHG spectrum are presented in the figure 2.

Common feature for all three samples is that emission is not polarized which is natural for the powder samples. Intensity is almost isotropic in the hemisphere facing incident beam. Wavelength of the generated green emission was 532 nm, that is exactly one half of the wavelength of incident light.

Dependence of the SHG intensity on the pump intensity is presented in the fig. 3. Sample ZnS-SA has very short linear segment of SHG intensity vs pump intensity dependence and then saturates.

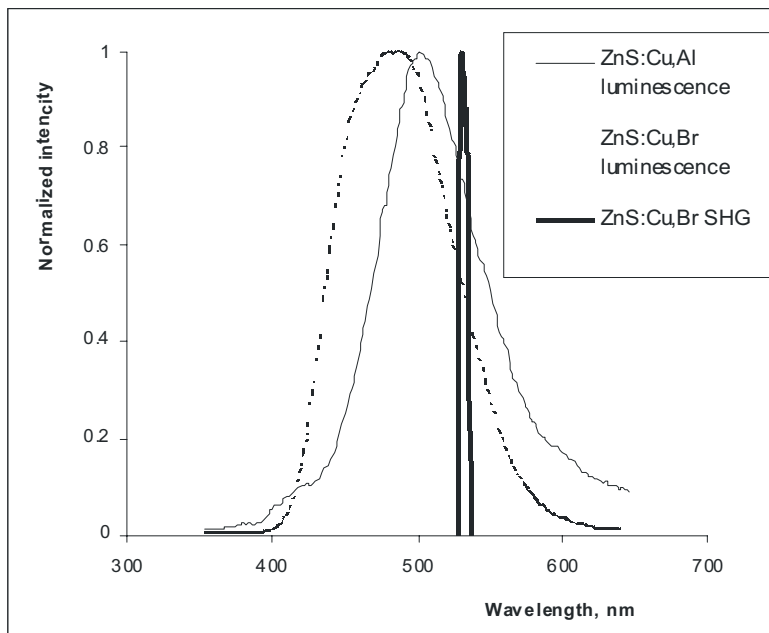


Fig. 2. Emission spectra

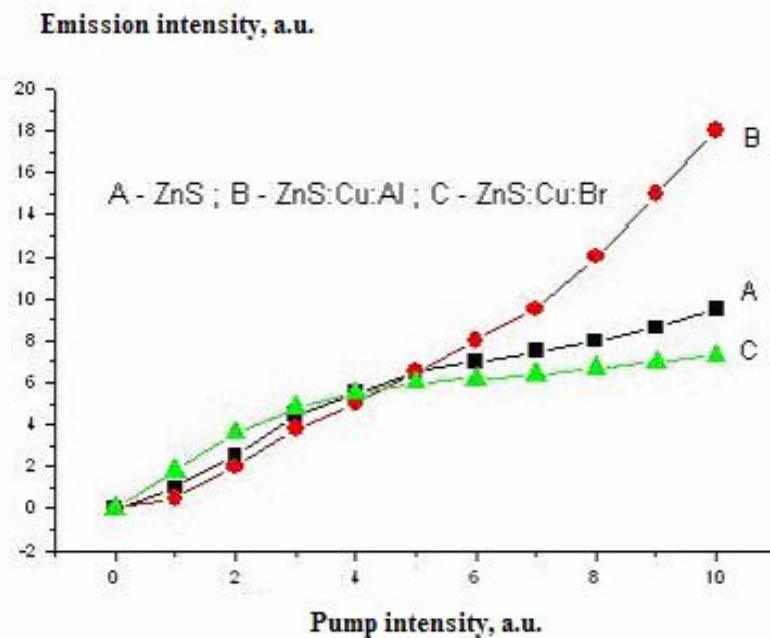


Fig. 3. SHG intensity vs pump intensity

Sample ZnS:Cu,Br firstly showed superlinear increase of SHG intensity but then also saturated, therefore it may be concluded that copper doping is needed for the non-linear behavior probably because of creation of energy levels suitable for the efficient multiphoton processes. Finally sample ZnS:Cu,Al showed superlinear increase of SHG intensity in the whole range of studied pump intensities (i.e. up to 0.25 MW/cm²) and thus have best non-linear properties. Co-doping with Al improves Cu solubility in ZnS and increases copper content in the phosphor more than two times (from 0.05 to 0.12 % wt.) thus high copper content is crucial for the non-linear behavior.

References

1. S. Enoch, H. Akhouayri, C. Deumié and C. Amra. Optics Communications, 161 (4-6), 1999, p.177-181
2. V. Kityk, M. Makowska-Janusika, J. Ebothéb, A. El Hichoub, B. El Idrissic and M. Addouc. Applied Surface Science 202 (1-2), 2002, p.24-32
3. Phosphor Hand Book. Ed. S.Shinoya and W.M.Yen. CRC Press, NY 1999, đ.320

Testing of p-n junction on silicon surface in nematic cell

Gritsenko M.I., Kucheev S.I., ¹Litvin P.M., ²Tkach V.M., Yelshansky V.B.

Chernigov University, G. Polubotka str.53, Chernigov, 14038, Ukraine,

¹ Institute of Semiconductor Physics, pr. Nauki 45, Kiev 03028, Ukraine

² Institute of Super-Hard Materials, Kiev, Ukraine

Abstract

In the work the testing method of p-n junctions on silicon surface and protective silicon oxide film in liquid crystal cell is considered. It has been shown that p-n junctions and defects of SiO₂ can be visualized by 1) pseudo-coloration change due to birefringence retardation; 2) deformation of homeotrop nematic with $\Delta\epsilon > 0$ due to charge accumulation; 3) depletion and/or enrichment of Si surface induced by ion charge in liquid crystal layer.

Introduction

The pixels both direct and reflect types made by LCoS technology are controlled by MOS transistors. Key elements of MOS transistor are p-n junctions. As known the p-n junctions within silicon wafer are fulfilled by means of donor or acceptor implantation through windows in mask silicon oxide (SiO₂) film¹. When there are defects in SiO₂ film, not deep p-n junctions are formed in the vicinity of these defects thanks to implantant penetration into silicon through defects of SiO₂². Therefore visualization the defects of SiO₂ film before implantation and not deep p-n junctions is important task of silicon device testing on early stages of production. Well known methods as REM and AFM have a lot of advantages but need a method of mapping of large surface. One from such methods is liquid crystal method which enables to test a large area.

In present work visualization of crystalline SiO₂ (quarz) microcrystals assemblage² and not deep p-n junctions on Si surface appearing after implantation in the vicinity of these quartz microcrystals assemblage (QMA) are considered.

Experiment and discussion

In the work monocrystalline silicon wafer of p-type conductivity and 4,5 Ωcm of specific resistance has been tested. Figure 1 demonstrates a REM image of quartz SiO₂ microcrystals assemblage in amorphous SiO₂ of $\sim 0,4$ mkm thickness and an AFM image of not deep p-n+ junction on Si surface after SiO₂ etching respectively. Note, not deep p-n+ junction on Si surface are optically not resolved. As p-n+ junction model there used p-n+ junctions formed by means of photolithography and donor implantation through windows in SiO₂ film, Fig.2.

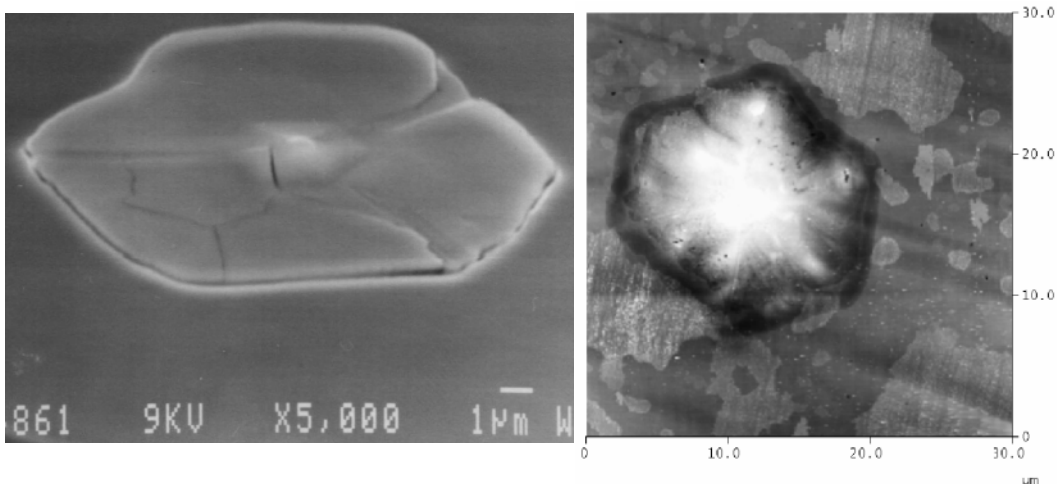


Figure 1. a) REM image of defect of amorphous SiO_2 - quartz microcrystals assemblage. b) AFM image of Si surface with not deep p-n junction.

In the work we used nematic cells of two types: Si/5CB/ITO and Si/ SiO_2 /5CB/ITO on Al substrate with homeotrop and planar(hybrid) orientation of nematic of 5 mkm thickness. For aligning of nematic we used lethitin covering on ITO and SiO_2 surfaces or rubbed polyimide film respectively. Si surface was not subjected any treatment.



Figure 2. 3D AFM image of SiO_2 surface at borderline of p-n junction. 1, 2- amorphous SiO_2 over p-Si and n-Si respectively. K- microcrystals assemblage.

Visualization QMA defects in homeotrop cell.

When switching on a dc voltage with “-” U polarity relatively Si substrate, in 5-40 seconds time, depending on specific defect, a deformation of homeotrop nematic appears, Fig.3a. The time delay between the deformation of nematic and voltage switching on means that the deformation is caused by ion charge accumulation in the vicinity of QMA defects. AFM image analysis indicates

that there are deep splits between microcrystals and amorphous SiO_2 . We believe that negative charges penetrate into liquid crystal namely through these splits.

It should be noted that the centers of deformation of nematic near border of p-n junction displaces in direction of thick part of SiO_2 film, Fig.3a. It means that in spite of thin SiO_2 over n-region of p-n junction (See Fig.2) ions penetrate through thick part of SiO_2 film where p-Si substrate. Absent of deformation of nematic over n-Si area(2 one, Fig,3a) can be explained that “-” U biased p-n junction is energy barrier for negative charges.

When switching on a voltage with “+” U polarity, deformation of nematic near defect appears simultaneously with applying voltage and rapidly (1-5 seconds) relaxes to the stationary state, Fig.3b. Deformation is caused by not uniform electric field because of non-uniformity of QMA surface. Accumulation of injected charge is absent by such polarity of voltage³. Relaxation of deformation is due to accumulation of polarized charge and inside electric field formation.

Visualization of QMA defects without electric field.

The QMA defects in thin cell (<5 mkm) is not visualized by means of change of pseudo-coloration. AFM image analysis of QMA defects surface indicates that their surfaces are higher than surface of amorphous SiO_2 on 100-150 nm, Fig.2. Obviously such a overfall of liquid crystal thickness is not enough to change a retardation of birefringence. On the other hand the overfall of liquid crystal thickness on border of p-n junction, approximately equal to 400nm, Fig.2, is enough to change of pseudo-coloration over QMA surface.

Figure 4a demonstrates a frequency dependence of voltage threshold of nematic reorientation over p- and n- regions of p-n junction. As seen, the visualization p- and n- areas of p-n junction is good for frequencies less than 10^3 Hz. Difference between the thresholds over p- and n- areas of p-n junction is due to different SiO_2 thickness over these areas, Fig.2.

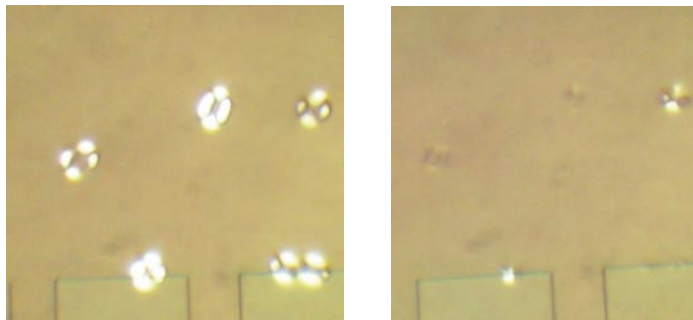


Figure 3. Deformation of homeotop nematic in the vicinity of QMA defects in Si/SiO₂/5CB/ITO structure. 1, 2 - SiO₂ over p-Si and n-Si respectively. a-left) -5,5 B. b-right) +5,5 B.

AFM image of not deep p-n junction analyses indicates that overfall between planes of p- and n- areas of not deep p-n junction does not exceed several nm.. Therefore visualization of not deep p-n junction by means of pseudo-coloration change is not possible.

It has been stated that after switching on ac voltage to Si/5CB/ITO structure there is redistribution of applied voltage between Si and LC layers. Figure 5 demonstrate the voltage change dynamic on LC layer after, switching on external voltage. Such a change of voltage indicates that there is major carriers (holes) concentration (enrichment) within Si surface layer. Carriers enrichment is caused by field effect of negative ions accumulated in LC layer near Si surface⁴ due to dc bias on Si/AL Schottky barrier.

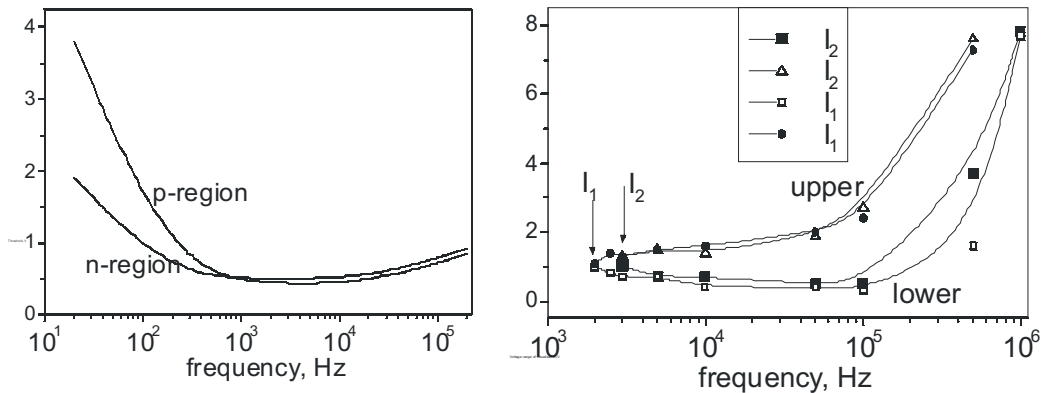


Figure 4. a-left) Dependence of threshold voltage of nematic reorientation over p- and n- regions of p-n junction in Si/SiO₂/5CB/ITO structure on frequency. b) Dependence of voltage range of p-n junction visualization in Si/5CD/ITO structure. I₁ and I₂ are levels of illumination (I₂>I₁).

Figure 4b demonstrate the dependence of the voltage range of visualization of p-n junction on frequency by different levels of illumination. As seen, a p-n junction resolution by liquid crystal takes place at high frequencies. Besides there is dependence on level of illumination: for higher level illumination the p-n junction resolution occurs at higher frequency (marked with arrow 2, Fig.4b). Such behavior means that a p-n junction capacity influences on threshold voltage: generation of non-equilibrium carriers because of illumination decreases a p-n junction capacity.

An illuminated p-n junction injects no-equilibrium carriers into neighboring depleted region of p-Si. This causes the reorientation of nematic over this neighboring region thanks to redistribution of voltage applied to structure. Figure 6 shows typical size (L) of reoriented area of nematic far from laser spot.

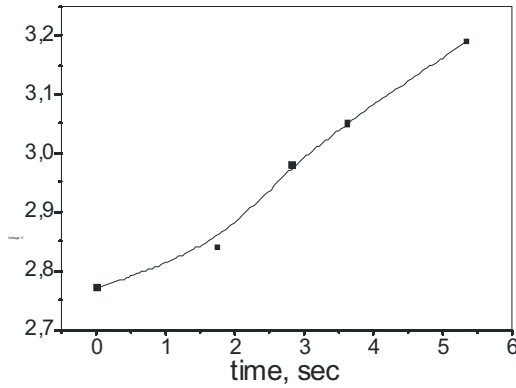


Figure 5. Dependence of voltage drop across LC layer in Si/5CB/ITO structure on time after switching on the external voltage.

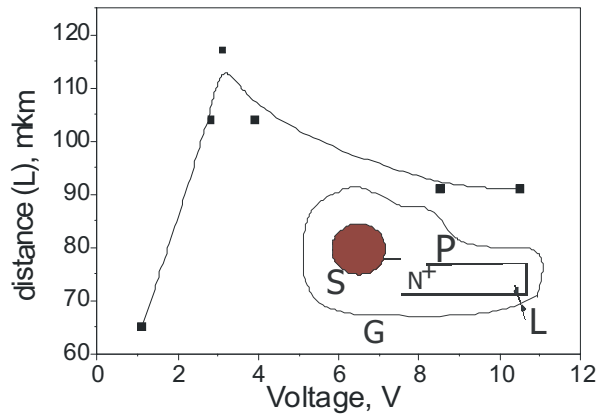


Figure 6. Typical dependence of reoriented area (width L) of nematic near border of p-n+ junction on applied voltage. Frequency 10^5 Hz. S-He-Ne laser spot. G-border of reoriented area.

Preliminary dc voltage with “+” U relatively Si substrate action makes worse a p-n junction visualization. After “+” U voltage action there is an edge smearing due to appearing of zone of reoriented nematic along p-n border. For dc voltage greater than 1V and action period more than ~ 10 seconds p-n junctions cease to visualize. It means that the depleted layer in Si has given down lower than the underlay of not deep p-n junctions.

After “-” U voltage action the p-n junctions visualization disappear. Figure 7 demonstrates dependence of duration of returning into visualization mode on dc action period. As seen, returning into visualization mode takes pair tens seconds. We believe that positive charge accumulated near Si surface during dc action period continues to influence on Si surface conductivity by means of field effect⁴ during returning period.

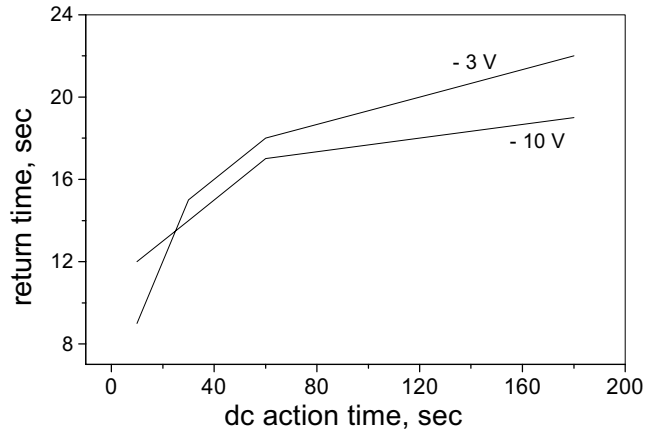


Figure 7. Dependence of returning time on dc action period.

Let us note an interesting effect of semi-bistability. Figure 8a demonstrates an AFM image of rubbed polyimide film with microcracks. By threshold crossing, along such microcracks, the change of initial orientation of nematic takes place. This changed orientation keeps after switching off of external ac voltage, Fig.8b. Returning in initial state of orientation can be carried out by mechanical deformation of liquid crystal layer. Such semi-bistability can be explained by small anchoring on Si surface. In this case director on Si surface can switching between two states.

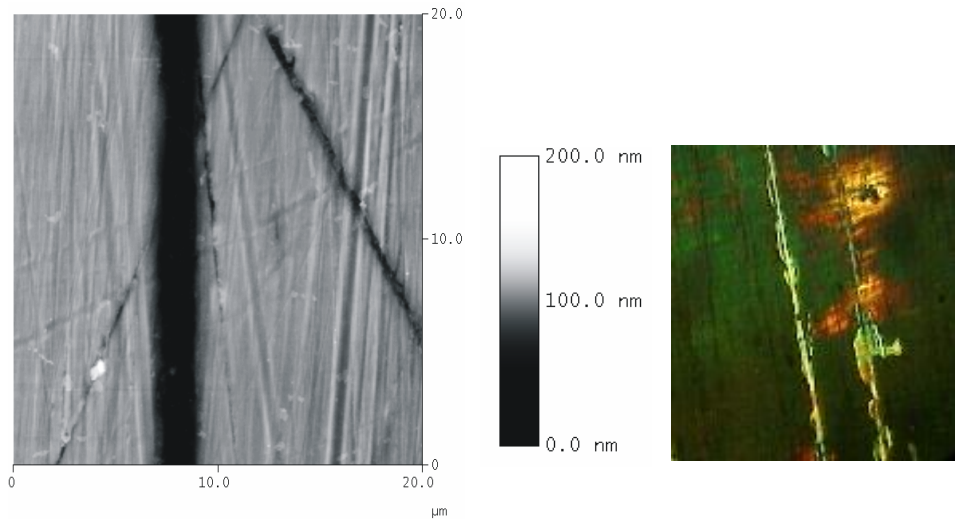


Figure 8. a-left) AFM image of rubbed polyimide surface with microcracks. b-right) Changed orientation of nematic in Si/5CB/ITO structure taking place along the microcracks. $U=0$.

Reference

1. R. Muller, T. Kamins *Device Electronics for Integrated Circuits*, Willey, 1986.
2. R.M. Burger, R.P. Donovan. *Oxidation, diffusion and epitaxy. Fundamentals of silicon integrated device technology*. V.1 "Mir" Moskow (1969) (in Russian).
3. M.I. Gritsenko, S.I. Kucheev. Proc. of SPIE. 3318, 242(1998).
4. M.I. Gritsenko, S.I. Kucheev. MCLC, v.246, 103(2005).

The Research on Plasma Display Panels in Kyiv National Taras Shevchenko University: History and Possible Modern Application

O.I. Kelnyk, T.E. Lisitchenko

Kyiv National Taras Shevchenko University, Radio Physics Faculty, 60
Volodymyrs'ka St., 01033, Kyiv, Ukraine, oles@univ.kiev.ua

At present time, plasma display panels (PDPs) applications are prevailing for the information displays with large screen size. This work include the brief historical review of gas discharge and PDPs research in the Electron Physics Cathedra of the Kyiv National Taras Shevchenko University and possible modern application of some results those were obtained.

The Electron Physics Cathedra in the Kyiv National Taras Shevchenko was founded at 1932 by Corresponding Member of the Ukrainian Academy of Sciences, professor Naum Morgulis [1] . From the beginning of Cathedra activity, physics of low temperature plasma and gas discharges is one of the main direction of its experimental and theoretical research. In particular, the directions of Cathedra studies were glow and arc discharges, radio frequency (RF) discharge, plasma sources, interaction between the plasma and electron beam etc. Many results in those fields were obtained for the first time. For instance, at 1952, S.Levitsky discovered the phenomenon of the electrode sputtering in RF discharge, including the discharge between isolated electrodes [2]. Also, N.Morgulis with collaborators discovered the photoresonant plasma [3] at 1966. In the subsequent years, plasma technological and ecological applications also were the directions of Cathedra research as well as the computer simulation of plasma phenomena.

PDPs researches on the Cathedra were performed during the 1970th years under the supervision of professor Yu.Chutov [4-7]. Plasma indicators (old term for PDPs) with discharge own glow and the bus and cell (a and b on Fig.1 correspondingly) structure were studied. For these experimental research purposes, the capillary and flat models were developed with the parameters similar to the real PDP cells. Practically all of the known plasma diagnostic methods, such as probe diagnostics, optical and spectroscopic diagnostics, RF diagnostics, were applied for the measurements of the parameters and characteristics of the PDP cell discharge. The main goal of these researches was the increase of the efficacy of the PDP cell discharge own glow.

One of the most effective ways to increase the discharge glow efficacy is the optimization of power supply voltage. Changing the waveform of that voltage, on can shift the electron energy distribution to the non-maxwellian shape. That is important for the discharge efficacy because the most low-energetic electrons in the maxwellian distribution are useless for the discharge glow purposes, as it shown on Fig.3 (if one applies the discharge own glow, excitation and ionization bands are adjacent). Note that the discharge with DC power supply has very small efficiency so different types of alternat-

ing discharge power supply voltage were studied [4-5]. Those types are sinusoidal, triangular, trapezoid and various sorts of pulses combinations. It was noticed that some leading pulses increase the efficacy of the glow.

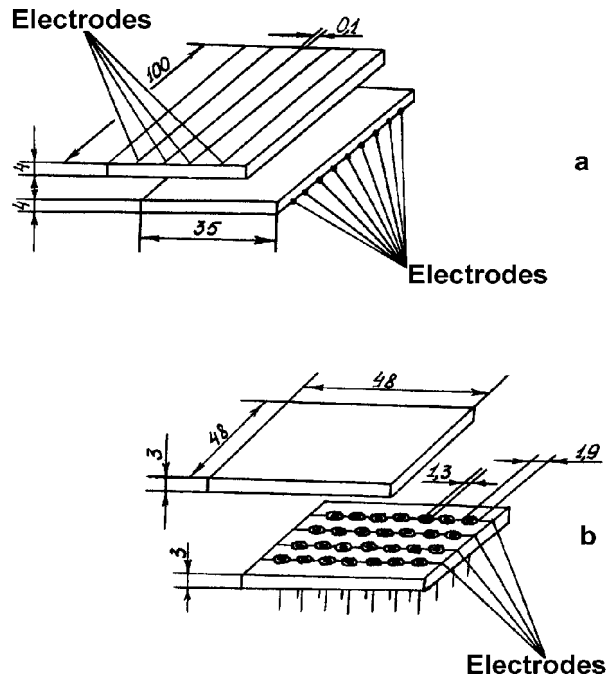


Fig.1. Plasma indicators (old term for PDPs) with bus(a) and cell (b) structure.

Another way of efficiency increase is the optimization of the gas mixture inside the PDP cells. Cathedra researchers tried many kinds of gases, such as pure rare gases (He,Ne,Ar,Kr,Xe) and various mixtures of them. It was noticed that Penning mixtures of xenon are most effective for the discharge glow. The influence of the other substances, e.g. materials with small electron affinity for the cell covering, was also studied and the optimal conditions were found out [5-6].

There were some other Cathedra researches related to the PDP technology. For example, the possibility of the creation of the color plasma display based on discharge own glow was studied. Such a PDP is principally possible, but it is not capable for display of full-color images. Also, the glowing waves in the pulse discharge were investigated for the purposes of plasma indicators [7].

Based on the researches described above, the plasma indicator device was developed (Fig.2). The efficacy of the monochromatic PDP in this device is about 5%.

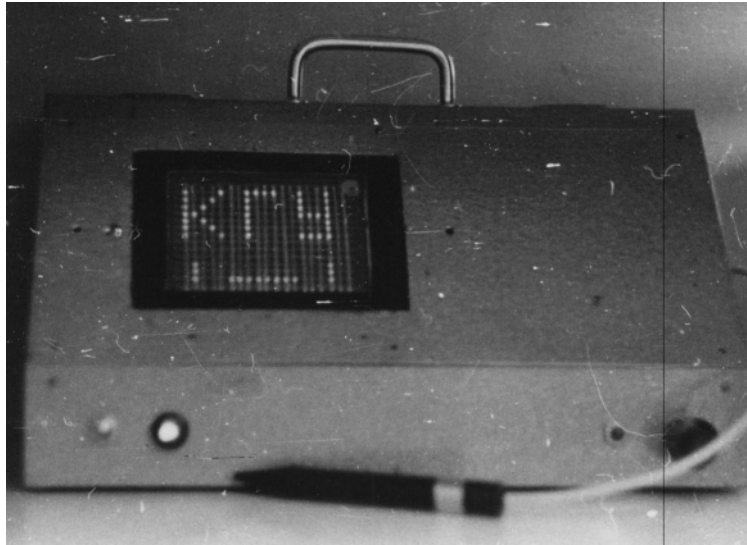


Fig.2. Plasma indicator device developed by Electron Physics Cathedra (photo 1972)

Devices based on one described above were later (at 1980th-early 1990th) produced serially by the electronic plants in Ryazan' (Russia) and Rivne (Ukraine). Electron Physics Cathedra also participated in the improvement of these devices [8].

The main difference between modern PDPs and older ones is luminescent screen presence. That screen allows obtaining a full-color image but causes the additional efficacy losses on the stage of energy conversion from discharge own glow to phosphor luminance. Fig.3 shows the electron velocity distribution with the bands of phosphor excitation (1) and gas ionization (2). In particular, for this case the excitation band is much smaller than corresponding band for the discharge own glow. So the efficacy of the best modern PDPs lies below 1%.

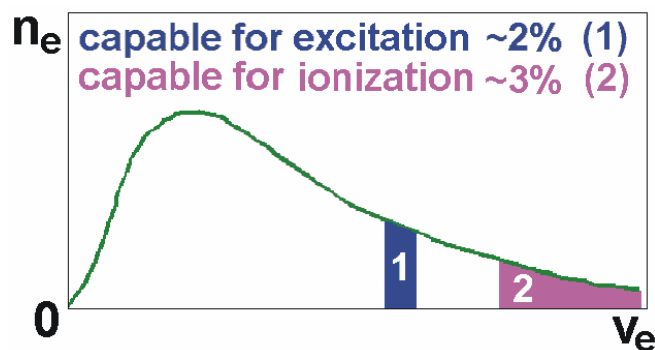


Fig.3. Electron velocity distribution in the PDP cell discharge with the excitation and ionization energy bands

Results obtained by Electron Physics Cathedra for the older types of PDP strongly corresponds to the main problem of modern type PDPs those also need the optimization of power supply voltage and gas mixture in the discharge cell. So the application of these results may increase the efficacy of PDPs of modern types.

References

1. N.D.Morgulis – 100th anniversary. // Bulletin of Kyiv National Taras Shevchenko University. Radio Physics & Electronics. 2004, 6, P.p. 5-7 (In Ukrainian)
2. S.M.Levitsky. Spatial potential and electrodes' sputtering in the high frequency discharge. // ZhTF, 1957, 27, #5, P.p.1001-1009 (In Russian)
3. N.D.Morgulis, Yu.P.Korchevoi, A.M.Przhonsky. Obtaining of the cesium plasma via resonant irradiation method and some physical properties of this plasma. // ZhETF, 1967, 53, #2(8), P.p.417-420 (In Russian)
4. Yu.I.Chutov, N.S.Baranchuk, M.R.Lofovich, V.G.Danilov. Some physical properties of pulse discharge in glass cell filled with gas. // ZhTF, 1974, 44, #2, P.p. 355-362 (In Russian)
5. Yu.I.Chutov, T.E.Remnyova, O.V.Korolyuk. The plasma production by pulse discharge development in the gas cell. // Proc. XIII Int. Conf. Ioniz. Gases. Berlin. 1977, P.375
6. Yu.I.Chutov, N.S.Baranchuk, T.E.Remnyova. Radiation of the pulse discharge. // Zhurn. Prikladn. Spektroskopii, 1978, 28, #2, P.p. 340-343 (In Russian)
7. Yu.I.Chutov, A.I.Kravchenko, T.E.Lisitchenko. Glowing waves in the pulse discharge. // ZhTF, 1981, 51, #4, P.p. 706-713 (In Russian)
8. T.E.Lisitchenko, V.L.Melnichenko. Pulse discharge parameters in the plasma character synthesizing indicators. // Proc. Conf. "Actual Problems of Electronic Device Manufacturing". Novosibirsk. 1992, Vol.1, P.p. 65-69 (In Russian)

Index matching coatings for LCD

E. Khokhlov, S. Fetisenkov, K. Krivetski

IZOVAC Ltd, Minsk, Belarus

Abstract.

The results of development of index matching coatings for LCD are presented. This type of coating is used for decreasing medium boundary reflection by matching of LC and conductive ITO layer refractive indexes. Application of such films allows to improve customer properties of displays. The results of structures calculation for visible range basis on ITO and SiO₂ layers are presented. The possibilities of adjusting coating taking into account glass, LC and alignment layer refractive indexes are demonstrated. The results of two type coatings practical realization and its characteristics are shown. The structures were formed by ion beam sputtering in one vacuum cycle. First type is characterized by low reflection in visible range (less than 0,1%), and possesses sheet resistance about 300 Ohm/□. Second type has higher conductivity (resistivity less than 70 Ohm/□), but reflection is less than 0,7%

1. Introduction

Modern requirements to LCD constantly become tougher and it is especially in image quality. From optical point of view LC panel is multilayer system of different optical materials. The presence of numerous medium boundaries, which causes partial losses of transmitted light flux, will influence on image quality. All elements of LC cell should be optically matched to decrease reflectivity ratio of such boundaries. This will cause enhancement of image contrast. One of most expanded example of such matching is using of AR coating, which decrease reflection of outer boundary glass – air. Concerning of inner boundaries the possibility of this improvement could be applying of matching coating, which ensures abrupt reduction of reflection of structure glass – ITO – LC. The results of development and investigation of matching coatings for LCD of different applications are presented in this paper.

2. Background

Two types of LC cells are used in modern LC devices. First operates on transmission, second – on reflection. For first type light from the light source passes cell one time (Fig.1). For second type it passes it twice because of reflection on mirror surface (Fig.2) First structure is characteristic for LCD broad use, second is typical for LCOS display.

Cell layer structure consist of material with different refractive indexes: glass – 1,55 – 1,65; ITO – 1,9 – 2,1; LC – 1,45 – 1,65; alignment layer – 1,45 – 1,9. Each medium boundary will make its contribution in light loss because of different reflective indexes. For material with close indexes this difference could be minimized by correct selection of their properties.

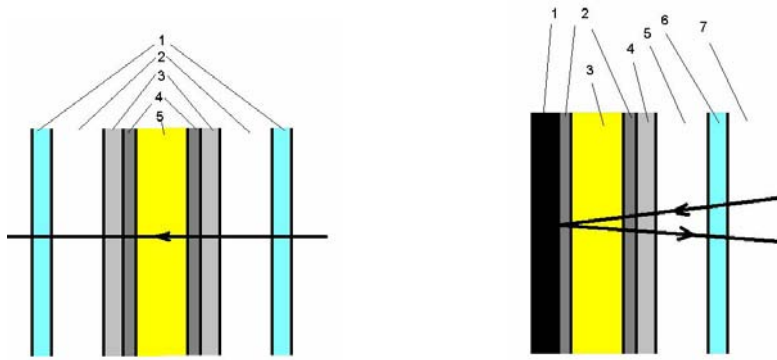


Fig.1.(left) Transfective LC cell: 1 – AR coating; 2 – Glass; 3 – ITO; 4 – Alignment layer; 5 – LC.

Fig.2.(right) Reflective LC cell: 1 – Mirror layer; 2 – Alignment layer; 3 – LC; 4 – ITO; 5 – Glass; 6 – AR coating; 7 – Air

Another approach is required for medium boundary with high difference of indexes. The problem of boundary glass – air is solved by AR coating [1]. The reduction of reflection of boundary ITO layer could be achieved by creating of index matching coating. The main idea of this method is substitution of ITO layer for optical structure basis on ITO, which at the expense of interference phenomena will suppress parasitic reflection and reduce it to minimum in all visible range of wavelength [2, 3, 4]. At the same time this coating should possess the same electrical conductivity as single ITO layer.

The constructions of index matching coating of ITO – SiO₂ – ITO type for different LC cells were developed basis on calculations with using of special program of optical coating calculation OptiLayer. The real values of refractive indexes of material composing cell and direction of parasitic light were taken into account during calculations. It also should be taken into consideration that LC in different states possesses different refractive indexes (n_o , θ , n_e). We used “average” magnitude during calculation. In this case using of index matching coating will result to improvement of image in switched on state of LCD and reduction of reflection in switch off state. Constructions are notable for technological simplicity of deposition and stability of error during deposition. Examples of such structures and their electrical and optical characteristics are demonstrated below.

3. Index matching coating for LCOS devices

The first type of coating was created for application in LCOS cell. According to operating requirement it should possess extremely low reflection on inner boundaries ($R_{ave} < 0,1$ in range 420 – 650 nm). LC with “average” refractive index 1,62 was used. Sheet resistance for devices of this type should be less than 300 Ohm/□. After analysis of structure calculation it was found out that for achievement of required optical properties the thickness of the last ITO could not exceed 20 nm. For receiving of needed sheet resistance in case of minimal film thickness it is optimal to use of ion-beam deposition on

heated substrate technology. The temperature of substrate should be more than 350 degrees. Index matching coating is three-layer structure ITO – SiO₂ – ITO (14 nm – 48 nm – 16 nm respectively).

The calculated reflection spectra of the structures glass – ITO – LC with sheet resistance 300 Ohm/□ and glass – index matching ITO – LC with the same electrical conductivity are presented on Fig.3. It is clear that using of index matching allows sufficiently decrease reflection. The maximal reflection in visible range is less than 0,1%.

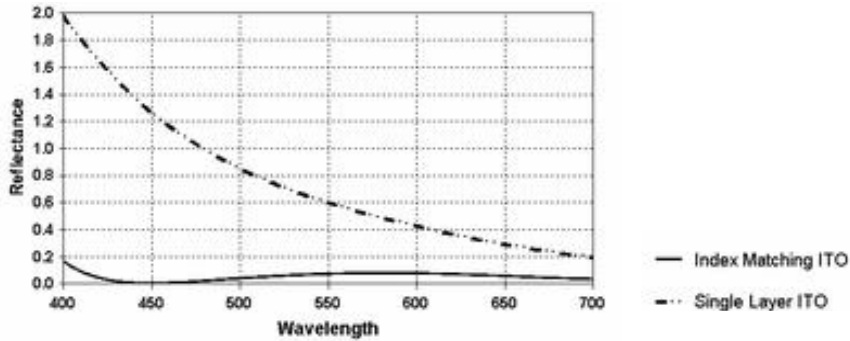


Fig.3. Reflection of ITO and ITO index matching coating.

Regarded construction is notable for simplicity and could be easily adjusted for LC and glass with other refractive indexes. However in real LC cell except current conductive layer alignment layer presents, which highly influence on optical characteristic of the reflection. Exception is case of equation (closeness) of LC and alignment layer refractive indexes, for instance like in case of organic alignment layer. However in present time developers and manufacturers of LCOS devices more often use inorganic materials for LC molecules alignment [5]. It is shown on the fig.4 how using of silicon dioxide film as alignment layer influence on reflection of the structure.

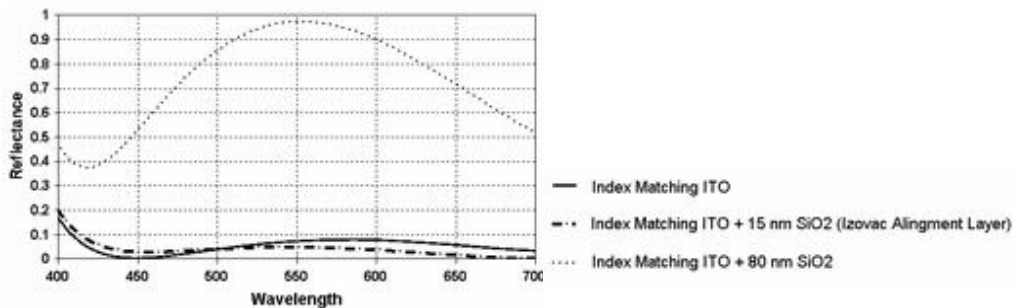


Fig.4. Reflection of ITO index matching coating with alignment layers.

4. Index matching coating for transfective LCD

Second type of index matching coating was created of transfective LC devices. The requirement for reflection of this structure is not so high. Re-

flection could not exceed 1% in range 420 – 650 nm. But sheet resistance should be less than 100 Ohm/□. The LC was the same as in first case. The refractive index of alignment layer is 1,85 and its physical thickness is approximately 150 nm. According to calculation index matching coating is a three layer structure ITO – SiO₂ – ITO (18 nm – 29 nm – 131 nm respectively). From optical point of view the best solution is using non heated technology of deposition. The reason is that ITO created by this method does not possess so high dispersion of refractive index like in case of heated technology. At the same time sheet resistance of index matching coating is obtained less than 70 Ohm/□. The analysis of influence of SiO₂ alignment layer has shown, that optimal reflection ratio is obtained in case of its thickness does not exceed 20 nm (Fig.5). Moreover in this case the range of low reflection (less than 1%) becomes wider 400 – 700 nm. In this case the structure ITO – SiO₂ – ITO is adjusted, moreover last layer of ITO becomes thicker (135 nm).

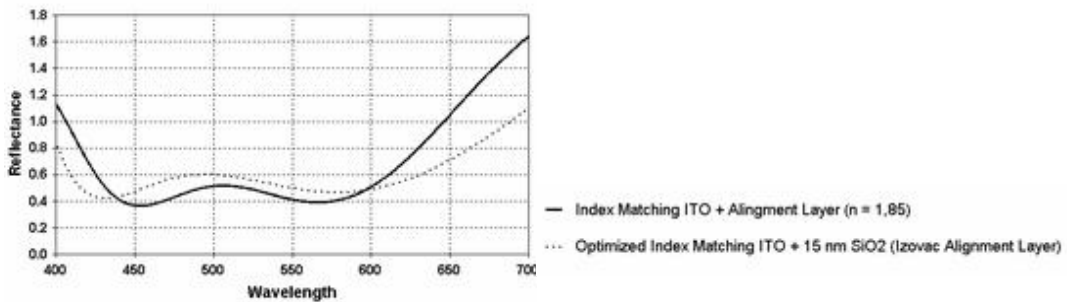


Fig.5. Reflection of ITO index matching coating with different alignment layers

5. Conclusion

The results of development of index matching ITO coating for different LC devices were presented. It was shown, that substitution of ITO for index matching ITO coating allows to reduce sufficiently reflection of LC cell in general. The properties of substrate, LC and alignment layer should be taken into account during development of such structures. Presented constructions were practically made on test samples of LC devices. Their checking has shown sufficient reduction of reflective ratio of inner boundaries. Unfortunately the methodical difficulty of precision measurements of spectral characteristics of received samples does not allow to compare it with theoretical calculations.

6. References

1. Chao-Ming Huang, C.-Y. Chen, Jyh-Jier Ho, Sen-Chrong Shiau, and W. J. Lee. The Improvement on Light Efficiency of Anti-Reflection Films by a DC Ion Source Sputter System in LCD Applications. Proceeding of IWD-05 ,p. 573-575
2. www.izovac.com/ii/IZOVAC-TB4-May-2005-rus.pdf

3. www.optics.unaxis.com/download/Pressetexte-pdf/PR-en-080404.pdf
4. www.tfdinc.com/imitopage.htm
5. A.Murauski, A.Khakhlou, U.Shiripov and A.Gerasimovich, "Ion beam sputter deposition process of inorganic vertical alignment layers", Proceeding of SID 2004, p.574-577.

Ion beam sputtering technology for deposition of thin films for FPD.

Shiripov V., Khokhlov A., Maryshev S., Leuchuk N., Khisamov A.

Izovac ltd, Minsk, Belarus

Abstract. We present design and application results of the ion beam deposition technology for display industry. This method allows to deposit a wide spectrum of films with various physical properties, covering most of the thin films used in modern flat panel displays. The discussed methods are based on “anode layer accelerator” type ion sources. The chosen type of sources can be scaled to meet new requirements for highly uniform processing of large area glass substrates. Several latest examples of industrial application of various ion sources are provided, with specific attention paid to optical coatings, TCO and alignment layers for LC.

1. Introduction

Thin films in modern flat panel displays (FPD) are their integral parts. The variety of functional purpose of the films conditions the application of a wide spectrum of film materials having various physical and chemical properties. The variety of applicable materials conditions the variety of the methods of their deposition. Among the vacuum methods of coating deposition, the methods of physical (PVD) and chemical (CVD) deposition have become the most commonly used practically. The most common physical method of coating deposition is the magnetron sputtering due to sufficiently low cost and good versatility. The method offers the possibility to deposit thin films with various physical properties and, above all, with high productivity and uniformity on large areas. However, continuously increasing requirements to the properties of the coatings cannot be met always in full measure using typical technologies and need using other technological approaches. The ion beam technology (IBT) can be referred to as one of the most promising directions in thin film coatings for such purpose. Although the principles of this technology were developed some decades ago, technological imperfection of its implementation retarded its practical use. The progress in this respect achieved to date allows us to hope that this method will get appropriate position in industrial display production.

2. Distinctive features of IBT

What is typical for ion beam technology? Firstly, it is the presence of an autonomous ion beam source and possibility to control both energetic and spatially-geometrical parameters of the beam. As a result, high degree of organizational freedom of the technology is ensured. The ion beam can be directed to the substrate surface at a required angle and the substrate surface can be processed for the purpose of either cleaning it or modifying it at the atomic level. The beam can be directed to the initial material (target), which is transformed then into a sputtered flux and deposited on the substrate as a coating. In this case, the regime of coating deposition by sputter-

ing the target is implemented. Secondly, it is the possibility of work with any kind of working gases and practically with any solid-phase materials independently on their physical properties. This conditions the high degree of the method versatility in terms of nomenclature of thin film materials to be deposited. The ion-beam technology is suitable for work with all the coating materials being used. Thirdly, the vacuum and energetic properties of coating process have such combination of parameters, with which the properties of the coatings approach to those of solid materials. Just due to that, the films obtained by such method have high adhesion and density, low roughness and stable physical properties. As regards to the physical properties, the coatings obtained by ion beam technology are considered as the most advance compared to other deposition methods. Fourthly, the organizational freedom of the method makes it possible to use simultaneously several independent ion beams and perform combined kinds of coating-formation operations. For instance, the film can be deposited and exposed to the ionic radiation at the same time. Such technique makes it possible to improve the film adhesion and to modify the film microstructure and stoichiometry. The combining principle increases the technological potential of the method. Fifthly, the today's technical developments are based on using the generators of linear ion beams. As a result, they make it possible to carry out the processes with large-sized substrates.

The above-described features of the IBT justify its advantages such as versatility of application, high degree of controllability, process flexibility and quality of the coatings. The technological and engineering capabilities of the IBT condition the potential advantages and real prospects of its use in manufacturing the FPD.

3. IBT Technique

The practice of use of the IBT is based mainly on two types of ion sources, the grid ones including mainly Kaufmann's sources, and the griddles ones, such as plasma accelerators with closed electron drift. The first of them has dominated in the worldwide practice until recently, but, at the same time, retarded the wide industrial application of this technique due to its disadvantages. The second type was developed on the territory of the former USSR as early as in the seventies; however, due to secret nature of works could not be a worthy competitor to the first one. By now, due to the information openness and high level of engineering developmental works as applied to the construction of plasma accelerators, the last have become the subject of close attention from the side of users of vacuum technologies. Now it might be said with confidence that the future of the IBT is connected with the use of just plasma accelerators.

The anode layer accelerator (ALA) is one of variants of an accelerator with closed drift. This type of sources is featured by the designing and operating simplicity and reliability. It operates without filaments and makes it possible to implement sufficiently easily various geometry of the ion beam. Just for this reason, the industrial-purpose technological systems are being de-

veloped actively today. The scheme of such source is shown in Fig. 1. The principle of its operation is based on creation of a plasma discharge in crossed magnetic and electric fields in the working gas medium, which is a source of the directed ion beam. The physical peculiarities of the discharge predetermine also the shape of the ion beam, which is directed narrowly in the form of a continual band closed over the contour. In this case, the beam shape could be implemented to be the most various, such as axial, extensive, with the fluxes directed in parallel and at various angles (convergent or divergent). The flexibility of construction of the source makes it possible to implement various types of coating systems.

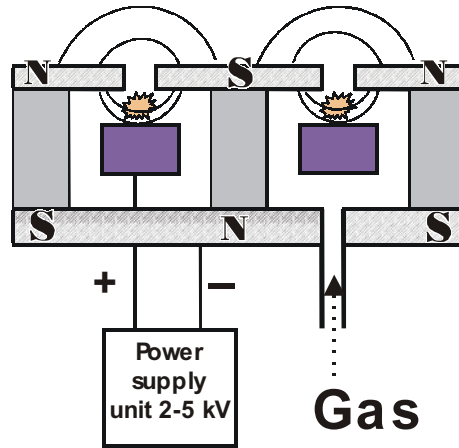


Fig.1. Scheme of the anode layer accelerator

Fig. 2 shows the scheme of the ion treatment process of the substrate surface with the purpose of cleaning or modifying it. In this case, the ion source generates the parallel ion flux, which can act on the surface at right (\vec{i}) or oblique (B) angle. Since the beam is narrowly localized, it is necessary to ensure the motion of the beam. In case of use of the linear-extensive configuration of the ion beam, the cross linear motion is sufficient. The processing area can be as large as a few square meters.

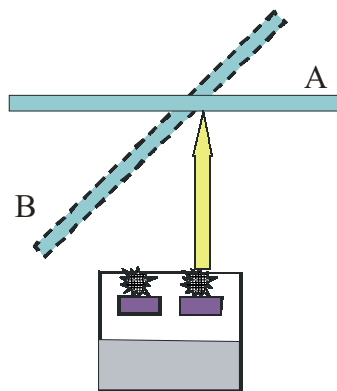


Fig.2. Scheme of the ion treatment process of the substrate surface

Figs. 3 and 4 show the thin film deposition schemes by sputtering the target material. The first one has the ion source with a convergent beam, which is focused on the target surface while the second one has a parallel beam. The advantage of the first scheme consists in using the target with minimum size, while the advantage of the second scheme – in the convenience of depositing onto oblique surfaces (B). In both cases, the target assembly can be made in the form of a rotary prism and contain several sides with different target materials. Using the extensive-design ion sources and, respectively, extensive targets solves the problem of uniform deposition of coatings on large surfaces. In this case, it is sufficient to ensure the relative movement of the substrate.

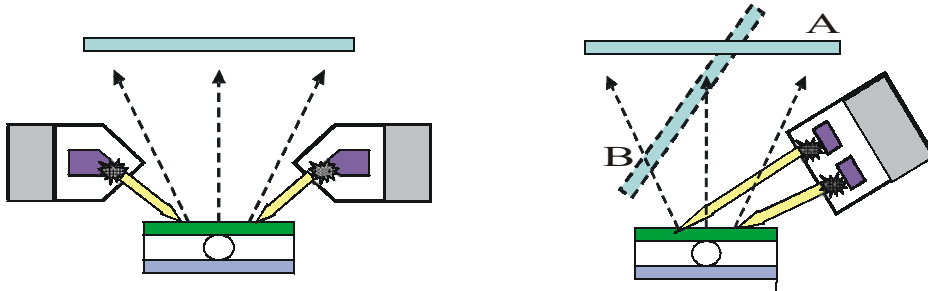


Fig.3 (left). Scheme of sputtering the target by the convergent flux

Fig.4 (right). Scheme of sputtering the target by the parallel flux

The Izovac Ltd has a rich experience in developing the ALA-based process systems for forming the coatings. Figs. 5-8 show some examples of ion-beam systems for cleaning and sputtering which are used successfully in the production of displays. The arsenal of developments includes the designs of ion-beam systems for working with the substrates having the size of up to 3 m that conforms completely to the technological size of modern glass LCD bases.

4. IBT Coatings

The practical use of the IBT for deposition of the display coatings has shown its clear advantages, firstly, for obtaining of optical structures. These coatings are intended for improving the quality of images provided by the display devices. It includes various types of antireflecting, absorbing and matching coatings, which contribute to the improvement of the contrast and brightness of the image. These coatings are, as a rule, multilayer ones and include optical materials with different properties. As the practice has shown, the films obtained by ion beam sputtering have the best optical properties due to favourable deposition conditions. It provides for high quality of such structures. The quality of the coatings is also improved due to such technological peculiarity as implementation of the whole multilayer deposition process in a single cycle (using interchangeable targets and appropriate control systems).

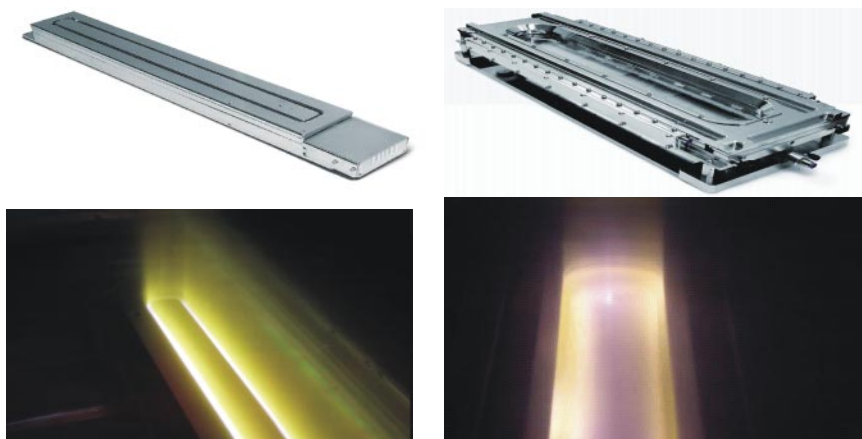


Fig.5 (left). Ion beam device for cleaning the substrates 500*500 mm and its operation in the chamber.

Fig.6 (right). Ion beam sputtering device for depositing the films onto the substrates with the size of 500*500 and its operation.

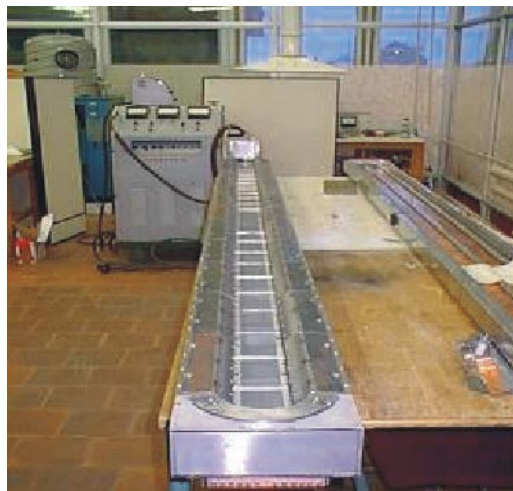
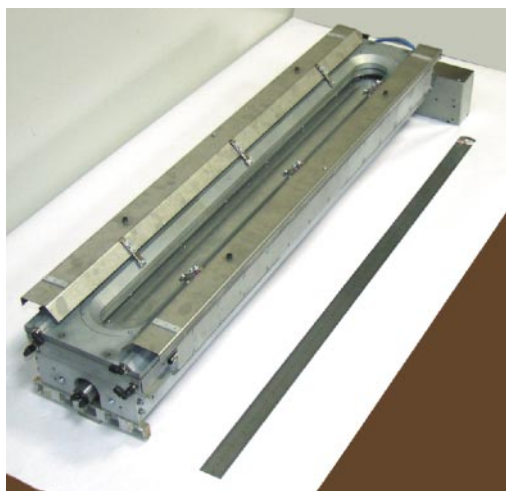


Fig.7 (left). Ion beam sputtering device for substrates with the size of 1000 mm

Fig.8 (right). Ion beam sputtering device for substrates with the size of 3000 mm

The transparent conducting coatings (TCO) obtained by the IBT are featured by high density and low surface roughness. This fact is very attractive for using them in a new generation of displays based on the organic light emitter diodes (OLED). As it is known, they are very critical in respect to the quality of the initial surface. It should be also noted that other inorganic coatings (protective or contact) used in the OLED structures shall have very good physical and technical characteristics, which are sometimes difficult to

achieve by traditional methods. Therefore, it could be said about the favourable prospects of using the IBT just in the production of the OLED displays.

It was recently ascertained that the IBT could be also very usable in developing the new methods of obtaining the alignment layers for liquid-crystal devices. It has been practically discovered that inorganic films with good orienting properties could be obtained with the use of directed ion beams and principle of oblique action upon the surface. Based on these principles, we have developed the processing techniques of the SiO₂ alignment layers for both negative and positive liquid crystals.

Conclusion

At present time, the IBT experiences the real renaissance caused by the increasing requirements to the quality and format of the coatings deposited. It is especially appreciable in the developing sphere of production of today's and future displays. The engineering and technological achievements in the field of the IBT make it already possible to offer new technological solutions for manufacturers of displays. At the same time, the technological potential of the IBT has not been yet disclosed completely. Today it may be said with confidence that the IBT has good prospects.

Acknowledgment.

The authors would like to acknowledge INTAS for partial support of research investigation under the project N03-51-5448 .

Liquid crystal light modulators created from glass ceramic materials with ultra low thermal expansion coefficient

Kolomzarov Yu.V., Maslov V.P.

V. Lashkaryov Institute of Semiconductor Physics, NAS of Ukraine, pr. Nauki 41, Kiev, 03028, Ukraine.

E-mail: kolomzarov@yahoo.com, vpmaslov@ukr.net

Abstract

Construction and technology of high stable liquid crystal modulators of light parameters (intensity and polarization) are proposed. Using of glass ceramic materials with ultra low thermal expansion coefficient with heaters from transparent conductive layers and temperature sensors give possibility to stabilized the temperature and therefore parameters of created liquid crystal light modulators.

Keywords. – TN LC modulator, stability, glass ceramic material, ultra low thermal expansion coefficient.

1. Introduction

Analysis of polarized light is an important diagnostic tool in many applications including remote sensing ¹, solar astronomy ², atomic and molecular spectroscopy and material analysis. For example, surface roughness and anisotropy of materials can be determined by investigating the depolarization of light upon reflection or transmission. On the other hand, some optoelectronic systems, for example an optical communication networks consist of a source of light, modulator for control of different parameters of light from the source, some medium (for example optical fiber) to guide the light and a detector to convert the optical information to electronic signal form. The rate of data transmission is limited by optical effects that give possibility to spread and eventually overlap the individual light pulses ³. For describing all states of incoherent light polarization, including mixtures of polarized and unpolarized light the Stokes vector was proposed in 1852. It is used to predict the effect of combining two incoherent beams and the effect of adding a polarizer or a retarder such as a half waveplate. The Stokes vector consists of a four components that completely characterizes the polarization of a light beam. The Stokes vector S can be represented as vertical matrix-vector with four simple components:

$$S = \begin{pmatrix} I \\ Q \\ U \\ V \end{pmatrix} \quad 1)$$

where I is the total light intensity, Q is the intensity difference between hori-

zontal and vertical linearly polarized components, U is intensity difference between linearly polarized components oriented at $\pm 45^\circ$, and V is the intensity difference between right and left circular components.

The Poincaré sphere is a convenient three-dimensional model for representation of different polarization states. It is schematically represented in Figure 1 and it is used as a map to plot the effect on a polarized beam of adding a polarization sensitive component such as a LCM. A point representing the initial polarization state is located on the sphere and an arc drawn on the sphere surface to locate another point that represents the new polarization state.

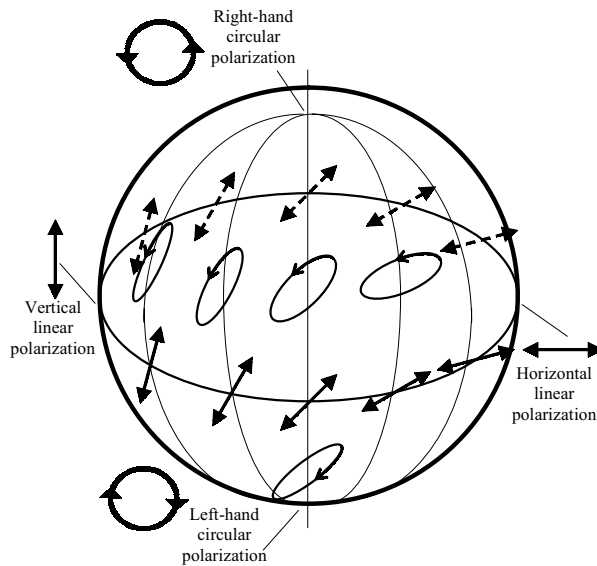


Figure 1. The Poincaré sphere is a three-dimensional surface on which all polarizations states can be represented.

For polarized monochromatic light the polarization state can be represented on a sphere of radius I , which for convenience is taken as unity. The X, Y, Z coordinates of a point on the surface of this sphere corresponds to next lights parameters: X represents horizontal linear polarization, Y represents linear polarization at 45° and Z - right-handed circular polarization. When the beam is completely polarized, $I^2 = X^2 + Y^2 + Z^2$. When the beam is partially polarized $I^2 > X^2 + Y^2 + Z^2$. Points on the equator represent linearly polarized light. The “north pole” represents right-hand circularly polarized light and the “south pole” represents left-hand circularly polarized light. Other points represent elliptically polarized light.

The liquid crystal modulators (LCMs) is tunable waveplates that, in conjunction with linear polarizers, form the circular and oriented linear polarizers that are required to characterize the polarization of an unknown light beam in a Stokes Polarimeter. Liquid crystal retarders are electrically variable waveplates. Retardance is altered by applying a variable, relatively low volt-

age waveform. These retarders are made by placing a thin liquid crystal layer between parallel windows spaced a few microns apart. Different liquid crystal materials range in birefringence from 0.07 to 0.26, enabling fabrication of thin, true zero-order retarders in the visible to near infrared region. The functional medium of LCM is aligned nematic liquid crystal placed between precision glass plates. Applied external electric field change the optic retardation by changing of the optic axis orientation. The response time and output light polarization of a LCM depends on several factors, including the LC layer temperature, thickness, viscosity, and surface treatment as well as the waveform of driving signal. ⁴ If create the twist-nematic LC structure and applied polarizing films in both sides of LCM it is possible to modulate intensity of transmitted polarized light when external electric field are applied. The same LC structure without polarizer can be used for control of light polarization.

The main goal of presented work is to propose the technology and construction ways for stabilized of temperature and LC thickness under the influence of environment conditions, mainly temperature.

2. Design of LCM and technological process.

Design of developed LCM is shown on Figure 2. LCM consists from two leakproof connected with glue glass ceramic substrates 1 and 2. On internal surfaces of substrates are deposited transparent ITO electrodes 5,6 and spin-coated with poliimid layers that are rubbed for creation of alignment layers. ITO electrodes 5,6 and transparent heaters 9, 10 have a metal contact pads 7, 8, 11, 12, 13, 14 with external metal electrodes. Liquid crystal material was injected in the gap between two substrates.

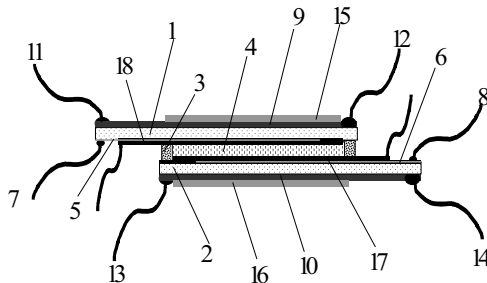


Figure 2. Design of TN LCM from glass ceramic material with thin film transparent heater and temperature sensor.

Liquid crystal ZLI-3145 by Merck with additive C-15 was used as material with wide temperature range of nematic (from -40 up to +93°C). The necessity of LCM temperature stabilization ⁵ provide by using of transparent heaters 9, 10. The design of heater must take into account the next requirements: heater reliability, capacity passes the heat to liquid crystal as soon as possible; it must be transparent and not obstruct to backlight and observe. Different designs of heater analysis showed ⁵ that the most effective is

to place heater inside of LC cell for direct contact with liquid crystal. But such design is technological very difficult for realization because it required creation of transparent thick insulating layers. Therefore more convenient way is to deposit transparent heater on the outside surface of the substrates. Conductive transparent ITO layer created by reactive cathode DC sputtering from In+Sn target in argon-oxygen gas mixture has a high adhesion to substrate. Film polarizer 15, 16 can be glued on the outside surface of substrates. Both heaters have contact pads with joined external metal connectors for applying of voltage to heater. For stabilization of LC temperature the thin film metal strip sensor from Ni+Cr 17, 18 was deposited on the inside surfaces of glass ceramic substrates. The resistance of this metal strip depends from temperature and it was used as temperature sensor. Such sensor has an extremely short response times and react on the temperature changes immediately.

The technological process for production of LCM was developed. Metal contact pads for soldering of metal contacts of transparent electrodes and heaters were deposited by vacuum DC magnetron method of duplex coating (Ti+Ni or V+Ni) or three-layered coatings (Ti+Cu+Ni or V+Cu+Ni) on glass ceramic material. For creation of metal contact pads and ITO transparent electrodes with special shapes we used chemical etching of these layers (together or separately if needed), deposition through special mask or laser lithography process. As adhesive layers were used thin layers of vanadium or titanium with thickness 10 – 30 nm. Thickness of copper and nickel layers were 80 – 100 nm. Chemical etching agents for removing of Ti, Ni and ITO layers based on acids mixtures were elaborated. For the tinning of contact pads covered with Ni and for soldering of copper wires (with diameter 50 - 80 μm) we used the liquid flux and low temperature solder described in ⁶. The pull strength of Ti+Ni tinned layers were investigated. Ti+Ni tinned layers demonstrated pull strength 40 – 55 kgf/cm^2 if it was deposited on ITO with surface resistance 300 – 800 Ohm/square and 50 – 65 kgf/cm^2 if it was deposited on glass. Such values of pull strength are satisfied for LCM and allow excluding the applying of additional external capsulation of wire connectors.

For gluing of glass ceramic substrates the butyral resin and novolac copolymer mixture 3 was used. This gluing process gave a possibility exclude additional external capsulation of LCM since glue was plotted accurately on the age of substrate and has high adhesion and strength.

3. Glass ceramic materials for LCM substrates.

Typically, when a nematic liquid crystal material is used in LCM, it speed characterized of switching times. Switch on time τ_{on} is the response time after turning on the applied voltage and switch off τ_{off} is the time after turning off the applied voltage. For given thickness d times τ_{on} and τ_{off} depended from temperature T and applied voltage U . These dependencies can be described by the follows expressions ⁸:

$$\tau_{on} = \frac{4\pi\gamma_1 d^2}{\Delta\epsilon U^2 - 4\pi^3 \left[k_{11} + \frac{1}{4}(k_{33} - 2k_{22}) \right]} \quad 2)$$

$$\tau_{off} = \frac{\gamma_1 d^2}{\pi^2 \left[k_{11} + \frac{1}{4}(k_{33} - 2k_{22}) \right]} \quad 3)$$

$$U_{th} = \left\{ \frac{4\pi}{\Delta\epsilon} \left[\frac{1}{k_{11}\pi^2 + (k_{33} - 2k_{22})\theta_0^2} \right] \right\}^{\frac{1}{2}} \quad 4)$$

where U_{th} is the threshold voltage, γ_1 is the rotational viscosity of the liquid crystal composition ($\gamma_1 = A \cdot e^{\frac{B}{T}}$, where A and B are constants), k_{nn} is the elastic constants of the liquid crystal material, $\Delta\epsilon$ is the dielectric anisotropy of the liquid crystal material and Θ_0 is the twist angle of LC molecules (for TN LCM $\theta_0 = \frac{\pi}{2}$). Rotational viscosity γ_1 exponentially decreasing with temperature increasing. It means that temperature maintenance is more effective and simple way for reducing of switching times in comparison with another ways, such as reducing the thickness of the liquid crystal cell, increasing the voltage applied to drive the liquid crystal display, and changing of the physical parameters of the liquid crystal material. At the same control voltage U switching times essentially increasing with decreasing of the temperature. Moreover, at -40°C and below the ZLI-3145 liquid crystal mixture become frozen and not respond to the applied voltage. With heating above -40°C the TN LCD operability recovers.

4. LCM characteristics for light intensity attenuation.

We investigate the next electrooptic characteristics: dependence of LCM light transmission from time after applying the driving voltage (bipolar meander 25V 1kHz), dependence of switch on time and contrast ratio from value of applied driving voltage (bipolar meander 1kHz) at 20°C . These characteristics represented in Figures 3, 4 and 5.

5. Analysis of LCM output light polarization dependence from control voltage.

We investigate the polarization of output light transmitted through created on glass ceramic materials LCM dependent from value of control voltage. The scheme of measurement set-up⁹ is shown in Figure 6. The results of these measurements are shown in figures 7 and 8 for different positions of LC TN cell.

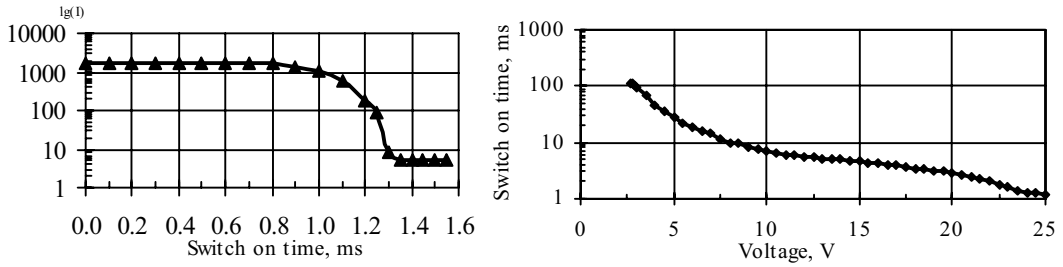


Figure 3 (left). Dependence of light transmission from time after applying of driving voltage bipolar meander 25V 1kHz at 20°C.

Figure 4(right). Dependence of switch on time (logarithm scale) from value of applied driving voltage bipolar meander 1kHz at 20°C.

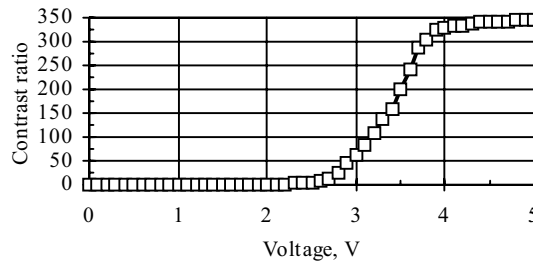


Figure 5. Dependence of contrast ratio from value of applied driving voltage (bipolar meander 1kHz at 20°C) on wavelength 550 nm.

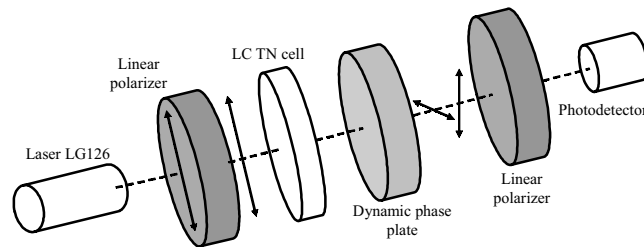


Figure 6. The scheme of set-up for LC TN cell properties measurement.

LC sample was lighted by the radiation with linear polarization. s - and p - polarization components of output light can be changed on a corner 90° with frequency 50 kHz (the period $T=2 \times 10^{-5}$ sec) without change of light intensity by electrically controlled dynamic phase plate. By the rotation of dynamic phase plate around optical axis it is possible to obtain such its position related to a LC sample, that the planes of linearly polarized light are parallels to the axes of LC sample.

Stokes vector components¹⁰ of LCM output light analysis shown that the created liquid crystal cell can be used as electrically controlled light polarization state modulator. For example company Meadowlark Optics proposed

to use two electrically controlled Liquid Crystal Modulators placed in series optically for measuring of light Stokes vector components as shown on Figure 9. The equations for calculation of Q, V and U components and correspondent values of voltage applied for each LCM are represented in Table 1.

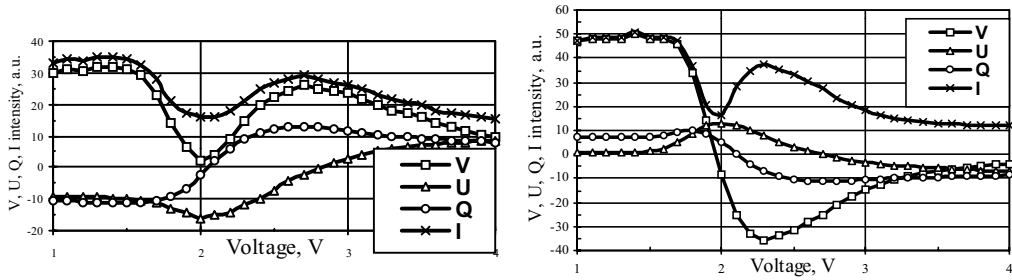


Figure 7 (left). Dependence of Stokes vector components of LCM output light from value of control voltage. Direction of LC molecule directors is parallel to plane of input light polarization.

Figure 8 (right). Dependence of Stokes vector components of LCM output light from value of control voltage. Direction of LC molecule directors is 45° to plane of input light polarization

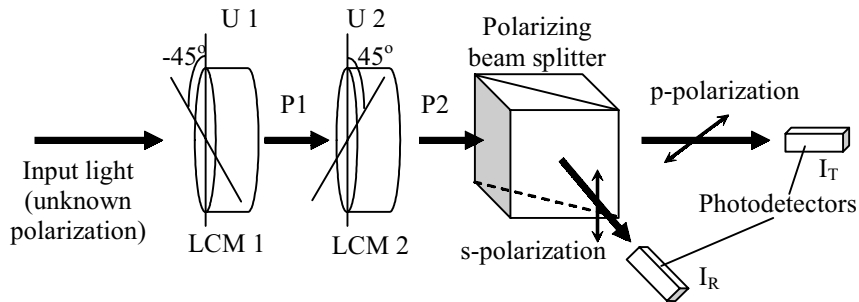


Figure 9. Using of LCM for light polarization investigation ¹¹.

Table 1.

U1	U2		Formula for Stokes parameter calculation
7V (0)	7V (0)	2V ($\frac{-}{2}$)	$Q \frac{1}{2} \frac{I_T 0 \quad I_T \frac{-}{2} \quad I_R 0 \quad I_R \frac{-}{2}}{I_T 0 \quad I_T \frac{-}{2} \quad I_R 0 \quad I_R \frac{-}{2}}$
7V (0)	4V ($\frac{-}{4}$)	4V ($\frac{-}{4}$)	$V \frac{1}{2} \frac{I_T \frac{\square}{4} \quad I_T \frac{3\square}{4} \quad I_R \frac{\square}{4} \quad I_R \frac{3\square}{4}}{I_T \frac{\square}{4} \quad I_T \frac{3\square}{4} \quad I_R \frac{\square}{4} \quad I_R \frac{3\square}{4}}$
4V ($\frac{-}{4}$)	4V ($\frac{-}{4}$)	4V ($\frac{3}{4}$)	$U \frac{1}{2} \frac{I_T \frac{\square}{4} \quad I_T \frac{3\square}{4} \quad I_R \frac{\square}{4} \quad I_R \frac{3\square}{4}}{I_T \frac{\square}{4} \quad I_T \frac{3\square}{4} \quad I_R \frac{\square}{4} \quad I_R \frac{3\square}{4}}$

6. Conclusions

1. The technological process of LCM fabrication was developed. Adding of titanium and nickel layers on contact pads allow to apply a soldering process for jointing of copper wires. We proposed to use thin film metal strip sensor from Ni+Cr for measuring and stabilization of LC temperature. Such thin film sensor can be formed inside of LCM and has an extremely short response times and react on the temperature changes immediately.

2. Using of glass ceramic materials with ultra low thermal expansion coefficient and transparent thin film heaters allows fabricate high stable LCM.

Acknowledgments

This work was made and presented in the frame of Project # 3045 of Science and Technological center in Ukraine. The authors are grateful to prof. Serdega B.K. and prof. Bereginskij L.J. from V. Lashkaryov Institute of Semiconductor Physics, NAS of Ukraine for measuring of LCM parameters and discussion of results.

References

- [1]. *Baur T., Elmore D.E., Lee R.H., Querfeld C.W., Rogers S.R.* Stokes II - A New Polarimeter for Solar Observations // Solar Physics. – Vol.70. – 1981. – P. 395.
- [2]. *Baur T.* Optical Polarimeters for Solar Research // Opt. Eng. – Vol. 20. – 1981. – P. 2.
- [3]. *Kliger D.S., Lewis J.W., Randall C.E.* Polarized Light in Optics and Spectroscopy. - Academic press, San Diego, California, 1990.
- [4]. *Herke R., Jamal S., Kelly J.* An improved polarizer representation for liquid crystal display modeling // Journal of the SID/ - Vol. 3, No. 1. - 1995.
- [5]. US Patent US2004/0036834 A1 Feb. 26, 2004.
- [6]. *Brodovoy G.V., Kolomzarov Yu.V., Tsurkynov Yu.A.* Improvement of the performance reliability of cockpit TN LCDs // Proc. of the XIth Int. Symposium «Advanced Display Technologies». - Crimea, Ukraine, September 8-12, 2002. - P. 24-29.
- [7]. *Kolomzarov Yu.V., Maslov V.P.* Reliable cockpit TN LCDs created from glass ceramic materials with ultra low thermal expansion coefficient // Proc. of the 13th Int. SID Symposium «Advanced Display Technologies» ADT-2004. - Raubichi, Belarus, September, 7 – 10, 2004. - P. 76-79.
- [8]. *De Gennes P.G., Prost J.* The physics of liquid crystals // Oxford University Press. - New York. - 1993.
- [9]. *E.F. Venger, E.V. Nikitenko, B.K. Serdega.* Study of properties of radiation polarization modulator in polarimetric optical systems (in Russian) // Optoelectronica i Poluprovodnikovaya Tekhnika, N 33, 1998. - P. 102 – 108.
- [10]. *Clarke D., Grainger J.F.* Polarized Light and Optical Measurement. - Pergamon Press, Oxford, 1971. Chapter 4.
- [11]. Catalog of Meadowlark Optics. 2003. Meadowlark Optics, 5964 Iris Parkway, P.O. Box 1000, Frederick, CO 80530. – P. 33 – 45.

Nano- and Micro-relief of High Reliability for Optical Systems

Yu. Timoshkov¹, T. Orekhovskaya¹, V. Timoshkov¹, V. Kurmashev²

¹Belarus State University of Informatics and Radioelectronics, P. Brovka Str., 6, Minsk, Belarus. (E-mail: timoshkov@tut.by)

²EC "Plasmoteg", National Academy of Sciences, Kuprevich Str., 1/3, Minsk, Belarus

Abstract

Problems of reliability of nano- and micro-reliefs are fundamental for series of technologies and devices including optical systems. Improvement of properties is provided by application of the composite materials, in particular, codeposited metal and alloy with inert hard particles by electroless or electrochemical processes. Wear resistance of reliefs increased in 2-3 times, microhardness increased in 1,5 times.

1. Introduction

Nano- and micro-relief are widely used in displays, microelectromechanical systems and other high-tech devices [1,2].

A lot of technologies are suitable for nano- and micro-relief production. The main materials are alumina, silicon carbide, metals, silicon nitride, sapphire, quartz, gallium nitride and so on [3, 4]. Reliability of the reliefs is determined by material features; especially wear and corrosion resistance of their thing surface layer. Increase of reliability can be provided by material modification. Composite materials are found wide applications in industry and are heterophase materials, which represents a volume combination of two or more chemically heterogeneous materials (components). Electrochemical composite material is obtained by simultaneous deposition of metal matrix and inert particles of high-wear-resistant and/or antifriction material. Particles of oxides, carbides, nitrides, graphite, diamond and polymer are used as strengthening phase. Its mass content in composite material is 1-5 per cent generally, at use a nanodimensional particles (50-100 nm) – less than 1 per cent. They must be chemically stable and inert in the used bath, do not distort nano- and microreliefs. Particles should not have significant abrasive properties and have high wear and corrosion resistance.

It was determined that during Ni and ultra-fine particles codeposition nanocrystalline structure is formed. Nanocrystalline materials have a very high density of grain boundaries due to very small grain size. It results in improvement of physical-mechanical properties [5-8].

2. Experimental details and results

Nickel sulfamic bath was used for nano- and microreliefs plating. Nickel gitters with 1,33 μm step (750 lines/mm) were applied as test reliefs. They were cathodes during the co-deposition process. The thickness of composite copies was 40 μm .

Particles of dispersed phase described in table 1 were used.

Microhardness was measured by Knup method.

Structure of nickel foils (copies) was researched by transmission electron microscopy (EM-123, USSR) with accelerating potential 100 kV. After separation from substrate foil was thinned by electrochemical method at current density 15 mA/cm² from both sides. The solution consists of 640 ml of orthophosphoric acid, 200 ml of sulphuric acid and 150 ml of water.

Table 1. Particles used in this work

Type of particles	Average size of particles	Producer
Alumina (Al ₂ O ₃)	47 nm	SIGMA-ALDRICH
Ultra-dispersed diamond (UDD)	7 nm	SPC "SINTA", Minsk, Belarus
Aluminum monohydrate (AlOOH)	20 nm	SPC "POWDER METALLURGY", Minsk, Belarus

Reliefs of nickel initial test gitters and nickel test copies modified with ultra-dispersed particles (Al₂O₃, UDD, AlOOH) were investigated by atomic force microscopy.

Reliefs were tested by method of mechanical indentation on heated surface of aluminizing lavesan tape.

Nickel foils were deposited from Watts sulfate bath as well. They are characterized by fibrous structure, which enlarge with thickness. Structure of deposits changes from large-grained columnar at pH 2,5 to small-grained columnar at pH 5. Layer structure with inner splits is observed at higher pH.

One of the main characteristics of nickel deposits is internal stress. Big stress can be reason of crack formation at deposition process or exploitation. Strain and compressing stress is typical for nickel deposits. Sign of stress to a great extent depends on dopes in electrolyte. Its value is up to nature of electrolyte. Deposits from sulfate electrolyte has high internal stress, while from sulphamate electrolyte – small stress [9]. Internal stress in nickel deposits depends on concentration of basic components in electrolyte. It's determined that tendency to decrease internal stress to zero with following transfer to compressing tensions is observed in sulphamate electrolyte with concentration change of nickel salt from 100 till 800 g/l. Significant change was in concentration range 350-650 g/l. Boric acid don't influence almost on properties of nickel deposits. Variation of pH in solution has big influence on value of internal stress. Minimum of stress displaces to range of higher pH with lowering of nickel amidosulfate concentration. Internal stress of deposits decreases with increase of electrolyte temperature. There are small stresses at deposition temperature 60^oP. It can be explained by crystal enlargement at high temperature.

Hardness of nickel deposit depends on nickel amidosulfate concentration slightly. But it changes noticeably with increase current density and pH of electrolyte. It can be explained by structural changes of deposit. Structure refinement is observed at increase of pH. It goes with increase of hardness. Hardness decreases sharply at high current density. It increases insignificantly at current density 1-5 A/dm². Hardness of nickel deposits reduces on 15-20 per cent with increase of electrolyte temperature from 20 till 60 °C as a result of enlargement of its structure. Hardness increases at addition in electrolyte organic additives, which promote to refinement of structure. These additives are saccharin, benzenesulphide, propargyl alcohol. Hardness can be increased by codeposition nickel with ultradispersed particles. Hardness of nickel deposits from sulphamate electrolyte increases till 600-700 kg/mm² [10].

Nickel foils are deposited from bath: nickel sulfamic-acid water – 400-420 g/l, boric acid – 35-40 g/l, saccharin sodium salt – 0,5-1 g/l, surfactant – 0,2-2 g/l, ultra-dispersed particles – 2-10 g/l, temperature – 38-42 °C, current density – 2,2-2,5 A/dm², pH – 4,0-4,2. Deposition rate is 30 µm/h. Optimal concentration of ultra-dispersed particles is defined experimentally: Al₂O₃ - 4,0 g/l; UDD – 2,0 g/l, AlOOH – 5,0 g/l. Increase of particles concentration in electrolyte influences on increase of foil microhardness slightly. Fragility increases significantly. It deteriorates reliability during exploitation.

Reliefs of gitter copies before and after test are shown on Fig. 1. It has been tested by stamping method on 2000 m aluminizing lamsan tape.

Microhardness of such non composite nickel foils does not exceed 200-300 kg/mm². There are significant defects of diffraction pattern (Fig. 1b,c). Results of TEM structure investigations are shown in Fig. 2.

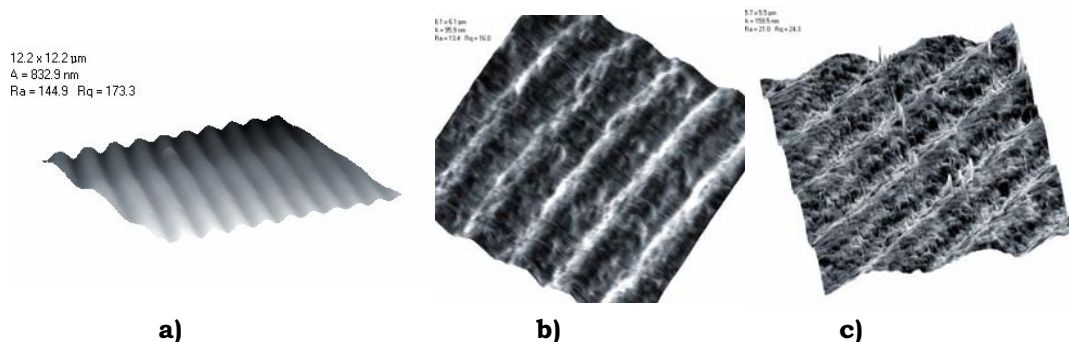


Figure 1. Reliefs of gitter copies before (a) and after test (b, c).

Structural investigation shows that pure Ni coatings contain twins, dislocation aggregates inside the grains, and a concentration of solitary dislocations and dislocation walls of 20 nm thick along the grain boundaries. The average grain size is about 150 nm. As for composite coatings the grain size reduces up to 30-70 nm.

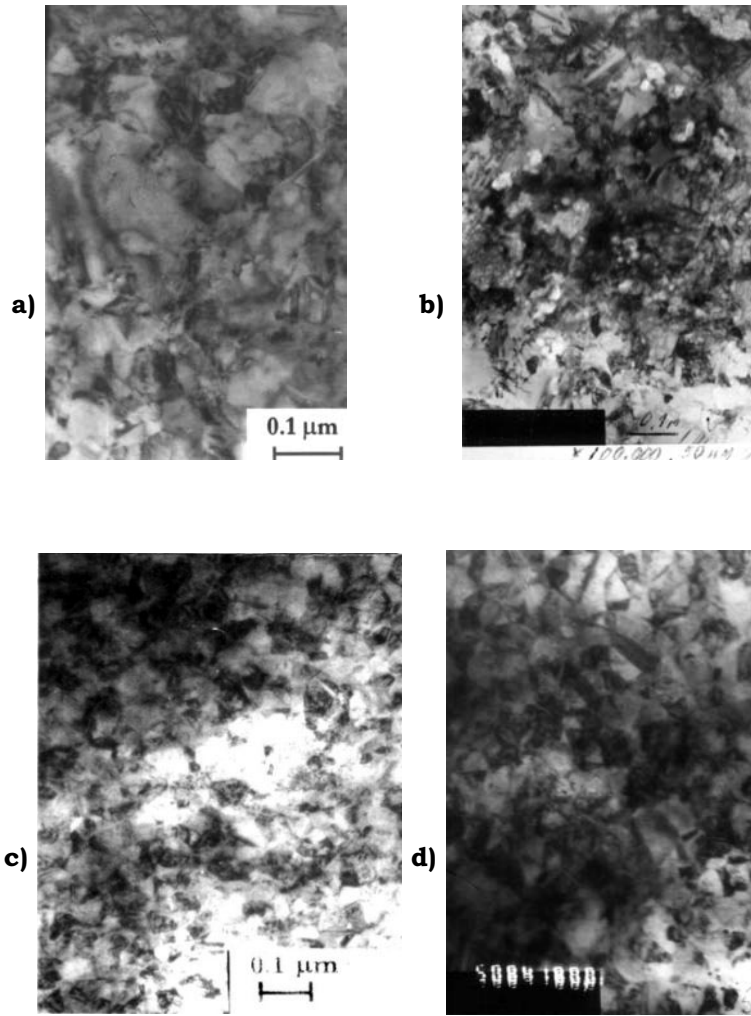


Figure 2. TEM micrographs of Ni and composite coatings: a - Pure Ni, b - Ni with alumina, c - Ni with diamond particles, d - Ni with aluminum monohydrate.

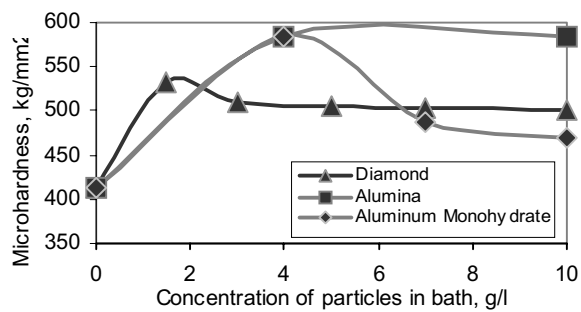


Figure 3. Microhardness vs concentration of particles in bath.

It was determined that microhardness of nickel copies modified by ultradispersed particles in comparison with pure ones increase by 30-50 per cent (Fig. 3).

Wear profiles of pure and composite nickel foils after 10000 fretting cycles are shown in Fig. 4.

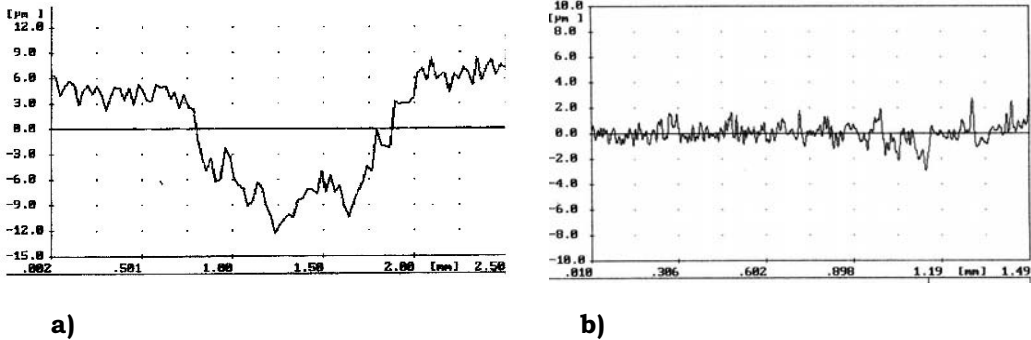


Figure 4. Position-depth profiles of fretting scars after 100,000 fretting cycles : a - pure nickel coating, b - composite Ni-diamond coating (2,0 g/l).

Wear volume of composite nickel foil is lower in 3 times in comparison with pure.

Relief of test copies, modified by Al_2O_3 , UDD, $AlOOH$, replicates relief of test forms of gitters (Fig. 5).

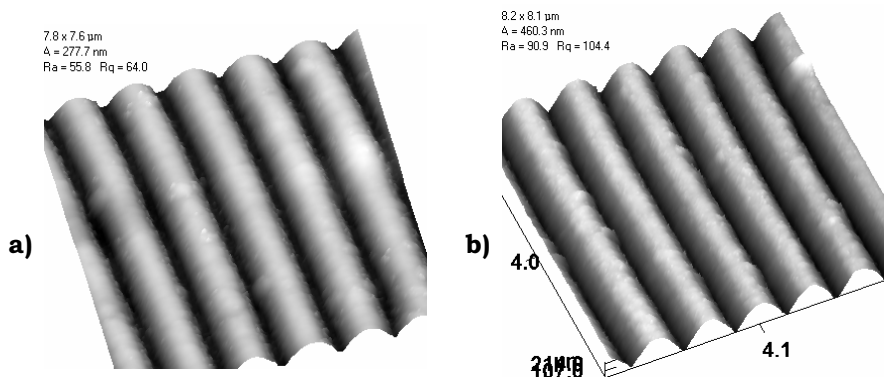


Figure 5. Images of test samples of copies: a – pure Ni, b – Ni with Al_2O_3

Al_2O_3 , UDD, $AlOOH$ particles provide equal increase of microhardness of composite nickel copies and repetition of microrelief. Wear resistance increased in more that 2 times at test of reliefs. Samples of gitter copies, obtained form sulphamate electrolyte with 1,5 g/l UDD particles, before and after test are shown in Fig. 6.

Microhardness of such composite nickel foils is 530 kg/mm^2 . There are some changes in the form of dirt, small local defects in Fig. 6. They can't influence on holographic image seriously.

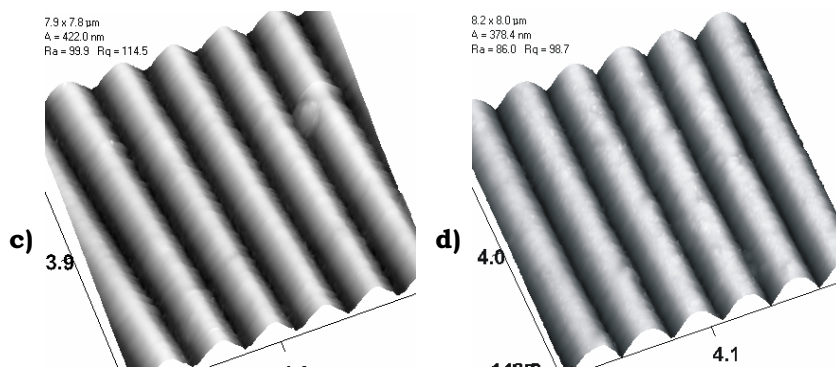


Figure 5. Images of test samples of copies: c – Ni with diamond particles, d – Ni with aluminum monohydrate.

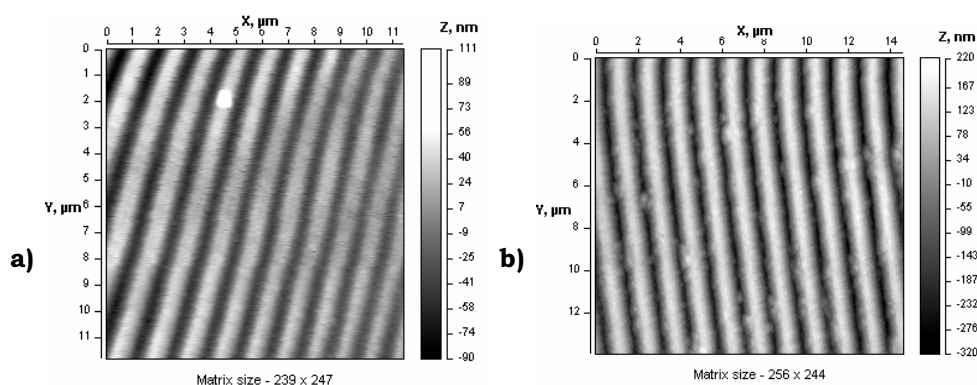


Figure 6. Composite Ni-diamond gitter copies (1,5 g/l) before (a) and after test (b).

3. Conclusion

Thus, the obtained results show availability of using composite materials with alumina, aluminum monohydrate and ultradispersed diamond particles for hardening nano- and microreliefs in optical systems. Nanoparticles provide for increase reliability and cost efficiency.

4. References

- [1] P.V. Malcev, Microsystem Technics: Successful Big Step in Microelectronic Technics, Microelectronics, volume 30, no. 1, pp 32-34, 2001 (in Russian).
- [2] V.M. Kravchenko, N.I. Muhurov, A.M. Chaplanov, About Evolution of Investigations in Microelectronics Sphere, Vesti NAN Belarusi, Seria Fiziko-Matematicheskikh Nauk, no. 4, pp 64-75, 2003 (in Russian).
- [3] Routkevitch D., Govyadinov A. N., Mardilovich P.P., High aspect ratio, high resolution ceramic MEMS, MEMS, vol. 2, pp 39-44, 2000.

- [4] Linkov L., Muhurov N., Microstructures based on anodic alumina technology, Minsk, Bestprint, p 216 , 2002.
- [5] Yu.V. Timochkov, T.M. Gubarevich, I.S. Molchan, S.V. Labunov, V.I. Kurmashev, J. Fransaer, J.-P. Celis, Microstructure and wear behavior of Ni-composite coating with different types of ultra-dispersed diamond particles, Surface Modification Technologies, vol. XI, pp 991-1000, 1998.
- [6] Yu.V. Timoshkov, T.I. Orekhovskaya, I.S. Molchan, T.M. Gubarevich, I.F. Fomihina, V.I. Kurmashev, Nanocrystalline Nickel Deposits Obtained by Electrochemical Codeposition, Poroshkovaya Metalurgia, no.23, pp 15-20, 2000 (in Russian).
- [7] Yu.V. Timoshkov, T.I. Orekhovskaya, I.S. Molchan, T.M. Gubarevich, V.I. Kurmashev, Properties of Composite Nickel Coatings with Different Types of Ultradispersed Diamond Particles, Galvanotekhnika I Obrabotka Poverhnosti, vol. 7, no. 2, pp 20-26, 1999 (in Russian).
- [8] Siegel R.W., Synthesis and Properties of Nanophase Materials, Mater. Sci. Eng., vol. A, no. 168, pp 189-197, 1993.
- [9] El-Sherik A. M., Erb U., Synthesis of Bulk Nanocrystalline Nickel by Pulsed Electrodeposition, J. Mater. Sci., no. 30, pp 5743-5749, 1995.
- [10] <http://www.reper.ru/technology/>

NEW PATHS TO HIGH TWISTING CHIRAL COMPONENTS FOR SHORT-PITCH CHOLESTERIC LIQUID CRYSTALS

T.G. Drushlyak, V.V. Abakumov, L.A. Kutulya, I.M. Gella, S.V. Shishkina, N.S. Pivnenko, N.I. Shkolnikova, O.V. Shishkin

Scientific and Technological Corporation «Institute for Single Crystals» of National Academy of Sciences of Ukraine
60 Lenin Ave, Kharkiv 61001, Ukraine, E-mail: kutulya@isc.kharkov.com

Abstract

Two paths are discussed to new high twisting chiral photo stable compounds which allow obtaining short-pitch cholesteric liquid crystals (LC) with a slight temperature dependence of visible selective light reflection. The first one is based on the 1(*R*),4(*R*)-2-arylidene-*p*-menthan-3-ones in molecules of which the photoactive double bond is replaced with the cyclopropane ring thereby forming the photo stable 1(*S*)-(4*X*-phenyl)-5(*R*)-isopropyl-8(*R*)-methyl-3(*R*)-spiro[2,5]octane-4-ones (*X* = F, Cl, C₆H₅, C₆H₄OC₃H₇). The second path includes transformation of initial 3(*R*)-methylcyclohexanone 2,6-bis-arylidene derivatives into photo stable 3,3*a*,4,5,6,7-hexahydroindazole derivatives which possess high helical twisting power on mixing with a nematic liquid crystal.

Keywords: Induced cholesteric liquid crystals, chiral components, 1(*S*)-aryl-5(*R*)-isopropyl-8(*R*)-methyl-3(*R*)-spiro[2,5]octane-4-ones, photo stable 3,3*a*,4,5,6,7-hexahydroindazole derivatives, selective light reflection, temperature dependence.

1. INTRODUCTION

Elaboration of liquid crystal (LC) compositions possessing capability to the selective visible light reflection is of significant importance for advanced display technologies [1]. Along with LC mixtures based on cholesterol esters, induced cholesteric LC systems containing a nematic «host» and a chiral highly twisting component (CC) («guest») attract the great interest in this respect.

On the base of our vast experimental data concerning the influence of molecular structure peculiarities of the components on the macroscopic parameters of LC systems [2–4] as well as the literature data apropos of this (see for example, [5–10]) we formulated demands to physicochemical properties of the chiral dopants to induced short-pitch cholesterics:

- First of all and mainly, the CC must possess HTP being high enough in order to allow formation of the compositions with visible selective light reflection (preferably in the 520 – 560 nm ranges) under a moderate concentration (8 – 15 %);

- Sufficient solubility of the CC in the selected nematic LC host system should allow compositions of required concentrations as well as stability to exfoliation with time;

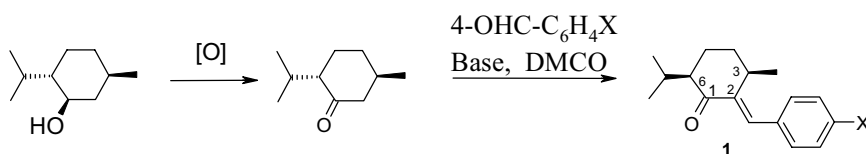
– The CC should primarily determine a required type of the temperature dependence of the helical pitch and the selective light reflection maximum; the CC forming compositions with dP/dt or $d\lambda_{\max}/dt \approx 0$ are needed most often;

– The absence of the CC own smectogenic properties is highly desirable to avoid appearance of the smectic mesophases in the composition that could influence unfavourably on a selective light reflection change with temperature;

– An influence of the CC on the mesophase thermal stability (revealing itself by a change of the clearing temperature with the CC concentration, dT_i/dC) must be as weak as possible;

– High photochemical stability is of importance for target CCs.

In order to accomplish the development of short-pitch cholesterics the selection of convenient initial chiral materials is of significant importance. Natural *l*-menthol [11] and its oxidation product, *l*-menthone [2, 3], were used widely for this purpose. Several series of CCs **1** belonging to α,β -unsaturated ketones were synthesized on the base of *l*-menthone according to Scheme 1 [2, 3].



X = F, Cl, Br, CN, NO₂, OCH₃, Ph, C₆H₄OCnH_{2n+1}

Scheme 1

The final CCs were established (NMR, X-ray data) to be 1(*R*),4(*R*)-diastereomers [3]. Of them, representatives with an extensive conjugated arylidene fragment (X = C₆H₄OCnH_{2n+1}, n = 1–7) took on a special significance due to their high HTP and sufficient solubility in nematic LC. They allow obtaining LC compositions with the visible selective light reflection (λ_{\max} 528 – 615 nm) at moderate concentrations (10 – 13 % of CC) [3, 12].

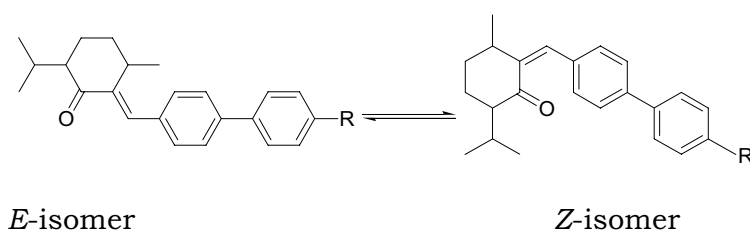
The only disadvantage of CCs **1** is insufficient photochemical stability as a result of the photochemical *E,Z*-isomerisation (Scheme 2) which was revealed both in isotropic solvents and LC mixtures [3]. The disadvantage mentioned is accompanied by a large difference in HTP of *E*- (Table 1) and *Z*-isomers (was determined as equal 0 ÷ –1.5). One of the factors which causes such a difference was considered to be a strongly differing molecular shape of the isomers [2, 3].

In this respect, the search parts to chiral compounds which possess high HTP and could be used to induce short cholesteric pitch, i.e., manifesting visible selective light reflection, is a great present day challenge.

Table 1. Data on HTP and temperature dependence of induced helical pitch for CCs 1 in 5CB*

	X	- b, mm ⁻¹ mol.fract ⁻¹ [13]	dP/dt, mm/degree
1a	OCH ₃	27.8 ± 0.4	—
1b	Ph	36.9 ± 0.6	0.000 ± 0.003
1c	C ₆ H ₄ OC ₃ H ₇	40.1 ± 2.4	0.010 ± 0.002
1d	C ₆ H ₄ OC ₅ H ₁₁	41.2 ± 2.9	0.015 ± 0.004
1e	C ₆ H ₄ OC ₆ H ₁₃	42.4 ± 2.4	0.019 ± 0.002

* 5CB is 4-pentyl-4'-cyanobiphenyl



Scheme 2

2. EXPERIMENTAL

2.1. Materials

Nematic 5CB and E-63 (Merck KGaA, Darmstadt) were used as LC hosts.

Syntheses of CCs **2a** – **2c** were described in [1]. Main products of the reaction in all cases were separated after two re-crystallizations from ethanol or isopropanol with purity of 98 – 99 % (according to high performance liquid chromatography, HPLC). For **2d** synthetic protocol according to Scheme 3 will be presented elsewhere.

Compounds **4a** and **4b** were obtained by the reaction of a,b-unsaturated ketone **3a** (R = OCH₃) with the methylhydrazine sulphate according to Scheme 4. Synthetic protocol for CCs **4** according to Scheme 4 and separation of isomers **4a** and **4b** will be presented elsewhere. Unsaturated ketone **3a** as the initial material in preparation of the indazole derivatives **4** was synthesized by interaction 3(*R*)-methylcyclohexanone with 4-methoxybenzaldehyde according to recommendations of [2].

2.2 Measurements

Chromatography analyses were carried out with a Bischoff system, reversed-phase Prontosil 120-3-C18-H column, UV detector, eluent acetoni-

trile – water 78 : 22 and direct phase Prontosil 120-3-Si column, eluent 1.5 % BuOAc in heptane or with a Milichrom-5 (Oryol, Russia) in similar conditions.

^1H NMR spectra for compounds studied were recorded on a Bruker Avance DRX 500 MHz (CCs of series **2**) and on a Mercury 400 (Varian, 400 MHz) spectrometer (25 IC, CDCl_3 (compounds 4). Spectra simulation was carried out using NUTS 4.35 program.

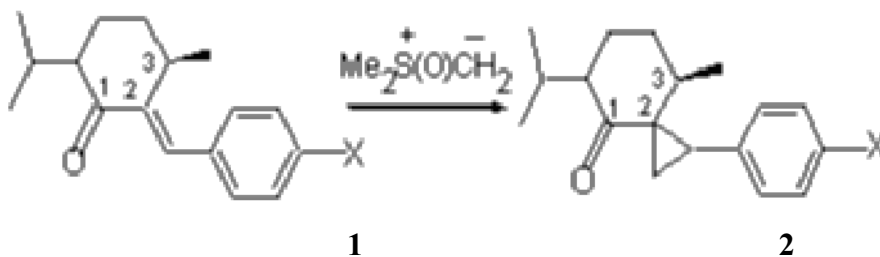
The X-ray diffraction study for **4a** was carried out on an automatic “Xcalibur-3” diffractometer (graphite monochromated MoK_α radiation, ω scanning, $2\Theta_{\text{max}} = 50^\circ$). The structure was solved by direct method using SHELXTL package. Details will be published.

The measurements of the induced helical pitch, P , in 5CB were performed by the Grandjean—Cano method as was described in [16]. The concentration of chiral dopants in LC solutions was 0.01 – 0.02 mol fract. The parameter dP/dT values were calculated as the slope of the measured dependences $P(T)$ in a linear approximation (with a correlation coefficient obtained of 0.95 – 0.99). The HTP values were calculated from $\beta = (PC)^{-1}$ equation, where C is the CC mole fraction.

The selective light reflection spectra as well as their temperature dependences for short-pitch N^* systems on the base of E-63 were recorded using a Perkin Elmer Lambda 35 UV/VIS spectrometer. The sample thickness was 15 μm . The cell had $\pm 0.5^\circ$ temperature control accuracy.

3. RESULTS AND DISCUSSION

In this work, two ways of the structural modification of compounds **1** were used avoiding disadvantages mentioned in introduction. In one of them, the double bond in molecules of CCs **1** was replaced by the cyclopropane ring (Scheme 3), a hard and photo stable fragment.



Y = F(**a**), Cl(**b**), Ph(**c**), $\text{C}_6\text{H}_4\text{OC}_3\text{H}_7$ (**d**)

Scheme 3

The four possible diastereomeric reaction products were determined from the theoretical modeling within the framework of the semi-empirical quantum-chemical AM1 method. The *trans-trans* diastereomer (Figure 1, *a*) proves to be the most energetically favorable. Its structure implies, on the one hand, the *trans* mutual position of the carbonyl group and benzene ring and, on

the other hand, the *trans*-orientation of the cyclopropane substituted methylene group with respect to the axial methyl one in the cyclohexanone ring. Through the NMR ^1H studies [14] and X-ray analysis [17] the *trans-trans* diastereomer was established to be the main reaction product in all cases. Its spatial structure is rather similar to those of the initial enones **1** (Figure 1, *a* and *b*). Taking into account regularities revealed earlier [2, 3] similar HTP values should be expected for the CCs **1** and **2**. This assumption is confirmed with the experimental data (Table 2). Observed selective light reflection for the LC composition E-63 — CC **2d** (CC concentration was 12.3 mass %) (see Figure 2, *a*) being almost temperature independent is of great importance.

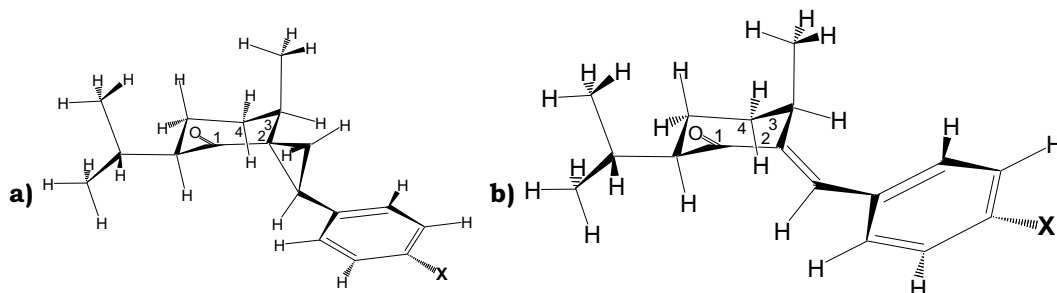


Figure 1. Spatial structures of chiral compounds 2 (a) and 1 (b)

Table 2. HTP values and temperature gradient of induced helical pitch for CCs 1 and 2 in 5CB

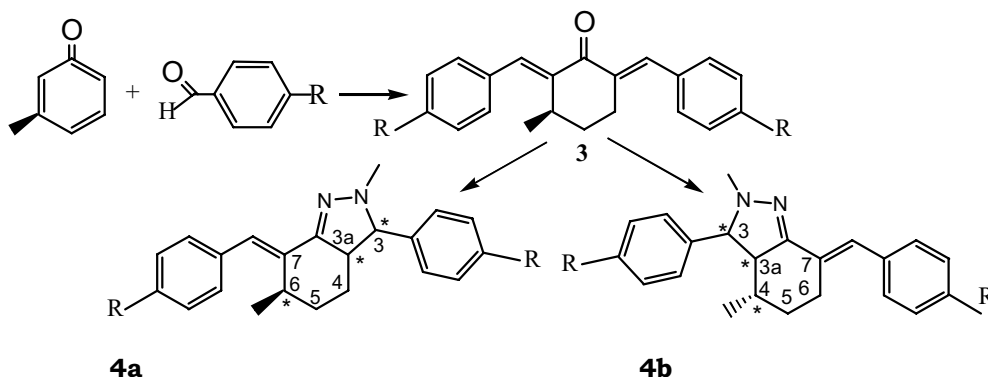
CCs	X	$-b, \text{mm}^{-1} \text{mol. fract}^{-1}$		$dP/dt, \text{mm/degree}$	
		1	2	1	2
1, 2a	F	17.0 ± 0.7	23.4 ± 0.6	0.023 ± 0.006	0.0024 ± 0.0002
1, 2b	Cl	23.2 ± 1.5	29.3 ± 2.1	0.028 ± 0.004	0.0034 ± 0.0008
1, 2c	Ph	27.4 ± 1.1	36.9 ± 0.6	0.018 ± 0.001	0.0000 ± 0.0003
1, 2d	$\text{C}_6\text{H}_4\text{OC}_3\text{H}_7$	34.1 ± 1.6	—	0.006 ± 0.002	—

In contrast to enones **1** earlier studied [2, 18, 19] their *spiro* analogues **2** are photo stable. Absorption spectrum of **2c** in octane did not change after irradiation during 5 hours with the light from DRSh-250 high pressure mercury lamp (l 313 nm). The induced helical pitch did not also undergo any variation under the similar action in LC composition 5CB – CC **2c** with the concentration of 1.3 mole %.

In the second approach, the chiral components for short-pitch cholesterics were based on 3(*R*)-methylcyclohexanone (Scheme 4). Two main of possible indazole derivatives **4a** and **4b** were separated as main reaction products.

Their molecular structures were determined by the ^1H NMR and X-ray analysis. The results will be presented in detail elsewhere.

Chiral α,β -unsaturated ketone **3a** (R is OCH_3 group) of quasi-symmetrical structure served here as an intermediate for indazole derivatives **4**. Nevertheless, this compound exhibits helical twisting properties, which in comparison with isomenthone derivatives **1** are of great importance in general studies of the influence of molecular structural factors on the HTP values of CCs in induced cholesteric mesophases.



Scheme 4

Comparison of structures and the HTP values for derivatives of isomenthone **1a** and **1b**, 3(R)-methylcyclohexanone **3a** and indazole **4a** are shown in Table 3. As can be seen in the table the structure of compound **3a** differs from **1a** *per se* only in presence of the second arylidene fragment in place of isopropyl group. What is a result of this structural difference? So, HTP for CC **3a** is low in spite of the presence in its molecules of an arylidene fragment with a-methyl group similarly to CCs **1** (this fragment in **3a** is situated from the left of a dashed line, Table 3). An axial orientation of the methyl group in the cyclohexanone ring was established [20] to be typical for **3a** as well as for arylidene isomenthones **1**. The striking similarity exists also concerning a character of the twist in enone groups for these compounds (the torsion angle sign is positive for any **1** and **3a**) [3, 15, 20].

Table 3. Comparison of the helical twisting power for structure similar CCs 1, 3 and 4 in 5CB

<i>Chiral compound</i>	<i>Structure</i>	$-\beta, \mu\text{m}^{-1}\text{mol.fract}^{-1}$
Arylidene-isomenthone 1a		27.8 ± 0.4

<i>Chiral compound</i>	<i>Structure</i>	$-\beta, \mu\text{m}^{-1}\text{mol}\cdot\text{fract}^{-1}$
Arylidene-isomenthone 1b		40.1 ± 2.4
Arylidene-3(<i>R</i>)-methylcyclohexanone 3a		17.2 ± 0.4
Arylidene indazole 4a		39.4 ± 0.4

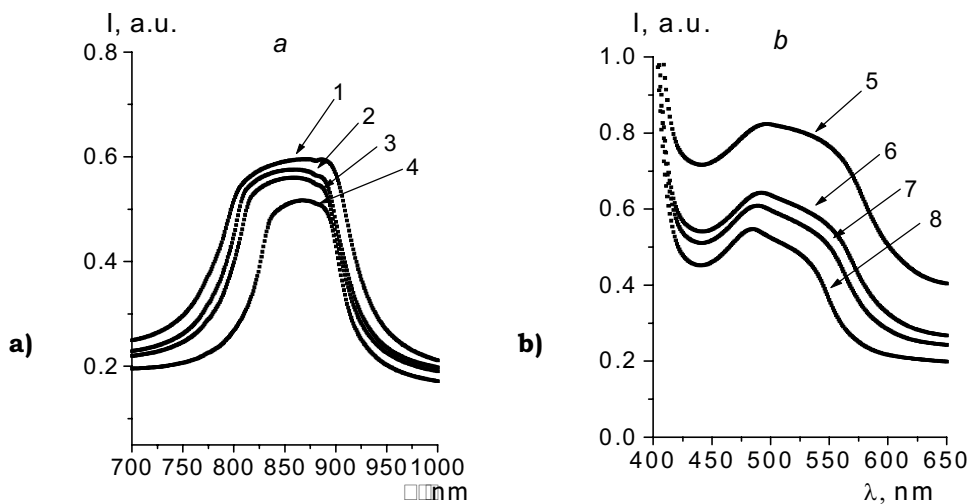


Figure 2. Spectra selective light reflection for mixtures of E-63 with CCs 2d (*a*, curves 1 – 4) and 4a (*b*, curves 5 – 8) at various temperatures: 1 – 24; 2 – 38; 3 – 46.5; 4 – 63.5; 5 – 28.5; 6 – 35; 7 – 42; 8 – 57.5 C

As the main cause of revealed essential difference in HTP values for compounds **1a** and **3a** should be considered just the presence of the second enone group located from the right of a dashed line (see Table 3, 3a). This

enone group is characterised with the torsion angle having sign opposite to that for the first one mentioned above (opposite spiral chiralities [3, 15, 20, 21]). This result for compound **3a** is of fundamental importance due to the fact that in conjugated molecular systems an influence of spiral chirality becomes essential for the effective inducement of the helical supra-molecular ordering in mesophases.

Moreover the opposite spirality of two enone groups as a factor lowering HTP should be expected to be eliminated in the case of bicyclic compound **4a** which is one of the reaction product according Schema 4. Indeed, the β value for **4a** is twice as much than that of starting **3a** (see Table 3). This value exceeds essentially that for the isomenthone derivative CC **1a** having the same substitute OCH_3 and is also similar to HTP for CC **1b** with the enlarged number of benzene ring in the arylidene fragment.

Structure peculiarities of CC **4a** derived from NMR ^1H and X-ray results (see Figure 3) allow throwing light on origins of its high HTP. These peculiarities of CC **4a** coincide in general with the criteria of strongly twisting chiral dopants which were formulated by us earlier [2, 3]. Thus, conformational molecule homogeneity and the axial orientation of the methyl group in the essentially predominant conformation are characteristic of **4a** similarly to CCs **1**. Spiral chirality of twisted fragment $\text{N}(1)=\text{C}(1)-\text{C}(2)=\text{C}(8)$ (torsion angle is -36.2° according to X-ray data) as well as presence of extensive p-electronic system including arylidene and hydrazone $\text{C}(1)\text{N}(1)\text{N}(2)$ groups with high polarizability are determinant to achieve high HTP.

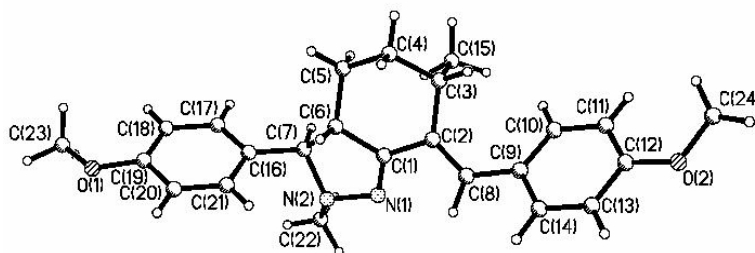


Figure 3. Molecular structure of CC 4a from X-ray investigation.

It is very attracting attention in respect of this work that CC **4a** as well as **2d** in mixtures with nematic E-63 form short-pitch cholesterics at rather moderate concentration (12.2 – 12.3 %) with selective light reflection being temperature independent (Figure 2, *b*, curves 5 – 8). Such a property of these compounds seems to be very important for applications in display technologies.

CONCLUSIONS

Two approaches used for the structure modification of chiral α,β -unsaturated ketones based on (-)-menthone and 3(*R*)-methylcyclohexanone al-

lowed obtaining photo stable dopants to induced short-pitch cholesterics as a result of elimination of the photoactive double bond. Temperature independence of the selective light reflection revealed for new cholesterics is their important positive property.

The obtained new materials can be utilised in developments of the cholesteric reflective screens and colour filters for display devices.

5. ACKNOWLEDGEMENTS

The authors are thankful to Dr Alexander Turov (Taras Shevchenko Kiev National University) for measurements of ¹H NMR spectra of CCs 4.

Authors are grateful to Merck KGaA, Darmstadt, for supplying with LC E-63.

References

1. A. Kozachenko, V. Sorokin, Yu. Kolomzarov, V. Nazarenko, R. Zelinskii and P. Titarenko. Multicolor surface-stabilized cholesteric LCD // *Proceeding of SPIE ECLC'97*, V. **3318**, pp. 496 – 499, 1998.
2. L.A. Kutulya. Chiral organic compounds in the induced cholesteric mesophases // *Proceeding of SPIE, International Conference on Nonlinear Optics of Liquid and Photorefractive Crystals*. Partenit, Crimea, Ukraine, October 1997, V. **3488**, pp. 84 – 96.
3. L.A. Kutulya. Chiral organic compounds in liquid crystal systems with induced helical structure. In: *Functional Materials for Science and Engineering: Collected Articles*. Editor by V.P. Seminozhenko. Kharkiv: «Institute for Single Crystals», 2001, pp. 381 – 418.
4. L.A. Kutulya, A.I. Krivoshei, N.S. Pivnenko, N.I. Shkolnikova. Molecular conformation effects on mesomorphism and twisting ability of chiral cyclohexanones in mesophases // *Journal of Structural Chemistry*, V. **45** (3), pp. 395 – 404, 2004.
5. G. Gottarelli, P. Mariani, G.P. Spada, B. Samori, A. Forni. Induction of cholesteric mesophases in nematic liquid crystals and correlation of absolute configurations of some chiral oxiranes and tiiranes // *Tetrahedron*, V. **39**, pp. 1337 – 1344, 1983.
6. G. Heppke, Löttsch D., Oestreicher F. Chirale Dotierstoffe mit außergewöhnlich hohem Verdrillungsvermögen // *Z. Naturforsch.*, Bd. **41a**, pp.1214 – 1218, 1986.
7. A.I. Galatina, A.A. Gerasimov, R.V. Kondratyeva, N.L. Kramarenko, V.E. Kuzmin, I.B. Stelmakh, N.M Shkabara. Peculiarities of temperature dependences of helical pitch of R,R-tartaric acid derivatives // *Mol. Mat.*, V. **2**, pp. 213 – 223, 1993.
8. J. Park, S. Sternhell, S.C. Vonwiller. Highly efficient chirality inducers based on steroid-derived 2,6,9-trioxabicyclo[3.3.1]nonanes // *J. Org. Chem.*, V. **63**, pp. 6749 – 6751, 1998.
9. S. Superchi, M.I. Donnoli, G. Proni, G.P. Spada, C. Rosini. Induction of Cholesteric Mesophases by Simple Cyclic Derivatives of *p,p'*-Disubstituted 1,2- Diphenylethane-1,2-diols: Importance of Shape and Polarizability Effects // *J. Org. Chem.*, V. **64**, pp. 4762 – 4767, 1999.

10. D. Seebach, A.K. Beck, A Henckel. Taddols, their derivatives, and taddol analogues versatile chiral auxiliaries // *Angew. Chem. Int. Ed.*, V. **40**, pp. 92 – 138, 2001.
11. G.S. Chilaya. Physical properties and applications of liquid crystals with induced helical structure // “Mezniereba”, Tbilisi, 1985, 87 p.
12. G.M. Zharkova, I.V. Samsonova, L.A. Kutulya, V.V. Vashchenko, S.A. Streltsov, V.M. Khachaturyan. Selective optical properties of induced cholesteric containing dispersed network polymer // *Functional materials*, V. **7** (1), pp.126 – 131, 2000.
13. L. Kutulya, V. Vashchenko, G. Semenkova, N. Shkolnikova, T. Drushlyak and J. Goodby. Niral Organic Compounds in Liquid Crystal Systems with Induced Helical Structure // *Mol. Cryst. Liq. Cryst.*, V. **361**, pp. 125 – 134, 2001.
14. I.M. Gella, N.S. Pivnenko, L.A. Kutulya, T.G. Drushlyak, A.Yu. Kulikov, N.B. Novikova. New chiral spiro[2,5]octanones — products methylenation of (3*R*,6*R*)-2-arylidene-3-methyl-6-isopropylcyclohexanones with dimethylsulphoxonium methyllide. Synthesis, stereochemistry and behavior in liquid crystalline systems // *Russian Chemical Bulletin*, 2005 (in press).
15. A.I. Krivoshey. Chiral arylidene derivatives of 3-methylcyclohexanone: synthesis, structure, mesomorphism and behaviour in liquid crystal systems. Ph.D. thesis, Kharkiv: «Institute for Single Crystals», 2004, 162 p.
16. L.A. Kutulya, G.P. Semenkova, S.N. Yarmolenko, A.P. Fedoryako, I.E. Novikova, L.D. Patsenker. New chiral imines based on S-a-phenyl-and S-a-benzylethylamines for induction of cholesteric and smectic mesophases. I. Structures and twist characteristics of the chiral additives in the induction of cholesteric mesophases in 4-alkyl-4'-cyanobiphenyls // *Kristallografiya*, V. **38** (1), pp. 183 – 191, 1993.
17. S.V. Shishkina, R.I. Zubatyuk, I.M. Gella, T.G. Drushlyak, N.S. Pivnenko, L.A. Kutulya, O.V. Shishkin. Molecular and crystalline structures of some (3*R*)-methyl-6(*R*)-isopropylcyclohexanone (isomenthone) 2-arylidene derivative cyclopropanation products // *Journal of Molecular Structure*, (in press).
18. S.N. Yarmolenko, L.V. Chepeleva, L.A. Kutulya, V.V. Vashchenko, T.G. Drushlyak, O.A. Ponomarev. Photochemical properties of chiral 2-arylidene-*p*-menthan-3-ones // *Zhurnal Obshchei Khimii*, V. **65** (1), pp. 145 – 54, 1995.
19. L.A. Kutulya, S.N. Yarmolenko, V.V. Vashchenko, L.V. Chepeleva, L.D. Patsenker, O.A. Ponomarev. Molecular structure of isomeric 2-arylidene derivatives of *p*-menthanones and *p*-(4-menthen)one and their capacity for “twisting” of a nematic phase // *Zhurnal Fizicheskoi Khimii*, V. **69** (1), pp. 88 – 95, 1995.
20. N.S. Pivnenko, A.I. Krivoshey, L.A. Kutulya. Study of molecular structures for arylidene derivatives of 3*R*-methylcyclohexanone by ¹H NMR and molecular simulation // *Magn. Reson. Chem.* V. **41** (7), pp. 517 – 525, 2003.
21. A.I. Krivoshey, L.A. Kutulya, N.I. Shkolnikova, N.S. Pivnenko. Arylidene derivatives of 3*R*-methylcyclohexanone as chiral dopants for induced cholesterics // *XVI International Conference on Spectroscopy of Molecules and Crystals. Editor(s): Galyna O. Puchkovska, Tatiana A. Gavrilko, Olexandr I. Lizengevich, Sergey A. Kostyukevych, SPIE Proceedings*, V. **5507**, pp. 249 – 256, 2004.

Ellipsometrical parameters of the polymer dispersed liquid-crystal film with nanosized nematic droplets

V.A. Loiko, A.V. Konkolovich, A.A. Miskevich, P.G. Maksimenko

B.I. Stepanov Institute of Physics of the National academy of sciences of Belarus
Scaryna Avenue 68, 220072, Minsk, Belarus, e-mail: loiko@dragon.bas-net.by

Abstract

A method to calculate ellipsometrical parameters of light transmitted through a polymer dispersed liquid-crystal film is proposed. It is based on the Rayleigh-Gans approximation for independent scattering regime. Functional dependencies of ellipticity and azimuth of polarization ellipse of scattered light on order parameter of the polymer dispersed liquid-crystal film are presented.

Introduction

Polymer dispersed liquid-crystal (PDLC) films are of great use in numerous technical devices due to their special properties. Molecules of liquid crystal (LC) in the PDLC film change the orientation of their optical axes under the external electric field [1-6]. As a result the optical characteristics of LC are changed, for example, ordinary and extraordinary refractive indices [1, 7]. Plane wave transmitted through a PDLC film in general is elliptically polarized, azimuth and ellipticity depending on the orientation order degree of LC droplets. Therefore changing an external electric field it is possible to obtain different polarization states (circular, linear, elliptic with different ellipticity) of transmitted light or to rotate the plane of polarization. Due to this property, the PDLC films can be widely adopted in different information displaying and light modulating devices as tunable polarizers and optical filters [1, 8].

The method for calculation ellipticity and azimuth of scattered light is described in the present work. It allows one to establish the link between ellipsometrical parameters and morphological properties of the PDLC film. As it was said above, these properties strongly depend on an external electric field. Therefore, this method permits obtaining different polarization states of transmitted light by varying the electric field, applied to the PDLC film.

Basic equations

Let a PDLC film with nematic droplets is illuminated normally to its surface by a linearly polarized plane wave. As a rule, relative refractive indices of LC are close to unity, and we assume that the amplitude of the light wave at every point of LC is the same as amplitude of incident wave. Let us suppose that the light scattered by one part of the droplet leaves the film not changed by other parts of the droplet and other droplets. In this case we can use the Rayleigh-Gans approximation to find the polarization state of the transmitted light.

The phase shift between extraordinary and ordinary waves is:

$$\Delta\Phi = \Phi_o - \Phi_e = \frac{lk_c v}{3} \frac{\Delta\varepsilon_d}{\varepsilon_p} (S_x - S_y) \quad 1)$$

$$\Delta\varepsilon_d = (\varepsilon_e - \varepsilon_o)SS_d \quad 2)$$

where l is the thickness of the PDLC film; $k = 2\pi/\lambda_p$; λ_p is a wavelength in the polymer; c_v is the volume concentration of the LC in the film; S_x and S_y are the components of the tensor order parameter of the PDLC film; ε_e and ε_o are the extraordinary and ordinary permittivities of LC, ε_p is the polymer's permittivity, S is the molecular order parameter of LC, S_d is the order parameter of LC droplet.

As seen from equation (1) the phase shift depends on the morphological properties of the PDLC film (order parameters, volume concentration of the LC), optical anisotropy of the LC and the wavelength of the incident light. The expression for polarization ellipse can be written in the form:

$$\left(\frac{E_x}{a_e}\right)^2 + \left(\frac{E_y}{a_o}\right)^2 - 2\frac{E_x E_y}{a_e a_o} \cos \Delta\Phi = \sin^2 \Delta\Phi \quad 3)$$

where E_x and E_y are the components of transmitted wave along x - and y -axes; a_e and a_o are the amplitudes of the extraordinary and ordinary components of transmitted wave.

In the coordinate system concerned with the ellipse, its semiaxes are:

$$A^2 = \frac{(a_e a_o \sin \Delta\Phi)^2}{(a_e \sin \beta)^2 + (a_o \cos \beta)^2 - a_e a_o \sin 2\beta \cos \Delta\Phi} \quad 5)$$

$$B^2 = \frac{(a_e a_o \sin \Delta\Phi)^2}{(a_e \cos \beta)^2 + (a_o \sin \beta)^2 + a_e a_o \sin 2\beta \cos \Delta\Phi} \quad 6)$$

$$\text{tg } 2\beta = 2\frac{a_e a_o}{a_e^2 - a_o^2} \cos \Delta\Phi \quad 7)$$

Results

Using Eqs. (4)-(7) we analyze the ellipticity and azimuth of the polarization ellipse. Define the ellipticity η as a ratio of the semiminor axis of the ellipse to the semimajor; and azimuth ζ as an angle between the major axis and the x -axis as the coordinate system concerned with the PDLC film, counted off from the x -axis anti-clockwise. These ellipsometrical parameters depend on the components of tensor of order parameter of the film S_x , S_y and S_z .

Choose the thickness of the film so that the phase shift is changed from 0 ($S_z = 1$) up to π ($S_z = -1/2$). The functional dependencies of the ellipticity and azimuth on the component S_z of tensor of order parameter are presented in Figs. 1 and 2, respectively. Analyzing the ellipticity we see that in the case of small droplets influence of the average diameter is very weak and the curve reaches the maximum at $\Delta\Phi = \pi/2$ (see Fig. 1). With increasing of the average diameter of the droplets, the dependence of the maximum position on it becomes stronger. In this case the maximum is shifted towards larger magnitudes of S_z and, respectively, towards smaller magnitudes of $\Delta\Phi$ (see Fig. 1). The results are shown in comparison with the Rayleigh approximations for different sizes of the LC droplets. The calculations are carried out for extraordinary and ordinary refractive indices of LC $n_e = 1.74$, $n_o = 1.511$ ($\varepsilon_e = n_e^2$, $\varepsilon_o = n_o^2$); refractive index of the polymer $n_p = 1.524$ ($\varepsilon_p = n_p^2$); order parameters $S = 0.6$ and $S_d = 0.7$; the maximal angle of droplets' director deviation from the x-axis $\varphi_d^{\max} = 5$; volume concentration of the LC in the film $c_v = 0.075$; the film thickness $l = 41.3 \mu\text{m}$; the wavelength of the incident light in vacuum $\lambda = 0.6328 \mu\text{m}$.

At $\Delta\Phi = \pi/2$ circular polarization of the transmitted light can be obtained, when the polarization angle of the incident light is:

$$\text{tg}\alpha = \exp\left(-\frac{1}{2}(\sigma_e - \sigma_o)Nl\right) \quad 8)$$

Here σ_e and σ_o are the scattering cross-sections [9] for extraordinary and ordinary waves.

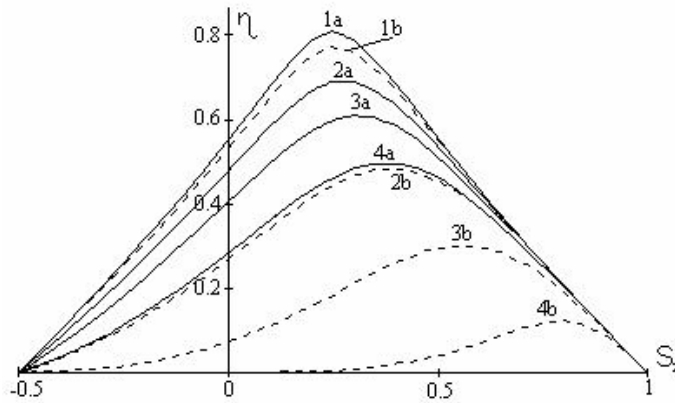


Figure 1. Dependence of the ellipticity η on S_z calculated under the Rayleigh-Gans (a) and the Rayleigh (b) approximations. The mean diameter of the droplets (d) = 0.075 μm (curve 1), 0.15 μm (2), 0.2 μm (3), 0.3 μm (4). Polarization angle $\alpha = 50^\circ$.

At $\Delta\Phi = 0$ the ellipticity is equal to zero. It means that we obtain linear polarization of transmitted light, and the polarization angle of the transmit-

ted light is equal to α . So when all molecules of the LC are aligned along z -axis, the PDLC film does not change the polarization state of the incident light. At $\Delta\Phi = \pi$ the transmitted light is linearly polarized too, but the polarization plane rotates and the angle of polarization can be found from the next equation:

$$\operatorname{tg}\alpha_1 = -\exp\left(-\frac{1}{2}(\sigma_o - \sigma_e)Nl\right)\operatorname{tg}\alpha \quad 9)$$

In other cases the transmitted light is elliptically polarized with ellipticity and azimuth that can be calculated using Eqs. (4)-(6).

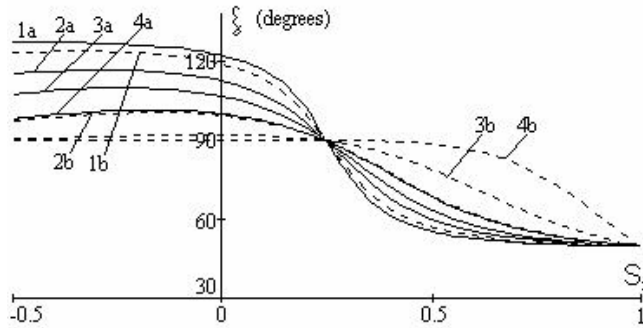


Figure 2. Dependence of the azimuth ζ on S_z calculated under the Rayleigh-Gans (a) and the Rayleigh (b) approximations. The mean diameter of the droplets (d) = 0.075 μm (curve 1), 0.15 μm (2), 0.2 μm (3), 0.3 μm (4). Polarization angle $\alpha = 50^\circ$.

In Figure (2) we see that the polarization ellipse rotates clockwise with increasing of S_z . All curves cross at a point $S_z = 0.25$. It corresponds to the phase shift $\Delta\Phi = \pi/2$. At this point $\zeta = \pi/2$ and in the case of small droplets the maximum of the ellipticity is reached. At a point $S_z = 1$ the azimuth is equal to the initial polarization angle $\alpha = 50^\circ$.

The ellipticity η is π -periodical function of $\Delta\Phi$ and at $S_z = 0.25$ ($\Delta\Phi = \pi$) and $S_z = -1/2$ ($\Delta\Phi = 2\pi$) the transmitted light is linearly polarized. At $S_z = 1$ the transmitted light has its initial state of polarization. The circular state of polarization can be reached at $\Delta\Phi = \pi/2$ ($S_z = 0.375$) and $\Delta\Phi = 3\pi/2$ ($S_z = -0.125$). In the first case ($\Delta\Phi \in [0, \pi]$) the change of the order parameter leads to smaller change of the ellipticity than in the second case ($\Delta\Phi \in [0, 2\pi]$). It means that we can obtain the same change of ellipticity by smaller change of the external field in the second case, than in the first case.

Conclusion

The proposed method allows calculating the scattering cross-sections, phase shift and ellipsometrical parameters of the polarization ellipse of the light, transmitted through the PDLC film. Different parameters of the film

(such as the thickness, volume concentration of the LC, order parameters, average size of the droplets), the LC (optical anisotropy), and the incident light (the wavelength) are connected with the ellipticity and azimuth of the polarization state of scattered light. The results of the calculations are presented in comparison with ones obtained in the Rayleigh approximation. They can be used at the development of the patterned retardation and polarization layers for LC display applications.

Acknowledgement

The research was supported in part by the Belarus scientific Research and Development program "Coherence".

References

- [1]. P.S. Drzaic, "Liquid crystal dispersions", World Scientific, London, 1995.
- [2]. G.M. Zharkova, A.S. Sonin, "Liquid-crystal composites", Nauka, Novosibirsk, 1994.
- [3]. T. Bouchaour, M. Benmouna, X. Coqueret, U. Maschke, V. Rachtet, P. Le Barny and P. Feneyrou, "UV-cured polymer dispersed LC with nanosized droplets", *Mol. Cryst. Liq. Cryst.* 413, pp. 2165-2170, 2004.
- [4]. O. Francascangeli, V. Stanic, L. Luccetti, C. Ferrero and M. Burghammer, "X-ray microdiffraction study of the liquid crystal ordering in confined geometries", *Mol. Cryst. Liq. Cryst.* 412, pp. 1669-1677, 2004.
- [5]. J. Kelly, W. Wu and P. Palffy-Muhoray, "Wavelength dependence of scattering in PDLC films: droplet size effects", *Mol. Cryst. Liq. Cryst.* 223, pp. 251-261, 1992.
- [6]. V.A. Loiko, V.A. Konkolovich, "Polarization of radiance transmitted through polymer film with nanosized LC droplets", *JETP* 99 ¹², pp. 343-351, 2004.
- [7]. T. Ikeda, S. Yoneyama, T. Yamamoto and M. Hasegawa, "Refractive-index modulation by means of photosensitive LC", *Mol. Cryst. Liq. Cryst.* 375, pp. 45-60, 2002.
- [8]. W.A. Crossland, T.D. Wilkinson, I.G. Manolis, M.M. Redmond and A.B. Davey, "Telecommunications applications of LCOS devices", *Mol. Cryst. Liq. Cryst.* 375, pp. 1-13, 2002.
- [9]. C.F. Bohren, D.R. Huffman, "Absorption and scattering of light by small particles", Wiley & Sons, New York, 1983.

VFD modules for wide application

Malyayeva N.A., Neudakhin A.V., Zhukov N.D., Frolov V.L., Zotov N.A., Zhidkikh V.V.

Now, vacuum-fluorescent modules (VFD modules) for replacement (emulation) of LC-modules in communication systems and aviation technics, have a wide spread occurrence. Feature of VFD-modules application in the specified areas is determined by their profitability, wide temperature range of operation, high brightness providing correct information reading at external light exposure up to 100 thousand lux.

The leading manufacturers of the modules are “Noritake” and “Futaba” companies.

Table 1 shows the modules nomenclature by use of vacuum-fluorescent indicators (VFD). The manufacturer is firm “Noritake”.

Table 1

Chars	Height	Alpha Part Number	Font	PCB mm	Intf	PowerV/mA
16 x 1	9.0	AU169-K2SS	Alpha	225x37.8	SS	5.0/250
	9.0	AU169-KV12CS	Alpha	195x35	SS	12.0/150
	12.5	AU1613-K2SS	Alpha	217x45	SS	5.0/600
	12.5	AU1613-KV12FS	Alpha	217x45	SS	12.0/300
Chars	Height	5x7 Dot Part Number	Font	PCB mm	Intf	PowerV/mA
14 x 1	8.0	CU1418SCPB-KV90B	5 x 7	126 x 30	S	5.0/260
20 x 1	9.1	CU209-TW200A	5 x 7	214 x 41	P/S	5.0/300
	8.8	CU209-TW202A	5 x 7	164 x 34	P/S	5.0/300
20 x 2	4.7	CU20025-TW200A	5x7+C	124 x 40	P/S	5.0/280
	5.0	CU20026SCPB-T30A	5x7+C	161 x 34	P/S	5.0/400
	5.0	CU20026SCPB-KS20AB	5x 7+C	176 x 44	P	5.0/320
	5.0	CU20025SCPB-KT70A	5x7	127 x 57	P	5.0/400
	5.05	CU20026-TW200A	5x 7+C	155 x 39	P/S	5.0/290
	9.0	CU20029SCPB-KV90B	5x 7+C	190 x 55	S	12.0/260
2x20x2	9.0	CU2X20029SCPB-KV91B	5x 7+C	190 x 55	S	12.0/520
20 x 4	5.0	CU20045SCPB-T28A	5 x 7	133 x 53	P/S	5.0/400
	5.0	CU20045SCPB-W20A	5 x 7	133 x 53	P/S	5.0/400
	5.0	CU20045SCPB-KT70A	5 x 7	140 x 62	P/S	5.0/350
	5.0	CU20045SCPB-T31A	5 x 7	150 x 64	P/S	5.0/310
	40 x 2	5.0	CU40026-TW200A	5x 7+C	240 x 43	P/S

Table 2 shows the modules nomenclature c by use of vacuum-fluorescent indicators (VFD). The manufacturer is firm “Futaba”.

Table 2

Model	Symbols X lines	Symbolic format	Symbol size, mm	Overall dimensions, mm	Number of specified symbols	Supply voltage, V
M202SD08 HA/HJ	20 x 2	5 x 7, курсор	3,5 x 5,0	155,0 x 39,0 x 20,5	-	5
M20SD03 GA/GJ	20 x 1	5 x 7	3.5 x 5.0	150.0 x 31.0 x 27.0	-	5
M202SD01 LA	20 x 2	5 x 7	2.3 x 4.2	100.0 x 35.0 x 26.3	4	5
M202SD08 HA/HJ	20 x 2	5 x 7, курсор	3.5 x 5.0	155.0 x 39.0 x 20.5	-	5
M204SD01 AA/AB	20 x 4	5 x 7	3.2 x 5.0	135.0 x 70.0 x 31.0	AA3/AB4	5
M202MD07 HB	20 x 2	5 x 7, указатель	5.5 x 10.5	190.0 x 64.0 x 25.0	-	5

Table 3 shows the modules nomenclature of firm “Noritake” with use of actively matrix vacuum-fluorescent indicators (AM VFD) on silicon crystals with the built-in scansion, with luminosity up to 3500 cd/m².

Table 3

	Dot Pitch >	0.347mm			0.308mm		
No. of Chips	Dot Config.	Display Area (mm)	Outer Dimension LxH(mm)	Standard Item	Display Area (mm)	Outer Dimension LxH(mm)	Standard Item
4	64x16				19.6x4.8	45.0x16.0	MW06416DB
5	80x16				24.5x4.8	50.0x16.0	
6	96x16				29.4x4.8	55.0x16.0	
8	128x16	44.2x5.4	70.0x17.0	MW12816A	39.3x4.8	62.0x16.0	MW12816DB
12	192x16				59.1x4.8	85.0x16.0	
16	256x16	88.6x5.4	115.0x17.0	MW25616L	78.7x4.8	102.0x16.0	MW25616NB
4x2	64x32				19.6x9.7	45.0x20.5	
5x2	80x32				24.5x9.7	50.0x20.5	
8x2	128x32	44.2x11.0	70.0x22.5	MW12832D	39.3x9.7	62.0x20.5	MW12832GB
12x2	192x32				59.1x9.7	85.0x20.5	MW19232BB
16x2	256x32	88.6x11.0	115.0x22.5	MW25632C	78.7x9.7	102.0x20.5	MW25632E

A parametrical line of modules offered by the noted firms is extremely various and cover practically whole range from one-line modules up to four-line ones with character cell number from 8 up to 40, and also graphic modules with 32u256 format.

Figures 1, 2, 3 shows the elements of structure of active-matrix vacuum-fluorescent modules.

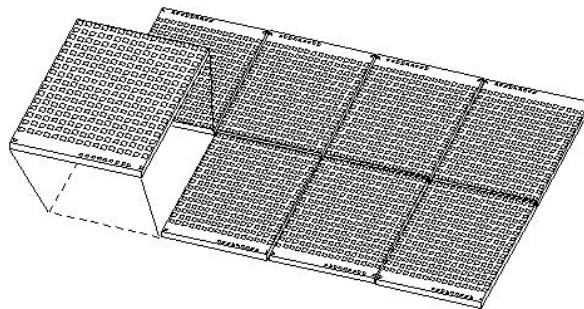
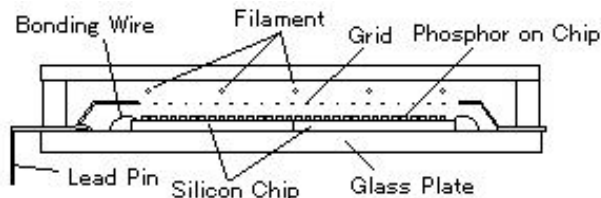


Fig 1



Out Model

Fig 2

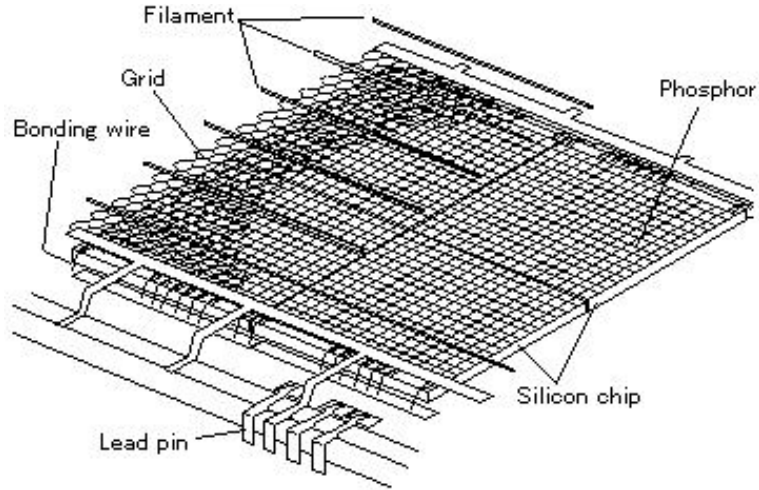


Fig 3

Fig. 4 shows the system of symbols of a decoder. This system is compatible with LC-modules on the base of controller HD 44780 (KS0076), used in modules on VFD base.

0	1	2	3	4	5	6	7	A	B	C	D	E	F
0	1	2	3	4	5	6	7	A	B	C	D	E	F
!	!1	!A	!a	!n	!+	!N	!B	!	!	!	!	!	!
"	"1	"A	"a	"n	"+	"N	"B	"	"	"	"	"	"
#	#1	#A	#a	#n	#+	#N	#B	#	#	#	#	#	#
\$	\$1	\$A	\$a	\$n	\$+	\$N	\$B	\$	\$	\$	\$	\$	\$
%	%1	%A	%a	%n	%+	%N	%B	%	%	%	%	%	%
&	&1	&A	&a	&n	&+	&N	&B	&	&	&	&	&	&
'	'1	'A	'a	'n	'+	'N	'B	'	'	'	'	'	'
((1	(A	(a	(n	(+	(N	(B	((((((
))1)A)a)n)+)N)B))))))
*	*1	*A	*a	*n	*+	*N	*B	*	*	*	*	*	*
+	+1	+A	+a	+n	++	+N	+B	+	+	+	+	+	+
,	,1	,A	,a	,n	,+	,N	,B	,	,	,	,	,	,
<	<1	<A	<a	<n	<+	<N	<B	<	<	<	<	<	<
>	>1	>A	>a	>n	>+	>N	>B	>	>	>	>	>	>
=	=1	=A	=a	=n	=+	=N	=B	=	=	=	=	=	=
~	~1	~A	~a	~n	~+	~N	~B	~	~	~	~	~	~
?	?1	?A	?a	?n	?+	?N	?B	?	?	?	?	?	?

Fig 4

Fig. 5 shows the examples of AM VFD module design. The module includes: VFD, circuit board, controller, voltage changer, control drivers.



Fig 5

Typical parameters of modules are shown in Table 4.

Table 4

Chars	Height	Part Number	Font	PCB mm	Power V/mA
16x2	4.8	<u>CU16025ECPB-W6J</u>	Std	80 x 36	5V@ 150
	4.8	<u>CU16025ECPB-W30J</u>	Std	80 x 36	3.3V @ 300
	4.8	<u>CU16025ECPB-W2J</u>	Std	84 x 44	5V @ 150
	8.0	<u>CU16029ECPB-W1J</u>	Std	122 x 44	5V @ 350
20x2	4.7	<u>CU20025ECPB-W1J</u>	Std	116 x 37	5V @ 130
	9.2	<u>CU20029ECPB-W1J</u>	Std	146 x 43	5V @ 400
20x4	4.7	<u>CU20045SCPB-W5J</u>	Std	98 x 60	5V @ 275
	8.8	<u>CU20049SCPB-W2J</u>	Std	146 x 62.5	5V @ 650
24x2	4.7	<u>CU24025ECPB-W1J</u>	Std	125 x 36	5V @ 155
40x2	4.7	<u>CU40025SCPB-W6J</u>	Std	182 x 33.5	5V@ 330
40x4	4.9	<u>CU40045SCPB-W1J</u>	Std	190 x 54	5V @ 550

Creation of such VF modules is of interest on domestically produced radioelements which are inferior to no foreign ones by their parameters and surpassing them on brightness and temperature range. The domestic complete set includes VF-indicators, drivers of control of anode and gate circuits manufactured by FSUE R&DI "Volga", and also micro-controllers (MC) in the ceramic-metal case assembled on basis of unpackaged chips.

FSUE R&DI “Volga” has developed series of VFD-modules for various applications on the basis of its own development of vacuum fluorescent indicators and drivers.

Table 5 shows the parameters of 2- and 4-rows modules which are analogues of “Noritake”’s CU16025ECPB-W2J and CU20045SCPБ-W20D.

Table 5

Parameters	2-rows module	4-rows module
Supply voltage	5 V	5 V
Consumption current from 5V source	150 mA	450 mA
Input signals level of		
High level	2 V	2 V
Low level	0.8 V	0.8 V
Grades quantity	16	20
Brightness	800 cd/m ²	400 cd/m ²
Temperature range	-60 – +85 °C	-60 – +85 °C
Input signals diagram	analog CU16025ECPB-W2J	analog CU20045SCPБ-W20D.

In comparison with analogues, the domestic VFD modules provide wider temperature range (from minus 60°P up to plus 85°P), greater brightness, and smaller cost than the analogues have.

The developed line of modules will be widely applied in communication systems and in aviation technics. The modules can be also are used in the industrial equipment, measuring devices, the transport equipment and home appliances.

Polyacrylonitrile xerogel – nematic liquid crystal. Structure and properties

*V.I. Mashchenko, S.A. Udra, L.A. Kazarin, V.V. Sorokin, V.I. Gerasimov,
V.V. Belyaev*

M.V. Lomonosov Moscow State University, Chemistry Department

Abstract

Structure and properties of polymeric xerogel based on polyacrylonitrile filled in with a nematic mixture ZhK-1282 has been investigated. The morphology of the new composite material represents a polymer network with sizes of pores equal to 25 – 50 μm filled in with the liquid crystal. Electrooptical transition “opaque – transparent” is observed in the material at 15 V.

TECHNICAL SUMMARY.

(1) Objective and Background:

Currently many companies in electronic industry are actively investigating flexible displays and E-paper based on different types of liquid crystals (LC) [1,2]. It should be noted, that a flexibility of such devices is usually achieved by creation of flexible plastic polymer substrates. Another way is creation of an integer device based on different types of polymer-LC composites like polymer dispersed liquid crystals (PDLC) or polymer stabilized LC. An example of the PDLC flexible display and E-paper is described in [3]. The PDLC are used in such devices, because of possibility to change optical state of the system under action of the electrical field (“opaque-transparent” transition) [1, 2]. Large amount of works is dedicated to investigation of properties of different types of composites based on LC [4], including gels based on low molecular mass gelation component [5]. Formations of the composite structure, which may provide of obtaining of optimal electrooptical characteristics of device, attach high importance [6]. In our previous works [7, 8] a new method of creating the polymer-LC composites was developed. By this approach the structure of the LC-composite’s matrix is determined by the morphology of initial polymer gels. The structure of the matrix based on the polymer gel represents a spatial network of macromolecules linked by molecular interaction of different nature. Polyacrylonitrile (PAN) was used as the polymer component, because of its physical properties and low price owing to its commercial production for textile and clothes. Therefore a creation of flexible displays based on PAN is very perspective. It was shown in our previous works by X-ray analysis in wide angles, differential scanning calorimetry, optical microscopy and IR- and UV-spectroscopy, that the structure, type of mesophase and thermodynamic properties of the LC in the composites strongly depend on the gels morphology and can be controlled by varying the sizes of pores from 15 to 250 nm.

It is important to note, that polyacrylonitrile was used as the polymer component, because of its physical properties and low price owing to its

commercial production for textile and clothes. Therefore a creation of flexible displays based on PAN is very perspective.

The aim of this work was to obtain the xerogel based on PAN with pore size close to the pixel size in a display and to investigate the structure and properties of xerogel and LC-xerogel by the optical and the scanning electron microscopy.

(2) Results:

It is well known that the LC reorientation voltage in the confined geometry increases strongly with decreasing of size of its geometry. High operation voltage in the systems with pores less then 1 μm makes their use difficult. Therefore it is to obtain the system gel – LC with “opaque – transparent” electrooptical mode and the driving voltage close to the operation voltage of typical TN-cells. To realize this effect the xerogel structure was obtained. The structure of the xerogel is presented in Figs. 1, 2. It was shown by microscopic investigations in crossed polarizers that birefringent microfibers, which form the network, consist of little low oriented polymer crystals (Fig. 1).

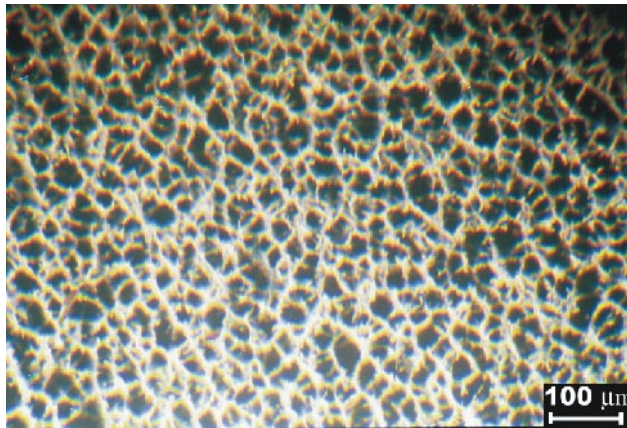


Figure 1. Microphotograph of the xerogel. Crossed polarizers. Scale in the right lower corner is equal to 100 μm .

The size of the dark parts is equal to 25 – 50 μm . The sample thickness is 22 μm . It is to conclude that the dark unbirefringent zones are through pores confined by the upper and lower glasses with the ITO coatings. The upper and lower glasses were separated and their surface was investigated by scanning electron microscopy (Fig. 2).

It was shown that on the glass surface there are boundary walls based on PAN which grow in the initial sample from the upper to the lower glass. In the microphotograph there are also pores with size 25 – 50 μm as well as with greater and smaller size. The structure of the pore with diameter $\sim 8 \mu\text{m}$ is presented in Fig. 2b.

The xerogel filled in with ZhK-1282 and formed by the method described above constitutes the polymer network filled uniformly with the LC (Fig. 3a). Characteristic LC birefringence is to watch. The sample has domain structure with size $\sim 50 \mu\text{m}$ separated by the sections of the polymer network. Such domain is corresponds apparently to one pore in the polymer xerogel. It is important, that the opaque state of the sample is to observe by a naked eye at the voltage absence (Fig. 4a).

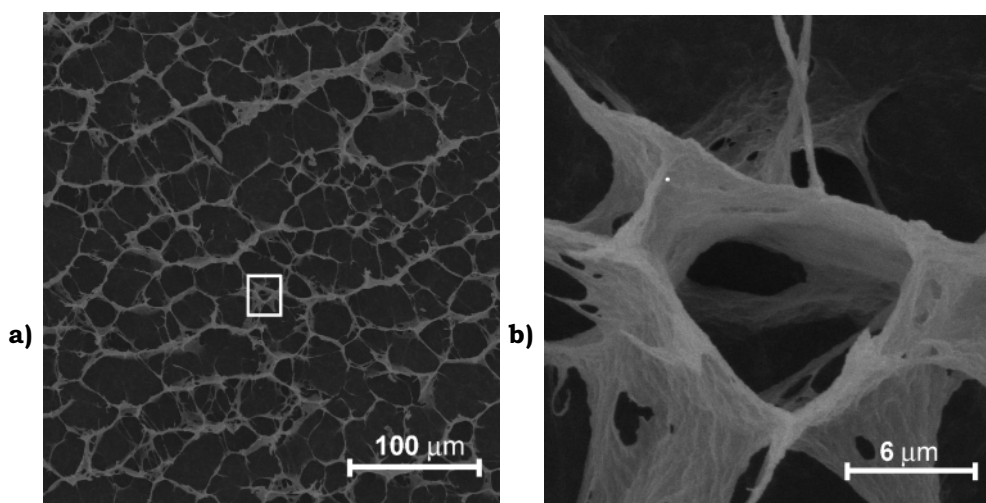


Figure 3. SEM microphotograph of the glass surface of the xerogel. Scale in the right lower corner is equal to $100 \mu\text{m}$ (a) and $6 \mu\text{m}$ (b) respectively. Microphotograph (b) is enlarged insert of the microphotograph (a).

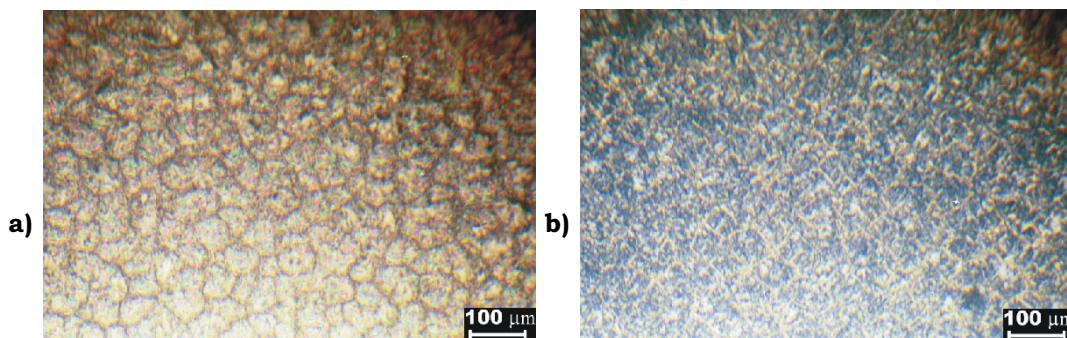


Figure 4. Microphotograph of the xerogel filled by LC without (a) and with (b) applied voltage 15 V. Crossed polarizers. Scale in the right lower corner is equal to $100 \mu\text{m}$.

In Fig 3b the sample is presented when the voltage 15 V ($0.68 \text{ V}/\mu\text{m}$) is applied. At this voltage almost transparent state of the sample is to observe by a naked eye (Fig. 4b). The change of the sample birefringence is apparently caused by the LC reorientation in the initial domains.

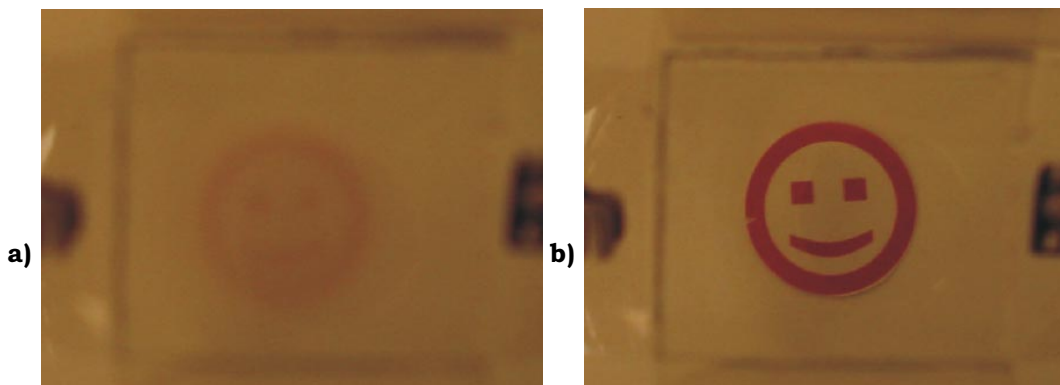


Figure 5. Photographs of the xerogel filled in by Ghk – 1282 without (a) and with (b) applied voltage 15 V (Distance between the smile and the sample is 20 cm).

This work was supported by the Russian Foundation for Basic Research (project 05-03-32711-ŭ), Programs “Universities of Russia” (project No. UR-06-02-550) and «Leading science schools» (project No. 902-2003-3)

(3) Originality

We present the new method of formation of LC - polymer composites (on example of PAN). PAN is an industrial large capacity and cheap polymer, which is used including in production of clothes. Creation of an electronic optical material on the base of the polymer can find the applications, for example, in flexible displays.

(4) Impact:

In this paper, we have presented one example of use of the method of obtaining of polymer gel – LC systems. These systems have at least three principle features:

1. Original approach to form LC composites on the base of polymer xerogels allow to control composite’s structure.
2. The new way of patterning of partition, this can increase mechanical strength of material and save the structure stability of LC between plastic substrates.
3. Reorientation of LC don’t required high voltage as in PDLC systems.

Results allow to conclude that the systems polymer xerogel – LC can be used for technologies of flexible displays and E-paper.

(5) References:

- [1] P. Slikkerveer, P. Bouten, P. Cirkel, J. de Goede, H. Jagt, N. Kooyman, G. Nisato, R. van Rijswijk and P. Duineveld, Digest of technical papers SID-2004, V. XXXV, p. 16.2, (Seattle, Washington, USA, 2004)

- [2] O.Buchnev, V.Reshetnyak, Yu.Reznikov, O.Tereshchenko, M.Dusheiko, L.Cross, Soon-Bum Kwon, Abstracts of Asia Display – 2004, p. 16-4, (Deagu, South Korea, August,. 2004)
- [3] M. Omodani, Digest of technical papers SID-2004, V. XXXV, p. 10.1, (Seattle, Washington, USA, 2004)
- [4] P. S. Drzaic Liquid Crystal Dispersions. Liquid Crystals Today, 1996.
- [5] T. Kato, T. Kutsuna, K. Hanabusa, M. Ukon, Adv. Mater. 10/8, 606 – 608 (1998)
- [6] K. Ralesh, H. Kikuchi, M. Stark, R. Guckenberger, T. Kajiyama, Mol. Cryst. Liq. Cryst., 329, 171-180 (1999).
- [7] V.I. Mashchenko, S.A. Udra, V.I. Gerasimov, V.V. Belyaev, Optical Journal Ru, 7, 33-35 (2003)
- [8] V.I. Mashchenko; S.A. Udra; L.A. Kazarin; V.V. Belaev; V.I. Gerasimov, Proceeding of the XII-th International Symposium “Advanced Display Technologies”, p. 119 (Korolev, Moscow region, Russia, August,. 2003).

(6) Prior Publications: The paper is original.

CHARGE TRANSPORT PROCESSES IN THE SENSOR MATERIALS BASED ON CONJUGATED POLYAMINOARENES

O. Aksimentyeva, P. Stakhira¹, Z. Mykytyuk¹, V. Cherpak¹, A. Fechan¹, V. Gural¹

Department of Chemistry of Ivan Franko Lviv National University, Lviv, Ukraine

¹Electronic Devices Department of Lviv Polytechnic National University, Lviv, Ukraine

Abstract: In order to study the physical and chemical properties of the new sensor materials based on organic polymer semiconductors (polyaminopenoles, polyaniline and its derivatives) the temperature dependence of conductivity in temperature interval 273-773 K, thermal stability and structure of such materials (powders and films) in have been studied.

It's found that temperature dependence of specific volume conductivity is followed by activation law with activation energy of conductivity 1,5-1,6 eV (polyaminohenoles) and 0,37-0,59 eV (doped and undoped polyaniline). Change of inclination of temperature dependence is compared with main extremums of thermogravimetical curves and elemental analysis confirm it is possible entailed by transformation of molecular structure and beginning of polymer thermal decomposition.

By the X-ray powder diffraction it is found that polyaminoarenes index of crystallinity may changes from 20-22 % (undoped polyaniline, poly-*meta*-aminophenole) to 40-44 % (acid doped polyaniline, poly-*orto*-aminophenol). Dimensions of crystallites are 15-25 ?. The effect of the acid doping on the thermal stability, structure and temperature dependence of specific resistance of doped by inorganic acid (H_2SO_4 , $HClO_4$, HCl) polyaniline have been investigated in the range $T=293-773$ K. It is manifested that acid doping causes to rising of total degree of crystallinity whereas the character of temperature dependence and thermal stability are determined by acid type used for conducting polymers doping .

1. INTRODUCTION

Conjugated polyaminoarenes (polyaniline and its derivatives) as conducting polymers have a potential technological application in chemical power cells, electrochromic coatings for organic displays and electrooptic devices [1,2] and recently attract a great attention as sensor materials [3,4]. These materials change the resistance under gases (ammonium, water and alcohol vapor); their electrochemical response is using to indicate the metallic ions (Ni^{2+} , Co^{2+} , Fe^{2+} , and Ag^+) and certain organic compound concentration [3,4]. The rate and mechanism of charge-transport in new sensor materials based on organic semiconductors (polyaminopenoles, polyaniline and its derivatives) are connected with their functions, particularly, sensitivity to certain type of physical and chemical influence.

If for conjugated polymers with unsubstituted macrochains (polypara-phenylene, polyacetylene) both donor (n-type) and acceptor (π -type) doping may be using, the polyaniline and its derivatives have achieved the high conductivity mainly in the case of strong proton acids using as doping agents [5].

We have studied the temperature dependence of conductivity; thermal stability and structure of such materials (powders and films) in temperature range 273-773 K.

2. EXPERIMENTAL

2.1. Polyaminoarene samples preparation

The powder samples of polyaminoarenes undoped and doped by 1N inorganic acid solutions were used. Undoped polyaminophenoles and polyaniline was prepared by the method of oxidizing polymerization of aniline in the presence of ammonium persulphate in 0,5 M sulfuric acid solution. Obtained product was neutralized by 5% ammonium solution, washed multiple by distilled water, acetone and dried in dynamic vacuum conditions at $T=353$ K during 8 hours. Following to IR-spectroscopy data of samples pressed to pellets with KBr ("Specord M-80"), the molecular unit of synthesized polyaniline (PAN) in undoped state is corresponded to emeraldine base [1,2]. Acid doping was carried out by exposition of undoped PAN samples in 1N aqueous acid solutions during of 24 hours. Obtained samples were filtered, washed by distilled water and acetone, dried in the same conditions that undoped polyaniline.

2.2. Measurement and investigation

Measurements of the specific volume resistance were made in temperature dynamic change conditions, commensurable with the heating rate in thermogravimetry (TG). The sample in the form of pressed under the pressure of $10 \text{ kg}/\rho\text{m}^2$ pellets ($d=2 \text{ mm}$, $h=2 \text{ mm}$) was placed to quartz cylinder between two nickel disk contacts with installed chromel-copal thermo-couple. During the measurements the sample was under pressure $100 \text{ kg}/\text{cm}^2$, at this pressure according to reference [3] resistance of organic semiconductors is approached to intrinsic value of specific volume resistance. Studies of polyaniline thermal stability were carried out on derivatograph Q-1500 D in the temperature range 273-1273K in air and argon atmosphere, with Al_2O_3 standard and heating rate $10 \text{ K}/\text{min}$.

For structure investigations the method of X-ray powder diffraction at $T= 295 \text{ K}$ has been used (diffractometer DRON-2.0, FeK α -radiation). The degree of crystallinity and crystallite size estimation were carried out in according to [5]. The dopant and moisture content have defined from the TG- and elemental analysis data as in [6]. The IR-spectroscopy of polymer materials (pressed in KBr pellets) was carried out on spectrophotometer "Specord M-80" in the range $400\text{-}4000 \text{ cm}^{-1}$.

3. RESULTS AND ANALYSIS

The polymer formation in the process of oxidative polymerization of aminoarene monomers proceeds by autocatalytic mechanism according to known scheme for electrochemical coupling reaction of aromatic amines and includes the steps of monomer oxidation over aminogen with cation-radical formation and coupling of cation-radicals accompanied by deprotonation [3,5]. The IR-spectroscopy of powder polymer material (pressed in KBr pellets) demonstrate for undoped polyaniline the absorption bands at 3330, 3288, 1590, 1497, 1307, 1166 $\mu\mu^{-1}$, which is characteristics for emeraldine base of polyaniline [1,3,5]. In the case of oxidative coupling of *m*-aminophenol only amino-group undergoes to oxidation while the hydroxyl group does not intervene. The absorption bands of *para*-substituted aromatic ring (3080, 1520, 760 cm^{-1}), amino-group (3350, 1574 cm^{-1}) and OH-group at 3600, 1410, 1200 cm^{-1} were found. In the case of *o*-aminophenol the subsequent oxidation by two functional groups proceed which leads to heterocycle formation [7,9]. This is confirmed by absorption bands at 1270-1200 cm^{-1} (ether oxygen) and 3400-3200 cm^{-1} (bound hydroxyl). The molecular structure of polyaminoarenes in comparison with polyaniline is presented in the Fig 1.

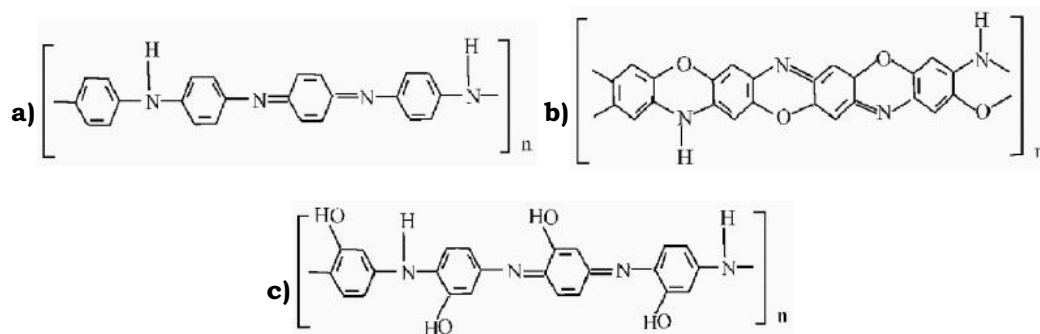


Figure 1. Molecular structure of polyaminoarenes: (a) polyaniline; (b) poly-*m*-aminophenol, (c) poly-*o*-aminophenol.

The temperature dependence of polyaniline specific volume resistance demonstrate the behavior, which is typical for organic semiconductors [3], however the molecular structure of polymer chaine and nature of doping acid has a strong effect on the shape of this dependence. As showed at Fig.2 (a, b), the change of specific resistance, normalized to resistance defined at room temperature, in the range 273-773 K includes some sections: the region of decreasing resistance, transition field and the region of resistance rising

. At the first section the resistance of undoped and H_2SO_4 , HClO_4 doped polyaniline are changed by known exponent low $r = r_0 \exp(e/2kT)$, (where e - activation energy of charge transport, r_0 - constant.) Performance of resistance temperature dependence in Arrenius coordinates $\lg r - 1/T$ for the first section permits to calculate the value of activation energy depended on the type of doping acid.(Table 1)

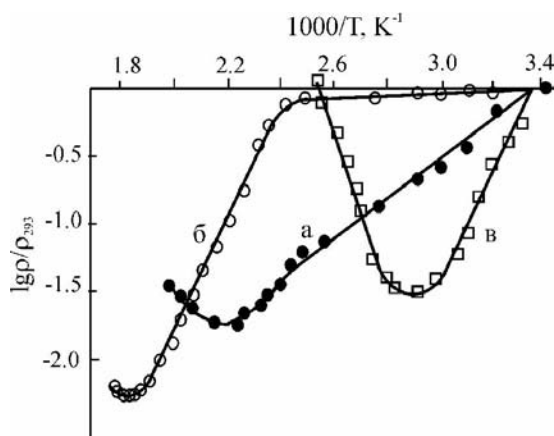


Fig.2. Temperature dependence of specific volume resistance of (a) poly-*ortho*-aminophenol (1), undoped polyaniline (2), poly-*meta*-aminophenol (3) and (b) undoped polyaniline (1), polyaniline doped by H₂SO₄ (2) and HClO₄ (3).

Table 1: Parameters of charge transport of polyaminoarenes

Polymer	Doping level, mol/unit	s_{293} , S .cm ⁻¹	e , eV	Temperature interval, K
Polyaniline, undoped	-	2.10^{-8}	$0,59 \pm 0,02$	293-423
ΠοΑΦ	-	5.10^{-10}	$1,59 \pm 0,03$	403-533
ΠΜΑΦ	-	7.10^{-9}	$1,61 \pm 0,03$	293-333
Polyaniline, doped by H ₂ SO ₄	0,43	3.10^{-3}	$0,35 \pm 0,03$	293-403
Polyaniline, doped by HClO ₄	0,45	7.10^{-3}	$0,49 \pm 0,02$	303-383

From studies of the thermal behavior of polyaniline it is found that for all samples the endothermic maximum ($T = 383-403$ K), associated with loss of chemisorbed moisture is observed. Following, the exothermic peak in the range 433-453 K, typical for aminocontained polymers, is connected with processes of crosslinking of polymer chains [6]. However, considering circumstance that in argon atmosphere the intensity of this maximum is very small, one may suggest that the exothermal oxidation of aminobenzene fragments with formation of iminoquinoid structures take a place [7]. This temperature region coincides with going out of the temperature dependence of resistance on «plateau» allotment (Fig. 1). The thermal decomposition of doped polymers starts on temperatures 453-473 K depended on the type of doping agent. Attached to temperatures of this maximum the sign change of temperature coefficient of resistance can be observed, that have been associated with a loss of doping admixtures and starting of macrochains thermal destruction processes.

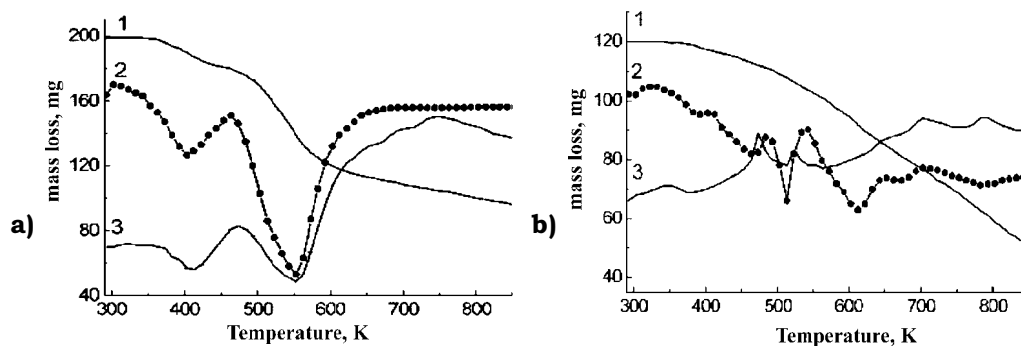


Fig.3. The derivatograms of polyaniline (a) and poly-ortho-aminophenols: 1-TG; 2-DTG; 3-DTG-curves.

As showed structural researches, obtained polyaminoarenes samples are quazi-crystal materials with the different degree of the structural ordering. Structure indexes, calculated on the base of obtained X-ray diffractograms (table 2) indicate that in result of polyaniline acid doping a change of diffraction maximums position and accordingly the interplane distances take a place. This is accompanied by a rising of the structural ordering level, may be by reason of salt forms formation. However the share of amorphous phase remains prettily high (60-75 %).

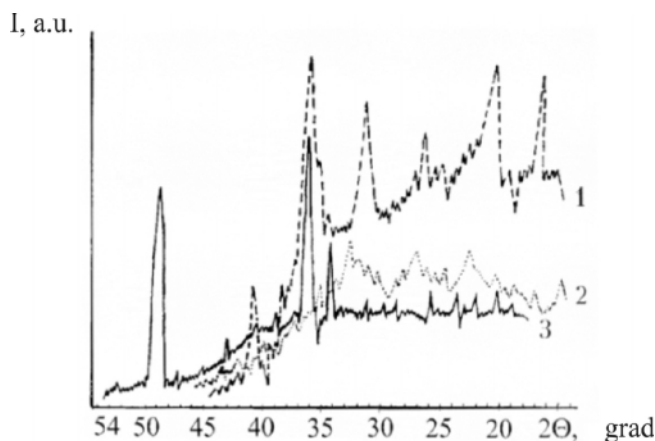


Fig.3. X-ray powder diffraction patterns of the undoped polyaminoarenes: 1- poly-ortho-aminophenol, 2- polyaniline, 3- poly-meta-aminophenol

Obtained results permit to applied for doped polyaniline the “domain” or “granular” model of the charge transport, developed in the papers [10,11]. According to these performances the ordering areas (domain or crystallites) with high conductivity are existence in polymer. Charge transport between these domains occurred by hopping mechanism across the low-conductive amorphous layers, which create the energetic barrier to charge transport.

Table 2. Parameters of X-ray diffraction, size of crystallites and the crystallinity degree of doped polyaniline

Polymer	Diffraction maximum, 2θ , degree	Interplane distance, d , Å	Crystallite dimension, $L \pm 10\%$, Å	Index of crystallinity, $I \pm 2\%$
Polyaniline (base)	25,0; 26,5; 31,4	4,47 4,23 3,58	15-20	25
Polyaniline, doped by H_2SO_4	18,7; 22,35; 25,6; 32,25	5,96 5,00 4,37 3,49	25-30	41
Polyaniline, doped by HCl	24,0; 26,0; 31,5;	4,66; 4,31; 3,57	20-30	43

One may suggest that at the high doping level in the amorphous phase percolation bridges with high conductivity are forming and when the critical content is achieved (percolation threshold) the polymer begins to demonstrate the behaviour similar to a conductor. As shown in structural researches, «granules» dimensions for powdery PAN sample compared with film samples (100-200 E [10]), are small and achieved to 20-30 E (table 2). Attached to such small domains of crystallinity the charge transport will be determined by resistance of disordered polymer phase. It is known, that the basic factor, influencing on conductivity of polyaniline and its derivatives is a degree of protonation [2]. At the high content of chemisorption moisture into NPI doped polyaniline all of atoms of imine nitrogen are protonated. It is shown [11], that a molecule of water can solvate the anions and decrease the electrostatic interaction between the positive polymer chain charge and Cl⁻ anions, that gives rise to charge and spin delocalisation along the polymeric chain. Hereupon the resistance of the amorphous phase sharply diminishes and charge transport passes with low activation energy. This gives a chance to explain the “anomalous” temperature dependence of the HCl-doped polyaniline specific resistivity.

References

1. Kohlman R.S., Joo J., Epstein A.J. *Conducting polymers: electrical conductivity/ Physical properties of polymers handbook*, ed. J.E.Mark.-Amer. Inst.Phys. Woodbury, New-York, 453(1996).
2. *Electrochemistry of polymers*, ed. by M.R.Tarasevich, E.S.Hruscheva, I., Nauka (1990) [in Russian].
3. Inokuty H., Amadu H. *Conductivity of organic semiconductors*.-M.: Izd.inostr.lit., 52(1963) [in Russian].
4. A.c.¹1772110 (UA) / Aksimentyeva E.I., Zakordonkyi V.P., Kovalchuk E.P. et al., 30.10.1992. B.I. ¹40. 3 ö.
5. Martynov M.A., Vilegzanina K.A. *X-ray analysis of polymers*. L.: Khimia, 94(1978) [in Russian].

6. Kulkarni V.G., Campbell L.D., Mathew W.R. *Synth. Met.* 30, 321(1989).
7. Aksimentyeva E.I. *Ukr.Khim.Journal*, 65, N7, 60(1999) [in Russian].
8. Aksimentyeva O.I., Artym V.T., Melnik O.Y., Plusnina T.A. *Acta Phys. Pol.*, 85, N1, 237(1994).
9. Aksimentyeva E.I., Baran M., Dyakonov V.P. et al. *Fizika tverdogo tela.* 38, N7, 2277(1996) [in Russian].
10. Savadi H.H.S., Angelopoulos M., Macdiarmid A.G., Epstein A.J. *Synth.Metals.* 26, 1(1988).
11. Chiang J.-C., MacDiarmid A.G. *Synth.Met.*, 13, 193(1986)

OPTICAL CHARACTERISTICS OF POLYANILINE IN MEDIUM WITH DIFFERENT PH VALUE

*Mykytyuk Z.M.¹, Stakhira P.Y.¹, Aksimentyeva O.I.², Hlushyk I.P.¹,
Sushynskyy O.J.¹, Fechan A.V.¹, Cherpak V.V.¹*

¹Lviv Polytechnic National University, 12 Bandera-St. Lviv, 79013, Ukraine

²Lviv Ivan Franko National University, 8 Kyryla-Mefodia, Lviv, 79005, Ukraine

Abstract: The possibilities of using of polyaniline as a sensitivity element for sensor pH with optical channel of information transfer are studied. The maximum of sensitive of polyaniline (PAN) to action of pH is developed in 750 nm, which determinate by using optical spectroscopy.

1. Introduction

The sensors industry in present day is the one of the important area of scientific and technological investigations, which needs to the developing. The hydrogen indicator of environment (pH) is an important parameter of technological and biological process. The pH value influence on the chemical reactions is important in chemicals, medicine and environment control. Because of such reason the most perspective are developments of simpler, cheaper and faster analisators, such as, optical sensors of environment hydrogen (pH) [1,2]. Using such sensors we can to provide the measurements in conditions of high electromagnetic background, because they not use the electrical signal. Coupling with fiber-optic waveguides permit to provide investigation in biologics and medicine.

On the base of conductive polymers in future will be propose the new technical modification of sensors for first exploring and identification the important substance in out laboratory conditions.

This article studies the optical changes, which take place in conductive polymers films – polyaniline due to pH level.

2. The method of experiment.

The PAN samples were obtained by electropolymerization on galvanic regime on 0.1M of aniline sulphate solution in 0,5M of H₂SO₄. As a work electrode was used glass plate of 30 x 15 mm dimension, covered on one side by conductive transparent layer of SnO₂ (surface conductance 20 Ω/□). Subsidiary electrode was platinum lead d = 0,3 mm. Compared electrode was saturated chlorine silver. Synthesis carried out on standard electrochemical cell with three separated parts. As a supply source was used potentiostat PI-50 M.

Spectral characteristics of obtained samples was investigated by spectrophotometer „SPECORD M-40” on wavelength rage 600-900 nm at temperature T=295K. The films thicknesses were determinate by microinterferometer “MII-4”.

Investigation of polymer films structure and morphology on an optical transparent electrodes was made by electron microscope (UEMB-100K, vacuum 10^{-5} mm.pH., resolution 0.2-0.5 nm, zoom 10^3 - 10^5) and by metal microscope "MMI-8". Electron graphic image were obtained for a polymers layers fabricated by using gelatine.

3. Results and discussion.

The structure and morphology of polyaniline layer, witch made on the solid surface depends on the methods and the polymerization mode. It leads to change the optical properties of polyaniline [3-5].

On process of PAN films formation during electrochemical polymerization on galvanic static mode, that was used on current paper, influence two main factors: current density (j) and electrolyze time (τ). A films morphology investigation shown that at low time of electropolymerization (τ less than 1 min.) and static current density ($j=0,07\text{mA}/\text{cm}^2$) created dense uniform film of 100-140 nm thickness. At the increasing of time electropolymerization above 5-7 minutes the center of crystallization are formed. The increasing time of electropolymerization formed the difficult amorphous crystal structures.

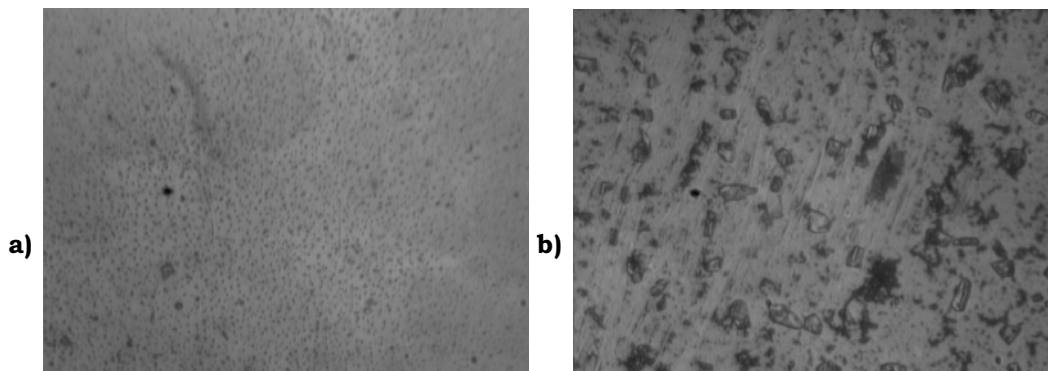


Fig.1. Polyaniline films photos after 1 min. electropolymerization (a) and 7 min. electropolymerization (b).

The optical spectra of conductive polymers, including PAN, characterized by two main and one additional line absorption: in 340-420 nm (π - π^* transition in band gap) and in 700-850 nm (absorption in free carrier or bipolarons) and optical changes is the one of important at the sensor.

The absorption spectrum of PAN films are shown in Fig. 2. The increasing of time electropolymerization and corresponding film thickness leads to the increasing of optical absorption in spectrum regions 700-800 nm (tabl. 1) and the initial shift of absorption maximum of second line to long wavelength region. Polychrome shift in spectrums of think PAN films based on the increasing concentrations of free charge carrier due to electrochemical doping. The 250-500 nm films, which characterized the small change of

maximum, were used in next investigating. The significant absorption observed in near infra-red regions 800-950 nm, that based on the wide „tail” density of bipolar zone [2].

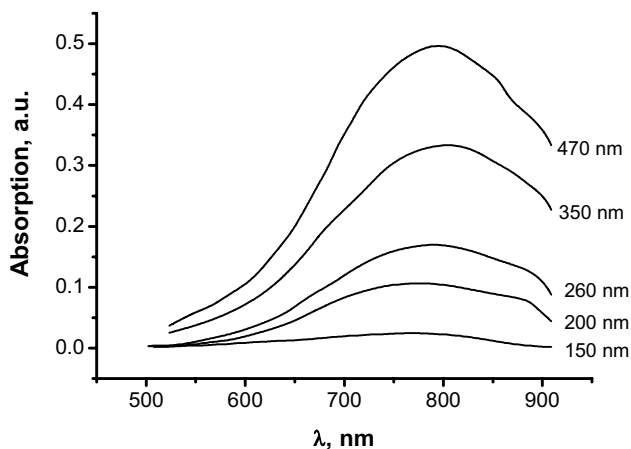


Fig.2. The absorption spectrums of polyaniline films with different thickness, obtained by electrochemical polymerization at the study value of current density $j=0,07 \text{ mA/sm}^2$.

The increasing of current density at the time of electrochemical polarization leads to the decreasing of control of PAN film optical characteristics. It was have negative influence on the uniform of sample optical characteristic.

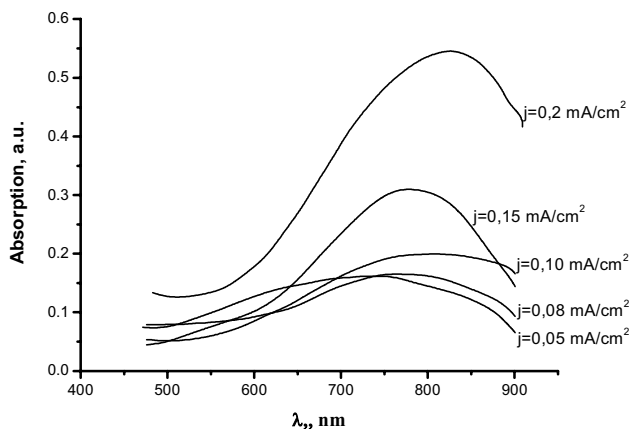






Fig.3. The absorption spectrums of polyaniline films with different thickness, obtained by electrochemical polymerization at the different value of current density.

The investigation of proton electrolyte influence on electron spectrum of 0,25-0,35 mm PAN films was carry out in 1M water solution of acid. The investigation of absorption optical spectrum change due to value pH carried out in standard buffer solutions. The increasing of pH value leads to the optical absorption maximum shift to short wave spectrum region, at $\text{pH} \sim 1 \cdot \lambda_{\text{max}} = 745 \text{ nm}$, $\text{pH} \sim 6 \lambda_{\text{max}} = 710 \text{ nm}$, $\text{pH} \sim 12 \lambda_{\text{max}} = 595 \text{ nm}$. However the semiwide of maximum absorption is a wider, which make more difficult to determinate of maximum position, and as the result, the value of the hydrogen indication.

We propose alternative method the pH determination from the value of optical density of polyaniline film at the wavelength (540 nm and 750 nm), were the maximum optical respond is observed. Then the pH level change, we observed the visual change of PAN film color. It permitted to lead the additional control of measurements. In tabl.1 the change of optical density and the change of color PAN film from pH value is proposed.

Table 1. The change of optical density and color of PAN film in depends of hydrogen indicator of solution.

pH value		3,8	5,5	7,3	9
Visual changes					
Color		green	emeraldyn	light bluee	blue
Optical density on wavelength	540 nm.	0,087	0,11	0,165	0,187
	750 nm.	0,215	0,162	0,13	0,05

The maximum changes of optical density observed at pH range 3-10, that is typical for the most chemical reaction on biological medium [4].

4. Conclusion

On the base of thickness of polyaniline film influence on a structure, morphology and optical absorption spectrum the optimal condition of PAN film fabrication with predicted morphological and optical characteristics, was suggested.

Due to nontoxic, biological compatibility and chemical stability polyaniline the using of this polymer as a sensitive element of optical sensor is a perspective in medicine and system of environment monitoring.

Including the high reversibility of process, which is in the polyaniline films in protoelectrolyte, the construction of optical sensor is proposed.

5. Reference

1. Sotomayor P.T., Raimundo Jr.I.M., Zarbin A.J.G., et al. Construction and evaluation of an optical pH sensor based on polyaniline-porous Vycor glass nanocomposite // *Sensors and Actuators*, 2001.-Vol. B 74.-P.157-
2. O.I.Konopelnik, O.I.Aksimentyeva, M.Ya.Grytsiv. Electrochromic transitions in polyaminoarene films electrochemically obtained on the transparent electrodes // *Materials Science*, 2002 Vol.20, N4.- P.49-59.
3. Zhe Jin, Yongxuan Su, Yixiang Duan. An improved optical pH sensor based on polyaniline. *Sens. Actuators B* 71 (2000) 118-122.
4. O.I. Aksimentyeva. Electrochemical methods of synthesis and conductivity of conjugate polymers. Lviv, Sviv, 1998. – P. 154.
5. Shin-Jung Choi, Su-Moon Park. Electrochemistry of Conductive Polymers. XXVI. Effect of Electrolytes and Growth Methods on Polyaniline Morphology.// *J.Electrochem.Soc.*, 2002, Vol.149(2), E26-E34.

LYOTROPIC CHROMONIC LIQUID CRYSTALS WITH NEGATIVE BIREFRINGENCE FOR DISPLAY APPLICATIONS

O. Boiko¹, Yu.A. Nastishin^{1,2}, R. Vasyuta¹ and V. Nazarenko¹

¹ Institute of Physics NAS Ukraine, Kyiv

² Institute of Physical Optics, Ministry of Education of Ukraine, Lviv

Summary

A new liquid crystal polarizer material based on chromonic lyotropic liquid crystal (LCLC) has been developed for optical applications. Thin LCLC polarizer are produced from an aqueous solution of organic dyes on glass substrate. A chromonic liquid crystal is a fine precursor of a final solid crystalline film. In this paper we present spectral characteristics of the LCLC of key chromonic materials. There is a strong correlation between optical parameters of LCLC liquid solution and final dried polarizing films. We describe two method of deposition of LCLC films on the glass substrate. The first technique to prepare aligned LCLC films of a nanometer thickness in the form of monomolecular layer and multi-layered stacks is the electrostatic layer-by-layer deposition from the mesomorphic state of the LCLC. The assembled dried films demonstrate a long-range orientational order as evidenced by the measurements of absorption and dichroic ratio as a function of the angle between the deposition direction and polarization of probing light. The second technique is direct deposition. In this paper we report the results of the optical characterization of the solid films, prepared by these techniques and compare the results to those for the chromonematic cells.

1. INTRODUCTION

Application of Lyotropic Chromonic Liquid Crystals (LCLC) takes its beginning since 1940s when Dryer [1] has proposed to use the light absorbing LCLCs for fabrication of light polarizers. According to the anisotropic light absorption is achieved by the deposition of isotropic dye solution and letting it to dry on an anisotropic polymeric substrate. The anisotropy of the polymer substrate is induced by unidirectional stretching of the film. The drying dye forms needle-like crystallites oriented along the stretching direction. Recent LCLC applications [2-5] are based on the liquid crystal property to be oriented with the director along an easy axis set by the surface or by an external action. This latter allows one to use isotropic substrates such as conventional glass substrates or glass substrates covered with thin polymer layer. The easy axis can be induced either by the shearing of the nematic LCLC (chromonematic) or by mechanical rubbing of the polymer covered substrate. It turns out, that the dried dye film preserves the orientation of the director (i.e. of the optic axis) along the easy axis set by shearing of the nematic. First possibility is usually employed for the preparation of dried solid thin films and the glass substrates covered with a rubbed polymer are used for the preparation of liquid crystal cells. Both geometries can be used

for display applications. Dried unidirectionally sheared dye films can serve as polarizers. Moreover applied directly on the internal surfaces of the cell substrates the dried films the anisotropic dye films simultaneously play a role of aligning layers [6]. Internal polarizers solve a problem of the parasitic birefringence of plastic substrates in flexible liquid crystal displays. Because of their negative birefringence the cells filled with optically transparent chromonematic have been proposed as optical compensators for thermotropic nematic display cells with positive birefringence to improve the viewing angle performance [7-9]. However usually the chromonematic is highly diluted, water based solution. Even for hermetically sealed cells the solvent has a tendency to evaporate from the cell. Any experimentalist closely working with the lyotropic cells knows that this little inconvenience becomes a big trouble if the cell has to be used during a long time. There are no commercial applications of the lyotropic cells and the problem of their hermetization is in underdeveloped state. There is no evidence that this problem can be solved for low costs. The alternative is to prepare dried solid films with optical characteristics identical to those for corresponding liquid crystal cells. We call such films as hard copies of the nematic cells. Moreover using so called layer by layer deposition technique (see below) for the preparation of the thin films one can design the films with the architecture variable through the thickness of the film, mimicking the distribution of the optic axis in the prototype liquid crystal cell.

Because of their potential applications the LCLC cells need to be optically characterized. Optical characterization can be correctly performed only if the nematic director is well uniformly oriented. Recently a technique for the planar alignment of the chromonematics was developed [10]. We have used this advantage for optical characterization of three chromonematics. The results are represented and fully discussed in [11]. In this report we inform the results of the optical characterization of the solid films, prepared by two techniques: direct deposition and layer by layer electrostatic deposition and compare these results to those for the chromonematic cells. The description of the deposition of the deposition techniques is given in the next Section.

2. EXPERIMENTAL:

2.1 Materials.

We work with three chromonic materials: one of them being optically transparent is called chromolyn (disodium chromoglicate or DSCG, chemical formula $C_{23}H_{14}O_{11}Na_2$) from Spectrum Company and the other two, namely Blue 27 (6,15-disulfonic acid-7,16-dichloro-6,15-dihydroindapho[2,3- α ;2',3'-h]phenazine-5,9,14,18-tetraone diammonium salt) and Violet 20 (2,5-disulfonic acid diammonium salt perylene[3'', 4'':3, 4, 5; 10'', 9'':3', 4', 5']dipyridino [1, 2- α :1', 2'- α']bisbenzimidazol-6,11-diol) from Optiva are dyes, absorbing light in the visible light wavelength range. Blue 27 is a derivative of indanthrone and Violet 20 is a derivative of perylene.

Their chemical formulae are schematized in Fig.1.

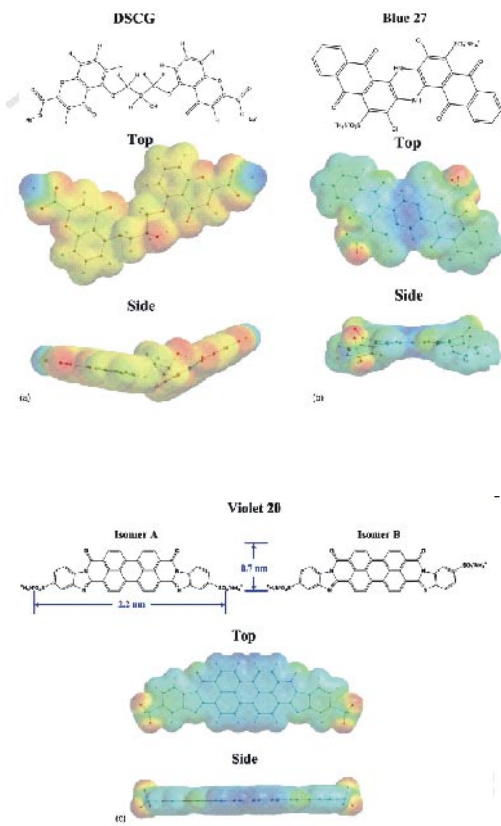


Fig.1 Chemical molecular structure of the studied materials.

The side groups indicated on each formula split from the molecules when dissolved in water and the ionic residues aggregating face-to-face and forming a rod like aggregates. At room temperatures these three materials form the nematic phase. The concentration of the cromolyn in water was 14% by weight and for Blue 27 and Violet 20 the concentrations were respectively 4.5% and 5% by weight respectively.

2.2. Deposition procedures:

2.2.1. Layer by Layer Deposition Technique

The glass substrates have been washed in an ultrasonic bath with soap detergent, then rinsed under distill water and dipped into a bath with the glass etching solution (mixture of 5% KOH water solution and isopropanol. After one hour the substrates were removed from the etching solution, rinsed under distill water and dried. Such cleaning procedure is known to make the surface negatively charged. Because the ionic residues forming the aggregates are negatively charged too the chromonic material can not be absorbed on the glass substrate with the same surface charge. To reverse the charge of the substrate we cover it by the solution of the polymer PDDA and let it to dry. Because the polymer residuals dissolved in water have positive charge they are electrostatically adsorbed on the negatively charged glass substrate

and the substrate becomes covered by a positively charged PDDA polymer monolayer after rinsing the substrate in distilled water. Unidirectionally spreading the chromonematic solution on such a substrate we form a nematic layer with the director parallel to the shearing direction. Drying of the chromonematic solution followed the water rinsing results in the presence of an oriented monolayer of the LCLC aggregates on the substrate. The chromonic material is electrostatically adsorbed to the polymer layer and can not be washed out similarly as it is for the PDDA polymer layer. Repeating the deposition procedure for PDDA followed by the deposition of the chromonic monolayers allows one to obtain a solid anisotropic chromonic film with the structure schematically shown in Fig.2.

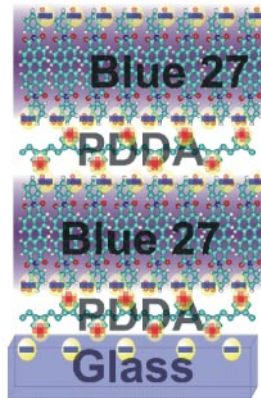


Fig.2. Structure of the chromonic (Blue 27) film obtained by the Layer by Layer Deposition technique.

2.2.2. Direct Deposition Technique

Glass substrates washed and cleaned as described above are covered by the chromonematic layer unidirectionally spreading it with a blade as it is schematically shown in Fig.3.

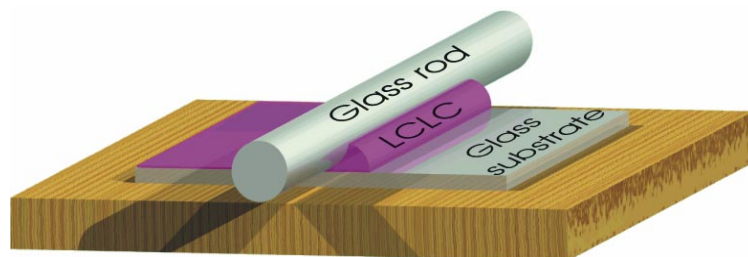


Fig.3 Direct Deposition Technique.

After drying the film displays a polarization microscopy texture which indicates that the director is on average oriented along the spreading direction although the texture is of the “tiger stripes” type revealing presence of numerous line defects. Using the results for the absorption of one 2nm thick

monolayer, we have deduced the thickness of the film obtained by the Direct Deposition Technique and found it to be 850nm.

2.2.3. Optical characterization procedure

The characterization procedure is summarized below. In the experiment we measure the transmission of the film placed between parallel polarizers at an angle α with respect to the polarizers direction (Fig.4):

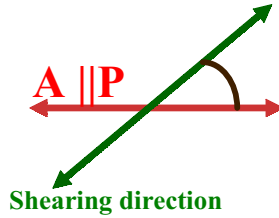


Fig.4. The orientation of the nematic director in the chromonic dried film with respect to the parallel polarizers.

The light transmission can be calculated as

$$T = \frac{e^{-\xi}}{2} \left[(1 + \cos^2 2\alpha) ch\delta - 2sh\delta \cos 2\alpha + \cos \Delta\varphi \sin^2 2\alpha \right];$$

where

$$\delta = \frac{2\pi(k - k_{\perp})d}{\lambda}; \quad \xi = 2\pi(k + k_{\perp})d; \quad k_{\perp} = -\frac{\lambda}{2\pi d} \ln T_{90}; \quad k = -\frac{\lambda}{2\pi d} \ln T_0;$$

$$\cos \Delta\varphi = \frac{4T_{45} - (T_0 + T_{90})}{2\sqrt{T_0 T_{90}}}; \quad \Delta\varphi = \frac{2\pi}{\lambda} \Delta n d.$$

Measuring the transmission T_0 corresponding to the orientation for which the nematic director is parallel to the polarizers ($\alpha=0^\circ$) we deduce the absorption index $k_{||}$. For $\alpha=90^\circ$ we measure T_{90} and calculate k_{\perp} . To calculate the phase retardation D_j one has to measure T_0 , T_{90} and T_{45} (transmission for $\alpha=90^\circ$). From the value of the phase retardation one can deduce the birefringence Dn . The results the dispersion of the birefringence for the directly deposited film 850 nm thick are shown in Fig.5

It is seen from Fig. 5 that the birefringence values obtained for two films almost coincide, implying that the thickness of the directly deposited film deduced from its light absorption is correct. Slight difference between the two curves is of the order of the measurement accuracy.

For comparison Fig.6 shows the dispersion of the birefringence measured for the 4.5% Blue 27 chromonematic cell. It is seen that the birefringence of the dried thick film is approximately 20 times higher than the birefringence

of the diluted chromonematic solution as it can be expected. The shape of the dispersion curve is anomalous. The anomaly can be explained by the presence of the absorption band (Fig. 6) with the maximum absorption at $\lambda \approx 640\text{nm}$. For comparison Fig.8 shows the dispersion indices for 4.5% Blue 27 chromonematic cell. As it can be expected the absorption indices for the solution are about 20 times lower than it is for the solid film.

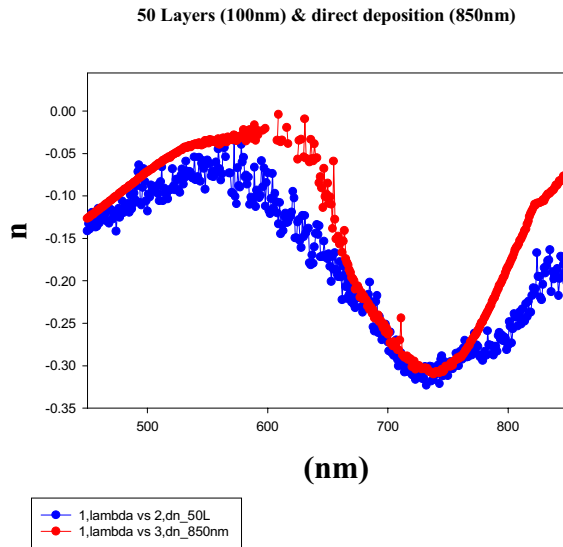


Fig.5. Dispersion of the birefringence for two Blue 27 films: 850nm thick directly deposited and 100nm thick (50 monolayers) obtained with Layer by Layer Deposition Technique.

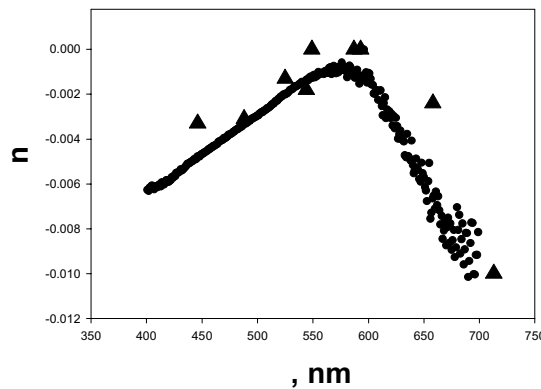


Fig.6. Dispersion of the birefringence for 4.5% Blue 27 chromonematic solution.

The birefringence has negative sign. This latter opens a possibility for the optical compensation of the positive birefringence of the thermotropic nematic cells used in liquid crystal displays if the chromonematic were transpar-

ent. Chromolyn is a transparent chromonic material. We have checked that the birefringent film can be obtained by the deposition of the 14% cromolyn chromonematic solution. The corresponding measurements are in progress.

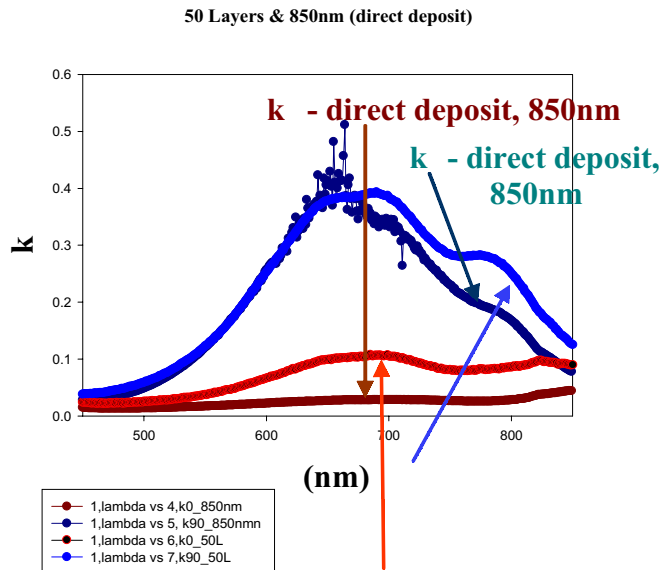


Fig.7. Dispersion of the absorption indices for directly deposited and electrostatically deposited films

LC state, 4.5% B27 in water

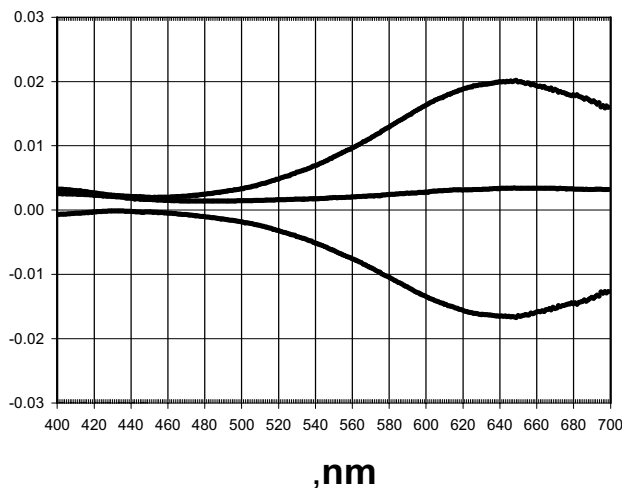


Fig.8 Dispersion of the absorption indices for the 4.5% Blue 27 chromonematic solution.

Having the results for $k_{||}$ and k^{\wedge} one can measure the scalar order parameter for the prepared films in a way as we did it for chromonematic cells

[11]. The results are as following. For directly deposited films the order parameter appears to be quite high, about 0.9. For the films obtained by the Layer by Layer Deposition Technique the order parameter is slightly lower than the value obtained for direct deposited films.

3. CONCLUSION.

The characterization of the LCLC layer and correspondent dried films was performed in terms of the anisotropic absorption coefficient, scalar order parameter, birefringence and the thickness of a LCLC film, which is a molecularly oriented film of an organic dye. The absorption coefficients, $k_{||}$ and k^{\perp} , of a polarized light are measured in the parallel and orthogonal directions with respect to the orientation field. The birefringence of both the nematic phase and LCLC dried films has a negative sign. The birefringence of the dried film is approximately 20 times higher than the birefringence of the diluted chromonematic solution. For the films obtained by the Layer by Layer Deposition Technique the order parameter is slightly lower than the value obtained for direct deposited films.

Reference.

1. J. F. Dreyer and C.W. Ertel, *J. Phys. Colloid Chem.* 52, 808 (1948).
2. Y. Bobrov, C. Cobb, P. Lazarev, P. Bos, D. Bryant, and H. Wonderly, *SID 2000 Digest*, report 47.4 (2000).
3. T. Schneider and O.D. Lavrentovich, "Self-assembled monolayers and multilayered stacks of lyotropic chromonic liquid crystalline dyes with in-plane orientational order", *Langmuir* 16, 5227-5230 (2000).
4. J. Lydon, *Curr. Opin. Colloid Interface Sci.* 3, 458-1998; 8, 480 (2004).
5. T. Schneider, A. Golovin, Jong Chan Lee and Oleg D. Lavrentovich, "Lyotropic chromonic liquid crystals in aligned films for applications as polarizing coatings," *J. Info. Display, The Korean Information Display Society* 5, No.2, 27-38 (2004).
6. T. Sergan, T. Schneider, J. Kelly, and O.D. Lavrentovich, "Polarizing-alignment layers for twisted nematic cells", *Liq. Cryst.* 27, 567-577 (2000).
7. T. Sergan and J. Kelly, "Negative uniaxial films from lyotropic liquid crystalline material for liquid crystal display applications", *Liq. Cryst.* 27, 1481-1490 (2000).
8. M. Lavrentovich, T. Sergan, and J. Kelly, "Planar and twisted lyotropic chromonic liquid crystal cells as optical compensators for twisted nematic displays," *Liq. Cryst.* 30, 851-859 (2003).
9. M. Lavrentovich, T. Sergan, and J. Kelly, "Lyotropic chromonic liquid crystals for optical applications - An optical retardation plate for twisted nematic cells," *Mol. Cryst. Liq. Cryst.* 409, 21-28 (2004).
10. Oleg. D. Lavrentovich and Tomohiro Ishikawa, US Patent US 6,411,354 B1.
11. Yu. A. Nastishin, H. Liu, T. Schneider, V. Nazarenko, R. Vasyuta, S. V. Shiyonovskii, and O. D. Lavrentovich *Phys. Rev. E* 72, 165509 (2005).

Latest Multi-user 3D Display Developments

*Phil Surman, Ian Sexton, Richard Bates, Wing Kai Lee,
Triantafillos Koukoulas*

De Montfort University, The Gateway, Leicester, LE1 9BH, United Kingdom
3DTV@dmu.ac.uk

ABSTRACT

The principle of operation of the De Montfort University (DMU) multi-user 3D display is described. The DMU display enables several viewers to move freely over a large area and to all see the same stereo image pair without the use of special glasses. A brief description of the first prototype, and the problems identified from this, will be given. Work on an improved prototype that is currently being built is described.

KEYWORDS

Autostereoscopic, 3D Display, Light Emitting Diode (LED), Liquid Crystal Display (LCD), Head Tracking, LCD Backlight.

INTRODUCTION

There are several techniques for presenting stereoscopic images to several viewers. The three basic methods are: **holographic** where the image is produced by wavefront reconstruction [1] [2], **volumetric** where the image is produced within a volume of space that may be either real or virtual [3] [4] [5] and **multiple image** displays where two or more images are seen across the viewing field.

The ideal stereoscopic display would produce images in real time that exhibit *all* the characteristics of the original scene. This would require the wavefront to be reproduced accurately and could only be achieved using holographic techniques. The difficulties of this approach are the huge amounts of computation necessary to calculate the fringe pattern, and the high resolution of the display, which has to be of the order of a wavelength of light (around 0.5 micron). Although holography may ultimately offer the solution to providing 3D images, the problem of capturing naturally lit scenes will first have to be solved and holography is unlikely to provide the basis of a viable 3D display in the near future.

Volumetric displays have the ability to display motion parallax in both the vertical and horizontal directions. This enables several viewers to see a 3D image that exhibits no rivalry between the accommodation and focus of the eyes. However, volumetric displays suffer from several disadvantages. In general the images are not opaque so that points of the image that lie behind a displayed surface will be seen through it. Whilst this might be acceptable for certain computer-generated images, it is not suitable for the display of real video images. Also, volumetric displays cannot show surfaces that have a non-Lambertian intensity distribution. Again, this would not be suitable

for real images, as a proportion of the content in these images invariably has regions with non-Lambertian distribution.

Multiple image displays fall within three fundamental types, these are: holoform in which a large number of views give smooth motion parallax and hence a hologram-like appearance [6] [7], multi-view where a series of discrete views is presented across viewing field [8] [9] and binocular where two views only presented in regions that may occupy fixed positions [10] [11] or follow viewers' eye positions using head tracking [12] [13]. Holoform displays must present a very large amount of information in order to provide motion parallax. Multi-view displays, although potentially very simple to construct, do not provide stereo over the complete area in front of the screen, leaving large unusable regions.

For these reasons DMU have chosen the head-tracked binocular option. This is particularly suitable for use in television applications as it requires the simplest image capture, transmission bandwidth and imposes the least demand on the display device in terms of resolution. There are several single-user head tracked 3D displays, but very little research has been carried out into multi-user head tracked 3D displays.

The DMU display locates the viewers' head positions and uses this information to direct regions, referred to as exit pupils, to the locations of the viewers' eyes. An eye located in the left exit pupil regions, denoted by the upper diamond-shaped green regions in Fig.1, will see left image over the complete screen area. Similarly, a right image is seen in the lower red regions. The DMU display optics is capable of producing several exit pupil pairs that can be moved independently of each other.

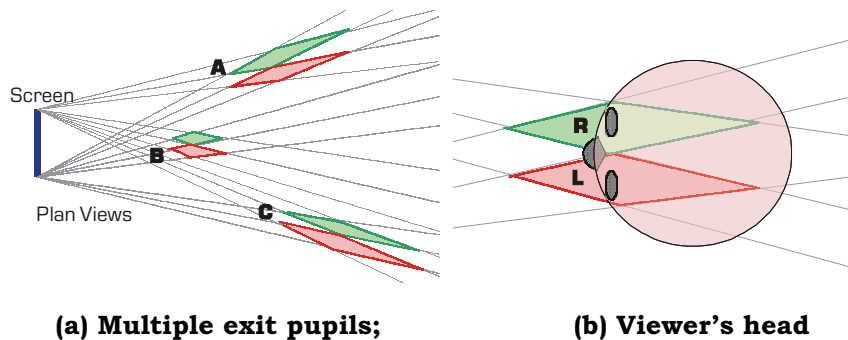


Fig.1 Exit pupils

PRINCIPLE OF OPERATION

The images of a stereo pair are presented on a single LCD by means of spatial multiplexing where left and right images are presented on alternate pixel rows. A lenticular screen with its lens axes running horizontally, and with a lens pitch of slightly less than double the LCD vertical pixel pitch, is located behind the LCD. This enables light from two sources that have different vertical positions to be focussed on the appropriate pixel rows.

The exit pupils are produced by novel optics located behind a direct-view LCD whose backlight is removed. It is possible to produce exit pupils with the use of a Fresnel lens located in front of the LCD to form real images of light sources that are positioned behind the LCD. A head tracked display incorporating a Fresnel lens to form exit pupils was built as early as 1985 [14]. DMU have built a display operating on this principle in order to test the spatial multiplexing arrangement. This display uses two halogen lamp sources that are displaced from each other in both the vertical and horizontal directions. Head tracking is not employed and the exit pupil positions are fixed. A Fresnel lens is not suitable for a multi-user display as off-axis and spherical aberrations prevent exit pupils being formed over the large region required for television. Also, a mobile pair of light sources would be necessary for each viewer.

In the first prototype the Fresnel lens is replaced by a lens array as in Fig.2. If the series of illumination sources moves laterally, the exit pupil also moves laterally. If the separation of the light sources varies, the position of the exit pupil changes in the z-direction. For example, if the sources have the same horizontal pitch as the lenses, a more-or-less parallel beam is formed giving an exit pupil that is effectively at infinity. As the separation becomes greater, the exit pupil moves closer to the screen.

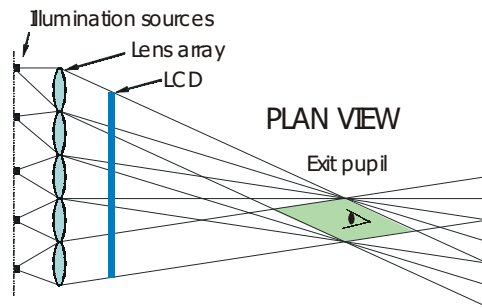


Fig.2 Multiple lens array

FIRST PROTOTYPE CONSTRUCTION

As the exit pupils must be formed over a large region, simple lenses cannot be used in the lens array as off-axis aberrations limit the angle of the emergent light. In order to overcome this limitation, optics as shown in Fig.3 are employed. The illumination is supplied from an array of white LEDs whose light enters the edge of the rear optical element and is contained by total internal reflection. This light passes through an aperture into the front element. It exits through the front refracting surface whose radius is approximately half that of the rear element. The centres of curvature and the centre of the aperture, all lie on the same axis; hence the optics is termed coaxial. Two versions of this display were built, the first using 80-element arrays of 3-millimetre LEDs, and the second using 256 one-millimetre surface-mount LEDs.

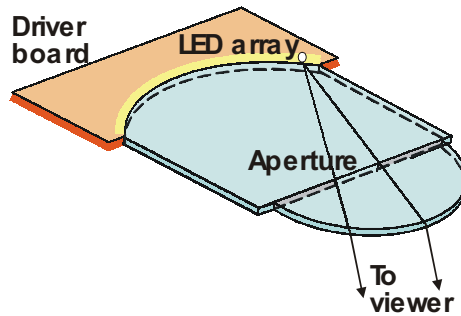


Fig.3 Coaxial optical element

Two ten-element steering arrays are used, one of these for the production of the left exit pupils, and one for the right pupils. Each array is assembled in the staggered configuration shown in Fig.4 (a). The effective backlight of the LCD is supplied from the virtual apertures whose appearance is shown in Fig.4 (b). These images are approximately 1.5 times the width of the apertures and lie in the same plane as them. The light must be vertically diffused at the screen otherwise the complete height of the screen will not be illuminated. In this case the illumination configuration of Fig.4 (b) forms a contiguous light source across the width of the screen. The edges of the apertures are soft in order to allow for constructional tolerances and for aberrations that cause the aperture image width to vary.

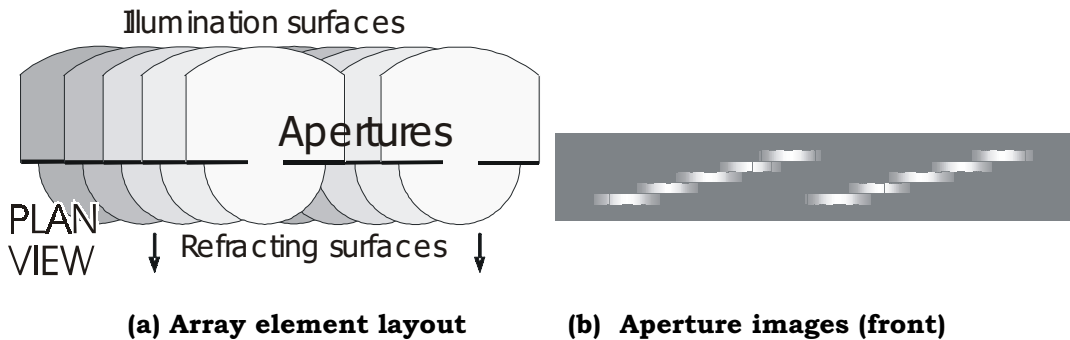


Fig.4 Array layout

As the included vertical angle of the light emerging from the arrays is around 23° , the distance between the front of the steering arrays and the screen assembly is 800 millimetres in order for the light to reach the complete height of the screen. One of the specifications for this prototype was that viewers could be accommodated 30° either side of the screen normal. This would need an array that was around three times the width of the screen. However, this can be avoided with the use of the side folding mirrors, one of which can be seen in Fig.5. These produce virtual images that increase the effective array width.

Two ten-element arrays, one positioned above the other, are mounted behind these folding mirrors. The screen assembly, located in front of the

mirrors comprises the lenticular multiplexing screen, the LCD, a vertical diffuser and a cylindrical lens. The vertical diffuser is a 0.51 x 20I elliptical diffuser from Physical Optics Corporation. Image brightness is increased by condensing the light to the viewers with the use a large oil-filled cylindrical lens with a focal length of 0.5 metres and whose axis is horizontal.

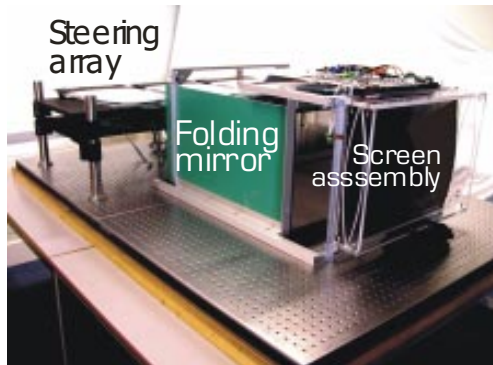


Fig.5 Prototype 3D display

FINDINGS FROM FIRST PROTOTYPE

Evaluation of the prototype identified several areas where further work is necessary. These have been previously reported, but to summarise, these are: low brightness, vertical banding, and crosstalk. The problem of crosstalk, which is caused principally by diffraction at the LCD, will be addressed in the next prototype by selecting a more suitable LCD or by rotating it through 90I. DMU will also investigate the design of an LCD that is more suitable for use in this application.

Low brightness and banding are caused by the use of white LEDs as the illumination source. It has not been possible to concentrate the light sufficiently from the output of the high-density surface-mount white LED arrays. Also, the variation in both the LED brightness and colour causes the appearance of vertical banding in the image. The use of soft apertures reduces the perceived effect to a certain extent but banding is still noticeable, especially where there are extensive areas of one colour in the image. The typical range of LED colour is shown in Fig.6, which is based in information from the Nichia Corporation. Even when LEDs from one batch are used, the variation is still high.

Fig.5 shows that the size the prototype is relatively large. The size of this display could be reduced to that of a current rear projected set with the use of folding mirrors. This was the original intention, however, since the advent of FPDs, customers generally now prefer displays that are compact in size and 'hang-on-the-wall'. Apart from size, another disadvantage of the folded optics is that they are difficult to manufacture as they incorporate several orthogonal surface-silvered mirrors that are butted up to each other. Also, a sealed dust-proof casing is required. A new approach, that uses the same underlying principles, is described in the following section.

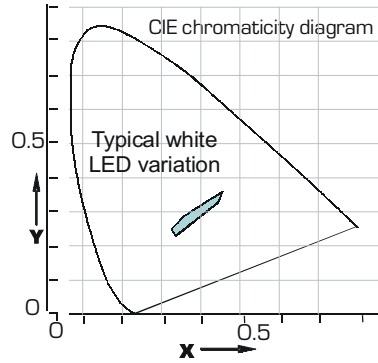


Fig.6 White LED colour variation

A NEW APPROACH

With careful design, the optical elements need not be fully coaxial, but can be as in Fig.7 (a) where the back illumination surfaces are flat. This is referred to as semi-coaxial and has the advantage that all the light input to the arrays lies within a single plane therefore enabling the possibility of using other types of illumination source.

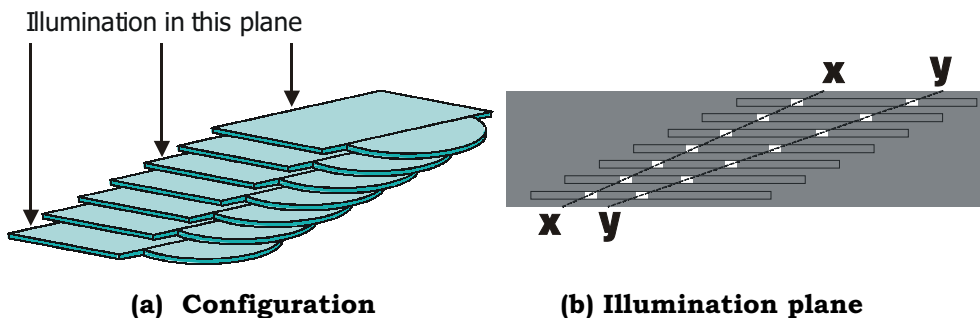


Fig.7 Semi-coaxial array

Fig.7 (b) shows the illumination pattern for the production of two exit pupils. The line XX, where every illumination source is in the same position along each array, will produce a parallel output beam, and therefore an exit pupil at infinity. Light sources that lie on the line YY will produce an exit pupil close to the array.

The use of a monochrome LCD as a spatial light modulator (SLM) was investigated originally. However, the low light throughput of these devices ruled out their use in this application. Projection is another option and this has been chosen for the next prototype. A short test array of 12 semi-coaxial elements has been constructed and is shown in Fig.8 where it is illuminated from a conventional projector located behind it. By projecting a pattern similar to that shown in Fig.7 (b) it is possible to steer a beam over an angle of around 40°. These elements have cylindrical front refracting surfaces. However, the use of optimised non-cylindrical surfaces will enable this angle to

be increased considerably. The optical elements are much smaller, with a front lens radius of 30 millimetres (as opposed to 90 millimetres in the first prototype).



Fig.8 Miniature Array

Examination of Fig.7 (b) shows that only a small proportion of the light is used (approximately 5%). This low light usage can be addressed with the use of a holographic projector where a computer-generated hologram is illuminated with coherent light. This has the advantage that the light delivered is controlled by diffraction rather than simply being blocked and the complete wavefront is made use of. Unlike conventional projection, this device utilises a laser light source, and a phase-modulating LCOS microdisplay on which a hologram pattern, rather than the desired image, is displayed. The hologram patterns are computer-generated such that, when the LCOS is illuminated by coherent laser light, the light interferes with itself in a complex manner through the physical process of diffraction resulting in the formation of a large, high-quality projected image. However, since the phase-modulating SLM devices are binary, a conjugate (mirror) image is produced, thus reducing the efficiency by half. Higher orders produced by the SLM pixellation effectively limit the diffraction efficiency to approximately 40%. It may however be possible to exploit the conjugate symmetry for this application, thereby doubling the efficiency to 80%, and this will be investigated. Fig. 9 is a simplified schematic system diagram of the proposed new configuration.

In order for the display to be 'hang-on-the-wall' the optical arrays will have to be located close to the back of the screen assembly. Fig.10 shows how this could be achieved. A series of arrays, as opposed to the single image pair used in the first prototype, would enable them to be close to the screen, and mirrors could be deployed to redirect their output thus giving the compact configuration shown.

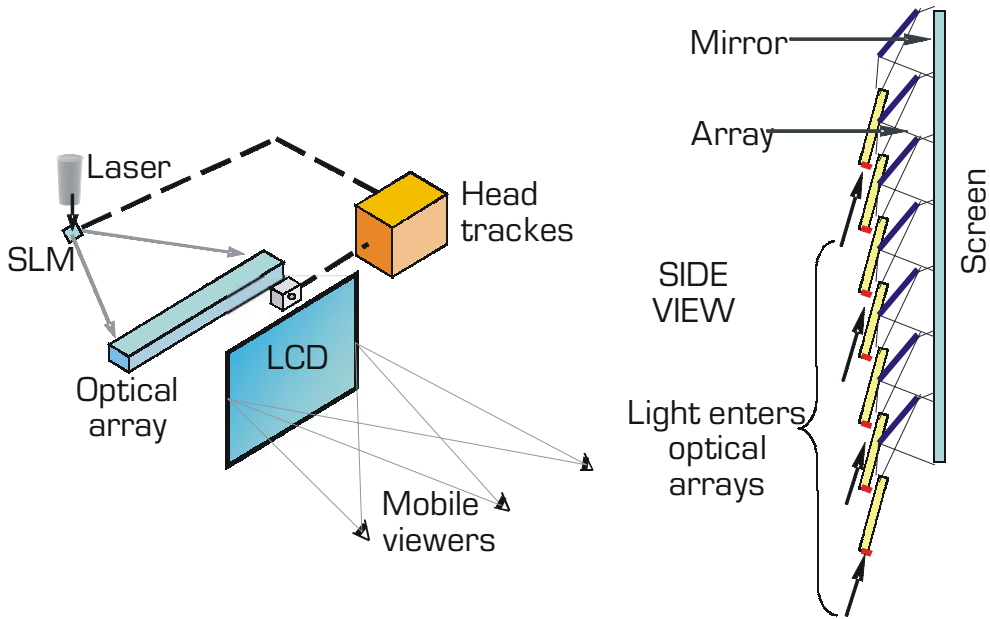


Fig.9 (left) Projection schematic diagram.
Fig.10 (right) 'Hang-on-the-wall' configuration

CONCLUSIONS

The first prototype, built under the EU-funded ATTEST 3D television project, showed that the concept of using an optical array whose illumination is controlled by the output of a head tracker provides a viable multi-user 3D display solution. Although this prototype has limited performance, it has proved to be extremely useful in guiding the route to further development. The most important conclusions drawn from its evaluation relate to the LCD and to the use of white LEDs.

The LCD used in the first prototype gives crosstalk levels in the region of 15% and is therefore not suitable for this application. Although some diffraction at the LCD is inevitable due to its pixel structure, it is fairly certain that there are means of reducing this to acceptable levels.

The use of white LEDs as the light source initially appeared promising, but there are many problems associated with them. However, in the long term, their use should not be ruled out as they are the subject of intensive research. They are widely seen as being the principal light source of the future due to their being environmentally friendly in terms of efficiency and the ability to be disposed of safely (unlike fluorescent lamps). One possible strategy for creating more consistent LEDs could be the use of a common phosphor for a matrix of blue junctions, or the use of RGB LEDs. However, in the immediate future the use of projection will be investigated.

Although there are many challenging problems to be addressed, the approach of using steerable exit pupils under the control of a head tracker in

order to direct a stereo pair to several viewers appears to be a strong contender for the next generation of multi-user 3D displays.

REFERENCES

- [1] LUCENTE M. (1997). "Interactive Three- dimensional Displays; Seeing the Future in Depth", *Siggraph "Computer Graphics - Current, New and Emerging Display Systems"*.
- [2] SON J.Y., Smirnov V. V., Asnis L. N., Volkonsky V. B., Chun J. H. and Kuznetsov S. V. and Lee H. S. (1999). "Real-time 3D Display with Acousto-optical Deflectors", *SPIE Proceedings, "Stereoscopic Displays and Virtual Reality Systems VI"*, Vol.3639, pp 137-142.
- [3] ANDREEV A., Bobylev Y., Gonchukov S., Kompanets I., Lazarev Y., Pozhidaev E. and Shoshin V. (2004). "Experimental model of volumetric 3-D display based on 2-D optical deflector and fast FLC light modulators", *SID Proceedings "Advanced Display Technologies 2004"*, pp 279-283.
- [4] BLUNDELL B. G. and Schwarz A. J. (2000). "Volumetric Three-Dimensional Display Systems", John Wiley & Sons, Inc., 2000.
- [5] FAVALORA G.E., Dorval R.K., Hall D.M., Giovinco M. and Napoli J. (2001). "Volumetric Three-dimensional Display System with Rasterization Hardware", *SPIE Proceedings, "Stereoscopic Displays and Virtual Reality Systems VIII"* Vol.4297, pp 227-235.
- [6] KAJIKI Y. (1997). "Hologram-Like Video Images by 45-View Stereoscopic Display", *SPIE Proceedings, "Stereoscopic Displays and Virtual Reality Systems IV"*, Vol.3012, pp154-166.
- [7] MOLLER C. and Travis A. R. L, (2004). "Flat Panel Time Multiplexed Autostereoscopic Display Using an Optical Wedge Waveguide", *Proceedings of The 11th International Display Workshops, Niigata, Japan*, pp1443-1446.
- [8] LEE C. M. G. and Travis A. R. L. (2004). "Flat-Panel Autostereoscopic View-Sequential 3D Display Backlight", *Proceedings of The 11th International Display Workshops, Niigata, Japan*, pp1479-1482.
- [9] ZWART S. T. de, IJzerman W. L., Dekker T. and Wolter W. A. M. (2004). "A 20-in. Switchable Auto-Stereoscopic 2D/3D Display", *Proceedings of The 11th International Display Workshops, Niigata, Japan*, pp1459-1460.
- [10] HARROLD J., Wilkes D. J. and Woodgate G. J. (2004). "Switchable 2D/3D Display - Solid Phase Liquid Crystal Microlens Array", *Proceedings of The 11th International Display Workshops, Niigata, Japan*, pp1495-1496.
- [11] SCHWERDTNER A. and Heidrich H. (1998). "The Dresden 3D Display (D4D)", *SPIE Proceedings, "Stereoscopic Displays and Applications IX"*, Vol.3295, pp203-210.
- [12] Stereoscopic Display", *Proceedings of IEEE International Display Research Conference*, pp 141-144.
- [13] WOODGATE G.J., Ezra D., Harrold J., Holliman N.S., Jones G.R. and Moseley R.R. (1997) "Observer Tracking Autostereoscopic 3D Display Systems", *SPIE Proceedings, "Stereoscopic Displays and Virtual Reality Systems IV"*, Vol.3012, pp187-198.
- [14] SCHWARTZ A. (1985). "Head Tracking Stereoscopic Display", *Proceedings of IEEE International Display Research Conference*, pp 141-144.

Operation steadiness and manufacturing prospects of passively addressed FLC displays possessing an inherent gray scale

E.P. Pozhidaev¹, V.G. Chigrinov², Yu.P. Bobilev¹, V.M. Shoshin¹, A.A. Zhukov¹, A.L. Andreev¹, I.N. Kompanets¹, Li Xihua², E.E. Gukasjan¹, P.S. Komarov¹, O.A. Shadura¹, H.S. Kwok²

¹ P. N. Lebedev Physical Institute of Russian Academy of Sciences, Moscow, Leninsky pr. 53, 119924, Russia

² The Hong Kong University of Science and Technology, Clear Water Bay, Kowloon, Hong Kong

A passively addressed 64'64 ferroelectric liquid crystal display (FLCD) has been developed. The display matrix has dimensions of 33'33mm², and the FLC layer thickness is (5.2±0.2)μm. The display device operates with the frame frequency 30 Hz (at $V_{row} = ±18V$, $V_{col} = ±9V$, $T = 23°C$) generating a continuous gray scale, which can be memorized for more than 10 days after the driving voltage is switched off. A new approach for multiplex electronic addressing of the FLCD gray scale is proposed. Necessary conditions for the gray scale generation at multiplex addressing, and the gray scale memorization after the voltage is switched off, as well as the steadiness of memorized images with time are considered.

Introduction

The gray scale of passively addressed FLCD can be obtained only if the FLC possess high spontaneous polarization $P_s > 50$ nC/cm² [1, 2], when ferroelectric domains exist, being one of possible reasons for the gray scale. Generally, any kind of spatial non-uniformity of helix free FLC's [3] coupled with minimization of the FLC free energy which arise because of high P_s can be considered principally as a base for the gray scale. On the contrary, at high P_s depolarizing field appear in FLC cells, suppressing the bistability, if aligning layers are thick enough [4]. Therefore extremely thin aligning layers is necessary condition for the development of passively addressed FLCD with the gray scale. One can even remove one of aligning layers, providing due to it the best quality of the FLC layer photo-alignment [6], but mentioned asymmetry of boundary conditions provides asymmetry of the FLC anchoring energy with boundaries. It can create problems with the steadiness of bistability that is necessary condition of the multiplex addressing; therefore this problem was considered in our work. A principle of multiplex electronic addressing of FLCD's with the gray scale at fixed frame time will be also discussed.

Experiments

Asymmetric boundary conditions [6] were used for modeling and manufacturing of the FLCD. At this approach only one ITO surface of FLC cells was covered with a photo-aligning substance - azobenzene sulfuric dye SD-1 layer [5,6], but another one was simply washed in N,N-dimethylformamide

(DMF) and covered with 5,2 mm calibrated spacers. The azo-dye solution was spin-coated onto ITO electrode and dried at 155°C. A polarized UV light was achieved by using a super-high pressure Hg lamp, an interference filter at 365 nm and a polarizing filter. The light with intensity of 6 mW/cm² and wavelength of 365 nm was irradiated normally onto SD-1 layers. The FLC FLC-497 (from P. N. Lebedev Physical Institute of Russian Academy of Sciences) was injected into the cells in an isotropic phase by a capillary action at T=85°C. This FLC possess the spontaneous polarization $P_s = 95$ nC/cm² and the tilt angle $\theta = 27^\circ$ at T=23°C, the phase transition sequence is as followed: Cr $\rightarrow^{40^\circ\text{C}}$ C* $\rightarrow^{57^\circ\text{C}}$ A* $\rightarrow^{76^\circ\text{C}}$ Is. The helix pitch of the FLC tends to infinity in all the bulk due to compensation by two chiral dopants with the same signs of the spontaneous polarization but opposite signs of their handedness [3]. Electrooptical measurements were carried out using an ordinary electrooptical set-up based on He-Ne laser, Hewlett Packard Infinum oscilloscope and rotating table for adjusting of angular position of FLC cells placed between crossed polarizers. A programmed generator was used for experimental simulations of the multiplex operation. Measurements of the anchoring energy of the FLC with aligning surfaces were carried out according to a method proposed in [7]. The idea is based on measurements of static hysteresis loops of FLC cells. "Static" means here the frequency interval 10⁻³÷10⁻² Hz, where there is no dependence of the voltage coercivity V_c on the applied voltage frequency. The voltage coercivity can be defined as

$$V_c = V_+ - V_- \quad (1),$$

where V_+ and V_- are the switching voltage thresholds at positive and negative voltage correspondingly [7] (Fig.1).

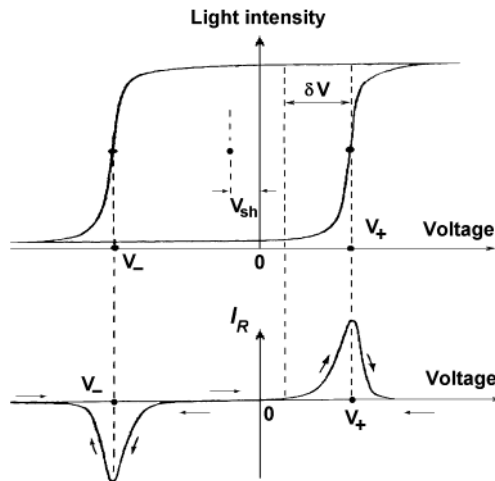


Figure 1. Top - a typical hysteresis loop of 6µm FLC-497 based cell (aligning layer thickness is 12 nm, the frequency is 0.02Hz) exhibiting a shift of the hysteresis loop center regarding zero voltage; bottom - a typical polarization reversal current of the cell.

A shift V_{sh} of the hysteresis loop center regarding zero voltage, which usually takes place in FLC cells, can be evaluated as (Fig.1):

$$V_{sh} = \frac{1}{2} (V_+ - V_-) \quad (2),$$

It is very important point in our analyses of the bistability steadiness, because if

$$V_{sh} \geq \frac{1}{2} V_c \quad (3),$$

the bistability evidently does not exist (Fig.1).

Results and discussion

Criteria of bistable FLC switching

For evaluations of the bistability steadiness of display cells both in static and dynamic cases we propose now a new criterion:

$$S_b = (\frac{1}{2} V_c - |V_{sh}|) / \delta V \quad (4).$$

The parameter δV in (4) indicates a region inside the hysteresis loop where the light intensity at the output of FLC cell depends on applied voltage, or the polarization reversal current is non-zero also (Fig. 1, bottom). Generally, one can evaluate the bistability steadiness even without any electrooptical measurements of hysteresis loops, simply measuring the polarization reversal current diagrams (compare top and bottom curves of Fig.1). The perfect bistability both for static and dynamic cases takes place, if $S_b \geq 1$, because under this condition both dark and bright saturation levels of the light transmission obtained at applied voltage $V > V_+$ and $V < V_-$ can be memorized at zero voltage (when the voltage is switched off and electrodes of the cell are shorted) without any change (Fig.1). If $S_b < 0$ then the hysteresis loop is completely located in positive or negative region of the voltage and perfect mono-stable operation of display cells occurs at this case - the cell can memorize only one fixed light transmission level after the voltage is switched off. This case is completely inappropriate for passive multiplex addressing of displays. An intermediate region of S_b magnitudes - $0 \leq S_b < 1$ - corresponds to continuous transition from perfect bistability to perfect mono-stability of display cells. The steady bistability with $S_b \geq 1$ for the static case (unlimited memory time) does not exist within the whole temperature region of smectic C* phase of the FLC because of strong temperature T dependence of $S_b(T)$. For example, the 6 μ m FLC-497 based cell with asymmetric boundary conditions manifests the temperature region with $S_b \geq 1$ at $T \leq 35^\circ\text{C}$, but at $51^\circ\text{C} \leq T \leq 56^\circ\text{C}$ the perfect mono-stability takes place because $S_b \leq 0$ (Fig.2). Evaluations of the temperature dependence of the bistability steadiness according to the criterion S_b have been confirmed by direct observations of bistable and mono-stable electrooptical responses in the corresponding temperature regions.

Optical manifestations and probable origin of ferroelectric domains modulation by the electric field

The FLC gray scale appears due to the so called ferroelectric domains appeared in FLC cell with a high spontaneous polarization [8] (Fig.3). The

electrically modulated structure of ferroelectric domains, between two crossed polarizers is characterized by a regular structure of black and white stripes elongated along smectic planes of the FLC with the period, which is almost equal to ferroelectric domains period (compare Fig. 3a and Fig. 3b). Bright stripes indicate spatial regions, where the FLC director is completely switched and memorized, while black stripes correspond to absolutely non-switched regions.

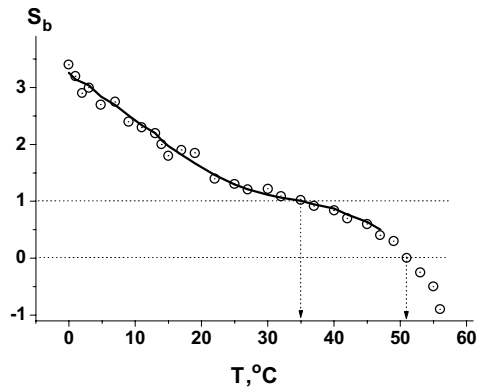


Figure 2. Temperature dependence of the bistability parameter S_b , measured with the 6 μm FLC-497 based cell at asymmetric boundary conditions, SD-1 layer thickness is 9nm, the frequency of triangular voltage $f=0,005\text{Hz}$, the voltage amplitude $\pm 3.0\text{ V}$.

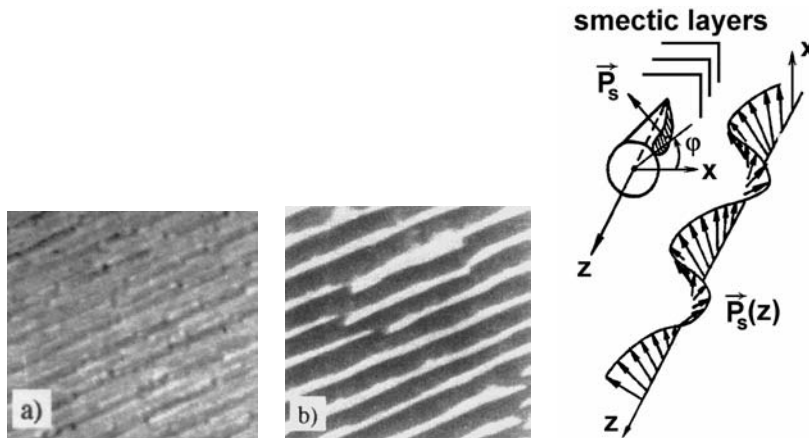


Figure 3: a) a 40'40 μm size micro-photo of ferroelectric domains typical texture (5.2 μm FLC-497 based cell at asymmetric boundary conditions, SD-1 layer thickness is 9 nm) before the driving voltage application; b) the same area of the FLC cell as in Fig3a but the texture is memorized after application of the driving voltage pulses sequence; c) a model of spatial modulation of the spontaneous polarization vector due to ferroelectric domains [8], x axis is perpendicular, z is parallel to solid substrates of the cell.

Sharp boundaries occur between black and white regions illustrating the fact that the FLC director possesses only two steady positions. That means each smectic layer manifests truth bistability without memorizing of any intermediate states between “black” and “white” states. The apparent light transmission of the structure shown in Fig. 3b is a result of a spatial averaging of “black” and “white” areas light transmission inside the light aperture, which is much larger than the structure period. The gray scale appears as a result of this averaging; therefore one can discuss multistability of the light transmission levels only. Memorization of all generated gray scale levels for unlimited time is possible and confirmed in our experiments.

Principles of multiplexing driving voltage development

Possible driving voltage shape to provide the gray scale of passively addressed FLCD have been developed taking into account two basic ideas. These are well-known Seiko-standard multiplexing scheme [9], which provides binary multiplexing mode of passively addressed FLC displays, and the pulse width modulation (PWM) principle which provides, for instance, the gray scale of STN displays [5,6]. Proposed modification of the Seiko-standard multiplexing scheme relates to the column voltage shape and polarity only while the row voltage shape is the same as for classic Seiko-standard. Instead of pair “negative-positive” row voltage pulses the modified pair of the same total duration should be generated (Fig.4). Only time interval τ (Fig.4) can be changed and additionally, polarity of the pulses can be reversed. A rate of pulse width modulation can be defined as τ/T . Figure 4 summarizes our approach.

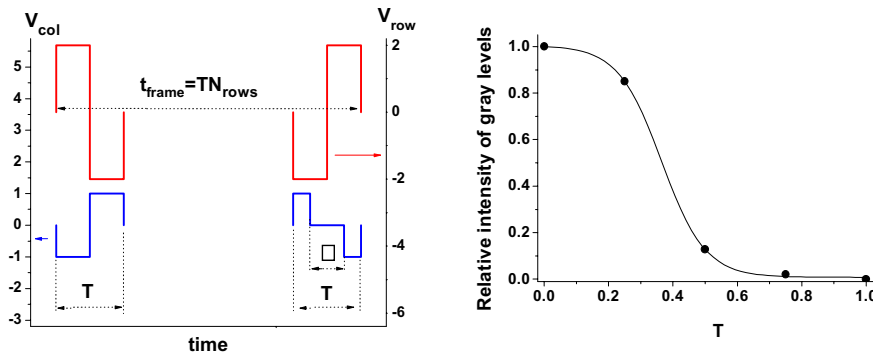


Figure 4. Left: Modified Seiko-addressing scheme for FLC display. Right: gray levels of the FLC cell. Variation of τ/T parameter inside an interval $0 \leq \tau/T \leq 1$ provides the gray scale generation. At $\tau/T = 0$ (the column pulse in left bottom corner) the binary mode takes place. Relative intensity of gray levels vs τ/T parameter measured at multiplex driving for FLC 497 photo-aligned display cell with the FLC layer thickness 5,2mm, $T=25C$ and the driving voltage parameters: $V_{row} = \pm 20V$, $V_{col} = \pm 10V$ are also shown in Fig.4

Hysteresis free and steady gray scale for passive addressing of the FLC display

The best condition for FLC bistable switching is the symmetrical hysteresis loop with $|V_{sh}| \rightarrow 0$ and $dV \ll 0$ (4), while the hysteresis free gray scale of FLCD requires also a certain relation between these two values. The relation can be found, if we suggest that the “black” state is the basic one, so the threshold V_{thB} of the bright levels addressing is not less than the saturation voltage V_{SD} of the dark state addressing (Fig.5):

$$V_{thB} \geq V_{SD} \quad (5)$$

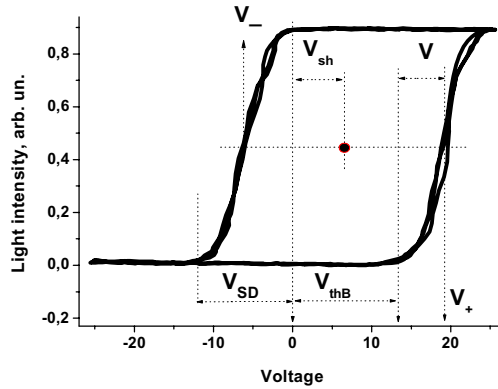


Figure 5. The hysteresis loop of 5.2 μ m asymmetric FLC-497, $L_{SD-1} = 9$ nm, the frequency of the triangular voltage $f=50$ Hz, amplitude ± 30 V, $T=23^{\circ}$ C.

V_{thB} the threshold voltage of bright levels addressing, V_{SD} is the saturation voltage of the dark state addressing.

The condition (5) provides the addressing of all the levels of the light transmission using the right branch of the hysteresis loop, as the left branch of the hysteresis loop is of no importance, when the driving voltage exceeds V_{SD} value. In this case the hysteresis free FLC addressing of all light transmission levels (gray scale) can be obtained.

The voltages V_{thB} and V_{SD} can be expressed as (Fig.5):

$$V_{thB} = \frac{1}{2}V_c + |V_{sh}| - \delta V, \quad V_{SD} = \frac{1}{2}V_c - |V_{sh}| + \delta V \quad (6)$$

and combining (5) and (6), we get:

$$|V_{sh}| \geq \delta V \quad (7)$$

Taking into account (4) and (7) we have necessary and sufficient conditions of the hysteresis free gray scale FLC addressing (Fig.5):

$$\delta V \leq |V_{sh}| \leq \frac{1}{2} V_c - \delta V \quad (8)$$

or

$$1 \leq \frac{|V_{sh}|}{\delta V} \leq \frac{V_c}{2\delta V} - 1 \quad (9)$$

Addressing of gray scale levels under conditions (8) and (9) is illustrated in Fig. 6 for the same FLC display cell and the same electric field frequency $f=50\text{Hz}$, which was used for measuring of the loop shown in Figure 5.

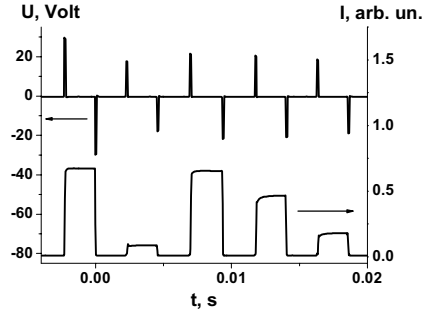


Figure 6. Electrooptical response of 5.2 μm asymmetric FLC-497, $L_{SD-1} = 9$ nm, the frequency of the triangular voltage $f=50\text{Hz}$; to provide the hysteresis free gray scale levels when the voltage amplitude varies from $\pm 18\text{V}$ to $\pm 30\text{V}$, $T=23^\circ\text{C}$.

Therefore, the relative intensity of the memorized gray levels in Fig. 6 exactly corresponds to the light transmission levels selected from the right branch of the hysteresis loop shown in Fig. 5.

An origin of the hysteresis loop center shift, which takes place really in experiments (Fig. 5) due to asymmetric boundary conditions, is straightforward and will be published elsewhere.

Potential of applications

The main potential of applications is memorizing of images possessing gray scale levels for unlimited time after the driving voltage switching off. A simple display device based on 64'64 and 33'33mm² photo-aligned FLC display matrix was made according to principles discussed above to illustrate this idea (Fig.7). As seen from Fig. 7 below any gray scale can be memorized. The display matrix has dimensions of 33'33mm², and the FLC layer thickness is (5.2 \pm 0.2)mm. The display device operates with the frame frequency

30 Hz (at $V_{\text{row}} = \pm 18\text{V}$, $V_{\text{col}} = \pm 9\text{V}$, $T = 23^\circ\text{C}$) generating a continuous gray scale, which can be memorized for more than 10 days after the driving voltage is switched off.

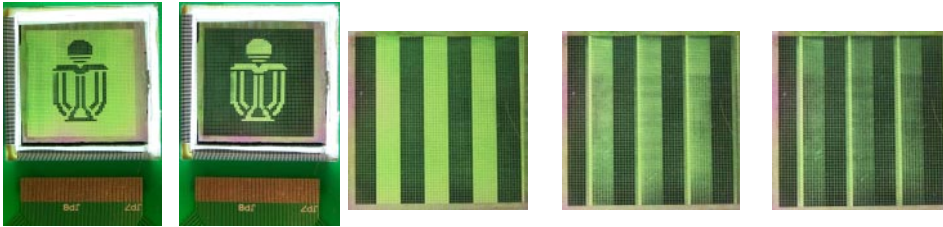


Figure 7. Left: 64'64 and 33'33mm² photo-aligned FLC display matrix. Left – the reference state of the 64'64 photo-aligned FLC is bright, right – the reference state is dark. Right: memorization of the gray scale in FLC display. All photos made 10 days after the power supply was switched off.

Conclusion

A passively addressed 64x64 ferroelectric liquid crystal display (FLCD) has been developed. A new criterion for FLC bistable switching was proposed based on FLC hysteretic behavior dependently on boundary conditions and temperature. An origin of FLC gray scale was discussed and a new way for the generation of the FLC gray scale was demonstrated. Criteria of steady and hysteretic free gray scale addressing are derived. The passive matrix addressed FLC display with a memorized gray scale was shown.

References

1. A. L. Andreev I. N. Kompanets, E. P. Pozhidaev, *Proc. SPIE*, 2771, 289-292, (1996).
2. E. P. Pozhidaev, A. L. Andreev, I. N. Kompanets. *Proc. of 7th Int. Conf. on FLCs*, pp. 164-165, (1999).
3. A.Z. Rabinovich, M.V. Loseva, N.I. Chernova, E.P. Pozhidaev, O.S. Petrashevich, J.S. Narkevich, *Liq. Cryst.*, 6(5), 533-543 (1989).
4. K. H. Yang, T. C. Chieu, *Jpn. J. Appl. Phys.*, 28, N°9, L1599- L1601, (1989).
5. D.D. Huang, E.P. Pozhidaev, V.G. Chigrinov, H.L. Cheung, Y.L. Ho, H.S. Kwok, *Displays*, 25, pp.21-29 (2004).
6. V. Chigrinov, H.-S. Kwok, D. Yakovlev, G. Simonenko, V. Tsoi, *J. of SID*, 12, pp.183-187 (2004).
7. E. P. Pozhidaev, V. G. Chigrinov, Yu. P. Panarin, V. P. Vorflusev, *Mol. Mat.*, 2, 255-238, (1993).
8. L. A. Beresnev, Ì. Pfiherr, W. Haase, Ì. V. Loseva, N. I. Chernova, P. V. Adomenas, , *Pisma v JETF*, 53, pp. 170-175, (1991).
9. T. Harada et al. *SID'85 Digest*, 131 (1985).

Approximation of dynamic hysteresis characteristics of a ChLC

A. Rybalochka, M. Chumachkova, M. Minyaylo, V. Sorokin

Institute of Semiconductor Physics, NASU, Kyiv, Ukraine

Abstract

In this paper we propose a method for an approximation of dynamic hysteresis volt-brightness characteristics of a cholesteric liquid crystal (ChLC). We have considered dynamic hysteresis characteristics that demonstrate response of a ChLC to the bias voltage pulse from the initial homeotropic and planar states. Our method allows to obtain all necessary approximated dynamic hysteresis characteristics through the experimental measuring only of six special electro-optical characteristics. Moreover for an approximation there is no need to know any other physical and electro-optical properties of a ChLC. Accuracy of proposed method is estimated by the comparison of volt-contrast characteristics of a ChLC obtained both by experimental measuring and proposed method of an approximation.

Introduction

Cholesteric materials have three main states: planar (P), focal conic (FC), and homeotropic (H). The planar and focal conic states are stable in case of zero external electric and magnetic fields. In the planar state the helical axes are parallel to the display cell surface normal direction. The planar state of a ChLC Bragg reflects a light. Therefore display's pixels with a ChLC in the planar state look bright [1]. In the focal conic state the helical axes are distributed almost chaotically. A ChLC in this state becomes slightly diffusely scattered. The value of scattered light power in this case is much lower than Bragg reflection of the planar state and that is why the ChLC cell with absorbed background seems dark when ChLC is in the focal conic state. Thus image on bistable ChLCD is formed by pixels with the planar and the focal conic states of a ChLC. Moreover, it is necessary to note that both the planar and the focal conic domains can be contained in the same pixel simultaneously. Reflectance of such pixel has an intermediate value. Gray scale operations for ChLCDs where such states are stable for a long time can be implemented [2-3]. In the homeotropic state helical structure in distribution of liquid crystal molecules is absent and all molecules of a ChLC are aligned along one direction. This direction (for a ChLC with $\Delta\epsilon > 0$) coincides with the direction of the external electric field. The transition of a ChLC to the homeotropic state can be achieved by applying external electric field that exceeds the threshold value E_C [4].

To rewrite the information on ChLCDs transitions between the planar and the focal conic states in pixels must be performed. A low voltage pulse can transform the planar state into the focal conic state. The value of electric field for this transition is always less than the threshold value E_C .

The transition of a ChLC from the focal conic state to the planar state is more complicated. Firstly, the transition to the homeotropic state must be performed. As the homeotropic state is unstable ChLC transforms into the planar state when external electric field is turned off quickly. It was studied that the transition of a ChLC from the homeotropic state to the stable planar state occurs through the transient planar state (P^*) [4]. The homeotropic-transient planar transition is very short. Investigation of this transition and its application in driving ideology for ChLCD allow to create dynamic drive schemes with addressing speed of about millisecond per row [5-7]. If the electric field is turned off slowly a ChLC transforms from the homeotropic state into the stable focal conic state. Thus from the homeotropic state a ChLC can be addressed both in the planar and the focal conic states.

Cholesteric material can be addressed in different stable states by the same voltage pulse depending on its initial state. For the fixed pulse duration there is a voltage range in which the field-induced homeotropic state is held and the planar, the focal conic and the transient planar states are addressed into the focal conic state. Such behavior demonstrates hysteresis properties of a ChLC that are widely used in the addressing of ChLCDs [7-8].

To choose a ChLC material for cholesteric displays a number of technical parameters of a display cell must be taken into account. There are the display cell gap, the deviation of the display cell gap on the whole area of a display cell, maximal driving voltage, an information content of a display (for passive matrix addressing – a number of rows of a display) and so on. The temperature condition of using of a ChLCD, an addressing method and necessary addressing speed are also important parameters for a determination of requirements to a ChLC material. Thus for the determination of all parameters and characteristics necessary for the correct choice of a ChLC material for a ChLCD a profound experimental study of physical properties and electro-optical characteristics of a ChLC must be performed. Therefore a search of ways for a decreasing of the duration of such experimental study is a very actual and important problem.

In this work we demonstrate the method of an approximation of electro-optical dynamic hysteresis characteristics of a ChLC that describe its behavior at transitions from the initial stable planar state and from the field induced homeotropic state [9-11]. This method is based on experimental measurement of six special electro-optical characteristics of a cholesteric material. All necessary parameters for modeling of hysteresis characteristics are obtained only from these characteristics and knowledge of values of different physical parameters of a ChLC is not necessary. Also the comparison of volt-contrast characteristics of a ChLC that were obtained both by experimental measuring and theoretical approximation are presented.

We performed all our measurements on the display cell filled with the liquid crystal mixture BL126 (Merck), cell thickness $d=4,4 \mu\text{m}$ at room temperature. Display Measuring System SV-200 was used for measuring of all experimental characteristics.

Experiment

For measuring of electro-optical characteristics that describe electro-optical response of the ChLC to voltage pulses from the field induced homeotropic state and the stable planar state we used the sequences of voltage pulses with the waveform that is demonstrated on Fig. 1.

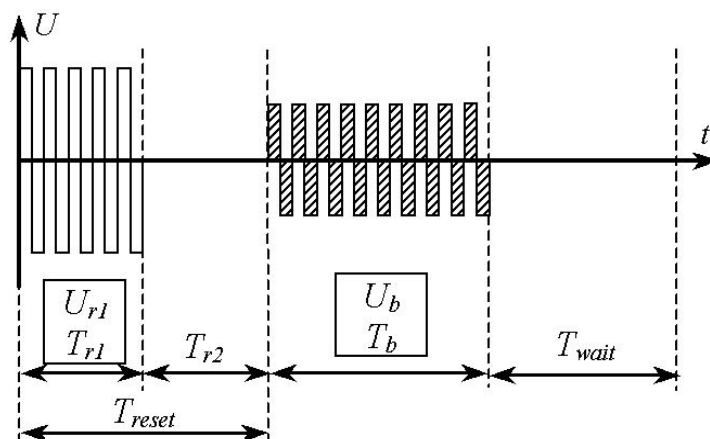


Figure 1. The voltage waveform for measuring of the electro-optical response of a ChLC.

For the measuring of “H-characteristics” (electro-optical characteristics that describe electro-optical response of the ChLC to voltage pulses from the initial homeotropic state) at the beginning a high voltage $U_{r1}=50V$ is applied to the display cell during the time $T_{r1}=1s$ to transform the ChLC into the homeotropic state irrespective of its initial state. Then the bias voltage pulse (U_b, T_b) is applied for studying of the response of the cholesteric material (at the measuring of “H-characteristics” $T_{r2}=0s$). The final reflectance of the ChLC is measured in two seconds ($T_{wait}=2s$) after the bias pulse at the absence of external field ($U_{wait}=0V$) when the reflectance no changes more with time. Ten “H-characteristics” for $T_b=0.05s, 0.1s, 0.2s, 0.3s, 0.5s, 0.7s, 1s, 3s, 5s$ and $10s$ have been measured. On Fig. 2 five ones are presented. Also analogous ten “P-characteristics” (electro-optical characteristics that describe electro-optical response of the ChLC to voltage pulses from the initial stable planar state) with $T_b=0.05s, 0.1s, 0.2s, 0.3s, 0.5s, 0.7s, 1s, 3s, 5s$ and $10s$ have been measured. At the measuring of “P-characteristics” in the waveform on Fig.1 time interval $T_{r2}=2s$. Thus during the reset time interval $T_{reset}=T_{r1}+T_{r2}$ the ChLC is transformed into the stable planar state before the bias pulse irrespective of its initial state. On Fig. 3 “P-characteristics” for $T_b=0.1s, 0.5s, 1s, 3s$ and $10s$ are presented.

Further the method for modeling of “H-characteristics” and “P-characteristics” and possibilities of approximation of dependences for some critical and threshold voltages will be presented.

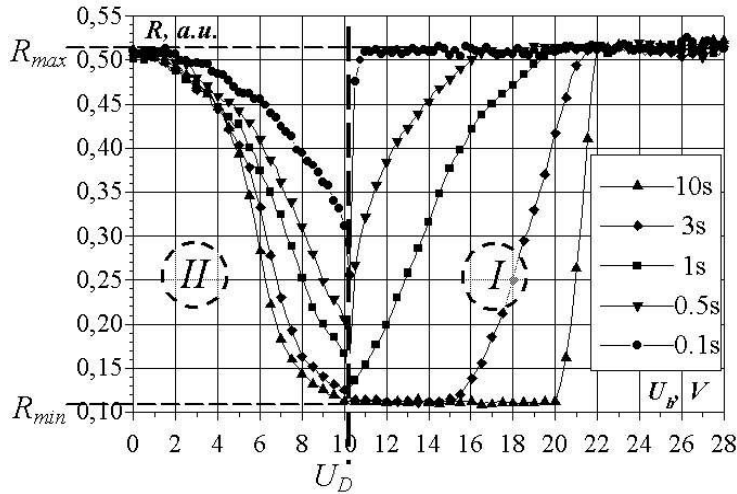


Figure 2. Experimental “H-characteristics”.

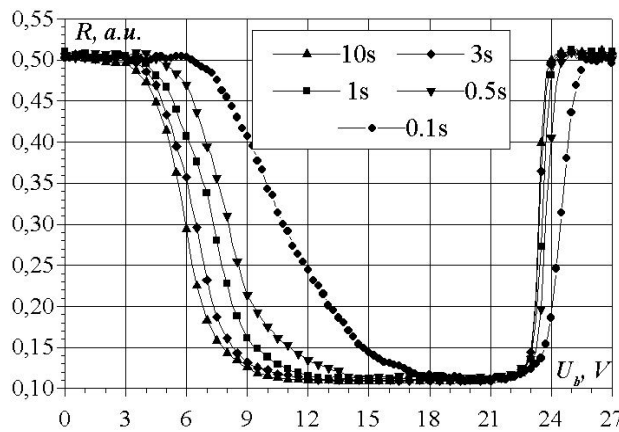


Figure 3. Experimental “P-characteristics”.

Modeling of “H-characteristics”

The stable state of a ChLC in display cell is a complicate domain structure with different preferred direction of orientation of helical axes in each domain. The stabilized reflectance of a display cell depends on a distribution of such domains relative to the cell surface normal direction. Determination of the real domain distribution is enough difficult problem. Let’s consider a simple model in wich we have assumed that the stable cholesteric state consists of the two type of domains: the “planar” domains where helical axes are strongly parallel and the “focal conic” domains where helical axes are strongly perpendicular to the display cell surface normal direction. It is possible to define through the parameter ν the part of the “planar” domains in a

stable state of a ChLC ($0 \leq \nu \leq 1$). So the reflectivity (R) of a stable state of a ChLC can be determined through the parameter ν in the following equation:

$$R(\nu) = R_{\min} + (R_{\max} - R_{\min}) \times \nu \quad (1)$$

where R_{\min} and R_{\max} are reflectivity of the focal conic and the planar states correspondingly. However an approximation of electro-optical characteristics of a ChLC by formula (1) is very simplified. Therefore on the basis of behavior of curves on the Fig.2, we propose the following dependence $R(T_b, \nu)$ that afterwards has given good concurrence of experimental and theoretical “H-characteristics”:

$$R(T_b, \nu) = R_{\min}(T_b) + (R_{\max} - R_{\min}(T_b)) \times \sin\left(\frac{\pi}{2} \times \nu\right) \quad (2)$$

where $R_{\min}(T_b)$ is a dependence of a minimal reflectivity of the focal conic state vs. the duration of the bias voltage pulse – T_b . The dependence $R_{\min}(T_b)$ is shown on Fig.4. From Fig.4 we can see that the point on this curve at $T_b = T_{FC}$ – is the point of a change of distinctive behavior of the curve $R_{\min}(T_b)$. At $T_b > T_{FC}$ the value of $R_{\min}(T_b) \approx R_{\min}$ practically does not vary, and at $T_b < T_{FC}$ the value of $R_{\min}(T_b)$ sharply increase up to R_{\max} at $T_b = 0$. The physical sense of the parameter T_{FC} can be formulated as follows: T_{FC} – is the minimal duration of the voltage pulse that address a ChLC in a display cell from the field induced homeotropic state to the stable focal conic state with the minimal reflectivity R_{\min} .

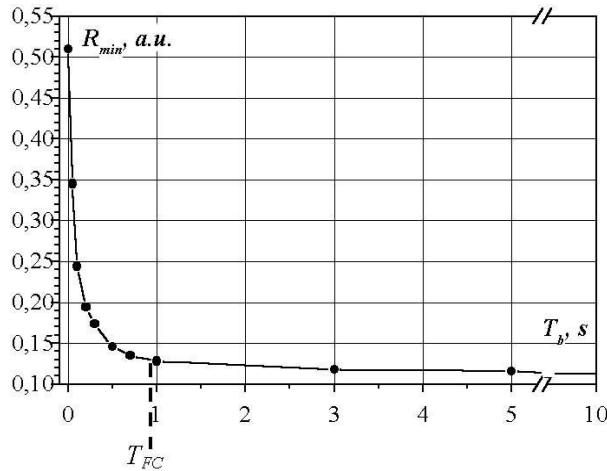


Figure 4. The experimental dependence $R_{\min}(T_b)$.

Each experimental curve on Fig.2 and our model distribution of the “planar” and the “focal conic” domains can be presented as it is shown on Fig.5 and Fig.6 (Fig.5 – for characteristics that have been measured at $T_b > T_{FC}$ and Fig.6 – at $T_b < T_{FC}$). For each curves on Fig.5 and Fig.6 four threshold voltages can be determined: U_h^c , U_{h-fc}^{max} , U_{h-fc}^{min} and U_{h-p} . The voltage U_h^c is the minimal

voltage that holds the field induced homeotropic state of a ChLC in the display cell during the bias time T_b . The voltages U_{h-fc}^{max} and U_{h-fc}^{min} – are the maximal and the minimal voltages that address the cholesteric material from the homeotropic state into the focal conic state with the minimal reflectivity. And the voltage U_{h-p} is the maximal voltage that doesn't hinder for transformation of a ChLC from the homeotropic state to the stable planar state with the maximal reflectivity.

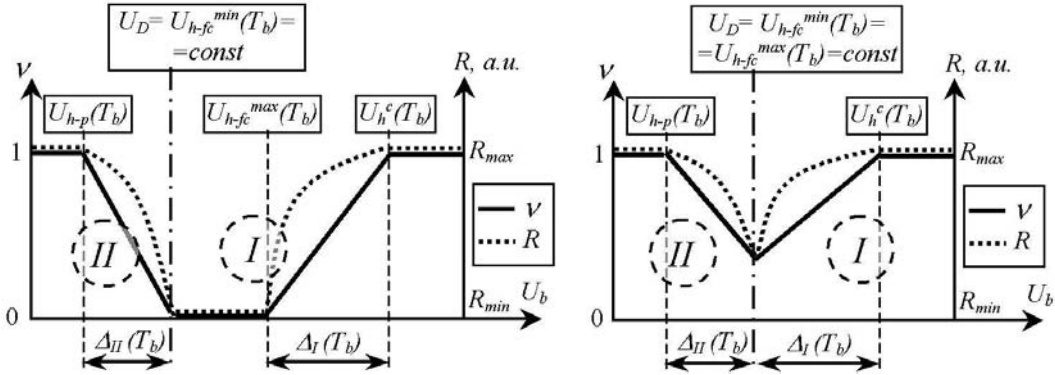


Figure 5 (left). Schematic form of experimental curves and model distribution of domains for “H-characteristics” at $T_b > T_{FC}$.

Figure 6 (right). Schematic form of experimental curves and model distribution of domains for “H-characteristics” at $T_b < T_{FC}$.

There are two ranges of changing of the voltage U_b where the electro-optical curves on Fig.2 have distinctive behavior: the first range «I» – is $U_b > U_D$ and the second range «II» – is $0 < U_b < U_D$ (see Figures 2, 5 and 6), where the voltage U_D can be determined as the minimal amplitude of a voltage pulse that can address a ChLC from the homeotropic state to the stable focal conic state with the minimal reflectivity.

For all curves on Fig.2 in both ranges there are stable states of a ChLC with the equal values of reflectivity from $R_{min}(T_b)$ to R_{max} . These states in our model have the same domain distribution and differ only in a sequence of textural transitions of a ChLC during applying of the voltage waveform from Fig.1 to the display cell. In the first range «I», the «planar» domains are formed after the end of the action of the bias voltage. In these domains at the end of the bias time a ChLC is in the homeotropic state and after removal of the bias voltage it transforms through the transient planar state to the stable planar state. In the “focal conic” domains a ChLC begins to transform into the focal conic state during the bias time and after removal of the bias voltage the stable focal conic state are formed. In the second range «II», the «planar» domains begin to form at once after the end of the reset time already during the action of the bias voltage. In the “focal conic” domains a presence of the bias voltage pulse prevents the transition of a ChLC from the homeotropic state to the transient planar state and the final focal conic state is formed.

As we can see from formula (2) for the approximation of electro-optical characteristics of a ChLC it is necessary to set the value of the maximal reflectivity R_{max} , the dependence of the minimal reflectivity vs. the bias time $R_{min}(T_b)$ and to lay down the law of a change of the parameter v as a function from two variables (first – is the bias voltage U_b and the second – is the bias time T_b): $v = F(U_b, T_b)$. The maximal reflectivity R_{max} and the dependence of the minimal reflectivity vs. the bias time $R_{min}(T_b)$ can be easily measured. In our case $R_{max} = 0.51$ and the dependence $R_{min}(T_b)$ is shown on Fig.4. Ways of determination of the function $v = F(U_b, T_b)$ for the range "I" (v_I) and for the range "II" (v_{II}) will be discussed below.

In the range "I" the parameter v_I is determined in the following:

$$v_I(U_b, T_b) = \begin{cases} 0, U_b \leq U_{h-fc}^{max}(T_b) \\ \frac{U_b - U_{h-fc}^{max}(T_b)}{\Delta_I(T_b)}, U_{h-fc}^{max}(T_b) \leq U_b \leq U_h^c(T_b) \\ 1, U_b \geq U_h^c(T_b) \end{cases} \quad (3)$$

where $\Delta_I(T_b) = U_h^c(T_b) - U_{h-fc}^{max}(T_b)$. For definition of the parameter v_I at any values of U_b and T_b it is necessary to lay down laws of a change of functions $U_h^c(T_b)$ and $U_{h-fc}^{max}(T_b)$ or $U_h^c(T_b)$ and $\Delta_I(T_b)$. On Fig.7 dependencies $U_h^c(T_b)$, $U_{h-fc}^{max}(T_b)$ and $\Delta_I(T_b)$ that have been obtained from experimental curves are presented.

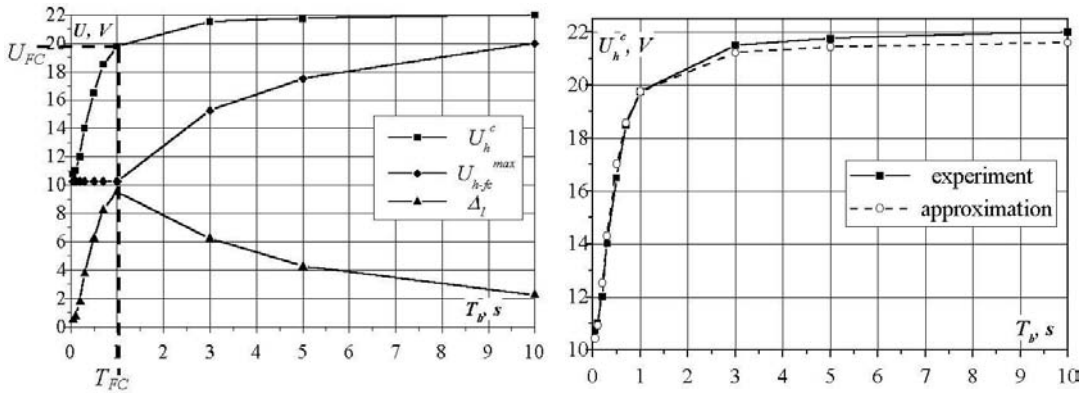


Figure 7 (left). Experimental dependencies $U_h^c(T_b)$, $U_{h-fc}^{max}(T_b)$ and $\Delta_I(T_b)$
Figure 8 (right). Experimental and approximated dependencies of the voltage U_h^c vs. the bias time T_b .

As we can see from Fig.7 at the $T_b > T_{FC}$ the value of the voltage U_h^c practically does not change and can be approximated by linear dependence with the small constant of proportionality. At the $0 < T_b < T_{FC}$ the change of the function $U_h^c(T_b)$ have explicitly nonlinear character. Such behavior of the function $U_h^c(T_b)$ be mathematically approximated in the following:

$$U_h^c(T_b) = U_h^{c(ST)} - \frac{U_h^{c(ST)} - U_D}{1 + a_1 \times \ln \left[1 + \left(\frac{T_b}{T_{FC}} \right)^2 \right]} \quad (4)$$

where $U_h^{c(ST)} = U_h^c(\infty)$ and a_1 – is a coefficient. The coefficient a_1 probably can be determined through the physical parameters of a cholesteric material. But in this paper this possibility is not considered. Here we determine this coefficient directly from formula (4) using experimental data from Fig.7 (curve U_h^c). We suppose that $U_h^{c(ST)} = U_h^c(10s) = 22.0V$. From Fig.2 we determine the value of the voltage level $U_D = 10.25V$. Also from Fig.7 we determine the value of the voltage level U_h^c at $T_{FC} = 1s$: $U_h^c(1s) = 19.75V$. Substituting these data in the formula (4) we determine the value of the coefficient $a_1 = 6.1$. On Fig.8 the experimental and approximated by formula (4) dependencies of the voltage level U_h^c vs. the bias time T_b are presented. The dependence $U_{h-fc}^{max}(T_b)$ can be approximated by the next way:

$$U_{h-fc}^{max}(T_b) = \begin{cases} U_D, T_b \leq T_{FC} \\ U_D + a_2 \times \ln \left(\frac{T_b}{T_{FC}} \right), T_b \geq T_{FC} \end{cases} \quad (5)$$

where a_2 – is a coefficient. The coefficient a_2 as well as the coefficient a_1 can be determined directly from the formula (5). Substituting to this formula the value of the voltage level $U_{h-fc}^{max}(3s) = 15.25V$ at $T_b = 3s$ we determine the value of the coefficient $a_2 = 4.5$. On Fig.9 the experimental and approximated by formula (5) dependencies of the voltage U_{h-fc}^{max} vs. the bias time T_b are presented. The experimental and approximated dependencies of the parameter $\Delta_I(T_b) = U_h^c(T_b) - U_{h-fc}^{max}(T_b)$ are presented on Fig.10. Substituting approximated dependencies $\Delta_I(T_b)$ and $U_{h-fc}^{max}(T_b)$ in the formula (3) we obtain the final equation for the parameter $v_I(U_b, T_b)$. Using this equation and the formula (2) approximated electro-optical characteristics of the ChLC in the range «I» can be obtained.

In the range "II" the parameter v_{II} is determined in the following:

$$v_{II}(U_b, T_b) = \begin{cases} 1, U_b \leq U_{h-p}(T_b) \\ \frac{U_D - U_b}{\Delta_{II}(T_b)}, U_{h-p}(T_b) \leq U_b \leq U_D \end{cases} \quad (6)$$

where $\Delta_{II}(T_b) = U_{h-fc}^{\min}(T_b) - U_{h-p}(T_b) = U_D - U_{h-p}(T_b)$.

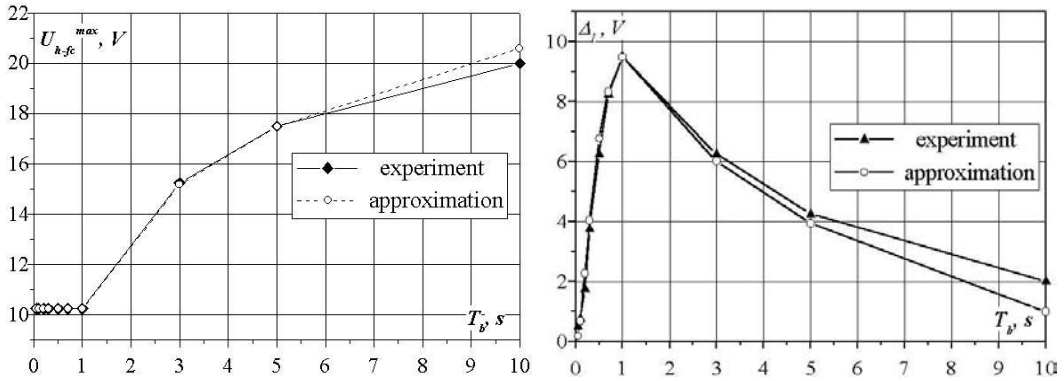


Figure 9 (left). Experimental and approximated dependencies of the voltage

U_{h-fc}^{\max} vs. the bias time T_b .

Figure 10 (right). Experimental and approximated dependencies of the parameter Δ_I vs. the bias time T_b .

Determination of $U_{h-p}(T_b) = \text{const} = 1,5\text{V}$ (see Fig.2) means that $\Delta_{II}(T_b) = \text{const} = 8,75\text{V}$ (see Fig.5). Substituting values of the parameter Δ_{II} and the voltage levels U_D and U_{h-p} to the formula (6) we obtain the final equation for the parameter $v_{II}(U_b, T_b)$. Using this equation and the formula (2) approximated electro-optical characteristics of the ChLC in the range "II" can be obtained. Five approximated "H-characteristics" are presented on Fig.11.

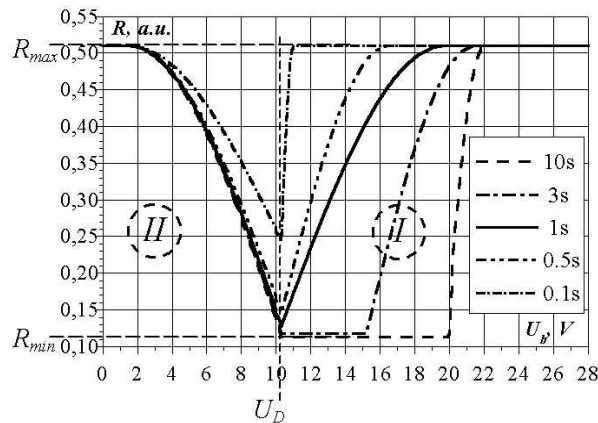


Figure 11. Approximated "H-characteristics".

Comparison of electro-optical characteristics on Fig.2 and Fig.11 shows that proposed method for modeling of "H-characteristics" gives good coinci-

dence of experiment and modeling. Some difference in experimental and modeling dependencies is explained by simplicity of presented method. For more correct coincidence the more complex model dependence of the reflectivity vs. the parameter v is needed. At the same time the curves on Figures 8, 9 and 10 demonstrate successful selection of functions approximation of threshold voltage dependencies $U_h^c(T_b)$ and $U_{h-fc}^{\max}(T_b)$.

Modeling of "P-characteristics"

Now we present implementation of proposed above method for modeling of "P-characteristics". We propose the following dependency $R(v)$ that gives good coincidence of experimental and theoretical "P-characteristics":

$$R(v) = R_{\min} + (R_{\max} - R_{\min}) \times \sin^2\left(\frac{\pi}{2} \times v\right) \quad (7)$$

Each experimental curve on Fig.3 and model distribution of the "planar" and the "focal conic" domains for it can be presented as it is shown on Fig.12. For each curve on Fig.3 and Fig.12 several threshold voltages can be determined: U_p^c , U_{p-fc}^{\max} , U_{p-fc}^{\min} and U_{p-p} . The voltage U_p^c is the threshold (critical) voltage that transforms a ChLC into the homeotropic state during the bias time T_b . The voltages U_{p-fc}^{\max} and U_{p-fc}^{\min} are the maximal and the minimal voltages that address the cholesteric material from the stable planar state into the final stable focal conic state with the minimal reflectance. And finally, the voltage U_{p-p} – is the maximal voltage that does not change reflectance from the stable planar state of a ChLC during the bias time T_b .

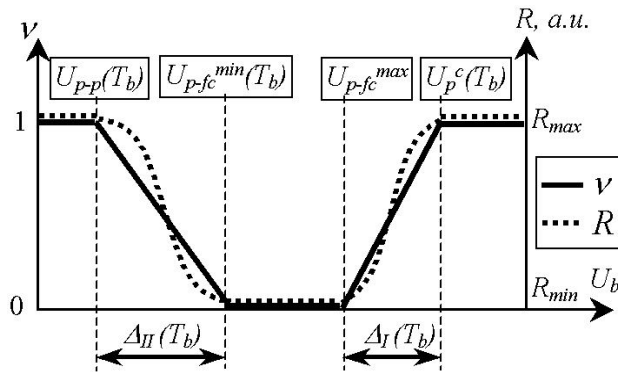


Figure 12. Schematic form of experimental curves and model distribution of domains for "P-characteristics".

As we can see from formula (7) for the approximation of "P-characteristics" of a ChLC it is necessary to set the value of the maximal reflectance R_{\max} , the minimal reflectance R_{\min} and the law of a change of the parameter v . The values of R_{\max} and R_{\min} can be easily determined from the experimental data on Fig.3: $R_{\max} = 0.51$ and $R_{\min} = 0.11$. As it was noted at considering of "H-

characteristics”, here also for each curve on Fig.3 there are two ranges of voltage U_b where reflectance is changing from R_{max} and R_{min} : in the range $\Delta_I(T_b) = U_p^c(T_b) - U_{p-fc}^{max}(T_b)$ reflectance increases from R_{min} to R_{max} and in the range $\Delta_{II}(T_b) = U_{p-fc}^{min}(T_b) - U_{p-p}(T_b)$ reflectance decreases from R_{max} to R_{min} with increasing of the voltage U_b . In order to define the parameter v as a function $v = F(U_b, T_b)$ following dependencies must be determined (see Fig.12): $U_p^c(T_b)$, $U_{p-fc}^{max}(T_b)$, $U_{p-fc}^{min}(T_b)$ and $U_{p-p}(T_b)$.

Then the function $v = F(U_b, T_b)$ can be expressed in the following:

$$v(U_b, T_b) = \begin{cases} 1, 0 \leq U_b \leq U_{p-p}(T_b) \\ \frac{U_{p-fc}^{min}(T_b) - U_b}{\Delta_{II}(T_b)}, U_{p-p}(T_b) \leq U_b \leq U_{p-fc}^{min}(T_b) \\ 0, U_{p-fc}^{min}(T_b) \leq U_b \leq U_{p-fc}^{max}(T_b) \\ \frac{U_b - U_{p-fc}^{max}(T_b)}{\Delta_I(T_b)}, U_{p-fc}^{max}(T_b) \leq U_b \leq U_p^c(T_b) \\ 1, U_b \geq U_p^c(T_b) \end{cases} \quad (8)$$

As we can see from Fig.3 and Fig.12 for each “P-characteristics” there are two states of a ChLC with the equal reflectance between R_{min} and R_{max} – the first in the range Δ_I and the second in the range Δ_{II} . These states in our model have the analogous domain distribution and differ only in a sequence of textural transitions of a ChLC during applying of the driving pulses. In the ranges Δ_I and Δ_{II} the “focal conic” domains are formed by reorientation of the initial «planar» domains during the bias time by the voltage U_b . These ranges differ in the formation of the final “planar” domains. In the range Δ_I the planar state in the «planar» domains is formed from the homeotropic state of a ChLC when the bias voltage is turned off. The «planar» domains in the range Δ_{II} are the initial “planar” domains that do not reorient by the bias voltage.

In order to define the parameter v in the range Δ_I it is necessary to know the behavior of functions $U_{p-fc}^{max}(T_b)$ and $U_p^c(T_b)$ (see from formula (7)). It is possible to suppose that $U_{p-fc}^{max}(T_b) = \text{const} = 22,8\text{V}$ (see Fig.3). Experimental and approximated dependencies $U_p^c(T_b)$ are presented on Fig.13. We approximate the function $U_p^c(T_b)$ in the following:

$$U_p^c(T_b) = U_p^{c(ST)} \times \left[1 + a_3 \times \left(\sqrt{1 + \frac{T^*}{T_b}} - 1 \right) \right] \quad (9)$$

where $U_p^{c(ST)} = U_p^c(\infty)$, a_3 - is a coefficient and T^* - is some characteristic time that we set to be equal to the characteristic time for this ChLC: $T^* = T_{FC}$

=1s. The coefficient a_3 can be determined directly from the formula (9) using experimental data from Fig.13 (curve U_p^c). From the experimental curve U_p^c we can determine $U_p^{c(ST)} = U_p^c(10s) = 23.8V$ and $U_p^c(1s) = 24.15V$. Substituting these data in the formula (9) we obtain the value of the coefficient $a_3 = 0.84$. In the range Δ_{II} in order to define the parameter ν it is necessary to know behavior of functions $U_{p-fc}^{\min}(T_b)$, $U_{p-p}(T_b)$ and $\Delta_{II}(T_b)$. On Fig.14 experimental and approximated dependences $U_{p-fc}^{\min}(T_b)$, $U_{p-p}(T_b)$ and $\Delta_{II}(T_b)$ are presented.

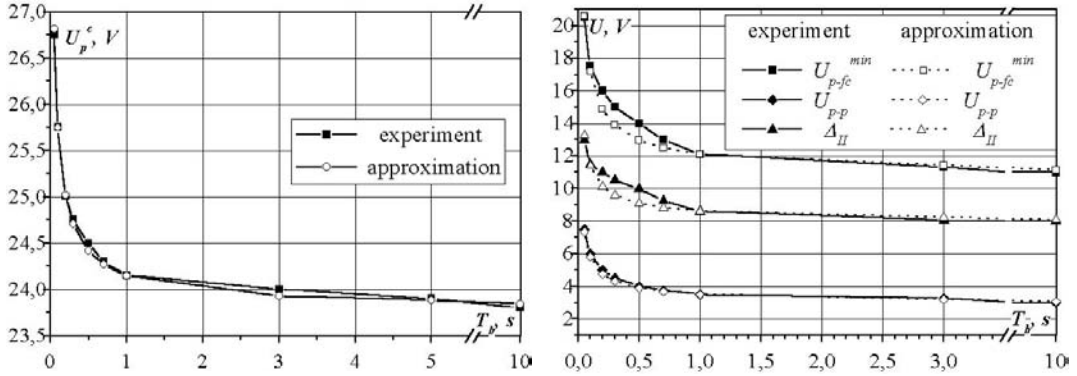


Figure 13 (left). Experimental and approximated dependencies of the voltage U_p^c vs. the duration of the bias pulse T_b .

Figure 14 (left). Experimental and approximated dependencies of voltages U_{p-fc}^{\min} , U_{p-p} and the voltage range Δ_{II} vs. the duration of bias pulse T_b .

We approximate functions $U_{p-fc}^{\min}(T_b)$ and $U_{p-p}(T_b)$ by expressions similar to presented earlier in formula (9):

$$U_{p-fc}^{\min}(T_b) = U_{p-fc}^{\min(ST)} \times \left[1 + a_4 \times \left(\sqrt{1 + \frac{T_{FC}}{T_b}} - 1 \right) \right] \quad (10)$$

$$U_{p-p}(T_b) = U_{p-p}^{(ST)} \times \left[1 + a_5 \times \left(\sqrt{1 + \frac{T_{FC}}{T_b}} - 1 \right) \right] \quad (11)$$

where $U_{p-fc}^{\min(ST)}$ – is the minimal voltage that address the cholesteric material from the stable planar state into the final stable focal conic state with the minimal reflectance during the bias pulse with $T_b = 10s$, $U_{p-p}^{(ST)}$ – is the maximal voltage level that does not change reflectance of the stable planar state of a ChLC during the bias pulse with $T_b = 10s$, a_4 and a_5 – are coefficients. Coefficients a_4 and a_5 can be determined directly from the formulas (10) and (11) using experimental data from Fig.14 (curves U_{p-fc}^{\min} and U_{p-p}): $a_4 = 2.68$ and $a_5 = 1.21$.

Substituting functions $U_p^c(T_b)$, $U_{p-fc}^{\min}(T_b)$, $U_{p-p}(T_b)$ and $U_{p-fc}^{\max}(T_b) = 22,8V$ in formula (8) we can obtain the final expression for $v = F(U_b, T_b)$. Substituting this expression in formula (7), we get the final expression for reflectance vs. the duration of the bias pulse: $R(T_b)$. Five approximated "P-characteristics" for different values of the bias pulse duration T_b are presented on Fig.15.

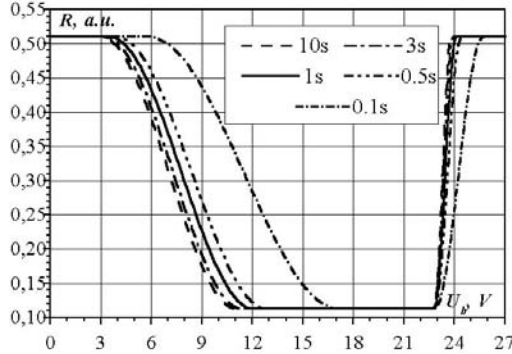


Figure 15. Approximated "P-characteristics".

Results and Discussion

And now we present results of our comparison of experimental and approximated electro-optical hysteresis characteristics of a ChLC. First we consider together one "P-characteristic" and one "H-characteristic" that were obtained at the same bias pulse duration, for example at $T_b=300ms$ (see Fig.16). The curves "0,3s-P" and "0,3s-H" show responses of the ChLC to the bias voltage pulse from the planar and the homeotropic states, correspondingly.

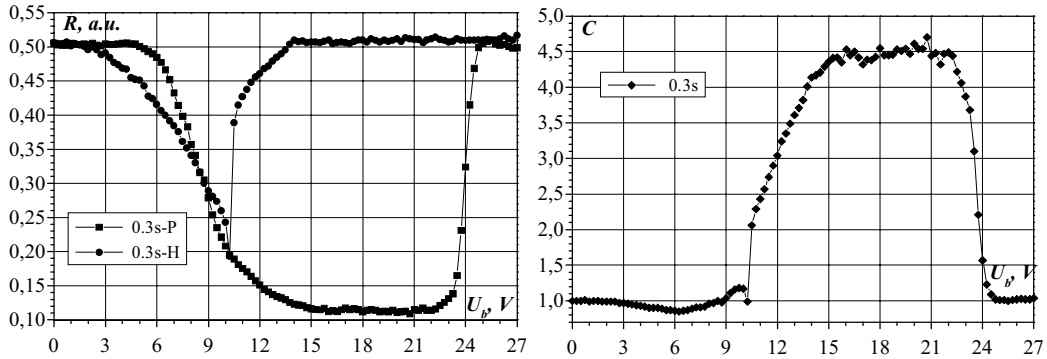


Fig.16 (left). Dynamic hysteresis volt-brightness characteristics of the ChLC.
Fig.17 (right). Volt-contrast characteristics of the ChLC.

For certain durations of bias voltage pulse there is the range of voltage U_b where the field induced homeotropic state is held and the planar state are addressed into the focal conic state. Such behavior of the electro-optical

characteristics of the cholesteric display cell demonstrates the hysteresis properties of a ChLC. Analogous dynamic hysteresis characteristic can be obtained for any others values of the parameter T_b . Also volt-contrast curves as a ratio of the data from "...-H"-curves to the data from the corresponding "...-P"-curves were obtained. The example of such volt-contrast curve is presented on Fig.17. This way we can obtain volt-contrast characteristics of a ChLC from experimental and approximated "P-characteristics" and "H-characteristics". On Fig.18 and Fig.19 such experimental and approximated volt-contrast characteristics of the ChLC are presented.

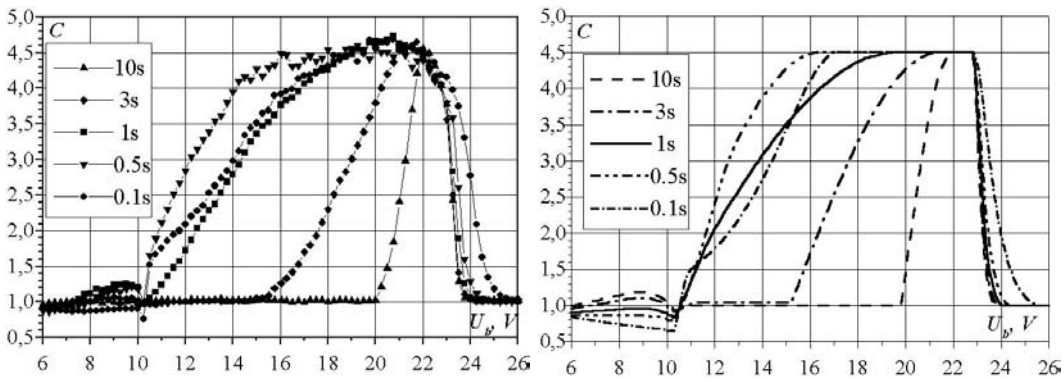


Figure 18(left). Experimental volt-contrast characteristics of the ChLC.
Figure 19(right). Approximated volt-contrast characteristics of the ChLC.

The comparison of these characteristics is carried out by calculations for each volt-contrast curve of the voltage range (ΔU) where contrast has a value not less than $P_1=4,2:1$ and $P_2=3,5:1$ (see Fig.20).

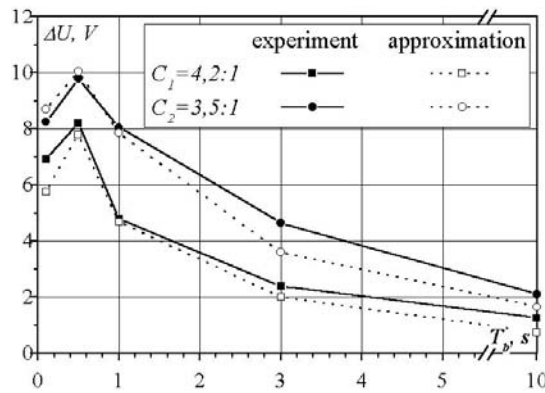


Figure 20. ΔU vs. T_b for experimental and approximated volt-contrast characteristics.

This comparison shows quite good coincidence of these voltage ranges both for experimental and approximated volt-contrast characteristics. It means that proposed simple method for the approximation of electro-optical

characteristics of a ChLC can be effectively used for the analysis of electro-optical hysteresis properties of a ChLC.

As a result for modeling of electro-optical volt-brightness and volt-contrast characteristics of a ChLC that describe its behavior at transition from initial homeotropic and planar states we need to measure the six electro-optical characteristics. Four electro-optical characteristics we need for modeling of "H-characteristics":

1. The measuring of the quasi-static electro-optical response of a cholesteric display cell from the initial homeotropic state. In this case the sequence of voltage pulses with the voltage waveform from Fig.1 with $T_2=0s$ and $T_b>10s$ is used. As a result from this characteristic we obtain the next parameters: $R_{min}^{(ST)} = R_{min}(\text{¥})$, R_{max} , $U_{h-fc}^{max(ST)}$, U_{h-p} and U_D .

2. The measuring of the dependence $R_{min}(T_b)$. For this measuring also the sequence of voltage pulses with the voltage waveform from Fig.1 is used. But in this case the bias voltage level is fixed ($U_b=U_D$) and the bias pulse duration is changed. As a result we obtain the experimental dependence $R_{min}(T_b)$ and the value of the parameter T_{FC} .

3. The measuring of the electro-optical response of a cholesteric display cell as in point 1 with $T_b=T_{FC}$. This dependence is necessary for determination of the coefficient a_1 by formula (4).

4. The measuring of the electro-optical response of a cholesteric display cell as in point 1 with $T_b>T_{FC}$. This dependence is necessary for determination of the coefficient a_2 by formula (5).

For modeling of "P-characteristics" and volt-contrast characteristics we need to measure two electro-optical characteristics additionally to four ones that had been measured at the modeling of "H-characteristics":

5. The measuring of the quasi-static electro-optical response of a ChLC from the initial planar state. In this case the sequence of voltage pulses with the voltage waveform from Fig.1 with $T_2=2s$ and $T_b>10s$ must be used. As a result from this characteristic we obtain the next parameters: $U_p^{c(ST)}$, $U_{p-fc}^{min(ST)}$, $U_{p-p}^{(ST)}$ and U_{p-fc}^{max} .

6. The measuring of the electro-optical response of a cholesteric display cell as in point 5 at $T_b=T_{FC}$. This dependence is necessary for determination of the coefficient a_3 , a_4 and a_5 by formulas (9), (10) and (11).

The duration of experimental measuring of these six characteristics is about two hours that is significantly less than duration of experimental analysis necessary for investigation of electro-optical properties of a ChLC by a standard way. Moreover, using proposed method of approximation, it is possible to obtain approximated electro-optical characteristics of a ChLC, similar to characteristics on Figures 11, 15 and 19 for any value of the parameter T_b .

Conclusion

In this paper the method for an approximation of electro-optical dynamic hysteresis characteristics of a ChLC, which describe a behavior of a ChLC at transitions from the homeotropic and planar states has been demonstrated. For modeling of volt-brightness characteristics we have assumed that the stable cholesteric texture consists of only two type of domains: the "planar" and the "focal conic" domains. The final reflectance from a cholesteric stable texture is determined as a function of the parameter ν (ν - is the part of the "planar" domains in a stable texture of a ChLC). These functions for electro-optical characteristics with the homeotropic and the planar prior states were specified. Also experimental dependencies of all necessary critical and threshold voltage levels were approximated. As a result this method allows to obtain approximated dynamic hysteresis and volt-contrast characteristics of a ChLC only due to the measuring of six special electro-optical characteristics. Comparison of experimental and modeling volt-contrast characteristics was carried out by calculations for each volt-contrast curve of the voltage range (U) where contrast is not less than certain values. This comparison shows quite good coincidence (10-15%) of these characteristics. Moreover this method allows to essentially decrease the duration of experimental analysis of hysteresis properties of a ChLC in comparison with the standard procedure of measuring of electro-optical characteristics. It means that proposed simple method for the approximation of electro-optical characteristics of a ChLC could be effectively used for the analysis of dynamic hysteresis properties of cholesteric materials.

Acknowledgements

The authors would like to gratitude Mr. P. Titarenko and Mr. Yu. Kolomzarov for their help in preparation of liquid crystal display cells.

References

- [1] П. Де Жен, *Физика жидких кристаллов*, издательство «Мир», Москва (1977) (in russian)
- [2] J. Gadhi, D. K. Yang, Gray Scale Drive Schemes for Bistable Cholesteric Reflective Displays // *Asia Display 1998*, pp. 127-130 (1998)
- [3] A. Rybalochka, V. Sorokin, A. Kozachenko, A. Sorokin, Electronic principle of gray scale realization for Cholesteric LCD // *Proc. of the 8th Int. Symposium "Advanced Display Technologies"*, p.59-64 (1999)
- [4] D. K. Yang, Z. J. Lu, Switching Mechanism for Bistable Reflective Cholesteric Displays: A Rapid Addressing Scheme // *SID 95 Digest*, p. 351-354 (1995)
- [5] X. Y. Huang, D. K. Yang, P. Bos and J. W. Doane, Dynamic Drive for Bistable Reflective Cholesteric Displays: A Rapid Addressing Scheme // *SID 95 Digest*, pp.347-350 (1995)

- [6] A. Kozachenko, P. Oleksenko, V. Sorokin, V.Nazarenko, Histeresis as a Key Factor for the Fast Control of Reflectivity in Cholesteric LCDs / / *Conference Record of the IDRC 97*, p.148-151 (1997)
- [7] A. Rybalochka, V. Sorokin, S. Valyukh, A. Sorokin, V.Nazarenko, Simple Drive Scheme for Bistable Cholesteric LCDs // *SID 2001 Digest*, pp. 882-885 (2001)
- [8] M. Kawachi, O. Kogure, Hysteresis Behavior of Texture in the Field-Induced Nematic-Cholesteric Relaxation // *SID 2001 Digest Japan J. Appl. Phys.*, Vol.16, No. 9, pp. 1673-1678 (1977)
- [9] A. Rybalochka, M. Chumachkova, V. Sorokin, Approximation of electro-optical characteristics of a ChLC at transitions from the homeotropic texture // *Semiconductor physics, quantum electronics & optoelectronics*, v. 6, N 3, pp. 411-416 (2003)
- [10] A. Rybalochka, M. Chumachkova, V. Sorokin, Approximation of electro-optical hysteresis characteristics of a ChLC, *Semiconductor physics, quantum electronics & optoelectronics*, vol.7, '3, p. 313-317 (2004)
- [11] A. Rybalochka, V. Sorokin, M. Minaiylo, Control of width of hysteresis characteristics for ChLC, *Proc. of the 13th Int. Symposium "Advanced Display Technologies"*, p. 61-65 (2004)

Silicon based integrated LED microdisplay

A. Smirnov

Laboratory of Information Displays and Optical Processing Systems, Belarusian State University of Informatics and Radioelectronics, Minsk, Republic of Belarus

V. Labunov, S. Lazarouk

Laboratory of Nanotechnologies, Belarusian State University of Informatics and Radioelectronics, Minsk, Republic of Belarus

Abstract

Design and manufacturing process of a cost-effective LED microdisplay for the NTE applications fabricated using standard CMOS technology and containing an array of aluminum- nanostructured porous silicon reverse biased light emitting Schottky diodes will be presented. Being of a solid state construction, this microdisplay is thin and light in weight due to very simple device architecture. Its benefits include also super high resolution, wide viewing angles, fast response time and wide operating temperature range. The advantages of full integration of an LED-array and driving circuitry on a Si-chip will be also discussed.

1. Introduction

Super miniature displays known as microdisplays can offer to date good picture quality in combination with small weight and size, low power consumption and cost. Optical magnification then allows to a user to view a magnified image. Microdisplays are finding the place in portable wireless communication devices, computing tools, digital still cameras, camcorders, advanced sell phones, and toys [1].

In principle, the simplest type of microdisplay is a light emitting device because it eliminates the need for an external light source and complicated optics, but its low luminance level limits their application to personal viewers. For example, such microdisplay technologies incorporating top light emitting polymers or small molecular layers directly on a silicon chip containing CMOS driving circuitry have been designed lately by eMagin Corp. and MicroEmissive Displays [2,3].

In this presentation we will propose the alternative cost-effective approach based on the usage of Al/nanostructured porous silicon (NPS) reverse biased light emitting Schottky diodes fabricated on a silicon chip together with addressing ICs (Fig.1).

The main advantages of such approach are:

- 1). The usage of a simple and cost-effective standard bipolar semiconductor manufacturing process providing the full integration of driving ICs with an array of Al/NPS light emitting diodes and helps to integrate a lot of functionality into the display's silicon backplane;

2). Very high resolution and nanosecond response time of a Al/NPS LED microdisplay;

3). Low cost and simplicity of Al/NPS LED microdisplay fabrication, especially in the case of passive addressing.

2. State of the art

The first reversed biased PS LED was demonstrated by Richter et al. in 1991 [4]. A PS-layer was formed on a n-type silicon sub-strate following with the deposition of a semitransparent Au-electrode in order to form the Schottky structure. Light emission with the efficiency of 10^{-5} was observed in the visible range with the peak of 650 nm. The lifetime of such devices varied from 45 min. to 100 h, after which the emission attenuation took place [5].

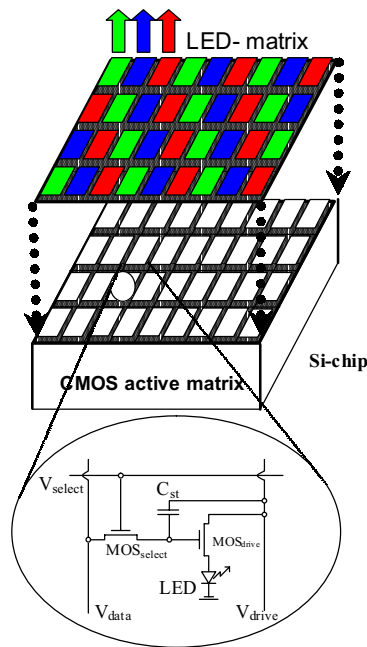


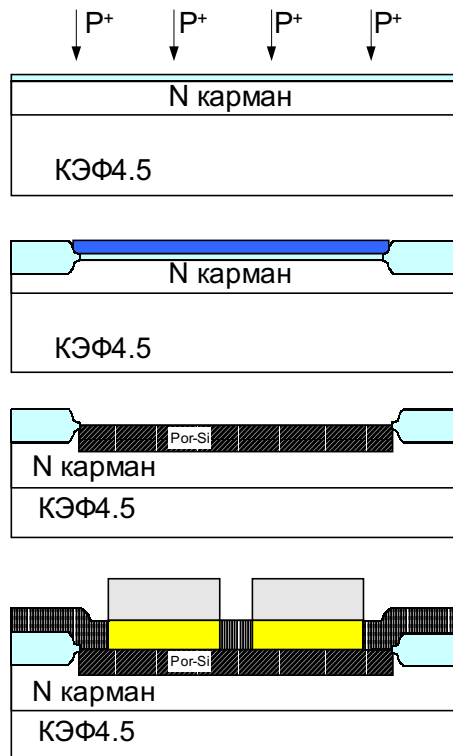
Figure1: The schematic view of a LED-array addressed by CMOS active matrix

In 1995, we made a significant improvement in the efficiency and stability [6,7] forming of an oxidized PS layer protected from atmospheric oxygen by the additional passivation. The oxidized PS layer was formed on a low resistivity n-Si substrate by anodization in the transition regime, providing a continuous anodic oxide on the surface. Moreover, the additional passivation layer of a transparent anodic alumina Al_2O_3 was formed on the PS layer by a selective Al-anodization in an oxalic electrolyte during formation of an Al-Schottky electrode. It ensured the stability of continuous PS LED operation during 1000 h without visible degradation effects and increased quantum efficiency (10^{-3} - 10^{-4}) [7].

In 2000, the more efficient reverse biased PS LEDs have been reported by B. Gelloz et al. [8]. The quantum efficiency of about 10^{-2} has been obtained by using oxidized PS. Porous layer was formed on n⁺-silicon at 0°C. Then, the PS layer without drying was electrochemically oxidized by anodization in an aqueous solution of sulfuric acid. A Schottky barrier was formed by a transparent ITO deposition. The advancement of the anodization process by this way decreased the size of nonconfined silicon nanocrystals in PS. The enhanced quantum efficiency can be explained by the reduction of leakage carrier flow through the nonconfined silicon nanocrystals. Recently, the highest quantum efficiency of about 1.2×10^{-2} has been obtained by pulsed excitation. Pulse LED operation allows one to reach the highest current density through a LED structure, which corresponds to maximum efficiency values.

3. Al/NPS LED array fabrication process

The fabrication process and a NPS LED structure are shown in Fig. 2. N-type single crystal silicon wafers with the resistivity of 4.5 Ohm·cm were used as substrates in our experiments. High doped n⁺-silicon layer of about 100 nm thickness was formed by diffusion of phosphorous gas phase at a temperature of 950°C during 40 minutes. After doping treatment the surface resistivity of a sample was 10 Ohm/□ (10^{20} dopant atoms/cm³). Then wafers were etched in hydrofluoric acid in order to remove the oxide formed during thermal treatment [9].



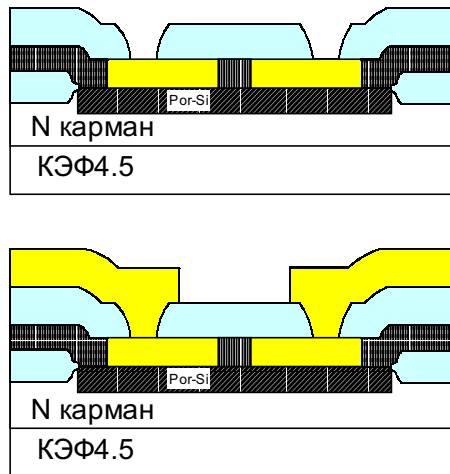


Figure 2: Schematic view of fabrication process and a NPS LED structure.

The NPS layer was formed by anodization in transition regime, in 1% HF aqueous solution at 2-5 mA/cm². The thickness of NPS film was higher than the n⁺-layer one, so that a thin layer of the n-substrate was also anodized. To obtain metallic contact, 0.5 μm thick aluminum film was deposited by magnetron sputtering onto the porous layer. The Al electrodes (pads) were obtained by standard photolithography and subsequent electrochemical aluminum anodization process. Aluminum anodization produced the transparent insulating alumina (Al₂O₃) areas between the aluminum pads so that light could be revealed. Light emission at the edge of negative biased pad is evidenced.

4. Experimental results

4.1. PL spectra

PL spectra were measured with the computer-aided spectro-photometer PEM-100, equipped with a cooled photomultiplier. PL spectra were measured under UV laser excitation at λ=337 nm.

Depending on NPS anodizing regimes the emission peak can be both in the blue and in the red. But the emission spectra are very broad, with examples covering the whole visible range [10, 11]. The other approaches are to be used for a color microdisplays to get a narrow light emission spectra, say, the integration of a NPS LED with a PS microcavity [12].

4.2. Response time

The shortest response time was published for forward biased PS LEDs [13]. However, our devices are faster, because they have no diffusion capacitance. The main mechanism of minor carrier generation in reverse biased Al/NPS junctions is impact ionization at avalanche breakdown at high electric field. A regular columnar NPS structure promotes

the very fast avalanche breakdown due to non-uniform electric field distribution inside the NPS layer. The time of the avalanche response is estimated to be as less as 1 ps. Thus, we have shown that our NPS LEDs can operate in the nanosecond region [10]. By further technology optimization, we hope to reach the sub-nanosecond range.

4.3. Colors

Initial wafers were boron doped silicon with resistivity of 12 Ohm·cm. Anodizing processes were performed in aqueous-alcoholic solution HF (48%) : H₂O:C₂H₅(OH)=1:1:2 electro-lytes. Forming current densities were 20 mA/cm² for green and yellow photoluminescence, and 50 mA/cm² for the red ones. The anodizing time was 10-20 min. We used a postanodizing process to get the photoluminescent blue shift. During the post-anodizing process the red PL transformed in orange and green PL. Samples were stood in an electrolyte in the dark condition during 10-35 minutes after the anodization.

Photoluminescent behaviour of different samples (without postanodizing treatment; standing in electrolyte during 20 minutes; standing in electrolyte during 30 minutes) is shown in fig. 3, where the first, second, and third peak intensity wavelengths are 680 nm, 640 nm, and 580 nm, respectively. These peaks correspond to red, orange, and green optical ranges.

It was suggested in the very first reports on PS that the strong blue shift of the PL was caused by a quantum size effect, mainly due to the presence of quantum wires [14-19]. This effect results in the band gap widening of semiconductor materials.

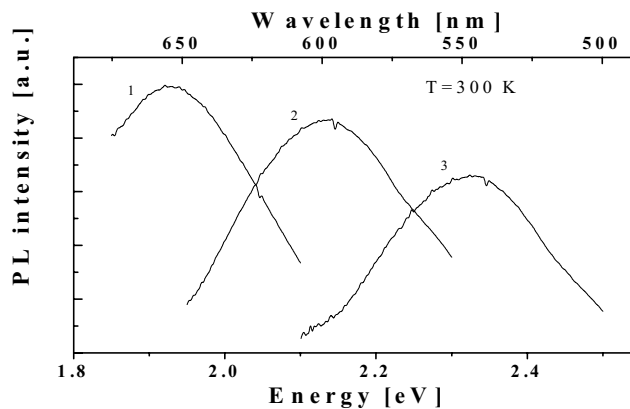


Figure 3: PL spectra of NPS samples: 1 - without postanodizing treatment; 2 - standing in electrolyte during 20 minutes; 3 - standing in electrolyte during 30 minutes.

The PL blue shift can be explained by the size reduction of silicon nanoparticles during drying process. SiO₂ layer development reduces fur-

ther silicon particle oxidizing, and results in increase of radiation wavelength stability.

Two models have been proposed to interpret the transition behavior based on the confinement effect. The first one is the band-to-band transition model [14]. And second one is the recombination-center-related transition model, involving surface states and disorder states [19]. However a basic lack of knowledge regards the ordering and the mean dimensionality and size dependence of these cores of freshly produced PS responsible for visible radiation from red to green.

5. Conclusions

The analysis of reverse biased NPS LED developments for the last ten years has shown considerable parameter improvement towards practical implementations of these devices in microdisplay technology. Bright and stable light emission was observed in Al / NPS reverse biased Schottky junction. The time stability of light emission was quite high thanks to reliable passivation of porous silicon surface in the presented device construction.

Developed light emitting devices are totally compatible with modern silicon IC technology. Thus, Al/PS light emitting structures fabricated onto a silicon chip containing driving circuitry can solve many practical problems for microdisplay technologies.

6. Acknowledgements

This work is partly supported by ISTC grant B276-2.

7. References

- [1]. Microdisplays: Design and Techniques, Seminar Lecture Notes, Seattle, USA, May 2004.
- [2]. I. Underwood et al., QVGA color microdisplay using light emitting polymer on CMOS, SID-2004 Digest, Seattle, USA, May 2004, pp. 293-295.
- [3]. www.emagin.com
- [4]. Richter A., Steiner P., Kozlowski F. and Lang W. Current-induced light emission from a porous silicon device, IEEE Electron Device Letters, 1991, No 12, pp. 691-693.
- [5]. Kozlowski F., Sauter M., Steiner P., Richter A., Sandmaier H., Lang W., Thin Solid Films, 1992, V. 222, pp. 196-199.
- [6]. Lazarouk S., Jaguiro P., Katsouba S., Masini, La Monica S., Maiello G., Ferrari A. Stable electroluminescence from reversed biased n-type porous silicon-aluminum Schottky junction device, Appl. Phys. Lett., 1996, V. 68, pp. 2108-2110.
- [7]. La Monica S., Lazarouk S. et al. Progress in the field of integrated optoelectronics based on porous silicon, Thin Solid Films, 1997, V. 297, pp. 261-264.

- [8]. Gelloz B., Koshida N., J.Appl.Phys., 2000, V.88, p. 4319-4322.
- [9]. Lazarouk S., Smirnov A., Labunov V. Fabrication of a full inorganic EL microdisplay integrated with addressing circuitry onto a Si - chip, Proc. Int. Conf. IDMC - 2003, Taipei, Tai-wan, February 2003, pp. P3-08 - P3-11.
- [10]. Jaguiro P., Lazarouk S., Pavesi L., Smirnov A., Electro-luminescence in porous silicon films of reverse biased Schottky junctions, Proc.ADT-2001, Minsk, Belarus, September 2001, pp. 112-115.
- [11]. Lazarouk S., Jaguiro P. et. al. Porous silicon light emitting diode and photodetector integrated with a multilayer alumina waveguide. Physics, Chemistry and Application of nano-structures, World Scientific, Singapore, 1999, pp. 370-373.
- [12]. Lazarouk S., Leshok A., Borisenko V. On the route to-wards Si-based optical interconnects, Microelectronic Eng., 2000, V.50, pp. 81-86.
- [13]. Cox T.I., Simmons A.J. et. al., J. Appl.Phys., 1999, V.86, pp. 2764-2773.
- [14]. L. T. Canham, Appl. Phys. Lett. 57, 1046, 1990.
- [15]. S. Lazarouk, Proceeding of the 7th Int. Symposium "Ad-vanced Display Technologies", December 1-5, 1998, pp 193-196.
- [16]. S. Lazarouk, P. Jaguiro, S. Katsouba, S. La Monica, G. Maiello, G. Masini, A. Ferrari, Thin Solid Film, vol. 68, 1996, pp. 2108-2110.
- [17]. Q. Zhang and S. C. Bayliss, J. Appl. Phys., 79, 1355, 1996.
- [18]. V. Lehmann and U. Gösele, Appl. Phys. Lett. 58, 856, 1991.
- [19]. J. M. Lavine, S. P. Sawan, Y. T. Shieh, and A. J. Bellezza, Appl. Phys. Lett. 62, 1099, 1993.

Lcos backplane layout verification method that uses computational models of lithography processes

S.N. Koukharenko, S.V. Volk, A.M. Zayats, A.G. Smirnov

Belarusian State University of Informatics and Radioelectronics (BSUIR)
P. Brovki Str. 6, 220027 Minsk, Republic of Belarus

Abstract. Design and manufacturing process of a cost-effective LCOS microdisplay for the NTE applications fabricated using standard CMOS technology based on the novel verification method that uses computational models of photolithography processes will be discussed.

Keywords: microdisplay, LCOS backplane, verification method

I. Introduction

Ongoing reduction of critical dimensions of a LCOS IC's manufactured elements significantly outpaces industry's adoption of new technological processes that use radiation of a smaller wavelength. As a result, chip manufacturers are forced to operate in a so called 'subwavelength area'. It creates a number of problems, with main issue being deviation of shapes of manufactured elements on a silicon wafer from the 'ideal' shapes shown on a layout. Layout designers are no longer allowed to neglect these deviations of real elements from their representations in the layout database and have to take into account distortions, created by technological manufacturing processes. Coherency between a mask layout and a printed image is broken, and consequently methods of creation and verification of layouts need to be revisited.

This paper presents an algorithm for numerical modeling of contours produced by a subwavelength lithography during LCOS backplane manufacturing and dwells on an application of the algorithm for layout physical verification.

II. Algorithm of Modeling of Lithographic Processes

Manufacturing process of modern LCOS IC microchips using optical subwavelength lithography is affected by a number of different factors, leading to distortion of shapes of manufactured elements from their topological description. Optical factors, etching, diffusion and implantation factors, as well as chemical-mechanical polishing are among them [1, 2]. The main factor causing distortions in a subwavelength lithography is an impact of optical discrepancies, produced by an optical system due to finite size of a pupil of a projection optical system and, as a consequence, limited resolution of an optical system as a whole [3]. Pure impact of optical factors is a good first-order approximation for a lithography manufacturing process [2, 4] therefore this article considers

only an algorithm for computation of an aerial image produced by optical system on the surface of a photoresist.

In this case, the most suitable method of computations is usage of special branch of optics, named Fourier-optics [5, 6]. The most important distinguishing feature of a modern optical photolithography from the modeling point of view is usage of partially-coherent illumination [2, 3] and this fact is reflected in the algorithm, described below.

Scheme of an optical system of a typical microchip manufacturing tool is shown on Fig. 1. Its mathematical model consists of the following elements (x and y denote canonical spatial coordinates [3, 6], while f and g denote coordinates in frequency domain):

1. Illumination source, described by two-dimensional brightness distribution function $S(x, y)$.

2. Photomask, described by two-dimensional complex transmission function $O(x, y)$. Transmission function characterizes amplitude and phase of the planar wave in each point right behind the photomask plane.

3. A pupil of a projection optical system is described by complex function $P(f, g)$, which describes impact of the pupil on a spectrum of a passing wave. From a point of view of the Fourier-optics, the pupil performs filtering of high-frequency components in the frequency spectrum domain of an optical image [5, 6].

4. Physical parameters, describing a lithographical tool: radiation wavelength, numerical aperture of the projection optical system lens, aberrations, etc.

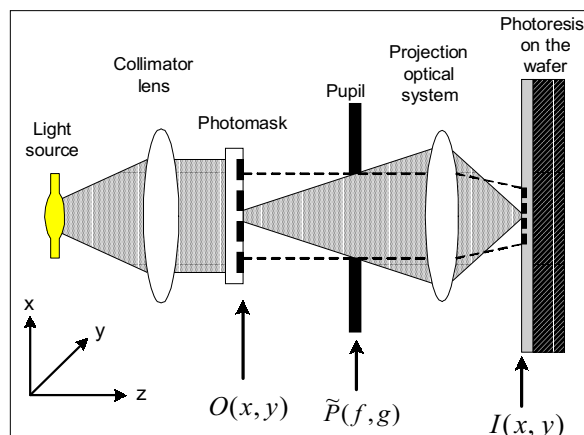


Figure 1: Scheme of the optical system

Algorithm for computation of light intensity distribution (called and aerial image) on a surface of a photoresist is based on the source integration method [6] and consists of the following steps:

1. A spectrum of spatial waves in a plane just after photomask is computed. The spectrum is computed using analytical formulas, which allow computation of a complex matrix $U(f, g)$, describing an image spectrum. This calculation uses coordinates of polygons of a photomask that are specified by a transmission function $O(x, y)$.

2. A spectrum of spatial waves in a plane right behind a pupil of a projection system is computed. The spectrum is computed by multiplying each element of the $U(f, g)$ matrix, obtained in the previous step, by a corresponding value of a function $P(f, g)$, shifted according to a point of an illumination source being currently considered.

3. Coherent image from a single illumination source point is obtained by inverse Fourier transform of the matrix computed in step 2. As we do all computations on a computer, it is reasonable to use an algorithm of Fast Fourier Transform (FFT) for that purpose [6].

4. Amplitudes of coherent images from each point of the illumination source, obtained by repeating steps 2-3 with different source points, are summed with weights determined by brightness distribution function S , to obtain final light intensity distribution ('aerial image') on a surface of the photoresist using partially-coherent illumination.

Result of the computation is a matrix of real numbers $I(x, y)$, describing distribution of light intensity on a plane of a wafer. It can be visualized or passed as an input to another mathematical model, which would build geometrical contours describing printed features. After that these contours can be viewed by the user or used for layout verification. The latter application is described in the following section.

III. Layout Verification Based on Lithography Modeling

Computational algorithms of modeling of lithographical processes can greatly augment traditional approaches to layout physical verification. Traditional DRC-based verification methods can be viewed as a set of geometric rules a layout must comply with. However, these methods give only a binary "yes-or-no" answer and don't take into consideration variation of process parameters and contour distortions.

A method has been developed by the authors that could accompany conventional methods of physical layout verification by removing its main drawback – conventional methods doesn't account distortions of layout features, which may occur after manufacturing using a submicron lithography [7].

The idea of the new approach is to substitute a large and complex modern DRC rule deck, which considers only shapes of original mask primitives, with a set of much simpler rules, which consider shapes of manufactured contours. These shapes are obtained using the computational model of lithography described above. Mask layout and param-

eters of optical system are passed to this model as an input, and the model outputs shapes of contours after lithography.

Verification is achieved by building a set of rules, which obtained contours should comply with in order a layout to be manufacturable. For example, there should be a “no bridging” rule and a rule of minimal allowed distance between two printed contours, etc. For each rule we elaborated an algorithm that performs a series of elementary geometrical operations (union, intersection, distance measurement, grow, shrink etc). Each algorithm creates a set of error markers and puts it over a layout for the user to inspect and fix. These markers highlight places where corresponding rules were violated (see Fig. 2). An approach like that is usually called a method of manufacturing rules checking (MRC). The paper [8] dwells upon this approach.

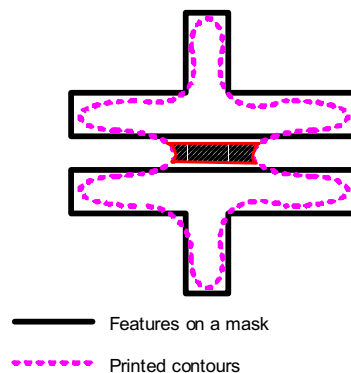


Figure 2: A result of a “Bridging” MRC rule calculation. Dashed error marker shows a place where a bridge between two originally independent features appears

However, each run of a computational model shows printed contours only for a particular combination of input parameters (defocus, exposure, etc). In real manufacturing environment it’s unable to fix parameters exactly, and they tend to vary around central values. In other words, instead of an exact value of a parameter only a certain probability law can be evolved (typically, a Gaussian one). Due to a high sensitivity of modern lithographical equipment, these slight variations may cause significant differences in printed contour shape. And since a lithographical model accepts only exact parameter values, a same piece of a layout needs to be modeled several times, varying input parameters of a model. In turn, each model run is time-consuming, what leads to a significant loss of time spent on iterative checks or makes the user to reduce size of an area under check. Apparently, there is a need to change MRC in a way that it could consider parameter variations and at the same time remain as time-cheap as possible.

The proposed method tries to get as many information from every single model run as possible by determining the extreme distortions of

printed contours with a given probability and applying conventional MRC rules to distorted contours. If a design remains MRC-clear after that, it means that it is tolerant to variations of technological parameters with the selected probability. This probability reflects overall yield.

All contour distortions can be split into two types – systematical and random ones. Systematical distortions affect contour shapes across the whole layout in a similar way. For example, stepper defocus produces this type of distortions. In circuit design it can be accounted for as a variation of some parameter value equally across all devices and structures of a design. Random deviations occur spatially across a chip on a non-uniform basis. They may be caused by local defects of a mask, random particles, etc. Both types of distortions have stochastic nature and can be described by certain probability laws that should be provided by foundry and correspond to a certain manufacturing process and equipment.

We illustrate our approach on an example of contour sizing defect. Size mismatch of a printed contour against its expected size is a sum of systematic and random components:

$$\Delta x = S_x + R_x,$$

where S_x is contribution of systematic factors, R_x is contribution of random factors. These factors take place independently.

Systematic sizing defects may occur mainly because of defocus or dosage variation. These dependencies are generally non-linear and are determined implicitly by the computational model, but we can deduce them by approximation. In order to do that, a special test layout should be prepared and passed as an input to lithographical model. The layout consists of a one large square. Since an image on a wafer is produced by mask features within a limited radius, a length of square edge should be no lesser than twice that radius. The radius is usually equal to five wave lengths [9], hence edges should have length at least ten wavelengths. The test layout is then modeled under different conditions and contour sizing is measured exactly in the middle of the edge. As a result, a dependency of sizing from a selected factor may be deduced. An equation $S_x = F(D)$ may be deduced where S_x is a systematic sizing error and D is a selected disturbing factor. Sizing along different axes may be evaluated separately in case of an asymmetric illuminator.

Since a law of distribution of the selected factor and a law of random sizing error distribution should be known from the foundry and a dependency between sizing and the factor was approximated, it is possible to deduce a law of distribution of a total sizing error via composition. Usually, both laws of distribution are Gaussian $N(m_D, \sigma_D)$ and $N(m_R, \sigma_R)$. If S_x is approximated linearly as $S_x = aD + b$, then the resulting distribution will be also a Gaussian one:

$$N(am_D + m_R + b, \sqrt{(a|\sigma_D)^2 + \sigma_R^2})$$

This formula may be more complex if a dependency of systematic sizing is approximated with a polynomial of a higher power or when several of lithographical parameters are considered, but this does not change the whole approach. Having the resulting formula, a diapason $[x_a, x_b]$ can be determined, in which sizing error falls with a given probability (say, 90%, 95% and 99%).

Now we can perform computational modeling of a piece of a layout with nominal values of parameters and obtain a set of “nominal” contours. Then a check of all MRC rules should be performed twice – the first time after over-sizing the nominal contours by x_b and the second time after under-sizing them by x_a . As a result, new defects can be discovered that don’t occur at nominal values of parameters but are probable in real manufacturing environment (see Fig. 3).

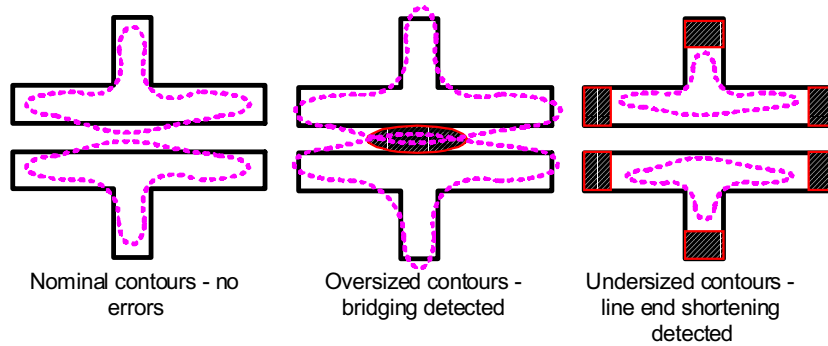


Figure 3: Resizing of “nominal” contours may help discovering hidden MRC errors.

If a layout is MRC-clear even with under- and oversized contours, it means that the design is robust and tolerant to sizing errors with a selected probability. Apparently, the closer probability is to 100%, the wider the diapason $[x_a, x_b]$ is, thus the more conservative a design requires to be. The layout on the previous figure exhibits low tolerance to contour sizing errors due to variation of manufacturing parameters and should be re-designed.

However, it should be noted that even after all these actions are performed, it cannot be guaranteed that all manufacturing defects were discovered, because different layouts and different pieces within the same layout have different sensitivity to defocus variations. Therefore, the proposed method needs calibration each time it is applied to a new piece of a layout. The method can be calibrated by selecting a test layout and places of measurement of deviations. For example, if contour deviation would be measured not in the middle of edges but along corner

bisector, then the [xa, xb] diapason may become wider, and therefore there will be more places of rule violations.

The described approach may also be used to detect places on a layout that exhibit high sensitivity to parameter variations. To do that, we need to compare contours obtained with the described scheme of over- and undersizing against contours obtained with direct computational modeling with manufacturing parameters set to deviated values directly. If a discrepancy between two contours is large then a corresponding mask feature exhibits a larger or smaller sensitivity towards varying of a selected set of manufacturing parameters than an expected average value.

IV. Conclusion

In this article we have described two core elements, which combination gives a new approach to layout verification; they are a computational algorithm for modeling of lithographical processes and a method for physical layout verification that uses output contours of that algorithm. Utilization of this approach allows improving quality of LCOS backplane physical verification, because it considers discrepancies between mask features and printed contours on a wafer.

V. References

- [1]. Clein D. CMOS IC Layout: Concepts, Methodologies and Tools. - Elsevier Science & Technology Books, 2000.
- [2]. Levinson H. Principles of lithography. - SPIE Press, 2001
- [3]. Wong A. Resolution Enhancement Techniques in optical lithography. - SPIE Press, 2001.
- [4]. Rai-Choudhury P. (Ed.). Handbook of Microlithography. - SPIE Press, 1997.
- [5]. Born M., Wolf E. Principles of Optics. 6th ed. - 1997
- [6]. Goodman J. Introduction To Fourier Optics. - 2nd ed. - 1996
- [7]. Markosian A., Rencher M., "Model-based approach allows design for yield". - eeTimes Online. [<http://www.eetimes.com/showArticle.jhtml?articleId=160900827>]
- [8]. Sahouria E., Granik Y., Cobb N., and Toublan O. Full-chip Process simulation for silicon DRC. Technical proceedings of the 2000 International Conference on Modeling and Simulation of Microsystems. [<http://www.nsti.org/procs/MSM2000/2>].
- [9]. Wong A., "Resolution Enhancement Techniques in optical lithography". - SPIE Press, 2001.

Perspectives of passive matrix LCD improvements

Studentsov S.A., Brezhnev V.A., Gorfinkel B.I., Zhukov N.D.

Research & Development Institute “Volga”, Saratov, Russia

ABSTRACT

Today situation for STN LCDs is discussed. The best achievements and main problems are named: low contrast, pure color, slow response. The ways for improvements are considered, that are driving methods, retardation film possibilities and memory displays. The last one is the most perspective, for authors opinion.

STN SITUATION TODAY

Up today STN LCDs remain ones of the most important display classes in the market. More than 65% of all producing devices have STN screen. Of cause, it is owing to small & medium display (from ~1” up to 10”) market. The volume of this market in 2004 was 22 billion USD (27% from total FPD Market) or 1.2 billion pieces (75% from total FPDs). Expected annual growth rate up to 2010 – not less than 30% (1.5-2.5 times better than annual growth rate for large FPDs market and 8-10 times better than for leading branches of industries). The main segment of STN are mobile phones (56 % of all production). As follows from Fig.1, for the nearest years STN (both monochromic and color) will be used in almost 50% of all handsets [1]. Total amount of STN LCD for this application will be about 300 millions pieces per year (Fig.2). The main regions for this application are China (310 million cellular phone users -25% of its population), Russia (60 million cellular phone users -40% of its population) and India (44.5 million cellular phone users - 25% of its population) [2].

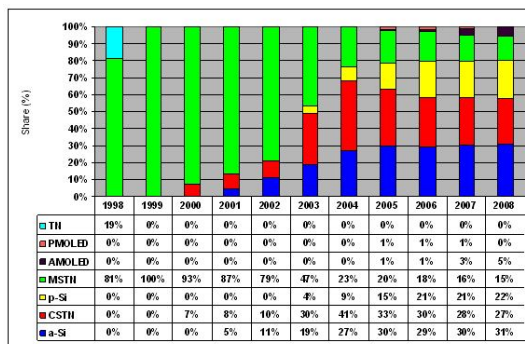


Figure 1. Trends for Mobile Phones Technologies Evolution [Display Search, December'04/February'05]

“Generally, TN & STN LCD manufacturers have experienced a profitable years. But due to a high concentration of products and the trend towards high quality handset color displays, TFT LCD will certainly influence the

development of STN manufacturers in the future. Therefore, it is urgent for these manufacturers to consider changes in the next two or three years to come up with relevant strategies for future growth”, - market analytics wrote [3]. Strained waiting of break in STN put in mistaken UFS STN-LCD with it’s 150:1 CR; 87% color gamut and 13.5 ms response time, as reported in [4]. But in reality it is B/W field-sequential TFT (see www.samsung.com./products).

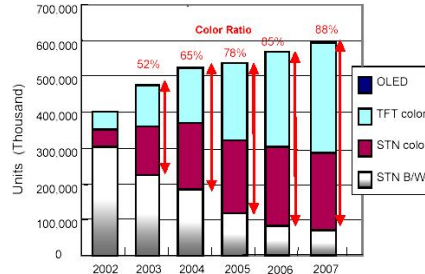


Figure 2. Shipment Volume & Color Handset Percent [Toray Industries Inc, Nov. 2004]

Why STNs are retreated? 1. Low contrast: 30:1 for STN against 150:1 for AM LCD. 2. Slow response: 200 ms for STN against 20-30 ms for AM LCD. 3. Multiplex level limitation (with high contrast): 1/240 for STN against 1/768 for AM LCD.

Why STNs but aren’t given way? 1. Low cost: 10-15 \$ for STN against 27-35 \$ for AM LCD [4]. 2. Technology simplicity: more than 100 producers STNs against 15-20 for AM LCDs.

So, there are three ways for STN producers now. 1. To produce in a few years only low cost TN LCD (15\$ for 14”x16” mother plate instead of 44.5-98 \$ STN). 2 To invest in a few years billion \$ for TFT LCD reorientation. 3. To sponsor research works for STN improvements. We think, only the last way is correct.

Results of our analysis of firm prospects and Internet sources are seemed in table 1. It is follows from Table 1, the main problem is response; the second is color purity and the third is contrast ratio for fast switching.

Parameter	Mass production FSTN		The best demonstrated result		Goal for 2-3 nearest years
	typical	The best			
Color	4096	221 000 (Tian-Ma)	221 000 (Tian-Ma)		65536 typical
Color purity, %	20	No data	No data		60-80
Contrast ratio	30:1	60:1 Tian-Ma (China)	100:1 Sharp	50:1 Hitachi	(100-150):1
Response time, ms	200	85; 60 expected (Picvue, Taiwan)	150 Sharp	80 Hitachi	30

Table 1 The Main Object of TN/STN Improvement

What are the reasons for low contrast of STN? T(U) curve for STN has to have high sharpness. The best voltage sensitivity effects are interfer-

ence ones. TN has only linear polarization, but STN – two interference waves. Minimization of one wave for TN is realistic goal, but perfect minimization of both waves for STN is impossible. If we use 240°twist and non-axis LC orientation in non-crossed polarisers and have the most sharp T(U), are we able to realize maximum contrast? The second problem is frame response phenomenon for multiplex displays. If we used interference effect, after high row voltage shut off, contrast must decrease. So, contrast for multiplex case is much worse.

How to overcome this problem by driving methods? In standard *line-by-line* only slow LCM can be used (it means, poor response) or higher frame frequency (with voltage distortions). In *active addressing*, when voltage form are calculated for all screen pixels for each row we have very large calculated volumes ($N^2 \times M$ for each frame *vs.* $N \times M$ for line-by-line); $(N+1)$ column levels *vs.* standard 3 (high complicated drivers); buffer frame memory; row time calculation (10-100 ms) *vs.* frame time (50 ms) for line-by-line. That is, high complicated drivers are needed in this case and the best results are only for $N \times 9$ [5].

In case of *multi-line addressing*, when we have L small row voltages with $L \times$ Frame increasing, simple driver are using. But there is only $2 \times$ CR increasing with high frequency distortion effects & some frame response. Moreover, higher sharpness requires for the same multiplex level as in line-by-line method.

What are the reasons for pure response of STN? The first is frame response, when we used slow LCM. The second is that energy levels for “on” and “off” states are most closeness. So, energy difference between those states is small and response time is slow.

The pure color & color gamut follow from CR and response STN disadvantages.

As calculated, compensator films are able to increase STN CR up to 300:1 [6]. But in practice, by thickness deviations, inner scattering, light passing through cell with angle averaging and voltage form distortions, CR isn't more than 50-60:1. Moreover, optical compensator can't improve response times significantly. Only multiplex level may be much better with films, because we are able to minimize any concrete ellipticity. For example, we produce 18:1 1/320 Reflective FSTN single matrix on 1/120 mixture with retardation film which compensate one of intermediate LC configurations.

WHAT IS THE EXIT

Where is the exit? As Alt / Pleshko noted, only displays with any static memory are RMS-independent [7]. So, only bistable effects (such as ferroelectric LC, BiNem, Zenithal Bistable Displays and Volga's MEMOMI) are perspective for parameter improvements.

Ferroelectrics LCD have many problems and produce only in scientific purposes now. Zenithal bistable displays with viewing angle (CR?10) 120°(H)/ 100°(V); max resolution 1200 x 700; 2 years zero-watt information storage; response 30ms-20ms seems very good [8]. But pure contrast 25:1; 0.42 s frame time and only 4 grey levels from one hand and technology complexity and electrochemical stability from the other hand prevent to wide use of ZBD. BiNem LCDs have CR 150:1; wide viewing angle (CR?40:1!) 100°(H) / 100°(V); 32 000 color prototype in 2004 and expected 64 000 colors in 2005; max resolution 640 x 480; response 10 ms; 2 months zero-watt information storage [9] and SID 2005 Silver Award in “Display2004” nomination [10]. But 0.2-1.0 s frame time; thickness 1.4 mm (disruption!); high pretilt angle degradation & short life time; narrow temperature range (from 15°C); narrow thickness & pitch range (? ±0.1mm) are serious problems for use.

LCM	d, mkm	Δnd, mkm	V ₁₀ , V	V ₁₀₀ , V	Sharpness ρ	N	State
LCM-028	2.5	0.505	1.85	2.7	1.46	8	realized
	3.5	0.707	2.2	2.8	1.27	18	realized
	4.0	0.808	2.3	2.8	1.22	28	realized
LCM-041	2.5	0.520	2.2	2.6	1.29	36	realized
	3.4	0.7				>75	expected
	3.9	0.8				>100	expected
LCM-039	2.0	0.516	1.6	2.0	1.25	21	realized

Table 2 MEMOMI Multiplex level perspectives

We think, MEMOMI is good alternative for abovementioned displays [11]. MEMOMI is R&DI Volga’s patented STN construction with self-compensated property, when optical activity of one half of LC lay is equal to another, but opposite by sign. Those configurations are existed not only under applied voltage but for some time after it’s shutoff. The next step was “off”-state transmittance minimization. For this goal Volga’s STN used crossed polarizers and enter LC molecule direction & polarizer axes coordination. As we got the same high contrast with & w/o voltage, it may be applied higher pulse with duty factor. So, U_{RMS} should be the same as for standard driving. Visual relaxation time is approximately a half of total relaxation time after high voltage ending. We can used more faster LC materials because there isn’t frame response phenomenon. MEMOMI LCD, based on 180°twist structure, crossed polarisers with axes aligned in LC –molecule direction, has CR 392:1; 31 ms total response; 20 ms frame (Fig.3). Although multiplex level is only 1/32 now, we are expected about 1/100-1/125 (table 2). It is enough for handset applications.

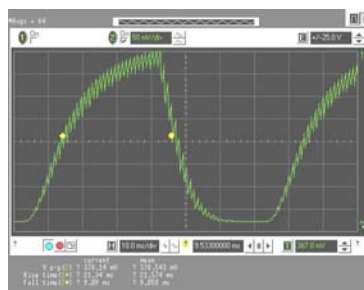


Figure 3. Optical response of 1/32 multiplex MEMOMI: CR =392:1; total response time 30.4 ms

CONCLUSION

We are discussed some problems of STN LCDs, which are principal for their future. The most perspective are passive matrix LCD with memory property. In this way high contrast up to 400:1, response time up to 30 ms, 32 000 colors and 1200 x 700 resolution are realized now for various constructions. We hope, total success will be achieved for 1-2 years.

REFERENCE

- [1]. Report on new handset displays in China's market for the first half year of 2004, No.419.
- [2]. [www. InternationalTelecommunication.com/](http://www.InternationalTelecommunication.com/) IT facts, February 19, 2005.
- [3]. Color Handset Displays Drive TN/STN LCD Industries, Industrial Economics & Knowledge Center (IEK) Report, ITRI, October 29, 2004.
- [4]. C. K. Chow, Information Display, p.p.18-20, v.21, No.1, 2005.
- [5]. T. N. Ruckmongathan, J. Phys. Letters, v. 53, No. 1, July 1999, p. 199.
- [6]. V.G. Chigrinov et al, SID 2004 Digest, p.982.
- [7]. P.Alt, P.Pleshko, IEEE Trans. on Electron Devices, v. ED-21, No.2, February 1974, p.146.
- [8]. [www. ZBD.com//Products//Capability](http://www.ZBD.com//Products//Capability), August 2005; M. Freeman, Electronics Talk Magazine, June 2003; J. C. Jones et al, SID 2002 Digest, p.90.
- [9]. I. Dozov et al, Information Display, vol. 18, January 2002, p.10.; J. Angele et al, EuroDisplay 2002, p.43. S. Lamarque, JEPA Seminar, January 29, 2004, Tokyo; P. Martinot-Lagarde et al, Electronic Imaging, No.2, 2003; A. Boissier, J. Angele, IMI 2nd Annual Paper-like Display Conference, February 11, 2005; I. Dozov et al, IDW'04 Proc., Japan, December 2004, p.819
- [10]. Information Display, v. 21, May 2005, p. 16.
- [11]. Studentsov S.A. et al, Euro Display 2002, p.437; Studentsov S.A., Euro Display 2002, p.873; Studentsov S.A. et al, Proc. 12th Int. Symposium Advance Display Technology, August 2003, Moscow, Russia, p.179.

Interactive displays

Trofimov Yu., Posedko V., Sivenkov V., Lishik S., Tsvirko V., Posedko A.

Institute of Electronics of the NAN of Belarus, Minsk, Belarus

In this report we review the current state-of-the-art of interactive displays (ID), describe the main principles of their operation, functional characteristics and possible fields of application. Special attention is given to the interactive displays with contactless control method, in particular, to photo-sensitive displays. The results of the authors' own research in this field are presented. A number of photo-sensitive display cell designs is considered, as well as the problems (with possible solutions) related to the production of such cells.

The human-machine interfaces are constantly being developed in order to improve the effectiveness of information interchange, allowing at the same time the maximum possibility for interactive dialog.

First of all, let us define more exactly, what we understand by the word-combination "interactive display" (ID). The term "interactive", when referring to a display, implies the presence of the additional devices for input and processing of information. However, the mere combination of such devices and a display cannot be called an ID, as we can see on an example of a traditional display of a PC. The term "interactive display" also implies the imitation of certain human senses. Thus the displays sensitive to the touch, sound and light can rightfully be called interactive.

The first family of interactive displays capable of receiving tactile input is widely known as touch screens. These IDs combine the information input and display functionality in the same surface. This allows for decreasing the overall dimensions and improves the ergonomics of the interactive system as a whole.

The recent advances in microelectronics allow for the creation of digital high-resolution photo-sensors for video-systems. The growing processing power of computers makes the application of speech and image recognition technologies possible. These innovations enable the creation of interactive systems that could be controlled using voice, gestures, eyes viewpoint, nose or eyelid movements.

The physical principle of the sensor operation determines the type of an ID, its advantages and disadvantages, and its possible applications. In Fig. 1 the classification of the ID sensor technologies proposed by the authors is presented. The current ID by the sensor type can be divided into three groups: tactile (touch screens), photo- and audio-sensitive.

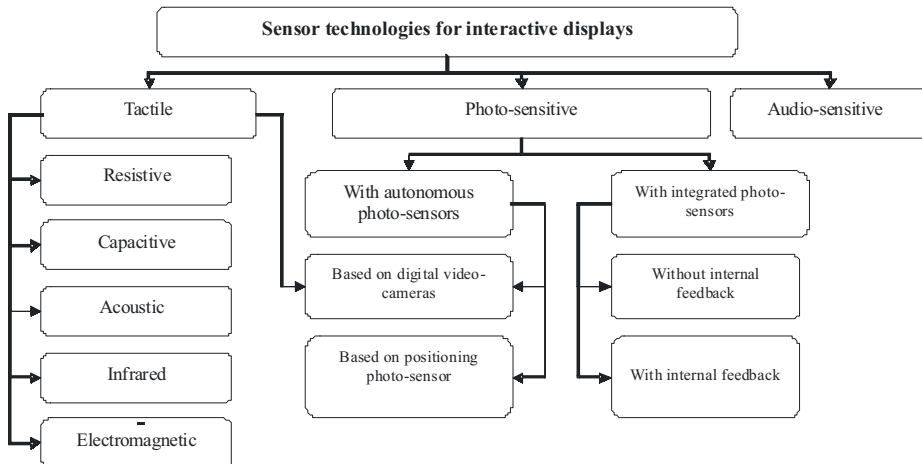


Fig. 1. Classification of the sensor technologies used in interactive displays.

The arrangement of the sensors in space can be distributed or concentrated. The devices with distributed sensors are easier to implement from the technical point of view, because the point of action on a given pixel is relatively straightforward to determine on the level of electronics. For the second class of devices, the special potentially computationally intensive algorithms are needed to calculate the point of action based on the data from several sensors.

The sensor systems of modern touch-screen can be based on various physical principles: resistive, electrostatic, acoustic, infrared light, electromagnetic resonance, etc. The sensor detect just one or two of the parameters of the touching action that allow the display to determine, for example, the coordinates of the contact point and/or the force (energy) of the action. In most cases this is sufficient for effective interaction with the software, input of the graphical symbols and image editing.

The modern sensor panels have the common ancestor, the George Hearst's digitizer created in 1970, which was using the resistive principle to determine the coordinated of the contact point.

Touch screen are currently widely used in many industrial branches: from game machines to production control systems, from architectural design (fig. 2) to CAD systems and 2D/3D animation (fig. 3), and presentations, etc. The grown on the PDA and tablet-PC markets also leads to proliferation of touch-screen IDs.



Fig. 2. ID in an architectural design [1].

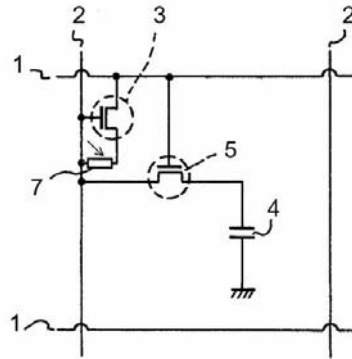
The consideration of audio-sensitive IDs is beyond the scope of this report. We will only give a common example of such a system: a PC with a microphone, and voice-to-text software package.

In photo-sensitive displays the information input is performed with a light-pen, a pointing device with a light source in the form of a ball-point pen. There are several known designs of the photo-sensitive cells used in interactive displays. [2]–[6]. In fig. 4 the electrical schemes of the two photo-sensitive display cells are presented. Each scheme has an own photo-sensitive element. Photo-sensitive and display elements, combined in a pixel unit, are not connected into a feedback loop neither electrically, nor optically.

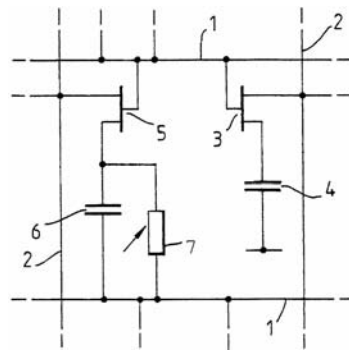


Fig.3. Capabilities of the ID Cintiq from Wacom, this display uses electromagnetic resonance principle to determine the coordinates of the contact point and the force-sensitive pen-tip to measure the applied force.

Registration of the light exposure is performed either by measuring of its photoconductivity (fig.4a) [2]–[4] or, by measuring the discharge current of the capacitor, connected to the photo-element (fig.4b) [5]–[6]. The read and display modes are time-separated, the same busses are used to implement both modes.



(a)



(b)

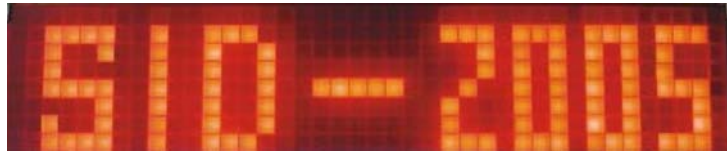
1, 2 – address and data lines;

3, 5 – thin-film transistors;

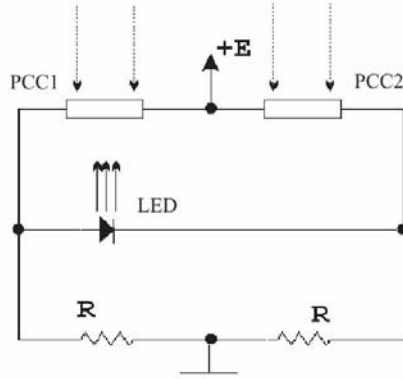
4 – liquid crystal element ; “6 – capacitor; 7 – photo-sensor.

Fig. 4. Display cells with integrated photo-sensors without internal feedback.

Qualitatively new properties can be achieved by the photo-sensitive displays with pixels consisting of electrically and optically interconnected photo-sensitive and display elements. For example, in the cells, presented in fig. 5 a positive feedback between the luminosity and the current, flowing through the serially connected photo-resistor and the LED, additionally implements the optical memory functionality. Switching on and off of the LED is done optically, for which the two signals differing in their spectral composition or polarization are used [7], [8]. A photo of an interactive tablet based on the photo-sensitive cell described above is shown in fig. 5. The successful development path for this type of photo-sensitive displays lies as we expect in the combination of the OLED technology with the stencil printing technique for the photo-sensitive structures. This combined technology is currently being developed in the Institute of Electronics NAN of Belarus.



(a)



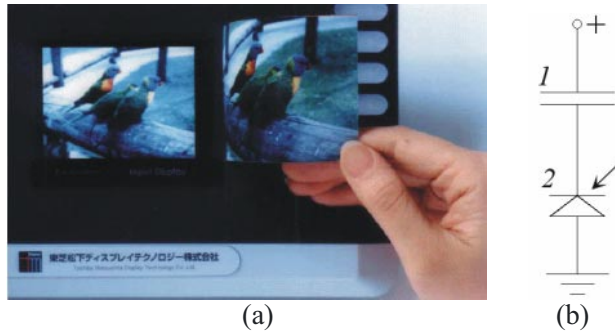
(b)

PCC1, PCC2 – photo-resistors; R – resistors.

Fig. 5. Electrical schematic of the multifunctional display optron.

The principle of combination of the photo-sensor and the indication element in one cell is also used in the recently announced by Toshiba America Electronic Components, Inc. innovative product, a display with scanning capability (fig. 6a) [9]. Every cell of this display contains a liquid-crystal element (LC) and a photo-sensor, placed on the transparent glass substrate. The incident light falls on the cell from the LC side of the cell 1, goes through it and then reaches the photo-sensor 2 (fig. 6b).

The charge induced by the incoming radiation reduces the transparency of the LC and in so doing reduces the rate of the photogeneration [10]. The negative electrical feedback implemented in this way allows one to make a unique correspondence between the incident light energy and the accumulated charge. The signal processing system periodically reads the accumulated charges and applies the corresponding voltages to the LC indicators. In this way the scanning of the image is achieved per pixel at the physical level. The image can be saved in the external memory and then displayed again, when needed. Such a display (diagonal 3.5", resolution 320X240, 260k colors), having the scanning functionality can be used in the field of personal identification and other related applications. Potentially, such a sensor system can register the both manual and light-based interactions. Ideally, the photo-sensitive display element must perform the following functions: indication, optical and electrical control, memory, and stable operation under ambient lighting conditions.



1 – LC element, 2 – planar photo-diode.

Fig. 6. Display form Toshiba America Electronic Components, Inc. with the scanner functionality (ü) and simplified electrical schematics of a mono-chrome pixel (b).

An important place among the photo-sensitive display systems is taken by the technologies combining the projecting and virtual systems for information display with photo-sensors based on the CCD video cameras and image analysis techniques.

For example, in fig. 7 an operating principle of a product by KEYTEC, Inc. (USA) is illustrated. In this setup a wide-angle digital camera is placed in front of the screen and the position of the laser pointer spot is tracked by analyzing the image captured with the camera with special software [11].

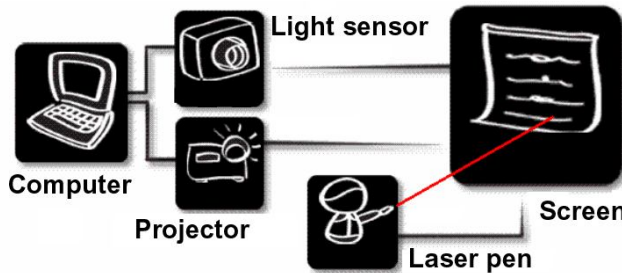


Fig. 7. The operating principle of the interactive display technology based on the digital video camera.

The application of the digital optical sensors together with the development of the image processing systems allows one to extend and improve the functional characteristics of touch screens, as well as to extend the nomenclature of the photo-sensitive ID. In the new touch screen technology DVIT (Digital Vision Technology), patented by SMART Technologies Inc. (Canada), several digital video cameras, placed in the corner of the screen, are used to determine the position of an object in front of the screen (fig. 8) [12].

In the modern light-sensitive ID analogue optical sensors are also widely used. Analogue sensors are noted (as opposed to the digital sensors) for their fast response and insensitivity to the distribution of the illumination on the surface of the sensor. They should be viewed as a critical limitation and can be still sufficient for controlling the display with a light beam. A positioning optical receiver is a good example of such a system. The position of the light beam is determined by measuring the differential photo-currents from the different sides of the receiver. An possible application of analogue optical sensors in interactive systems can be a laser shooting range [13].

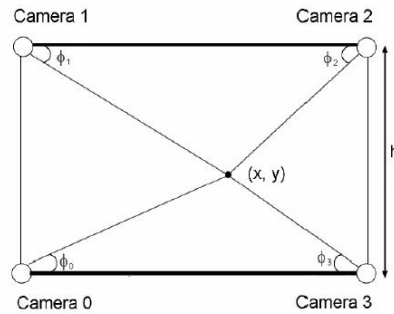


Fig. 8. Determination of the contact point with the help of the digital video cameras.

A very interesting combination of the infrared and video technologies is employed in the so-called virtual keyboard for mobile phones and PDAs. (fig. 10) [14]. The (QWERTY) keyboard layout is project onto any flat surface with the help of a miniature projector based on a red laser-diode. An separate infrared laser illuminates the keyboard input area as well as the fingers of the user. The precise location of the fingers is determined using an optical digital sensor and a computer. Analogous design can be used and for an ID.

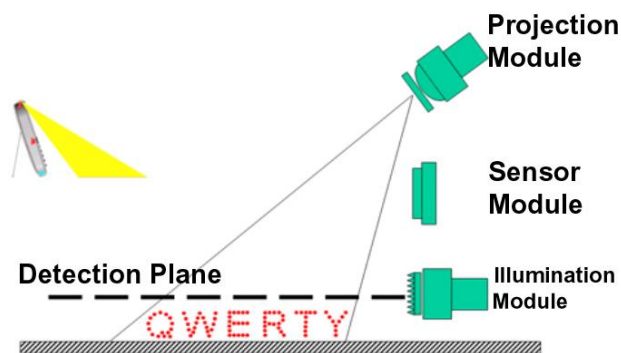


Fig. 10. Interactive virtual keyboard for a mobile phone.

One of the advantages of using video technology is that the hard screen surface is not required. This leads to the possibility to create three-dimen-

sional IDs, in which the “floating in the air” virtual objects can be controlled with gestures (fig. 11) [15], [16], [17].

The image analysis system recognizes certain finger movements and makes the connection to the corresponding commands, in order to manipulate a virtual object. Similar sensor systems are employed as well for tracking the human eye viewpoint, or the movements of eyelids, nose and lips.



Fig. 11. Projecting ID with the image freely floating in the air, tracking the movements of the embedded objects.

Digital optical sensors (CCD-cameras) not integrated with display elements, can be used in the computer vision systems. At the moment the video systems are cumbersome and limited in performance, due to the fact that CCD-devices operating using the charge accumulation principle. For the real-time image analysis the large computational resources are required. However, for projecting 3D displays the use of the video technology is irreplaceable.

References

<http://electroland.net/>

U.S. Patent No 4345248.

U.S. Patent No 5151688.

U.S. Patent No 5204661.

U.S. Patent No 4655552.

U.S. Patent No 5485177.

Belarus Patent No 4463, 05.04.1999.

Trofimov Yu., Posedko V., Sivenkov V., Posedko A., Lishik S. //
Proceedings of the SID 10th Symposium Advanced Display
Technologies. 2001. P. 181–185.

www.toshiba.co.jp/tech/review/2004/high2004/

high2004pdf/0403.pdf. P. 4;

U.S. Patent No 5532743.

<http://www.magictouch.com/ViewTouch.html>

<http://www.smarttech.com/dvit/>

<http://www.sitek.se/adventure.htm>

<http://www.vkb-tech.com/technology/foursteps.asp>

<http://www.io2technology.com/>

U.S. Patent No 6857746.

Grossman T., Wigdor D., Balakrishnan R. // Proceedings of UIST 2004.
ACM Symposium on User Interface Software and Technology. 2004.
P. 61-70.

AM VFD module on silicon substrate

*Usova T.V., Loginov A.P., Zhukov N.D., Gorfinkel B.I., Frolov V.L.,
Neudakhin A.V., Zotov N.A.*

Research & Development Institute "Volga", Saratov, Russia

Modern level of information display facilities allows to create the special flat display, on a silicon substrate with built-in, in single technological cycle, drivers for select of lines and columns and a array of memory elements in each pixel of an information area, on the basis of low-voltage cathodoluminescence. Such indicators, with the control, are based on the silicon technology of complimentary integrated circuits (CMOS highly integrated chip), and also precision phosphor deposition, and the circuitry defining of indicators work in quasistatic mode. It allows to achieve a necessary level of brightness (contrast) at low operating voltage.

The modern market of high-informative information display facilities is actively worked up by flat-panel displays. The most of these flat-panel displays are based on active matrix, for example, liquid crystal (LCOS) and polymeric (OLED) displays. Now, in our country, there is a problem of absence of drivers for all types of flat displays. Thus, for traditional cathodoluminescent and plasma screens, the high-voltage drivers for 150...250 V are required. It is a complicated organizational-technical problem. For control of LC-screens (including ones on active substrate), high-speed multi-leading-out-wire drivers on polyimide carrier, with 220 microns pitch, LH1536 or SN7709 types, with 160x240 leading-out wires, manufactured by the USA and Japan firms, are required.

Now, the flat modules of firm "Planar" are widely adopted.

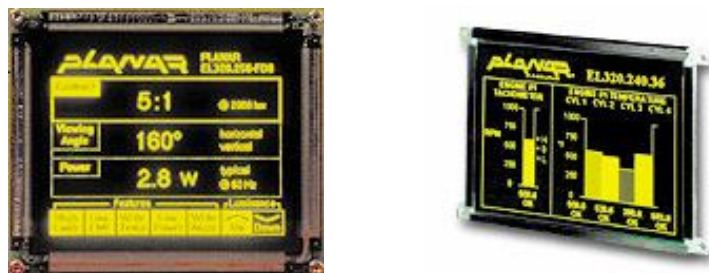
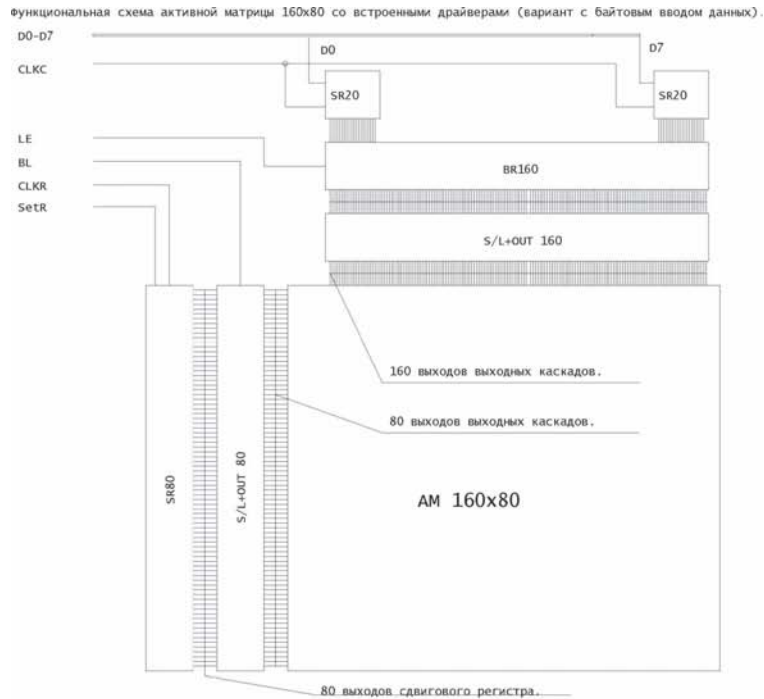


Fig. 1 shows the modules samples.

This samples lack is their yellow color luminescence which does not provide necessary contrast at high external light exposure.

FSUE "R&D I "Volga" has carried out recently a complex of works on iM VFD modules type-line creation. Their basic designs and technologies have allowed to solve the very complicated problems of creation of a flaw-free silicon substrate on the basis of existing industrial technologies of CMOS IC.

Two types of AM VFD modules, with 320x256 and 160x80 light-emitting elements, have been developed. Fig. 2 shows the flow-block of AKP with the built-in drivers for the module 160x80.



CLKC	входной сигнал частоты сдвига информации в сдвиговом регистре столбцового драйвера
D0-D7	входные данные столбцового драйвера
LE	входной сигнал записи в выходной регистр столбцового драйвера
CLKR	входной сигнал частоты сдвига информации в сдвиговом регистре строчного драйвера
BL	входной сигнал бланкирования выходных каскадов строчного драйвера
CLKR	входной сигнал частоты сдвига информации в сдвиговом регистре строчного драйвера
SetR	входной сигнал установки входного регистра строчного драйвера, подаваемый в паузе между нулевым и первым сигналом "CLKC"; при "SetR"=1 нулевой разряд входного регистра строчного драйвера устанавливается в состояние "1", а остальные 80 разрядов – в состояние "0".
Питание:	
для низковольтной части драйверов:	- 5В относительно +Ua активной матрицы
для выходных каскадов драйверов	- 15В относительно +Ua активной матрицы

При записи информации в сдвиговый регистр столбцового драйвера по переднему или заднему фронту импульсов CLKC период импульсов CLKC должен быть ~ 1,3 мкс.

При записи информации в сдвиговый регистр столбцового драйвера и по переднему и по заднему фронту импульсов CLKC период импульсов CLKC должен быть ~ 1,3 мкс.

Входной регистр строчного драйвера имеет нулевой служебный разряд, не имеющий выхода на выходной формирователь, который устанавливается в состояние "1" при подаче сигнала "SetR"=1, в то время как остальные разряды входного регистра строчного драйвера устанавливаются в состояние "0".

Вход данных нулевого разряда сдвигового регистра строчного драйвера соединён с потенциалом - 5 В.

Не указаны формирователи тактовых сигналов сдвиговых регистров строчного и столбцового драйверов.

Fig. 2

The developed active substrate simplifies the video-modules design, make the modules original, highly effective and competitive products. Moreover, the offered active substrate with the built-in drivers on mono-silicon can become a basis for creation of new classes of displays on the basis of electroluminescence, organic light-emitting diodes (AM OLED) and field emission effect (AM FED).

The main advantages and abilities of the developed displays are:

Tight single-whole video-module design including the flat vacuum display, anode plate as the silicon plate inside of which the array of memory elements under each pixel is created, and built-in lines and column drivers. The optical filter with anti-glare covering is placed on the display top cover;

high brightness up to 2500...3000 cd/m² independently of the on-off time ratio provided by quasi-static low-voltage mode of displaying;

reliability of work in extreme climatic conditions, external light exposure up to 100 thousand lux, ambient temperatures from a minus 45°C up to plus 85°C;

opportunity of their mass production on the basis of available industrial technologies of vacuum indicators and silicon integrated microcircuits.

Zero-defects is the most important and difficultly achievable moment of development.

The active silicon substrate for AM VFD is one "crystal" on one silicon plate containing 12800 transistors of array and 4800 transistors of drivers for 160x80 module, and 82000 transistors of array and 12000 transistors of drivers for 320x256 module. It is obvious that any defect of transistors results in whole substrate rejection. It can be estimated at the functional control (FC) of substrates drivers. The product yield on this operation is $\approx 30\%$. At the same time with FC, absence of short circuits on vertical and horizontal selection wires in array is being checked.

Functional scheme of active matrix 160x80 with built-in drivers (variant with byte-oriented data input)

160 outputs of output stages

80 outputs of output stages

80 outputs of shifting register

CLKC - Input signal of information shift frequency in shifting register of column driver

D0-D7 – Input data of column driver

LE – Input write signal to output register of column driver

CLKR – Input signal of information shift frequency in shifting register of line driver

BL – input signal of blanking of output stage of line driver

CLKR – Input signal of information shift frequency in shifting register of line driver

SetR – input signal of input shift of line driver being given in the pause between the zero and the first CLKC signals,

When SetR=1, zero bit of input register of line driver set to state “1”, and the other 80 bits set to state “0”

Power supply:

For low-voltage part of drivers – “-5V” relatively to U_a of the active matrix

For output stages of drivers - “-15V” relatively to U_a of the active matrix

At recording to shift register of column driver on leading-edge or trailing edge of CLKC impulses, the CLKC pulse period should be ~1.3 μs

At recording to the shift register of column driver both leading-edge and trailing edge of CLKC impulses, the CLKC pulses period should be ~1.3 μs

Input register of the line driver has zero service bit not having output to the driver which is set to "1" at "SetR" =1 signal injection, while other bits of the input register of the line driver are set to "0".

The data input of the zero bit of the shift register of the line driver is connected to “-5V” potential

Clock drivers of shift registers of the line and column drivers are not specified

One of essential lacks at creation of indicators on AKP is presence of uncontrollable ("burning") points-pixels on dark information field. Thus the quantity of such pixels is 5...10 ones for 160x80 module and 50...80 ones for 320x256 module, that corresponds to 0.04...0.08% and 0.05..0.085% accordingly.

The identical percent of defective pixels for each plate is evident. It corresponds to 99.9% yield. Undertaken constructive-technological measures, namely: insertion of "thick oxide" 1000...1500 Å into array transistors gates (instead of typical 60...100Å), increase of breakdown voltages of sink junctions and generally all ones up to 60...80V (instead of 40V), reduction of the area of all p-n junctions in the array, allowed to drive the defects level up to 2...5 (0.015...0.03%) for the module 160x80, and 15...25 (0.018...0.03%) for the module 320x256. It is obvious that the achieved figures reflect an existing technological level of substrate manufacturer and quality of source substrates.

The further decrease in unsoundness can be achieved only due to use of new design methods, for example, creation of a n-channel memory array instead of p-channel one. That will make defective pixel invisible; - use CMOS generator in the key transistor instead of the open sink, with simultaneous reservation of driving elements, for example, due to pixel division into 2 and more independent control circuits. One of cardinal design solutions is, probably, creation of memory transistors based on poly-silicon, not connected

with the main substrate, on the silicon plate with the built-in drivers of lines and columns of the array.

The second (the main) lack of substrates is the defect like separate line or column luminescence absence on the 1/3 or less than its length. This defect is caused by damage of the external part of the substrate (scratches) at its manufacturing. It is especially actual at the final stage of plates manufacturing: on photolithography operations on the second metal, opening of protective oxide on metallization, etchings and deposition of aluminium to the back side of plate, dicing (cutting) of the plates.

The necessary effect is achieved by the following order of carrying out of operations: covering of 2-nd metal by the protective oxide $0.7 \text{ SiO}_2 + 0.4 \text{ Si}_3\text{N}_4$ without carrying out of a photolithography. Thus the rigid layer of silicon nitride takes up all abrasions at contacting of face side with a track of the machine for aluminium deposition onto the plate backside.

Further, the following operations are carry out: photolithography on protective coat, photoresist deposition before the plates dicing, and delivery of plates coated by the photoresist in special "lace-frame" excluding contact between the plates at transportation.

During the work, joining of 5 inches diagonal plates among themselves to create the 10 inches diagonal information field (4 independent AKP fragments with the built-in drivers) was tested. The following technical problems are solved:

- cutting of plates with a width of cut providing 10 microns space between the plate edge and the beginning of information field segments (usually not less than 50 microns) for maintenance of fragments joining without loss of pixels pitch (space 30 microns);

- plates attaching by low-temperature solder;

- deposition of uniform phosphor covering onto the 640x512 information field consisting of 4 crystals, and liquidation of space at joining on internal sides of plates;

- deposition of 3 colors phosphor onto the substrate 320x3x240.

The developed video-modules provide correct reading information and necessary contrast at external light exposure up to 100000 lux. To provide these parameters, the following researches were carried out:

- providing of pixel luminescence brightness, in the indicator (without optical filter), not less than 1000-1500 cd/m^2 ;

- increase of information field contrast due to use of "blackened" mask, for example, of germanium monoxide;

- selection of optical filter with necessary transmission factor and spectral characteristics;

- exception of influence of high external light exposure, including IR-spectrum, onto silicon structure parameters.

Key parameters of the developed modules are resulted in the Table 1

Table 1

Parameter, units	videomodule ИЛГ72-320x256ЛВ	videomodule ИЛГ72-160x80ЛВ
Length, mm	142	115
Width, mm	110	70
Thickness, mm	20	18
Information field pixel pitch, mm	0.3	0.5
Information field dimensions, mm	96x77	80x40
Luminance color	green	green

The basic characteristics of the videomodules

- | | |
|--|--------------------|
| 1.1. Brightness, cd/m ² (no optical filter) | not less than 1500 |
| 1.2. Brightness, cd/m ² (with optical filter) | not less than 300 |
| 1.3. Contrast at external light exposure 100000 lux | not less than 0,6 |
| 1.4. Brightness non-uniformity, % | ±10% |
| 1.5. Anode voltage, V | 25- 30 |
| 1.6 Power consumption, W/dm ² | not more than 10 |
| 1.7 Readiness time after switch on, s | not more than 2 |

In FSUE R&D I "Volga", the development and industrial development of two types of video-modules with information capacity 160x80 and 320x256 are carried out. The developed base design and manufacturing techniques will allow to considerably expand type-line of videomodules on the basis of active silicon substrate, and to create a new class of high-bright information display facilities – low-voltage cathodoluminescent screens for special purposes with quasi-static mode of information displaying.

The work results allow to create a parametrical number of multipurpose full-color AM VFD video-modules for onboard and industrial equipment of special purpose, including ones with necessary brightness gradation number. The developed active substrate can become a basis for creation of new classes of displays based on electro-luminescence of organic light-emitting diodes (OLED) and field emission effect (AM FED).

The photosensitive polymeric composites from inorganic and organic semiconductors and prospects of their use.

James G. Grote,

US Air Force Research Laboratory, Materials and Manufacturing Directorate,
Wright-Patterson Air Force Base, Ohio USA

Yaroslav I. Vertsimakha,

Institute of Physics NAS (Kyiv, Ukraine)

Abstract

In this work photosensitive in near IR region composites, based on polymers and polymethine dye (HITC, meso-Cl and cyan green), nanoPbS and V_2O_5 were developed.

The stable holographic gratings recording is found in polymethine dye/polymer composites (at low dye concentration) films at low intensity continuous He-Ne laser (632 nm) illumination. The diffraction efficiency is maximal at 2-3% dye concentration.

In PbS nanocomposite films are shown high nonlinear susceptibility (1-3 orders greater than for CdS nanocomposite) and weak photosensitivity in wider spectral range, than CdSe and CuInS₂ - polymer nanocomposite films. A characteristic feature of the films is the presence of green and blue luminescence with intensity maxima at 2.25 and 3.02 eV, respectively.

On the contrary, the composite with high concentration of dye (20-50 weight %) are well photosensitive in the range 500-950 nm. The photovoltage is maximal for composites based on I-VK-OMA co-polymers.

The high photosensitivity of these composites films is concerned with formation of photosensitive dimmer H-aggregate.

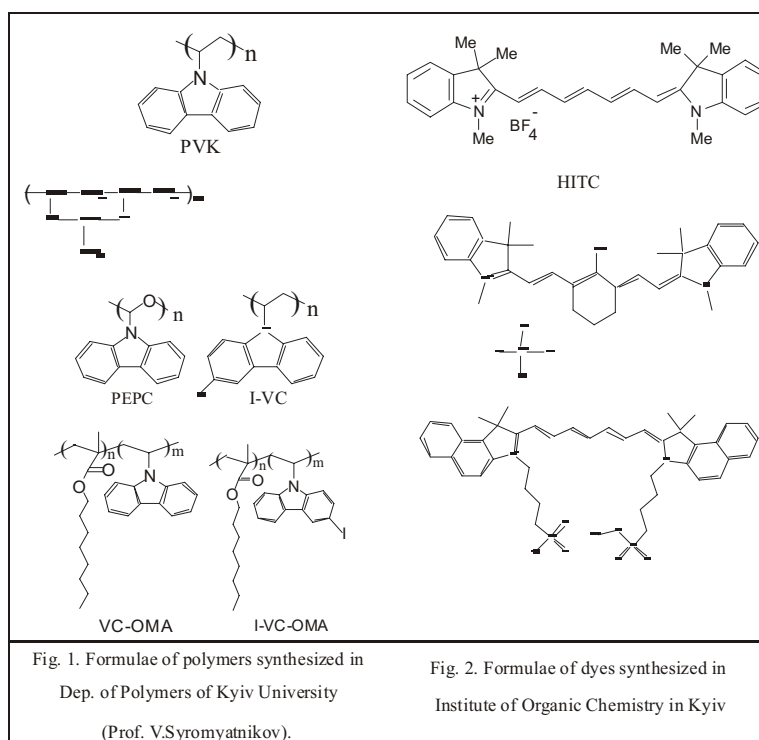
Introduction

In recent years the technology of polymeric nanocomposites films preparing for creation of recording media [1,2] and plastic solar cells [3,4] are actually developed. The most effective inorganic (Si and CuInSe₂) solar cells can effectively transform solar light in the range up to 1100-1200 nm. On the other hand the best of the nowadays-developed organic solar cells transform light only in the range 400-800 nm [3,4]. It is one of the reasons of their weak integral efficiency. Therefore our purpose was the development of polymeric composites layers, photosensitive in visible and near IR-region, which can be used for preparation of photoconverters and flexible low-cost media for holographic recording.

Experimental.

For composites films preparation we used as polymer matrix a polyvinilalcohol (PVA), polymers with carbazole groups, polyvinylethylal (PVE) (fig. 1) that are well soluble in volatile dissolvents and V_2O_5 xerogel. For photosensitivity increase I atoms to carbasole molecules (I-VC) while plasticity improvement the fatty acid tails (VC-OMA) were attached to polymeric chain (fig. 1).

The polymethine dyes were used as photosensitive component [5] that special modified by substitutes for solubility increase in organic dissolvent. The dyes solutions absorbance has maximum in the range 850-1050 nm. Also PbS nanoparticles were used. The composite films based on HITC, meso-Cl and cyan green were the most homogeneous and photosensitive (fig. 2).



The composite films based on polymethine dyes and carbazole-contained polymers were prepared by spin coating from dichloroethane solution.

The PbS nanocomposites films have been prepared by spinning of colloidal water solutions of PbS nanoparticles (19 wt.%) stabilized by PVA on glass substrates. PbS nanoparticles have been obtained mixing aqueous solutions of $Pb(NO_3)_2$ and Na_2S , followed by dialysis to remove Na^+ and NO_3^- ions. Technical details of obtaining the composite films have been described in [6]. The size of PbS particles embedded in the polymer matrix was determined from

the broadening of X-ray diffraction peaks. From the X-ray pattern we have estimated the average size of PbS nanoparticles: $D = (5 \pm 1)$ nm. For the X-ray analysis we have used a DRON-4.07 diffractometer (CuK α radiation).

The xerogel V₂O₅ layers were prepared by sol-gel method from colloidal solution, obtained with help Biltz method [7].

The thickness of the obtained films was 0.5 – 1 mm. Two kinds of substrates were used: plain glass was employed to prepare samples for optical measurements, whereas substrates covered with conducting ITO were used as transparent electrodes in photovoltaic experiments.

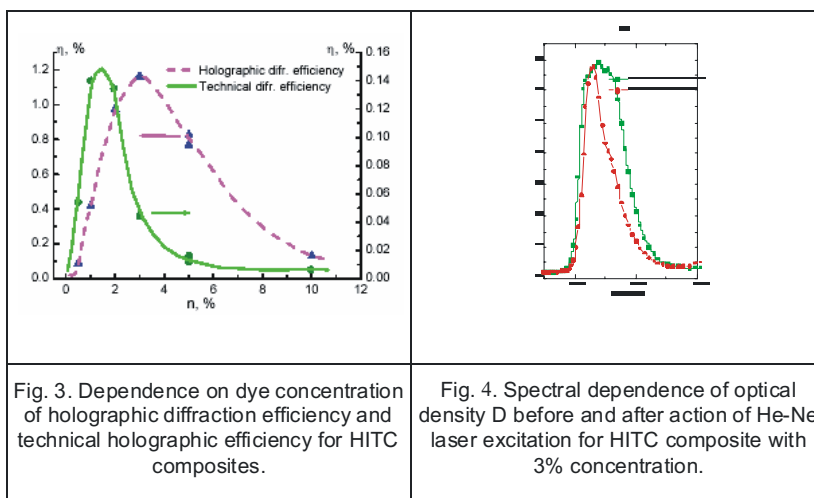
Absorption spectra (AS) were measured using a “Unicam UV-300” spectrophotometer, spectral dependence of a luminescence and its excitation – with help a “Hitachi” spectrophotometer.

The photovoltaic properties of the composites films have been investigated with help the Bergman method, modified by I. Akimov [8]. The method doesn't require any upper Ohmic contact on the samples which is an important advantage as the technology of deposition of such contacts hasn't been mastered yet. During the measurements, the samples were illuminated with modulated light (80 Hz) of different quanta energy (1.3-2.7 eV) from light-emitting diodes (LEDs). The photovoltage was measured with a Unipan type 232B nanovoltmeter. The modulated radiation power of LEDs was measured with a calibrated piroreceiver and the silicon photodiode.

Results and discussion

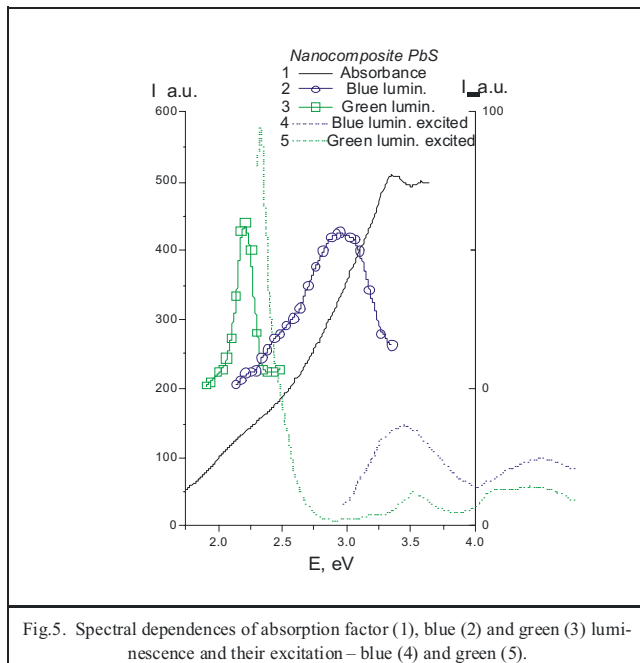
The properties of obtained polymeric nanocomposite films mainly depend on concentration of photosensitive component, polymer and dye molecular structure. At weak dye concentration in composites a luminescence and non-linear susceptibility show and photosensitivity are practically absent. On the contrary, at high dye concentration in composite photosensitivity are great, luminescence isn't visible and efficiency of diffraction media recording is weak. In is agree with luminescence and photosensitivity dependences on concentration for C60 nanocomposites.

For illustration as a sample in fig. 3 it is resulted in dependences of technical (ratio of first-order diffracted and ancient beams intensities) and holographic (ratio of diffracted first- and zero-order beams intensities) diffraction efficiency on HITS concentration in PVE.



It is shown that maximal diffraction efficiency is observed at 2-3% bulk concentration and exponential decrease at HITS concentration subsequent increase. The diffraction efficiency is proportional to laser illumination dose [9]. The compare of HITS AS in solution and polymeric composites after different illumination dose show that hologram recording is caused by dimmer H-aggregate destruction at laser irradiation absorption and increase of isolated molecules concentration that make less width of high-energy part of absorption band (fig. 4). The photovoltage measurements shown that charge carriers photogeneration efficiency is essentially greater at the aggregate illumination, than at isolated molecule illumination. And spectral dependence of V_s / D ratio has a maximums in the range aggregates absorption at 2.0 and 2.12 eV [9]. It is confirm H-aggregates formation at this energy.

The obtained PbS nanocomposites films in PVA matrix are photosensitive in the range 1.3-2.7 eV [10-12]. The PbS nanocomposites films have a green and blue luminescence with maximums at 2.25 and 3.02 eV, accordingly (fig. 5). The luminescence intensity depends on excitation energy and annealing temperature in air. The highest intensity of the green luminescence is observed at the excitation with the 2.35 eV radiation, whereas the intensity of the blue luminescence peaks under the 3.46 eV excitation. After annealing at 370 K, the intensity of the green luminescence decreases a few times whereas the intensity of the blue emission increases. The photovoltaic sensitivity of the PbS nanocomposite films does depend on the annealing conditions, attaining the maximum after annealing in air at approximately glass transition temperature of PVA (370 K). The spectral range of the photosensitivity of PbS nanocomposite films is wider than that of CdSe and CuInS₂ - polymer nanocomposite films.



The absorption bands maximums of the first electron transition for researched polymethine dyes solution (fig. 2) in organic dissolvents are visible in the range $E_s = 1.58-1.64$ eV, i.e. the transition energy weakly depends on molecular structure of these dyes (fig. 6). Naturally, at polymeric composites films formation the maximum energy shifting by 0.04-0.06 eV in low-energy range and asymmetric broadening of absorption bands occurs (fig. 7). The E_s shifting in low-energy range is the result of weak interaction in composites between dyes and polymers molecules. Strong asymmetry broadening of absorption bands, increased in some times at quantum energy grow in the range 1.5-2.2 eV, indicated that in polymeric nanocomposites films appears additional absorption in compare with low concentrated dye solution. The additional absorption is concerned with H-aggregates formation. It is typical for this polymethine dyes. And broadening of absorption bands in the range $h\nu < E_s$ is the result of statistic disordering of dyes molecules in composites film.

In the V_s spectra the band asymmetry are observed to be greater than in absorption spectra (fig. 7). It indicates that charge carriers photogeneration efficiency at light absorption by the aggregates (1.5-2.2 eV) is greater, than at absorption by isolated molecule. Naturally, some types of the aggregates form in composite films. These types are different both both molecules number and by the orientation in aggregate, and, consequently, they have different excitation energy. If charge carriers photogeneration efficiency at light absorption by the H-aggregates is greater, than by the isolated molecules, in spectral dependences of V_s the maximums should appear at aggregate exci-

tation. This maximums energies have to determinate H-aggregates energies while maximums magnitudes have to depend on both ratio of charge carriers photogeneration efficiency of aggregates and isolated molecules and efficiency of nonequilibrium charge carriers transport by aggregates across polymeric chain (polymer structure).

Our measurements of spectral dependences of V_s in meso-Cl/3I-VC-OMA composites films show presence some bends in the range $h\nu > E_s$ (1.65 - 2.1 eV). The aggregate energies may be determined more precisely by spectral dependences V_s/D ratio (fig. 8).

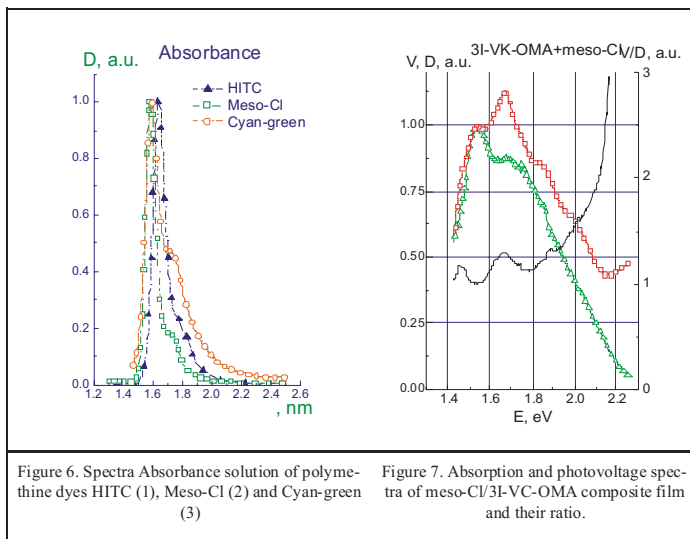


Figure 6. Spectra Absorbance solution of polymethine dyes HITC (1), Meso-Cl (2) and Cyan-green (3)

Figure 7. Absorption and photovoltage spectra of meso-Cl/3I-VC-OMA composite film and their ratio.

The well-defined maximums at 1.67, 1.89, 2.01, 2.09 and 2.2 eV are shown at these dependences, i.e. ratio of quantum efficiency of charge carriers photogeneration by aggregates and isolated molecules of dye is greater than one (1.29, 1.32, 1.63 and 1.87 times, accordingly).

The probability of defined aggregate type formation has to be proportional to ratio of this absorption band area to overall absorption bands area in the range of the first electron transition. For estimation of the probability it is necessary to fit by gauss components absorption band of the first electron transition. It may be done explicitly as energy position of all gauss components are sufficiently precisely determined from absorption spectra and V_s/D ratio. The analysis for meso-Cl/3I-VC-OMA composites shows that probabilities of aggregate formation at energies 1.67, 1.89, 2.01, 2.09 and 2.2 eV are 21, 14, 10, 11 and 5%, accordingly and total dye molecules amount which take part in H-aggregate formation consist of 60% and characterize aggregation efficiency in this polymer. In consequence of great charge carriers photogeneration efficiency in aggregate for 3I-VC-OMA composites their photosensitivity is greater, than for thermal deposited Cu and Pb phthalocyanines.

The charge carriers photogeneration efficiency by aggregate essentially depend on polymers [13]. For example, the efficiency of meso-Cl/VC-OMA composites films is in 3-5 times less, but efficiency of aggregate formation is practically the same.

For detail study of matrix influence on aggregation process we have prepared and researched composites films based on cyan green in V2O5 xerogel and PVA. As both PVA films absorb in ultra-violet range and aren't photosensitive and V2O5 xerogel films has weak photosensitivity only in the range $h\nu > 2.2$ eV [14], then their contributions in absorption and photovoltage spectra of composites based on cyan green are insignificant in the range $h\nu < 2.2$ eV and can be neglected. The compare of spectral dependences of V_s/D show that relative contribution of dimmer aggregates at energy 1.9-2.2 eV by V_s formation in polymeric composites is greater than xerogel composites [14]. It may be resulted of greater both probability of aggregate formation (greater content) and charge carriers photogeneration efficiency in polymeric composites, than in the xerogel. The compare of D spectra of these films exhibit that AS of these composites films are close, i.e. relative content of the aggregate in xerogel and PVA is practically coincident [14]. Consequently, in this dye and PVA composites the charge carriers photogeneration efficiency by high-energy aggregate is greater, than in xerogel composites.

Moreover in low-energy range of spectral dependence also the photosensitive center with energy near 1.34 eV are visible. As its energy is on 0.15 eV less, than energy of the first electron transition, probably, this center is the result of complex formation from dye and xerogel molecules [14].

It is shown in fig. 7 the V_s spectral dependences of polymeric composites received by us (curve 1-3) and C60 with conducted polymers [3,4] (curve 4,5) and one of most perspective inorganic semiconductors CdTe films (optimal semiconductor for solar light conversion) [15] (curve 6). At compare shown spectra (fig. 7) it make clear that solar light absorption efficiency of received by us polymeric composites aren't less, than barriers structures based on CdTe and are essentially greater, than in C60 polymeric composites.

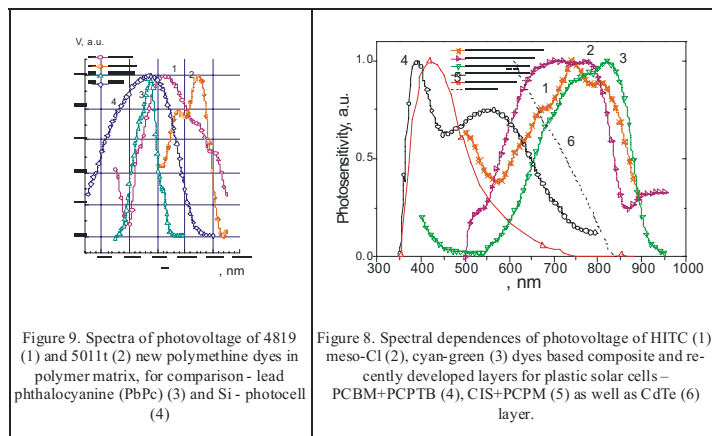


Figure 9. Spectra of photovoltage of 4819 (1) and 5011t (2) new polymethine dyes in polymer matrix, for comparison - lead phthalocyanine (PbPc) (3) and Si - photocell (4)

Figure 8. Spectral dependences of photovoltage of HITC (1), meso-Cl (2), cyan-green (3) dyes based composite and recently developed layers for plastic solar cells - PCBM+PCPTB (4), CIS+PCPM (5) as well as CdTe (6) layer.

However at present time received composites aren't inferior to structures based on Si in degree of solar light absorption and conversion in the range 850-1100 nm. Therefore for spectra broadening of polymeric composites in low-energy range we have made preliminary search of new polymethine dyes with absorption maximums in low-energy range that form photosensitive composites with PVE. The V_s measurements (fig. 9) confirm creation possibility of photosensitive materials for plastic photoconverters development that photosensitive in wider spectra range, than for Pb phthalocyanine [1] and Si.

Conclusions:

1. It is developed the basis of receiving technology of high-concentrated polymeric composites from inorganic and organic semiconductors (polymethine dyes) photosensitive in wide spectral range (including near IR-range). The degree of solar light absorption and width of photosensitivity spectral range of better of researched polymeric composites are greater, than plastic structures based on conducted polymers, sensitized by C60 derivative.

2. The composites with low concentration of polymethine dyes may be used for stationary hologram recording by low-power light sources (1mW) and/or nonlinear optics elements (dynamic hologram).

3. Great photovoltaic photosensitivity are shown at injection HITC, mesoCl θ cyan green dyes in polymeric matrix of J-VC-OMA. The cyan green is the most universal as let to prepare photosensitive composite with PVA, carbazole-contained polymers and V2O5 xerogel.

4. The main reason of the photosensitivity spectral range broadening of researched polymeric composites is H-aggregates formation and the stationary hologram recording is dye aggregates destruction at light harvesting.

5. The new polymethine dyes are found that let to wide photosensitivity spectral range in polymeric composites to 1.4 μ m.

6. Therefore at concentration 2-3% the studied dye composites can be used for stable holographic gratings recording, and at concentration 20-50% all studied polymeric composites and double-layer structures can be used for the development of plastic photoconverters sensitive in near-IR region, including organic solar cells.

References:

1. A.V.Kaznacheev, G.B. Nosov, A.S.Sonin, Soviet J. Optical Technol., 7, p.29 (1993).
2. I.A.Akimov, A.M.Meshkov, I.Yu.Denisyuk, Functional Materials, 5, p.363 (1998).
3. C.J.Brabec, N.Sariciftci, Erneuerbare Energien, 2, p.28 (1997); C.J. Brabec, N.C. Sariciftci, J.C. Hummelen, Plastic solar cells, Adv. Funct. Mater., 11, pp. 15-26, (2001).

4. Elif Arici, Serdar Saritifci N., Dieter Meisner, MCLC, 385, 129-136 (2002)
5. Ishchenko A.A., Theoretical and Experimental Chemistry, 34, 191-210, (1998)
6. A.S.Kutsenko, S.M.Maloletov, S.Ya.Kuchmii at al., Theoretical and Experimental Chemistry, 38, p.173 (2002)
7. Legendre J.-J., Livage J., J.Colloid and Interface Sci., 94, pp.73-83 (1983).
8. I.A. Akimov, Optical-Mechanic Industry, ?5, pp. 4-13 (1966) (in Russian).
9. O.Budnyk, R.Lymarenko, A.Savchuk at al., to be published Preceding of SPIE (2005)
10. P.Lutsyk, L.Dzura, A.Kutsenko, Ya.Vertsimakha, International Conference Polymers in XXI century, Kyiv, Ukraine, 27-30 October 2003, Abstract book, p.52
11. P.Lutsyk, A.Kutsenko, Ya.Vertsimakha at al, Semiconductor Physic, Quantum Electronic and Optoelectronics (in press, 2005)
12. Vertsimakha Ya.I., Lyakhovetsky V.R., Volkov at al., 7th Inter.Conf. on Frontiers of Polymers and Anvanced Materials (ICFRAM), Bucharest, Romania, 10-15 Juni 2003, p.
13. V.Syromyatnikov, Ya.Vertsimakha, A.Verbitsky, ICEPOM-5 Conference Abstracts, Kyiv, "Naukoviy Svit", 2004, -P.113.
14. L.I. Fenenko, A.A.Ishchenko, A.B.Verbitsky, Ya.I.Vertsimakha, Molecular Crystals and Liquid Crystals, 426, pp.157-169 (2005)
15. Pranab K., Raychaudhuri, J.Appl.Phys, 62, N7, 3025 (1987)
16. Kovalchuk A.V., Hamann C., Verzimakha Ja.I. u.a., Phys. stat. sol. (a), 74, K109 (1982).

INFLUENCE OF PREPARATION AND EXCITATION CONDITIONS OF ZnS:Er,F TFELS ON RADIATIVE CHARACTERISTICS IN VISIBLE AND NEAR-INFRARED SPECTRAL REGIONS.

N.A. Vlasenko, L.I. Veligura, Z.L. Denisova, M.A. Mukhlyo, Yu.A. Tsyrukunov

Institute of Semiconductor Physics, NAS Ukraine; Prosp. Nayki 41, Kyiv, 03028, Ukraine; e-mail: Vlasenko@isp.kiev.ua

V.F. Zinchenko, A.V. Bagazky

Physics-Chemical Institute; Lynstdorfska doroga str., 86, Odessa, 65080 Ukraine; e-mail: vfzinchenko@ukr.net

Abstract

The voltage (V) dependences of luminance and transferred charge of ZnS:Er,F TFELS prepared with varying of the annealing temperature (T_{ann}) are given at different frequency (f). The change in the relative intensity of the green band (523 nm) and the near-infrared bands (985 nm, 1530 nm) in the emission spectrum when V , f and T_{ann} are varied is considered too. The influence of the annealing temperature on the energy spectrum of defects in ZnS:Er,F film was studied by means of the photodepolarization spectroscopy. The revealed effect of the above excitation and preparation conditions on the radiative characteristics is discussed.

Introduction

Er-doped phosphors emitting at 1,54 μm are promising for application in optical fiber communications because this wavelength coincides with the absorption minimum of conventional silica-based fibers. There are many publications concerning the near-infrared (NIR) luminescence in Si- and SiO_x -based systems doped with Er (see, e.g., [1, 2] and references then). However, investigations of thin-film electroluminescent structures (TFELS) with this activator are scarce and mainly relates to their visible emission [3, 4]. The first study of ZnS:Er,F TFELS as emitters in the NIR region has been carried out recently [5 - 7]. The purpose of this paper is to study the influence of the applied voltage, its frequency and the annealing temperature of ZnS:Er,F film on the radiative characteristics, in particular on the relative intensity of the visible and NIR bands in the electroluminescence spectrum. To establish the origin of the revealed changes in radiative characteristics with the increase of T_{ann} , the energy spectrum of defects in the ZnS:Er,F film has been studied by means of the photodepolarization spectroscopy [8].

Experimental procedures

TFELS under study consist of an electroluminescent (EL) ZnS:ErF₃ films, two electrodes (ITO and Al films) and two insulator layers ($\text{Al}_2\text{O}_3/\text{I}_2\text{O}_3$ films), which separate the EL film from the electrodes. The ITO electrode deposited by magnetron sputtering was rather thin (~80 nm) to increase its optical

transmission in the NIR region. The insulator layers and the ZnS film were deposited by electron-beam evaporation at the substrate temperature of 170°C. Doping of the ZnS film was performed by the thermal co-evaporation of ErF₃. A part of the samples was annealed in vacuum after the deposition of the EL film at different temperature (from 300°C to 500°C). In other part of the unannealed samples, the ZnS:ErF₃ film was heated only up to 170°C during the deposition of the upper insulator layer.

The emission spectrum of the TFELS was measured by the spectrometer KSVU-23 with a photomultiplier as the detector in the range from 400 nm to 1050 nm and by a spectrometer based on a monochromator MDR-12 with a Ge diode as the detector in the range of 0.9 – 1.6 μm.

Electroluminescence was excited by sine-wave voltage of 1 – 20 kHz. The voltage and frequency dependences of the intensity in different bands in the EL spectrum as well as of the transferred charge were measured.

The energy levels of defects in the ZnS:Er,F film were studied by means of measuring of the photodepolarization (PDP) spectrum of the TFELS. The PDP spectrum is the spectral dependence of the photocurrent generated in the previously charged sample under action of the testing monochromatic light in a residual polarization field. This spectrum was measured as it was described in [8]. Charging of the TFELS was performed by a dc voltage equal to $\sim V_{th}/2$, where V_{th} is the threshold voltage of the EL. The interference extrema in the PDP spectrum were averaged. The samples were illuminated from the ITO electrode side.

Results and discussion

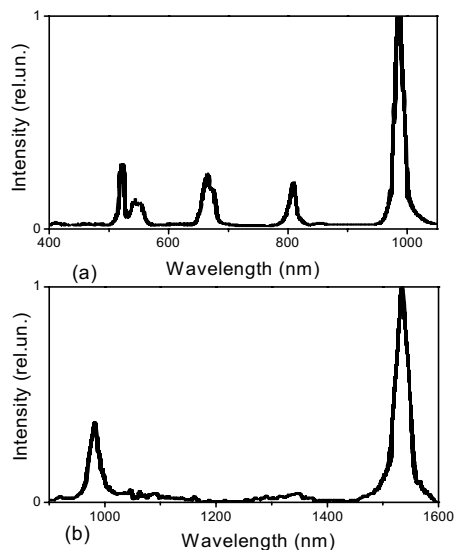


Fig. 1. Typical emission spectrum of ZnS:Er,F TFELS in ranges: 400-1050 nm (a), 900-1600 nm (b).

The emission spectrum of the ZnS:Er,F TFELS is shown in Fig. 1.

The intensity of the emission bands in the NIR region is significantly higher than that of the visible emission. The electron transitions and the lifetime for all bands are given in Table 1. The decay of the electroluminescence is more fast, the shorter wavelength of the band.

The typical voltage dependences of the luminance (L) and the transferred charge (Q) at different frequency are given in Fig.2 for the ZnS:Er,F TFELS annealed at 500°C. These dependences have some distinctions from analogous characteristics of ZnS:Mn TFELS. There is a marked section at voltage lower than the threshold voltage (V_{th}). The steep section at $V > V_{th}$ is shorter. The luminance at the saturation section is rather low. It increases nearly proportionally with increasing of f because it is due mainly to the green emission that decays very fast. The transferred charge at given V increases when $f < 5$ kHz.

λ_{max} , nm	Electron transition	τ , ms	τ_e , ms	Reference
1530	$^4I_{13/2} \rightarrow ^4I_{15/2}$	1,8	1,5	[7]
980	$^4I_{11/2} \rightarrow ^4I_{15/2}$	0,9	0,4	[7]
810	$^4I_{9/2} \rightarrow ^4I_{15/2}$	0,5	0,1	[7]
665	$^4F_{9/2} \rightarrow ^4I_{15/2}$	~ 0,3	0,05	[7]
547	$^4S_{3/2} \rightarrow ^4I_{15/2}$	0,06		[3]
525	$^2H_{11/2} \rightarrow ^4I_{15/2}$		0,02	[7]

Table 1. Electron transition, lifetime, and e-fold decay time for different excited states of Er³⁺ ion in ZnS:Er TFELS.

The influence of the annealing temperature on the L(V) and Q(V) dependences is illustrated by Fig.3.

The effect of T_{ann} on both characteristics is the same. The threshold voltage increases with T_{ann} up to 300°C, but becomes lower at further rising of the annealing temperature even against V_{th} of the unannealed sample. The magnitude of L and Q on the saturation section of these characteristics is almost independent on T_{ann} .

The comparison of the voltage dependence of the intensity of the green and NIR emission bands (Fig.4) shows that the dependence is stronger for the bands with the shorter wavelength. This is inherent for the impact excitation mechanism of the electroluminescence.

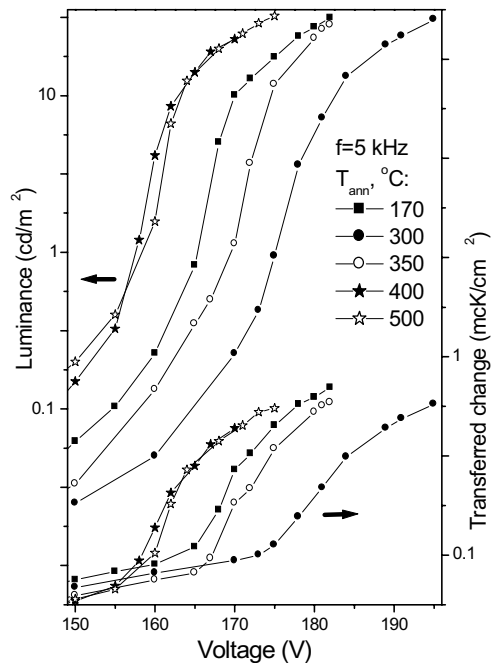


Fig.3. Voltage dependences of luminance and transferred charge of samples annealed at different temperature.

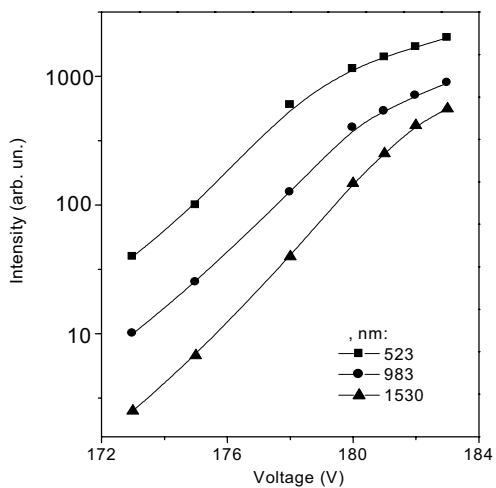


Fig.4. Typical voltage dependence of intensity of different emission bands of ZnS:Er,F TFELS.

The frequency dependence of the intensity of the green and NIR bands in the EL spectrum is also somewhat different (Fig.5). The former increases linearly with increasing of f . However, the intensity of the NIR bands, especially of the 1.53 μm band intensity, increases sublinearly with frequency. This correlates with the lifetime of the respective excited states.

The change of the annealing temperature results in some changes in the relative intensity of the bands in the EL spectrum. The intensity of the bands with the longer wavelength (λ) increases at first relative to the bands with the shorter λ with increasing of T_{ann} up to 350°C. However, it begins to decrease at further rising of the annealing temperature up to 500°C (Tab.2). It is possible that such a change of the relative intensity of the emission bands is due to a change in the crystal field symmetry near by Er^{3+} ion resulting from the thermal dissociation of the quasi-molecular centers (ErF_3) during annealing.

$T_{\text{ann}}, ^\circ\text{C}$	170	300	350	400	500
I_{1530}/I_{523}	15	16.8	18	16.8	13.2
I_{1530}/I_{983}	5.3	5.6	6	5.1	4.1

Table 2. Relative intensity of NIR and green emission bands

The appearance of new centers in the $\text{ZnS}:\text{ErF}_3$ film after its annealing is confirmed by the PDP spectra of the TFELS annealed at different temperature (Fig.6). The impurity photocurrent with the main maximum nearly the band-gap energy of ZnS (3,68 eV) dominates in the PDP spectra independent on T_{ann} .

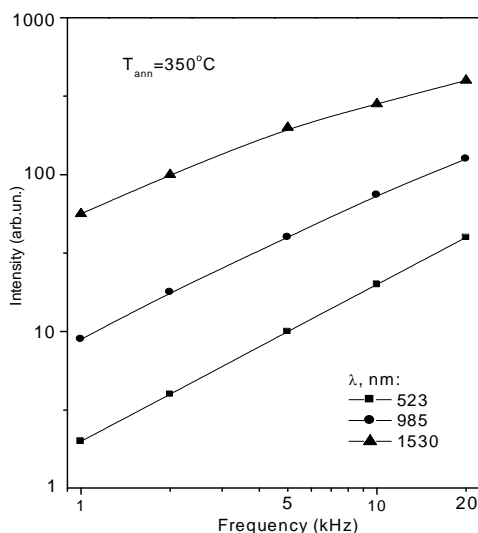


Fig.5. Typical frequency dependence of intensity (I) of different bands on saturation section of I(V) characteristic for $\text{ZnS}:\text{Er},\text{F}$ TFELS.

However, the energy of this peak somewhat differs in the samples annealed at low and high temperature, namely, 3,37 eV and 3,45 – 3,5 eV at 170°C and $\geq 400^\circ\text{C}$, respectively. There are both peaks in the case when T_{ann} is equal to 300 – 350°C. It is reasonable to assume that the peaks are connected with interstitial Fi atoms, which capture an electron due to the high electron affinity (3,4 – 3,5 eV). In the ZnS:ErF₃ films annealed at $\leq 200^\circ\text{C}$, these atoms are neighboring with Er³⁺ ion forming with it the ErF₃ quasi-molecular center. After the high-temperature annealing, single Fi- ions predominate because of the ErF₃ center dissociation. Both Fi- centers are present when $T_{\text{ann}} = 300 - 350^\circ\text{C}$.

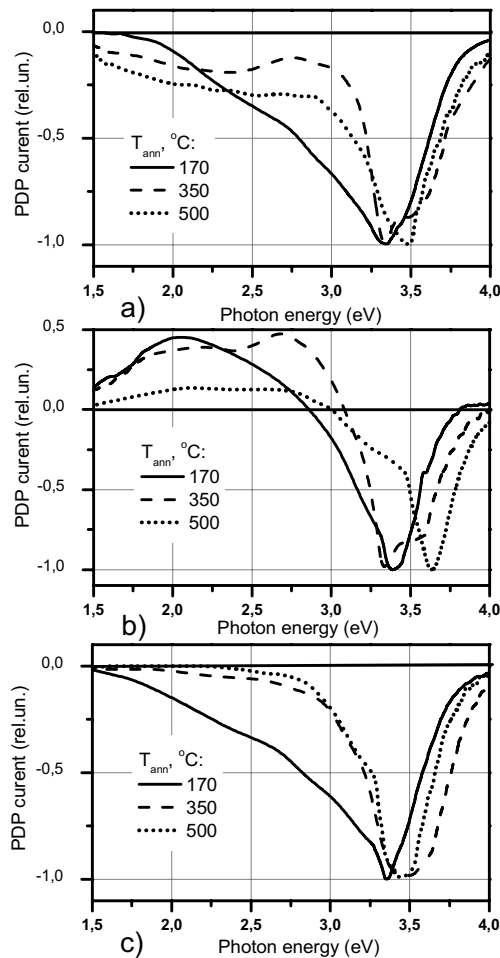


Fig.6. Normalized PDP spectra of ZnS:Er,F TFELS annealed at different temperature. Measuring of the spectra was after charging of sample by "-Al" polarity voltage (a), by "+Al" polarity voltage (b), and without of charging (c)

Other peaks, which appear in the PDP spectra after annealing in vacuum of the ZnS:ErF₃ films (2,0 eV; 2,25 eV; 2,75 eV), are also due to the ErF₃ dissociation and the appearance of such centers as donor-acceptor pairs (Er³⁺ – Fi; FS⁺ – Fi; VS⁺ – Fi, where VS is the sulfur vacancies) as well as the Fi- – Fi- complexes and another fragments of the dissociated quasi-molecules.

It should be noted that the PDP spectra measured after charging by the voltage of the "-Al" and "+Al" polarity have an essential difference. The former (Fig.6a) has the unidirectional photocurrent, but the latter (Fig.6b) consists of two regions with the oppositely directed photocurrent. In the case of the "-Al" polarity, the spectrum is very similar to the PDP spectrum of the uncharged TFELS (Fig.6c). The above features of the PDP spectrum indicate the following: 1) there is a negative space charge (NSC) in the ZnS:Er,F film in the equilibrium state and after the charging that results in the presence of the regions with the opposite direction of the polarization field; 2) the concentration of different centers differs in these regions. The NSC is due to the existence in the film of electron traps such as [ErF₃]0 and Fi0. The gradient of the concentration of different centers results from the diffusion of F to the film surface and its partial volatilization during the annealing in vacuum. The number of different centers and the gradient of their concentration depend on T_{ann}. The detail consideration of all features of the PDP spectra of the ZnS:Er,F TFELS and the nature of the centers responsible for the photocurrent peaks will be a subject of a special paper.

Conclusions.

The dominant emission band in the EL spectrum of the ZnS:Er,F TFELS is the 1,53 μm band that is rather narrow (~20 nm). This band is the most actual for application in fiber optical communications. The voltage and frequency dependence of this band is weaker than that of the green bands. This is due to the lower energy and the longer lifetime of the excited state of this NIR emission band than that of the bands in the visible region of the EL spectrum.

The increase of the annealing temperature results in: 1) a decrease of the threshold voltage of EL; 2) a decrease of the time necessary for the stabilisation of the voltage dependences of the band intensity and the transferred charge; 3) a change of the intensity of the NIR emission relative to that of the visible emission; the relative intensity of the NIR bands is somewhat higher when T_{ann} = 300 – 350°C.

The change in the emission characteristics with the increase of T_{ann} is due to the appearance of new defects and the change of their number, which results from the dissociation of the ErF₃ quasi-molecular centers. It is evidently that the quasi-molecular centers ErF₃ with the C_{3v} symmetry dominate at T_{ann} < 200°C whereas the substitutional Er³⁺ ions with T_d symmetry are predominant at T_{ann} > 400°C. Annealing at 300 – 350°C leads to the formation of Er³⁺ centers with the lower symmetry, e.g. of (Er³⁺ – Fi-) centers.

References

- G. Kocher-Oberlehner, W. Jantsch, L. Palmetshofer, A. Ulyashin. Appl. Phys. Lett. 83 (2003) 623.
- C.L. Heng, T.G. Finstad, R. Storås, I.J. Li, A.E. Gunnaes, O. Nilsen. Appl. Phys. Lett. 85 (2004) 4475.
- L.-J. Meng, C.-H. Li, G.-Z. Zhong. J. Lumin. 39 (1987) 11.
- T. Hirate, T. Ono, T. Satoh. Proc. 22th Intern. Display Research Conference, Oct. 1-4, 2000, Nice, France, p.693.
- A. Kale, W. Glass, M. Davidson, P. Holloway. Proc. 11th Intern. Workshop on Inorganic and Organic Electroluminescence. Sept. 23-26, 2002, Gent, Belgium, p. 57.
- Ya.F. Kononets, L.I. Veligura, N.A. Vlasenko, Z.L. Denisova, V.F. Zinchenko. Optoelectronics and Semicond. Technol. 38 (2003) 225 (in Russian).
- N.A. Vlasenko, Z.L. Denisova, Ya.F. Kononets, L.I. Veligura, Yu.A. Tsyrukunov. J. SID, 12 (2004) 1.
- N.A. Vlasenko, A.I. Beletskii, Z.L. Denisova, et. al. Proc. of SPIE "Optical Diagnosis of Materials and Devices for Opto-, Micro-, and Quantum Electronics", v. 3359, 1998, p. 512.

The method to suppress off-axis haze of PDLC

L.O. Dolgov, O.V. Yaroshchuk,

Institute of Physics, NASU, prospect Nauki 46, 03028 Kyiv, Ukraine
ph./fax: (38044)5252424, e-mail: olegyar@iop.kiev.ua

Abstract

Conventional polymer dispersed liquid crystals (PDLCs) suffer from discrimination of on-state transmittance for oblique incidence light (off-axis haze effect). The point is that refractive index of polymer component is usually adjusted to ordinary refractive index of liquid crystal (LC). So in the applied electric field there is transparent state with matching of LC and polymer refractive indices for the normal light incidence. At the same time, balance of refractive indices is broken and on-state transmittance is smaller for oblique light incidence. To diminish of-axis haze (to broaden viewing angle characteristic of PDLC), refractive index of polymer should be slightly higher than ordinary refractive index of LC. We propose to satisfy this condition by doping PDLC with high refractive index inorganic nanoparticles. In such a way one can continuously vary refractive index of polymer and so optimize system for minimal off-axis haze.

Keywords: PDLC, nanoparticles, transmittance, off-axis haze.

Introduction

Polymer dispersed liquid crystals (PDLC) [1,2] belong to scattering LC composites, which present an alternative for oriented LC layers in production of LCD, optical switches and shutters. In contrast to traditional devices based on oriented LC layers, PDLC don't need polarizers, alignment layers and high uniformity of cell gap. These features coupled with high brightness of composite layers make PDLC rather attractive for applications.

Typical PDLC consists of large amount of spherical LC droplets chaotically distributed in polymer (P) matrix. The refractive index of polymer, n_p , is usually adjusted closely to ordinary refractive index of LC n_{LC}^o . In the absence of driving electrical field the composite strongly scatters light. The main scattering reason is mismatching of refractive indexes of the polymer and chaotically oriented LC droplets [3]. The droplets orient in the external electric field so that their refractive index approaches n_p . For normal light incidence this matching of indices yields to the high on-state transmittance of PDLC layers. At the same time, for oblique light, the balance of refractive indices is broken so that scattering becomes stronger, while on-state transmittance becomes smaller. Such angular worsening of the on-state transmittance is known as off-axis haze of PDLC.

Per last years the problem of the off-axis haze suppression in PDLC has been intensively studied [4-7]. The simplest way consists in setting of polarizer in front of PDLC film with polarization direction perpendicular to the light incidence plane [4]. Indeed, light of this polarization (s-wave) is not

sensitive to changes of light incidence angle. However, polarizer decreases brightness of PDLC film at least in twice that makes this method not very attractive. The other solution [5] suggests to replace isotropic polymer by anisotropic one with ordinary and extraordinary refractive indices approximately equal to n_{LC}^o and n_{LC}^e , respectively. The serious problem of this method is selection of anisotropic medium and its proper alignment in PDLC.

The most common and realistic decision consists in selection of isotropic polymer with the refractive index satisfying inequality

$$n_{LC}^o < n_p < n_{LC}^e, \quad (1)$$

where n_{LC}^e is the extraordinary refractive index of LC [6,7]. When (1) is true, then peak of maximal transmittance for PDLC is shifted away from normal incidence so that range of viewing angles with sufficiently high on-state transmittance becomes broader.

In this paper we propose the modified version of the last approach. Instead of choosing polymer with proper optical parameters we suggest to modify optical properties of polymer, which is already optimized for the formation of PDLC with the selected LC. The refractive index of polymer can be continuously varied by doping it with nanoparticles (NP) having refractive index substantially higher than that of polymer. This method is based on the earlier ascertained fact that, in the course of phase separation of LC-P-NP mixtures, the nanoparticles are mainly absorbed by polymer changing its optical properties. The effectiveness of this method is experimentally demonstrated.

Experimental part

We used traditional materials: nematic liquid crystal mixture E7 from Merck and optical adhesive NOA65 provided by Norland Inc. (USA) for making PDLC [8]. Nematic mixture E7 consists of three cyanobiphenyls (5CB-51%, 7CB-25%, 80CB-16%) and n-pentylcyanoterphenyl (5 CT-8%). This mixture is characterized by relatively broad mesomorphic region (from -10°C to 58°C) and optical anisotropy (refractive indices are $n_{LC}^o=1.5216$, $n_{LC}^e=1.7462$) [8].

Norland optical adhesive NOA65 is a mixture of three monomer constituents: trimethylolpropane diallyl ether, trimethylolpropane trithiol, isophorone diisocyanate ester and photoinitiator. In the initial state it is transparent (refractive index $n_p=1.524$), liquid (density is $\rho = 1.12 \text{ g/cm}^3$) and viscous (1200 cps at 20°C) mixture. NOA 65 becomes hard under the action of UV light due to accurately balanced chemical reaction [9].

As filler for PDLC we used several types of inorganic NP with different refractive indices of their materials. They are SiO_2 NPs (size 10-20 nm, refractive index $n_{\text{SiO}_2}=1.46$) and Sb_2O_5 NPs (size 7-11 nm,

$n_{Sb_2O_5} = 1.7$). NP of silica and antimony pentoxide were provided by Nissan Chem. Inc. (USA) in the form of dispersions in alcohol medium.

We mixed components thoroughly for the preparation of composites. The range of filler's concentrations in the mixture was varied from 0 to 3 vol.%. In all samples the volume concentration of LC was 63 %. Such amount of LC is optimal for PDLC morphology [3, 10]. The alcohol presented in NP colloid was removed by intensive stirring. The complete removing of alcohol was achieved by applying a vacuum to the suspension at 10^{-2} Torr over 0.5 h.

To obtain desirable PDLC films we placed the drop of mixture between two glass slides having transparent ITO electrodes in the inner side. The cell gap was maintained by 20 μm spacers. Then the cells were irradiated with the full spectrum of a high pressure mercury lamp (100 mW/cm^2 , 20 min), in order to provide photopolymerization and corresponding phase separation of components.

We used typical setup, which test the optical transmittance of a laser beam through the tested sample [11]. The sample is powered by a sine-like voltage signal 0-200 V ($f=2$ kHz) synthesized by computer and, subsequently, amplified. Using this set up one can determine the sample transmittance

$$T = \frac{I_{out}}{I_{in}}$$

(I_{in} and I_{out} are the intensities of the probe beam before and after passing through the sample) as a function of the applied voltage U .

Angular dependences of the transmittance at the voltage corresponding to saturation of $T(U)$ curve were measured by means of sample rotation on 0, 15, 30, 45 50, 60, and 70 degrees.

Results and discussion

The $T(U)$ curves for pure PDLC and PDLC doped with 1 vol.% of inorganic nanoparticles of Sb_2O_5 and SiO_2 (Sb_2O_5 -PDLC and SiO_2 -PDLC, respectively) are presented in Fig. 1. Qualitatively, all dependences are rather similar: T rises with the increase of driving voltage U until reaching saturation level T_s . At the same time, saturation transmittances are different and reached at different values of applied voltage. In the following measurements of angular characteristics the applied voltage corresponded to saturation state of all samples.

Fig. 2 shows dependences of T_s vs. incidence angle θ for pure PDLC and PDLC doped with different types of NPs. The light is polarized in the incidence plane so that it is maximally sensitive to the changes in the incidence angle. One can see that in case of pure PDLC and SiO_2 -PDLC samples T_s monotonically decreases. In contrast, for Sb_2O_5 -PDLC T_s changes slowly and non-monotonically going through maximum. In the range of 0° - 50° the transmittance T_s changes inessentially, while for the higher angles it does not decrease abruptly as in the case of other samples (Fig. 2). In other words,

$T_s(\theta)$ curve considerably flattens that is the evidence of the substantial suppression of the off-axis haze.

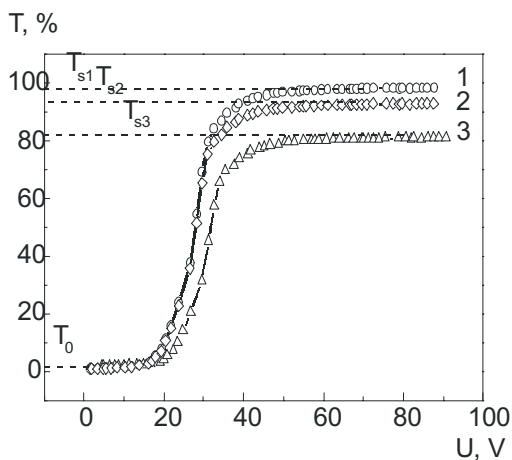


Fig. 1. $T(U)$ dependences for pure PDLC and PDLC doped with NPs. 1 - $\varphi_{LC} = 63$ vol.%, $\varphi_{NP} = 0$ vol.%, polymer - the rest; 2 - $\varphi_{LC} = 63$ vol.%, $\varphi_{NP} = 1$ vol.% (SiO₂ NP), polymer - the rest; 3 - $\varphi_{LC} = 63$ vol.%, $\varphi_{NP} = 1$ vol.% (Sb₂O₅ NP), polymer - the rest.

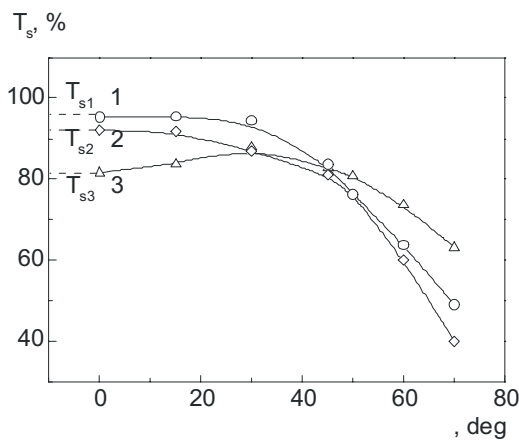


Fig. 2. The saturation transmittance T_s for pure PDLC and PDLC doped with NPs as a function of light incidence θ . The light is p-polarized. 1 - pure PDLC ($\varphi_{NP} = 0$); 2 - $\varphi_{SiO_2} = 1$ vol.%; 3 - $\varphi_{Sb_2O_5} = 1$ vol.%. For all cases $\varphi_{LC} = 63$ vol.%, the rest is polymer content.

According to Fig. 3 the shape of $T_s(\theta)$ curve for Sb₂O₅-PDLC composite is rather sensitive to concentration of NP. The increase of NP concentration leads to better flattening of $T_s(\theta)$ curve, but, simultaneously, to lowering of sample transmittance for small angles of light incidence. Thus, concentration of NP should be well optimized to obtain samples with acceptable electrooptic contrast and angular characteristic.

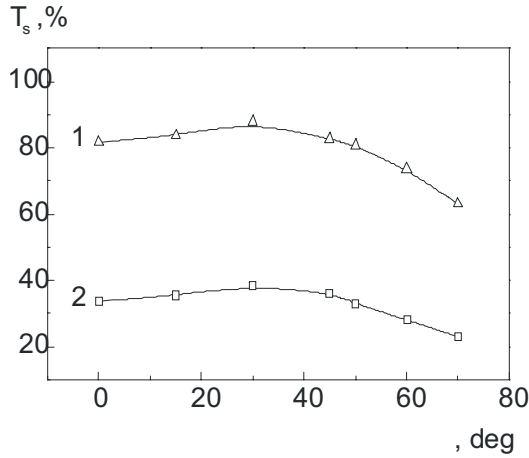


Fig. 3. The saturation transmittance T_s vs. incidence angle θ curves for PDLC doped with different amount of Sb₂O₅: 1 - $\phi_{NP} = 1$ vol.%, 2 - $\phi_{NP} = 3$ vol.%. For all cases $\phi_{LC} = 63$ vol.%, the rest is polymer content.

To explain the observed suppression of the off-axis haze let us remind results recently obtained [10, 12].

1. The addition of small amount of NP to LC-P mixtures (less than 5 vol.%) before polymerization does not change PDLC morphology of these samples.

2. In the course of the photoinduced phase separation the nanoparticles are mainly absorbed by the formed polymer matrix. In contrast to the pure polymer P we shall mark NP modified polymer as \tilde{P} .

3. The small amount of NP (less than 5 vol.%) changes refractive index of polymer rather than its optical uniformity.

The above means that NP vary refractive properties of polymer changing the refractive index balance of LC and modified polymer \tilde{P} . The changes in refraction can be qualitatively analyzed using the refractive indices diagram (Fig. 4). The refractive index of SiO₂ NP is close to polymer refractive index. So particles of this sort practically do not influence refractive index of polymer. This explains why $T_s(\theta)$ curves for PDLC and SiO₂-PDLC are of similar shape and close each to other. For both these systems, at $\theta=0$, $n_p \cong n_{LC} = n_{LC}^o$ so that light transmittance is high. With θ increase, n_{LC} grows approaching n_{LC}^e at grazing incidence. This causes growing of the refractive index mismatch, $n_{LC} - n_p$, and so light scattering in PDLC. Besides, light scattering grows because of lengthening of light pass in the composite layer. Consequently, light transmittance should demonstrate fast monotonic decrease that fully corresponds to experimental observation (curves 1, 2 in Fig 2).

Refractive index of antimony pentoxide is considerably higher than n_p (close to n_{LC}^e). So, doping of PDLC with Sb₂O₅ NP leads to an increase in the refractive index of the polymer phase \tilde{P} so as $n_{LC}^o < n_{\tilde{P}} < n_{LC}^e$. Since $n_{\tilde{P}}$ does not match n_{LC}^o , T_s at the normal incidence is not so high as in the case of PDLC and SiO₂-PDLC composites.

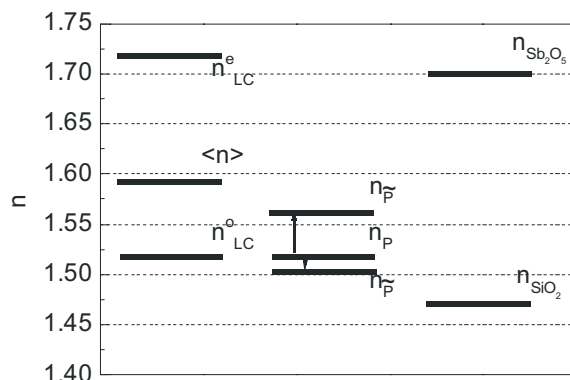


Fig.4. The refractive indices diagram for the nanoparticles, polymer and LC.

The mismatch of n_p and n_{LC} changes non-monotonically with a grow of θ . It decreases, vanishes at some light incidence angle $\theta_c \neq 0$ and finally grows. The scattering tendency determined by the non-monotonic refractive index mismatch superposes with the scattering trend connected with the light pass grow with the incidence angle. In result, $T_s(\theta)$ should be non-monotonic: maximal transmittance should be shifted away from the normal incidence to the angle $\theta_c \neq 0$. Simultaneously, range of angles corresponding to relatively high transmittance should become broader. This explains well result for Sb_2O_5 -PDLC composite (curve 3 in Fig. 2).

Conclusions

In summary, modification of polymer's refractive properties by inorganic nanoparticles may be applied to suppress off-axis haze of PDLC. Using this approach it is not needed to find polymer with appropriated refractive properties. Instead, refractive index of any polymer can be modified by insertion of NP with high refractive index in PDLC to meet condition (1) required to suppress off-axis haze.

Acknowledgements

This work was carried out within the framework of the project “Development and investigation of multifunctional nanocomposite materials “organic matrix-inorganic nanoparticles” for new technologies” of the NASci. of Ukraine.

References

1. Liquid Crystals Applications and Uses / Edited by B. Bahadur. - Singapore: World Scientific, 1990. - Vol.1, 604 pp.
2. Chigrinov V.G. Liquid crystal devices: Physics and Applications. - Boston-London: Artech-House, 1999.- 357 pp.
3. Bouteiller L., Le Barny P. Polymer-dispersed liquid crystals: Preparation, operation and application // Liq. Cryst.-1996.- Vol. 21.- Д.157-174.

4. West J. L., Fredley D. S., Carrell J. C. Haze-free polymer dispersed liquid crystals utilizing linear polarizers // *Appl. Phys. Lett.* – 1992. – Vol. 61, No.17. – P. 2004-2005.
5. Doane J. W., West J. L., Tamura-Lis W., and Whitehead J. B. Polymer dispersed liquid crystals for haze-free, wide-angle view light shutters // *Pacific Polymer Preprints I.* – 1989. – P. 245-246.
6. Wu B.-G., West J. L., and Doane J. W. Angular discrimination of light transmission through polymer-dispersed liquid-crystal films // *J. Appl. Phys.* – 1987.- Vol. 62, No. 9. – P. 3925-3931.
7. Drzaic P., Konyonenburg P. V., US Patent 5,156,452 (1992).
8. Bhargava R., Wang S.-Q., and Koenig J. L. FTIR Imaging Studies of a New Two-Step Process To Produce Polymer Dispersed Liquid Crystals // *Macromolecules.* – 1999.-Vol. 32.-P. 2748-2760.
9. Norland Products Inc., P.O. Box 145, North Brunswick, NJ 08902.
10. Dolgov L. O., Yaroshchuk, O. V. Electrooptics of the Suspensions of Monodispersed Non-Organic Particles in Liquid Crystals // *Mol. Cryst. Liq. Cryst.*-2004.-Vol. 409.- P. 77-89.
11. Zakrevska S., Zakrevskyy Yu., Nych A., Yaroshchuk O., Maschke U. Electro-optics of LC-aerosil-photopolymer composites // *Mol.Cryst.Liq.Cryst.* -2002.- Vol. 375. – P. 467-480.
12. Yaroshchuk O.V., Dolgov L. O., Kiselev O. D. Electro-optics and structural peculiarities of liquid crystal-nanoparticles-polymer composites // Accepted to *Phys. Rev. E.*

Liquid crystal alignment on the films deposited by sputtering: dependence on target material and gaseous feed

O. Yaroshchuk¹, R. Kravchuk¹, L. Dolgov¹, E. Telesh², A. Khokhlov³,
J. Brill⁴, N. Fruehauf⁴, M.A Reijme⁵,

¹Institute of Physics, NASU, prospekt Nauki 46, 03028 Kyiv, Ukraine,

²Belarusian State University of Informatics and Radioelectronics,
Brovki Str. 6, Minsk, Belarus

³Izovac Ltd., Bogdanovicha 155, 220040 Minsk, Belarus;

⁴LfB, University of Stuttgart, Allmandring 3b, 70569 Stuttgart, Germany;

⁵Philips Research, Prof. Holstlaan 4, 5656 AA, Eindhoven, the Netherlands

The alignment of liquid crystals (LC) on the films made by oblique ion beam sputtering deposition is comprehensively studied. The sputtering setup was constructed on the base of anode layer source designed by Izovac Ltd. (Belarus). We used vitreous silica and graphite as target materials and Ar, CF₄, Ar/CH₄ and Ar/C₃H₈ as feed gases. Independently on deposition angle, the tested LC with $\epsilon < 0$ aligns in the incidence plane of particle beam (1st alignment mode), while LCs with $\Delta\epsilon > 0$ in the plane perpendicular to the incidence plane (2nd alignment mode). More specifically, LC with $\Delta\epsilon < 0$ shows high pretilt angles (87°-90°) on silica films (Ar, CF₄, Ar/CH₄ and Ar/C₃H₈ feed gasses). The value of pretilt angle on these films, in case of Ar/CH₄ and Ar/C₃H₈ gaseous mixtures, can be smoothly varied by varying the hydrocarbon gas concentration. On graphite films (Ar and CF₄ feed gasses) the initial alignment of LC with $\Delta\epsilon < 0$ is similar to that on the silica films. However, the pretilt angle relaxes to zero for about one week. The LCs with $\Delta\epsilon > 0$ on the silica films shows planar alignment in the 2nd mode independently of the type of gas that was fed. In contrast, on graphite films, the alignment of LC with $\Delta\epsilon > 0$ depends on the gas that was fed during deposition. Under Ar gas this LC aligns in the 2nd mode, while when feeding CF₄ gas it aligns in the 1st mode. The alignment in the 1st mode deteriorates within several weeks and so only planar LC alignment is stable on the films sputtered from the graphite target.

1. INTRODUCTION

The oblique deposition, as a method of liquid crystal (LC) alignment, was proposed by J. Janning three decades ago [1]. In his experiments highly uniform LC alignment was observed on SiO_x films obtained by oblique vapor deposition (VD). These results excited tide of research interest [2-7], because of excellent alignment uniformity, use of inorganic layers, non-contact processing *etc.* It was established that alignment of many LC (mainly LC with $\Delta\epsilon > 0$ and some LC with low $\Delta\epsilon < 0$) on VD layers is very sensitive to the angle of deposition α (in this paper, the angle between the film normal and particle flux). In case of a greater than some critical angle α_c , which usually is within 70°-80°, the easy axis of LC lies in the incidence plane of particle flux and tilts towards direction of particle flux incidence (1st mode). In the opposite case, $\alpha < \alpha_c$, planar alignment is induced with the easy axis perpendicular to

the particles' incidence plane (2nd mode). By analogy with the particle beam etching procedure [8,9] we define the described alignment types as the 1st and the 2nd alignment mode. They are schematically presented in Fig. 1a and Fig. 1b, respectively. For the LC with $\Delta\epsilon < 0$ developed for VAN LCD the VD technique provides homeotropic or tilted vertical alignment in the 1st alignment mode [5-7].

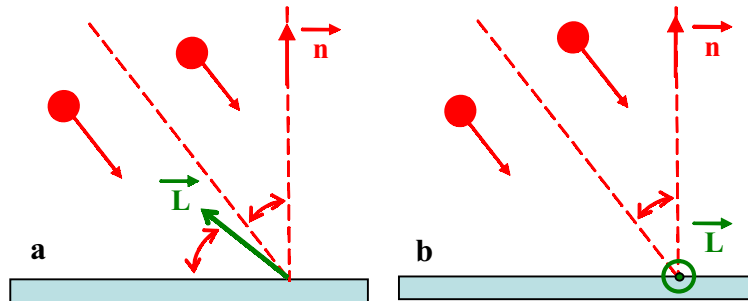


Fig 1.

In spite of big promise and great research efforts paid for VD technique it remains to be the technique for laboratory use. This is caused by technological limitations (e.g., it is hard to adapt this technique for the alignment coating on the large area substrates and for the mass line production) and non-suitable alignment parameters (e.g., pretilt angle of LC with $\Delta\epsilon > 0$ is higher than 10°).

The new impulse to the oblique deposition LC alignment technology gave the ion beam sputtering deposition (SD). In this process the material is only extracted from the top layer of the material (target) due to bombardment with ion beam. It substantially lowers power consumption, as compared with a vapor deposition. Using extended sputtering sources one can produce SD coatings on the large area substrates, including G6 and G7 fabs [10]. It is also important that SD operates with particles of substantial energy (several electronvolts and higher) that may bring alignment properties different from VD.

In spite of big promise, a small attention is only paid to this alignment procedure [11-14]. In fact, mostly LC alignment on SiO_x films is considered. There is lack of data concerning the dependence of LC alignment on the material and processing conditions, corresponding alignment modes and alignment stability.

With the present paper we try to fill partially this important gap. We extend the quantity of alignment materials by the use of two different targets. Besides, varying the beams sputtering target the type of gaseous feed during deposition is also varied. The LC alignment modes and pretilt angle control are investigated. Finally we consider the alignment stability in time.

2. EXPERIMENTAL

2.1 Setup

For film deposition we utilize sputtering device designed by Izovac Ltd. (Belarus). This device is based on the anode layer accelerator (the other common name is source with closed electron drift) [15] with circular area of glow discharge. The focused beam of ions or, precisely speaking, accelerated plasma (primary beam) bombards target that results in extraction of target's particles (mainly, atoms). The atomic flux formed (secondary beam) reaches substrate producing alignment coating. The substrate is positioned obliquely with regard to atomic flux. The general construction of sputtering device and the position of the aligning substrate under deposition are presented in Fig. 2. The target was a disc of vitreous silica or graphite with diameter of 6 cm. As a gaseous feed we used Ar, CF_4 , Ar/ CH_4 and Ar/ C_3H_8 gases and gaseous mixtures. The following operation parameters were used: residual pressure $2 \cdot 10^{-5}$ Torr, working pressure $5 \cdot 10^{-4}$ Torr, anode potential 4 kV, and discharge current 60mA. The deposition angle α was varied between 0° and 85° .

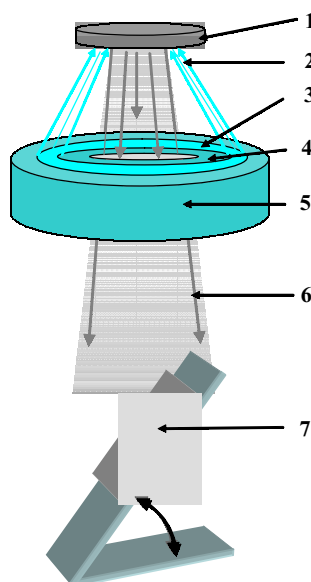


Fig. 2.

2.2 Samples

The substrates were $2 \times 3 \text{ cm}^2$ glass slabs coated by ITO electrode layers with a thickness of 50 nm. The alignment films were coated over ITO layers. Their thickness was about 20 nm. Before deposition the electrode films were pre-cleaned with ion beam from the anode layer source of etching type.

Two types of LC cells have been prepared: (1) tested substrate contains deposited layer, while the reference substrate has a rubbed polyimide layer (asymmetric cells); and (2) both substrates contain tested layers and assembled in an antiparallel fashion (symmetric cells). The asymmetric cells were used to determine easy axis direction on the tested substrate (LC alignment mode). The symmetric cells were used to measure the pretilt angle by crystal rotation method. The cell gap was kept with spacers of 20 μ m in diameter. We used TN mixtures E7 and ZLI2293 from Merck as LCs with $\Delta\epsilon > 0$ and VAN mixture MJ961180 from Merck Japan as LC with $\Delta\epsilon < 0$. The in-plane uniformity of LC alignment was tested by observation of samples in viewing box or in polarizing microscope. The out-of-plane uniformity was judged from the measurement of LC pretilt angle.

3. RESULTS

3.1. Alignment films sputtered from the silica target

For sputtering of silica target we used ion beams obtained from Ar, CF_4 , Ar/ CH_4 and Ar/ C_3H_8 feed gases. The atoms of these gases, together with target's atoms, may be presented in the sputtered films. On account of this the corresponding films are marked as SiO_x , $SiO_xC_yF_z$, and $SiO_xC_yH_z$. In case of normal incidence of atomic beam ($\alpha = 0^\circ$) and Ar or CF_4 feed we observed homeotropic alignment of LC MJ961180 and non-uniform alignment of LCs ZLI2293 and E7. The increase of deposition angle to 40° does not lead to the substantial change of LC alignment. The subsequent increase of a results in gradual decrease of pretilt angle θ for LC with $\Delta\epsilon < 0$ and 2nd mode alignment ($\theta = 0^\circ$) for LCs with $\Delta\epsilon > 0$. In case of tilted alignment, LC tilts towards deposition direction of atomic flux. With the increase of deposition angle up to 85° no transition from the 2nd to the 1st alignment is observed. This is in contrast with the vapor deposition (VD) study [2], where transition from the 2nd to the 1st mode at $\alpha_c = (70^\circ - 80^\circ)$ was detected. No difference in the type of alignment is observed for different feed gases, Table 1.

Table 1. LC alignment on the films obtained by sputtering silica target with plasmas of different gases. $\alpha = 55^\circ - 85^\circ$.

LC	Gas	Ar	CF_4	CH_4	C_3H_8
ZLI 2293, E7 ($\Delta\epsilon > 0$)		2 mode, $\theta = 0^\circ$, good time stability	2 mode, $\theta = 0^\circ$, good time stability	2 mode, $\theta = 0^\circ$, good time stability	2 mode, $\theta = 0^\circ$, good time stability
MJ 961180 ($\Delta\epsilon < 0$)		1 mode, $\theta = 88^\circ -$ 89.5° , good time stability	1 mode, $\theta = 86.5^\circ -$ 87.5° , satisfactory time stability	1 mode, $\theta < 30^\circ$, good time stability	1 mode, $\theta < 30^\circ$, good time stability

In case of Ar and CF_4 gases, similarly to VD experiments [7], LC with $\Delta\epsilon < 0$ shows 1st mode alignment with pretilt angle close to 90° . But the use of CF_4 gas gives slightly lower pretilt angle comparing with Ar gas (86.5° - 87.5° vs. 88° - 89.5°).

In case of Ar/ CH_4 and Ar/ C_3H_8 mixtures also the 2nd mode alignment for LCs with $\Delta\epsilon > 0$ and 1st mode alignment for LC with $\Delta\epsilon < 0$ is observed. In the latter case, pretilt angle substantially depends on the relative content of components: it gradually decreases with concentration of $\text{C}_n\text{H}_{2n+2}$ gas (Fig. 3). At 100% concentration of hydrocarbon gas the pretilt angle is within 40° and 15° . For LC with $\Delta\epsilon > 0$ the 2nd mode alignment is observed independently on the relative content of the components.

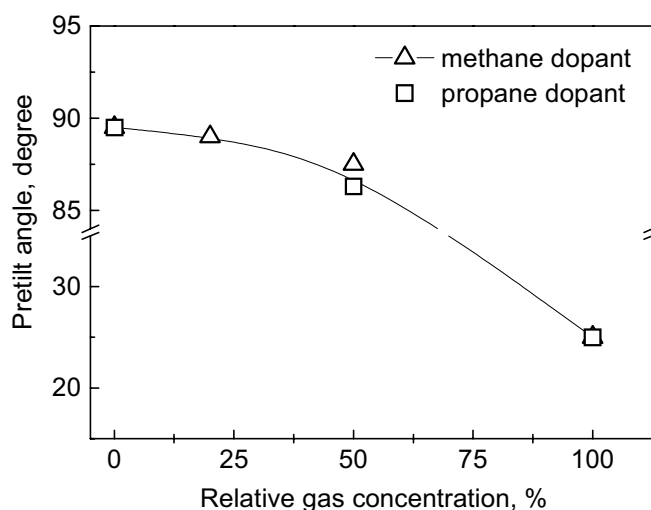


Fig 3.

The alignment was rather stable except some samples with silica films made under CF_4 gas. The reason of this is unclear yet. Possibly, fluorine is presented in chemically active form so that chemical reactions with LC occur that change boundary conditions.

3.2. Alignment films sputtered from the graphite target

In case of graphite target only Ar and CF_4 were used as a feed gas. The corresponding films are marked as C and CF_x . The LC alignment properties of these films are summarized in Table 2. In case of Ar feed, same as in case of silica target, we observed 2nd mode alignment for LCs with $\Delta\epsilon > 0$ and 1st mode alignment with high pretilt angle ($\theta = 87^\circ$ - 89°) for LC with $\Delta\epsilon < 0$. By contrast with Ar, use of CF_4 feed leads to the 1st mode alignment of LCs with $\Delta\epsilon > 0$ (the pretilt angle is about 10°). As far as we know, it is the first observa-

tion of the 1st mode alignment of LC with $\Delta\varepsilon>0$ on SD substrates. The LC MJ961180 with $\varepsilon<0$ demonstrates under CF_4 feed high tilt alignment in the 1st mode, just as in case of Ar feed, but with lower pretilt angle (within 85°-87°).

The stability of LC alignment on C and CF_x substrates is, unfortunately, poor. First of all, it relates to alignment on CF_x films. Within two weeks the 1st mode alignment of LCs with $\Delta\varepsilon>0$ deteriorates (Fig. 4, (1), (1')), while the high-tilt alignment of LC with $\Delta\varepsilon<0$ relaxes to the low-tilt and, subsequently, to the planar alignment in the 1st mode. The same happens with alignment of LC with $\varepsilon<0$ on C films. Interestingly that the 1st mode planar alignment of LC ($\Delta\varepsilon<0$) on C and CF_x films and the 2nd mode planar alignment of LCs ($\Delta\varepsilon>0$) on C films persisted over half year period of our observation (Fig. 4, (2), (2')). Thus, only planar alignment of the used liquid crystals is stable on C and CF_x substrates.

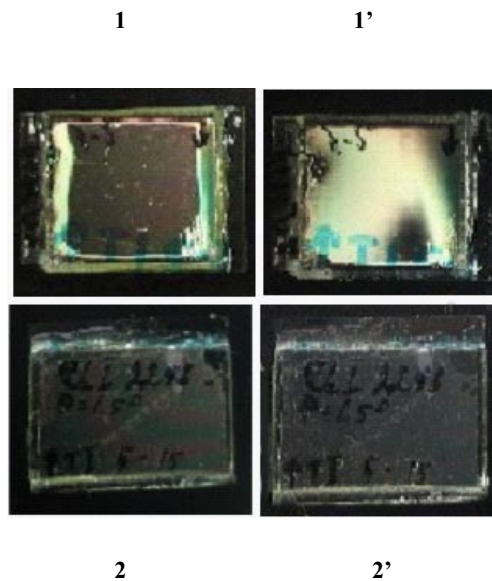


Fig 4.

4. CONCLUSIONS

The results obtained show big variety of LC alignment characteristics on sputter deposition (SD) films, which depend on the deposition geometry, target material and feed gas. The conclusions listed below can be drawn:

1. The conventional configuration (silica target and Ar feed) results in 1st mode high-tilt alignment (tilted vertical alignment) for VAN LC MJ961180 ($\Delta\varepsilon<0$) and 2nd mode alignment for TN LCs ZLI2293 and E7 ($\Delta\varepsilon>0$). The result for LC ($\Delta\varepsilon<0$) is rather similar to previous results described for VD [7]. The difference with VD is a lack of the 1st alignment mode for LCs with $\Delta\varepsilon>0$ in

case of grazing deposition ($\alpha > 80^\circ$). This might be caused by different surface morphologies of SiO_x films in case of VD and SD processes operating with particles of different energy. Namely, in case of thermal deposition, the adatoms have energy of several milli-electronvolts meV, while in case of sputtering deposition the energies are of several electronvolts eV and higher.

2. The feed gas can influence LC alignment. In case of $\text{C}_n\text{H}_{2n+2}$ gases the pretilt angle of VAN LC with $\Delta\varepsilon < 0$ is lower than in a case of Ar feed. This may be used to optimize pretilt angle for some operation modes, for instance for STN VA requiring lower pretilt angle as a common TN VA.

3. The use of fluorine containing feed gases is undesirable, because they usually accelerate alignment aging. Presumably, the fluorine presented in the alignment coating is not combined with other atoms so that it can react with LC in interface changing boundary conditions.

4. In case of graphite target and CF_4 feed (CF_x films) 1st alignment mode for LCs with $\varepsilon > 0$ is realized. The pretilt angle is about 10° . However, this alignment is unstable and deteriorates within several weeks.

5. Initially, VAN LC with $\Delta\varepsilon < 0$ shows tilted VA on the graphite films. However, this alignment is unstable: for about one week the pretilt angle falls to zero. Thus, summarizing (4) and (5), only planar LC alignment is stable on the graphite films (1st mode planar alignment for LC with $\Delta\varepsilon < 0$ and 2nd mode planar alignment for LCs with $\Delta\varepsilon > 0$).

We believe that majority of these rules are rather general and so applicable to the films obtained by other combinations of targets and feed gases.

Table 2. LC alignment on the films obtained by sputtering graphite target with plasmas of different gases. $\alpha = 55^\circ - 85^\circ$.

LC	Gas	
	Ar	CF ₄
ZLI 2293 (> 0)	2 mode, = 0 good time stability	1 mode, ~ 10 poor time stability: deterioration within 2 weeks
MJ 961180 (< 0)	1 mode, = $87^\circ - 89^\circ$ poor time stability: 0 for 1 week.	1 mode, = $85^\circ - 87^\circ$ poor time stability: 0 for 1 week.

Acknowledgment

These studies were supported by INTAS foundation (grant 03-51-5448).

References

1. J. Janning, "Thin film surface orientation for liquid crystal", *Appl.Phys.Lett.* 21(4), 173-174 (1972).
2. W. Urbach, M. Boix, and E. Guyon, "Alignment of nematics and smectics on evaporated films", *Appl.Phys.Lett.*, 25 (9), 479-481 (1974).
3. E. Reynes, D. Rowell, and I. Shanks, "Liquid crystal surface alignment treatment giving controlled low angle tilt", *Mol.Cryst.Liq.Cryst.*, 34, 105-110 (1976).
4. D. Meyerhofer, "New technique of aligning liquid crystals on surfaces", *Appl.Phys.Lett.*, 29 (11), 691-692 (1976).
5. A. Lackner, J. Margerum, L. Miller, and W. Smith, "Photostable tilted-perpendicular alignment of liquid crystals for light valves", *SID'90 Digest*, 98-101.
6. H. Vithana, Y.K. Fung, S.H. Jamal, R. Herke, P.J. Boss, and D.L. Johnson, "A well-controlled tilted-homeotropic alignment method and a vertically aligned four-domain LCD fabricated by this technique", *SID'95 Digest*, 873-876.
7. M. Lu, K. Yang, T. Nakasogi, and S. Chey, "Homeotropic alignment by single oblique evaporation of SiO₂ and its application to high resolution microdisplays", *SID'00 Digest*, 446-449.
8. O. Yaroshchuk, R. Kravchuk, A. Dobrovolsky, L. Qiu, O. Lavrentovich, "Planar and tilted uniform alignment of liquid crystals by plasma-treated substrates", *Liq.Cryst.*, 31 (6), 859-869 (2004).
9. O.V. Yaroshchuk, R.M. Kravchuk, A.M. Dobrovolsky, P.C. Liu, C.D. Lee, "Plasma beam alignment for the large area substrates: equipment and process", *J.SID*, 13 (4), 289-294 (2005).
10. V. Shiripov, A. Khokhlov, S. Maryshev, M. Levchuk, A. Khissamov, K. Krivetski "Display thin-film coatings produced by ion-beam processing", *J. SID*, 13(4), 315-320 (2005)
11. T. Motohiro and Y. Taga, "Sputter-deposited SiO₂ films for LC alignment", *Thin Solid Films*, 185, 137-144 (1990).
12. "Inducing tilted parallel alignment in liquid crystals", US patent 5,529,817 (1996).
13. Y. Kolomsarov, P. Oleksenko, V. Sorokin, P. Tytarenko, and R. Zelinsky, "Orienting properties of SiO_x films for high resolution LCD", *Proc. of ADT'04 (Sept. 7-10, 2004, Raubichi, Belarus)*, 83-88 (2004).
14. A. Murauski, A. Khakhlou, V. Shiripov, and A. Cerasimovich, "Ion beam sputter deposition process of inorganic vertical alignment layers", *SID'04 Digest*, 574-576.
15. V Zhurin, H Kaufman, and R Robinson, "Physics of closed drift thrusters," *Plasma Sources Sci Technol* 8, R1-R20 (1999).

Cholesteric LCD for creation of acoustooptical holographic image.

P. Oleksenko, V. Sorokin, P. Tytarenko, R. Zelinsky

V.Lashkarev Institute of Semiconductor Physics, NAS Ukraine, 41,
prospekt Nauki, 03028 Kyiv, Ukraine

Abstract.

The construction of acoustooptical display based on the hysteretic in cholesteric liquid crystals (CLC) is proposed for nondestructive holographic test systems. The influence oblique reactive sputtering deposited thin films of In_2O_3 , Al_xO_y , SiO_x , upon alignment properties of CLC, which are used as ultrasonic holographic recording media, is investigated. The technical characteristics and properties of developed acoustooptical display (AOD) are represented. It is shown the high sensitivity and planar texture reproducibility CLC an implicit advantage of AOD developed.

Keywords: cholesteric liquid crystal, acoustooptical display, ultrasonic hologram.

1. Introduction

Both fundamental and applied research of nondestructive control techniques are attracted very much attention recently [1,2]. Acoustic holography technique, which is a good supplementary technique for traditional nondestructive control techniques, play a special role in nondestructive research techniques.

The usability of acoustic holography techniques for nondestructive testing and defectoscopy lies in the very fact that the majority of materials and constructions are nontransparent for electromagnetic field in its optical range and, as a consequence, the internal structure of tested materials is invisible for visual observation. However, the optically nontransparent solid media may be transparent for ultrasonic acoustic waves of an appropriate frequency range. Therefore, interaction of ultrasonic acoustic waves with the defects and inhomogeneities in the media may provide information on structure and properties of defects. The success in further development and application of acoustic holography techniques depends very much on availability of a good sensor, which fulfill the numerous requirements like threshold sensitivity, resolution, reversibility, etc.

Cholesteric liquid crystal attract very much attention in that sense due to their periodic helical structure of molecular layers, which gives Bragg selective reflection accompanied by circular dichroism and strong rotation of polarization plane for short pitch cholesteric liquid crystals. The strong helical pitch dependence of above factors and their influence various external factors make possible to use cholesteric LCs for visualization of acoustic, heating and the other kind of fields.

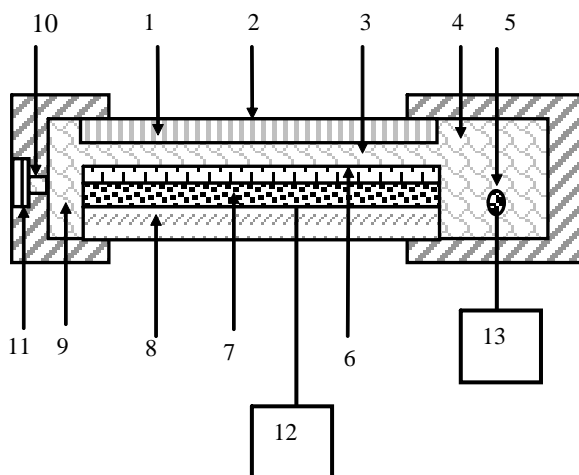
The general construction of acoustooptical display (AOD) is simple enough. It consists of optically transparent substrate and ultrasonically transparent but optically opaque substrate with the layer of CLC (e.g. mixture of cholesterolpelargonate and cholesterolchloride [3]) arranged between them. The theoretical threshold sensitivity for AOD of above described construction is calculated to be about 10^{-12} W/mm², whereas the practically achieved value is about 10^{-4} W/mm² only [4]. There are several constructions of above described AOD known for today [5-7]. The general feature of such devices is impossibility to erase recorded information quickly as well as to restore the planar texture of CLC. The recorded information erase and a planar texture restoration is performed by mechanical shift between substrates. This technique imply a significant disadvantage because liquid crystals could not be hermetically sealed, which result in life time restrictions and reproducibility of the results. The other shortcomings of such construction represent the thickness variation of LC after each sequential shift of glass substrates, which result in variation of reflection intensity for selected wavelength.

In order to avoid above mentioned shortcomings we have developed a new type of AOD based on hysteretic properties in CLC [8]. It features uniform high quality planar texture and possibility to erase information and restore the planar texture. Another feature of proposed AOD is CLC in fully hermetic and sealed volume which prevents any contact of LC with testing object and any aggressive environment for LC.

1. Experimental setup

The developed AOD is made up of (Fig. 1) the following parts: ultrasonically transparent substrate (1) with the optically dark opaque layer on top (8) and cholesteric liquid crystal film arranged between those substrates. Both substrates have embedded transparent electrodes (7) connected to a power source and transparent alignment layers (6). The sensor sandwich is sealed from opposite sites whereas the remaining two opened sides are directly connected to incoming (9) and outgoing (4) reservoirs sealed with LC. There is a heater (5) embedded into LC feeder which reservoir has a piping with a plastic membrane (11). The total erase of recorded information is performed by the application of voltage from the power source (12).

The proposed AOD operates in the following way. In order to prepare the sensor for information recording the voltage from the power source (12) is applied first. The transparent electrode is made of In₂O₃:Sn thin film deposited on top of glass substrate by cathode reactive sputtering deposition technique in the Ar:O₂ environment. The ingot has standard 95/5 ratio for In/Sn. Passing through the In₂O₃:Sn electrodes the electric current produces heat sufficient for isotropic phase transition of CLC. The temperature set both inside the drain and source must be below the isotropic temperature of CLC. After the power source (12) is turned off the heater (5) is launched the power source (13) at the very moment of reverse phase transition of LC from isotropic to cholesteric state.



Pic.1. The construction of AOD: 1 – acoustic transparent substrates, 2 – opaque layer, 3 – CLC thin layer, 4 – source, 5 – heater, 6 – alignment layer, 7 – transparent electrode, 8 – optically transparent substrates, 9 – drain, 10 – piping connection, 11 – membrane, 12,13 – power supply units.

The heater has enough power to transfer the content of reservoirs from LC phase to the isotropic state within a few seconds. Due to a natural thermal expansion of liquid in source it is flown through the sensor's capillary into drain. Unidirectional transportation of LC via capillary with alignment layer creates a good planar texture. The heating power and operation time is adjusted to provide isotropic phase transition completed by 30-60% of overall volume of LC in the source and to avoid the isotropic phase in sensor's capillary. The liquid crystal flown out of sensor's capillary is coming to drain. Excessive pressure is compensated by the membrane (11) via the floating of LC passing through the piping system (10). The membrane is made of a flexible elastic material covering the edge of a pipe system. The liquid crystal is cooling down after turn off the heater (5) in source and the volume of LC is shrinking unto original one at a room temperature. An excessive spread of CLC is moving through the piping into drain and eventually comes to source via sensor's capillary. A good planar texture is established after complete cooling down operation at room temperature and AOD is considered to be fully functional for information recording.

One should mention that located flow of LC in sensor's capillary due to a natural thermal compression facilitate the alignment of cholesteric liquid crystal via friction interactions at the boundary layer. The alignment of CLC is forced by the boundary alignment layer (6) having microgrooves like structure. The alike structures may be obtained in the different manner e.g. oblique deposition in vacuum such materials SiO_x , In_2O_3 , MgF_2 , GeO_x , Pt, Au etc.; unidirectional rubbing of organic polymer films and the others.

The optimum dimensions of drain and source for normal operation of AOD were defined in the following way. At a room temperature the volume V_{t_1} CLC in source is equal [10]:

$$V_{t_1} = V_o(1 + \beta_1 t_1)$$

where V_o - volume at $t = 0^\circ C$, t_1 - room temperature, β_1 - volume expansion coefficient of CLC at the range between $0^\circ C$ and t_1 .

While heating up to t_2 , the volume of CLC rises and reach the value V_{t_2} :

$$V_{t_2} = V_o(1 + \beta_2 t_2)$$

where β_2 - is the thermal expansion coefficient of CLC in the range $t_1^\circ C - t_2^\circ C$. The difference between two volumes ($V_{t_2} - V_{t_1}$) is equal to CLC volume ΔV , forced out the sensor's capillary:

$$V_{t_2} - V_{t_1} = V_o(\beta_2 t_2 - \beta_1 t_1) = \Delta V$$

If k_i - is is a part of volume which is necessary to pump through the capillary for reliable planar alignment (k_i is defined experimentally), and the capillary has defined square s and thickness d , then

$$\Delta V = s d k_i$$

Consequently,

$$V_o = \frac{s d k_i}{\beta_2 t_2 - \beta_1 t_1}$$

substitution of V_o into expression for V_{t_1} result in:

$$V_{t_1} = \frac{s d k_i (1 + \beta_1 t_1)}{\beta_2 t_2 - \beta_1 t_1}$$

Thermal expansion coefficients β_1 and β_2 for our CLCs were experimentally defined by PICNOMETR technique and gave the following values:

$$\beta_1 = 9,1 \cdot 10^{-4} K^{-1}, \beta_2 = 8,5 \cdot 10^{-4} K^{-1}$$

The experimental samples of AOD have been performed with the operation field square $7 \times 7 \text{ cm}^2$. The cell gap in capillary was selected to be $50 \mu\text{m}$. The experimental value defined for k_i coefficient was found to be 0,3. The source's heater was made of NiCr wire and allow to reach the environmental temperature in source around $50^\circ C$ after 7 sec. Both source and drain were made of PMMA Plexiglas. The optically transparent substrate was made of K8 optical glass with optically transparent $\text{In}_2\text{O}_3:\text{Sn}$ electrodes deposited by cathode reactive sputtering technique on top of the substrate. The conduc-

tivity of transparent electrodes was measured to be $50 \Omega/\square$ at the electrodes thickness 0,1 m. The strip wiring (1mm width) of Cr:Cu was attached to the electrodes. The alignment layer was cathode reactive sputtering oblique deposited at 15 deg. angle with respect to surface plane. The sensor was assembled to have the coincidence of LC flow direction in capillary with the groove easy action direction of alignment layer. Acoustically transparent substrate was made of PMMA Plexiglas 1mm thick and painted black from ultrasonique input side. The cell gap between two substrates has performed by mylar spacers of calibrated 50 m thickness. The overall sealing of AOD was made using T-111 glue with the addition of L-20 hardener.

1. Result and discussion

It is indispensable to know exactly and to control the wavelength of maximum selective reflection when using AOD of acousto-holographic registration element. It is very important to know the reflection intensity width, scattering cones and circular dichroism parameters additional to acoustic waves parameters like frequency, intensity and its relation to the information recording efficiency. There have been carried out studies of selective reflection spectra as well as the other parameters and characteristics of AOD.

We have found that selective reflection spectra taken from seemingly identical substrates have the different reflection intensity and its angular dependence. Some samples show narrow peak of high intensity, whereas the others offer low intensity but broader spectral width (Fig.2).

In process of study the influence of substrates preparation and further treatment on selective reflection spectra we have found that reflection intensity is associated with the helical axis ordering. The higher the ordering the higher reflection intensity and more narrow the peak. This could be understood from Bragg diffraction conditions:

$$2d \sin \theta = m\lambda$$

where d – helical pitch, θ - angle of incidence, λ - wavelength, $m = 1,2,3,\dots$

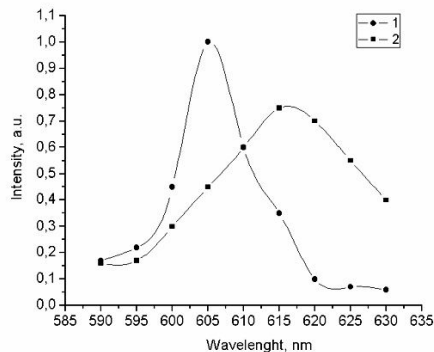


Fig.2. Scattering cones of CLC for aligned (1) and nonaligned(2) CLC layer.

For ideal planar texture, where the helical axes are strictly parallel to the surface plane, the diffraction conditions are satisfied for a single wavelength under the fixed angle of incidence. The disordering of helical axis result in broadening of the wavelength interval to fit the Bragg diffraction conditions. Eventually, there is no selective reflection in case of extreme focal conic texture and any wavelength is scattered in the similar way.

We have studied the influence of various substrate treatment techniques on texture uniformity of liquid crystals. It was tested in the very first turn mechanical treatment of alignment layer by means of unidirectional rubbing. It was also investigated the influence of various alignment layers like SiO_x , In_2O_3 , MgF_2 , Al_xO_y etc., deposited by oblique cathode reactive sputtering technique described in [10,11]. All above investigated techniques create microgrooves on aligning surface and result in special ordering of LC molecules at the boundary. In order to check alignment properties of CLC we measure the scattering cones, which are represented in Fig.2-6.

Fig.3 demonstrates the angular dependent of reflected intensity from LC layer for four different wavelength and 20deg. oblique light incidence with respect to surface plane. The substrate had no treatment in that case.

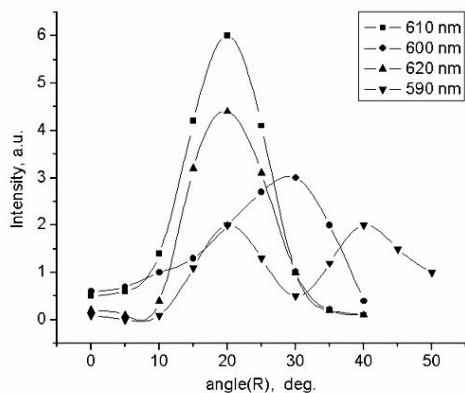


Fig. 3. Scattering cones of CLC for untreated surfaces.

As it could be seen from Fig.2-6 the intensity peak of selective reflection is around $\lambda= 610$ nm. For the others incidence angle the peak of selective reflection intensity is shifted .

The resemble lines in Fig.4 show somewhat higher reflectance intensity for SiO_x alignment layer.

For In_2O_3 , MgF_2 , Al_xO_y alignment layer as well as for various unidirectional rubbed materials on the substrate surface the intensity of selective reflection falls down (Fig.5-7). It is still pronounced for In_2O_3 layers and almost completely vanishes for mechanically rubbed layers.

Hence, it is shown from our measurement that the best results for alignment of CLC are provided with oblique reactive sputter deposited SiO_x alignment layers.

As to the other alignment layers and unidirectional mechanical rubbing of virgin surfaces with the different materials we cannot consider the results of our studies to be comprehensive and possibly more detailed studies should be performed in the future.

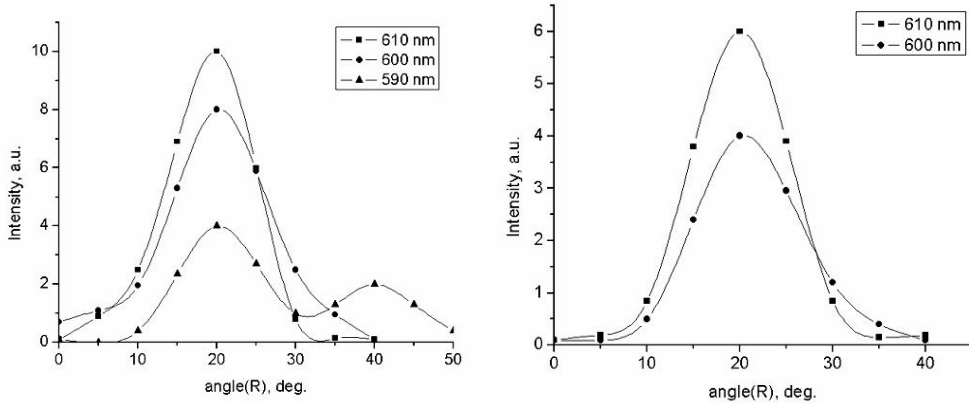


Fig.4 (left). Scattering cones of CLC for SiO_x deposited alignment layers.

Fig.5. (right) Scattering cones of CLC for rubbed substrates.

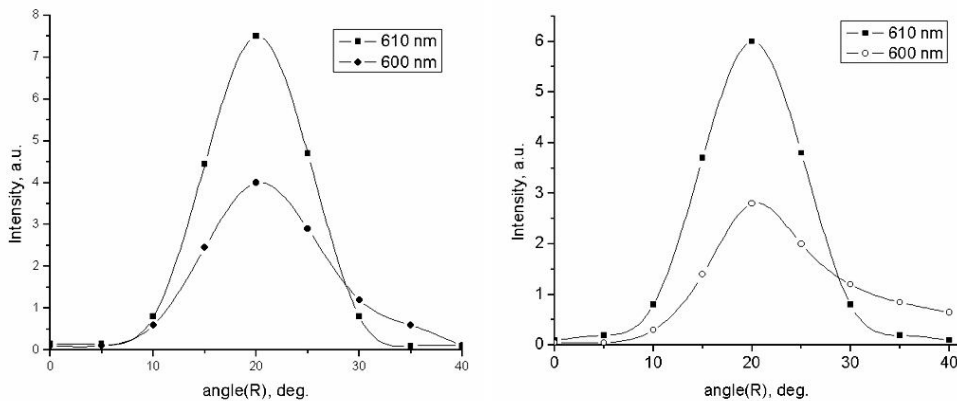


Fig.6 (left). Scattering cones of CLC for In_2O_3 deposited alignment layers.

Fig. 7 (right). Scattering cones of CLC for Al_xO_y deposited alignment layers.

The selective reflection spectra taken 1, 2, 5, 20 θ 60 min following the beginning of planar texture restoration process. As it could be seen from Fig.8 the intensity of reflection is low and the peak is wide at the onset. The reflection intensity rises shifting into shorter wavelength range and the re-

flexion band narrows while the time growth. In 60 min following the onset the reflection peak achieve its maximum and the peak width becomes narrow. Further changes in reflection spectrum are minor and mostly invoked by the environmental temperature fluctuations. Hence, the sample is ready for measurements following 1 hour after reset.

Fig.9 shows some characteristics of reflection spectra for AOD developed and their comparison with conventional AOD built according to a framework known from the literature. Both AODs use the same cholesteric LC material and spectral characteristics are measured for the same measurement conditions.

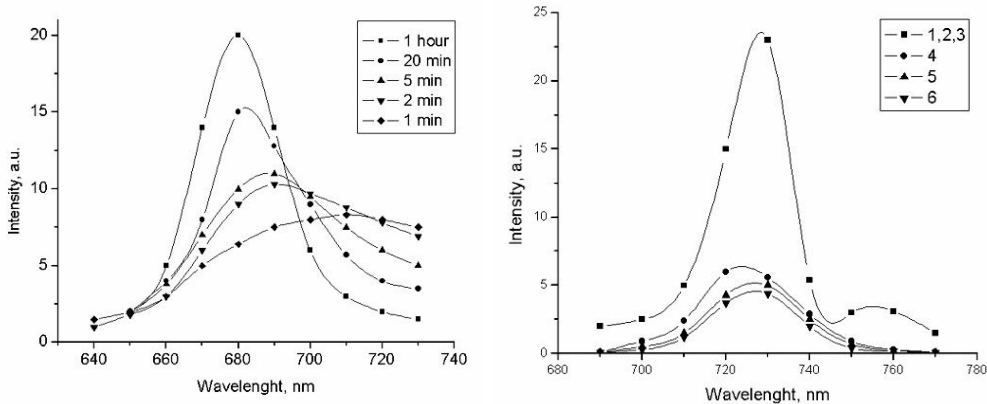


Fig.8 (left). Reflection spectra of CLC during the restoration of planar texture (the time legend after onset is shown next to reflection curves).

Fig.9 (right). Spectral characteristics of our AOD (1,2,3 curves) and AOD built according to a known scheme [] (4,5,6 curves).

The curves 1-3 correspond to the different peaks of erase-restoration and emphasize on a good reproducibility of our AOD. Besides of significantly lower intensity and wider reflection peak the curves 4-6 are characterized by different wavelength peaks, which certify is favor poor reproducibility of measurements for AOD that employs mechanical shift between upper and lower substrates for planar texture restoration.

The numerous test performed for our AOD have been shown the high reliability in the hard working environment. The measured lifetime resource was at least 2500 hours and the central wavelength shift was not more than $\Delta\lambda= 5-10$ nm after a year of continuous exploitation. The average erase and restore times for the planar texture were not exceeding 2 and 18 sec. respectively.

Conclusions

The AOD based on hysteretic properties in CLC featuring fast information erase time and recreation of planar texture, fully sealed CLC geometry that except LC contact with LC environment, has been developed.

The influence of oblique reactive sputter deposited In_2O_3 , Al_xO_y , SiO_x thin film upon the alignment properties of CLCs, which are used for ultrasonic holograms recording, has been investigated.

Grounding on studies of selective reflection spectra it has been shown that the high quality and uniformity of planar alignment over the whole working area as well as good reproducibility of the planar texture of CLC is an implicit advantage for our developed AOD over existing counterparts.

References

1. V.V. Kluev. Not destroying control and diagnostics. -M.: Mashinostroenie, 1995
2. L.D. Gik. Acoustic holography.-Novosibirsk.-Nauka, 1981
3. J.L. Fergasson. Liquid Crystal Detectors. Acoustic holography. -L: Sudostroenie, 1975
4. D.Casesent. Spatial Light modulators. Proc.IEEE, v.65, 1977 p.143-157
5. V.I.Maglovanny. The liquid crystal detector for visualization of acoustic field. A.S. # 516994, BI 121, 1976
6. V.I.Maglovanny. Equipment for visualization of acoustic fields A.S. # 797391
7. V.I.Maglo vannyy. Acoustooptic display A.S. # 550897
8. P.Oleksenko, V.Sorokin, P.Tytarenko, R.Zelinsky, V.I.Maglovanny, Bezruchko V.M. Acoustooptic display A.S. # 999810
9. A.K Kikoin, I.K Kikoin. Molecular physics.-M., Nauka 1976, p.315
10. Yu.Kolomzarov, P.Oleksenko, V.Sorokin, P.Tytarenko, R.Zelinsky. Vacuum method for creation of liquid crystal orienting microrelief. // Semicond., Phys., Quant., Electr., Optoelectronics, 6(4), pp.528-532 (2003)
11. Yu.Kolomzarov, P.Oleksenko, V.Sorokin, P.Tytarenko, R.Zelinsky "Peculiar properties of LC orientation by thin inorganic oxide films obtained by glow discharge plasma" in XV Conference on Liquid Crystals, edited by Jozef Zmija, Proceedings of SPIE Vol.5565 (SPIE, Bellingham, WA, 2004) 359-364.

Passive-matrix addressing of the display based on bistable PDChLC film

*A.V. Barannik, V.F. Shabanov, V.Ya. Zyryanov, V.M. Sorokin**

L.V. Kirensky Institute of Physics, SB RAS, Krasnoyarsk, Russia,

*Institute of Semiconductor Physics, NASU, Kyiv, Ukraine

Abstract

Cholesteric liquid crystals can be efficiently used in displays with passive-matrix addressing due to large hysteresis of volt-transmittance curve. The hysteresis is also characteristic of the polymer dispersed cholesteric liquid crystals (PDChLC) which are promising material for flexible displays. Erasing or rewriting of the information in PDChLC display in the direct or reverse scattering modes can be carried out by the electric pulse which displaces a bias voltage to the values determined by the hysteresis parameters. The switching of optical states of the pixel is provided with application of the rectangular pulses with fixed amplitude and variable phase on corresponding matrix electrodes. The amplitude of column pulses is so that all pixels are under action of bias voltage without row signals. The application of rectangular alternating voltage to the chosen row in combination with column signals of certain phases provides the recording of information in the required pixels of the row.

Keywords: flexible displays, cholesteric liquid crystals, polymer dispersed liquid crystals, electrooptical bistability, passive-matrix addressing.

Introduction

Now a renaissance of the interest to the cholesteric liquid crystals arises which is caused by the opportunity to develop flexible displays [1-3]. It is clear, that in this case, both the substrates with driving schemes and electrooptical materials must be flexible. Two ways in the technology of flexible LC displays are developing: one is based on active matrix formed on the polymer substrate, another uses the passive matrix addressing. The last imposes a limitation on the form of volt-transmittance characteristics of LC materials. The curve must be sharply threshold or reveal large hysteresis. PDChLC films satisfy the requirements on mechanical properties and light transmission curves (Fig.1) [4-9]. Electrooptical bistability of the composite films is provided for two stable director configurations within ChLC droplets at certain value of applied voltage (bias voltage U_b): spherulite cholesteric structure and uniform nematic aligned perpendicularly to the film plane. In the last case, the film is transparent for the normally incident light. The samples with spherulite droplets possess by strong light scattering.

The basic principals of the passive-matrix addressing of ChLC displays using dynamic drive schemes are described in detail in [10-15]. These schemes can be applied in large part for the PDChLC cells.

Experiment

PDChLC film under study was prepared by TIPS method [16]. We used the nematic mixture of cyanobiphenyl derivatives ($\Delta\epsilon > 0$) doped by cholesterol acetate and polyvinylbutyral as a polymer matrix. Cholesteric / nematic mass ratio was about 1:9.

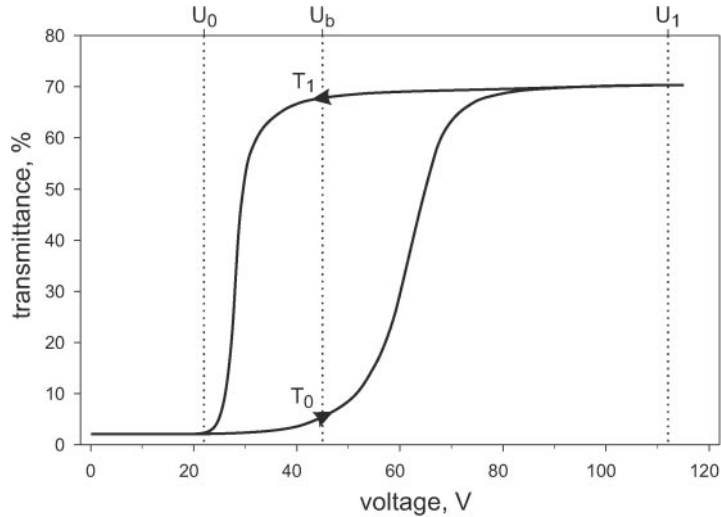


Figure 1. Light-transmission characteristic of PDChLC film obtained under the action of alternating voltage at 1 kHz.[6-8] The arrows on the curves indicate a direction of voltage change. U_b denotes a bias voltage.

The light-transmission characteristic (Fig. 1) was obtained in a quasistatic measurement mode, i.e., under the action of a high-frequency alternating voltage with a slowly variable amplitude up to 115V. In this case, the transmittance was averaged through the time exceeded the characteristic response time of director reorientation in LC droplets. The whole of electrooptical characteristics were measured only for the light component passed straightforward. He-Ne laser with $\lambda = 0,633$ mm was used in experimental setup.

Results

Figure 1 shows the variation of light transmission of PDChLC film when the applied alternating voltage goes up to value U_1 and after that decreases to zero. The unwinding of spherulite structure in ChLC droplets reveals distinctly at direct transmittance curves above U_0 . At saturation value U_1 , the cholesteric structure transforms in homeotropic (relatively to the substrates) nematic state. Here the light scattering becomes minimal. The reached transparent state keeps if the voltage decreases to bias value U_b . T_1 and T_0 indicate two stable values of transmittance at bias voltage and determine a maximum contrast ratio in direct scattering mode of the addressing.

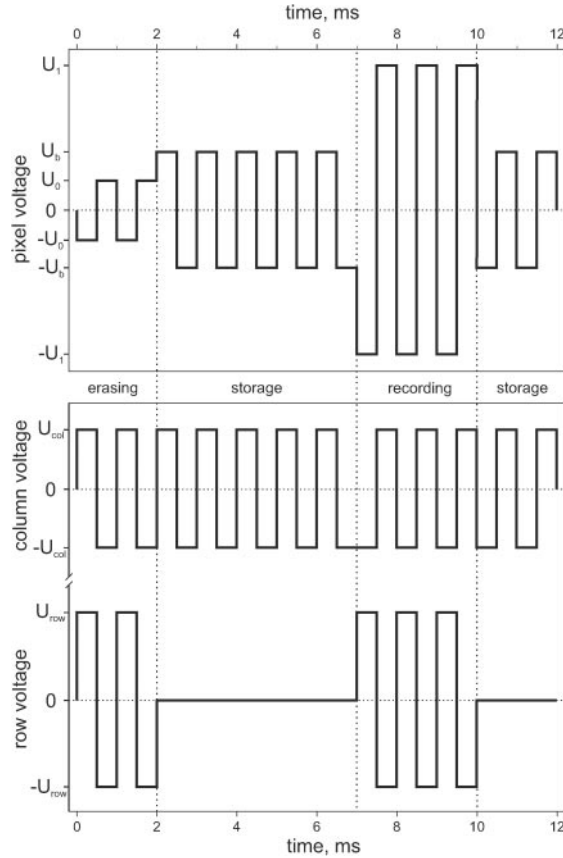


Figure 2. Schematic diagram of electric signals at addressed row and column and resultant waveform applied to across pixel.

The switching of chosen pixel from the light-scattering state T_0 to the transparent one T_1 and inversely can be performed by the application of two rectangular signals with the assigned amplitude and phase on the corresponding electrodes of passive matrix. In Fig. 2 the forms of controlled signals on the matrix row and column as well as the resulting voltage at addressed pixel are shown. The formation of the matrix pattern is realized in the following way. The bipolar voltage of $U_{col} = U_b$ amplitude is permanently applied to all columns. In storage regime the voltage U_{row} is equal to zero at the rows. In this case the only base voltage operates at all matrix pixels. Row-wise switching of pixels to the required state is performed applying the pulse of alternating voltage at the chosen row and assigning the phases of the column signals. At that the effective value of the voltage applied to each pixel of the chosen row is equal to $|U_{col} - U_{row}|$ taking into account the phase of pulses.

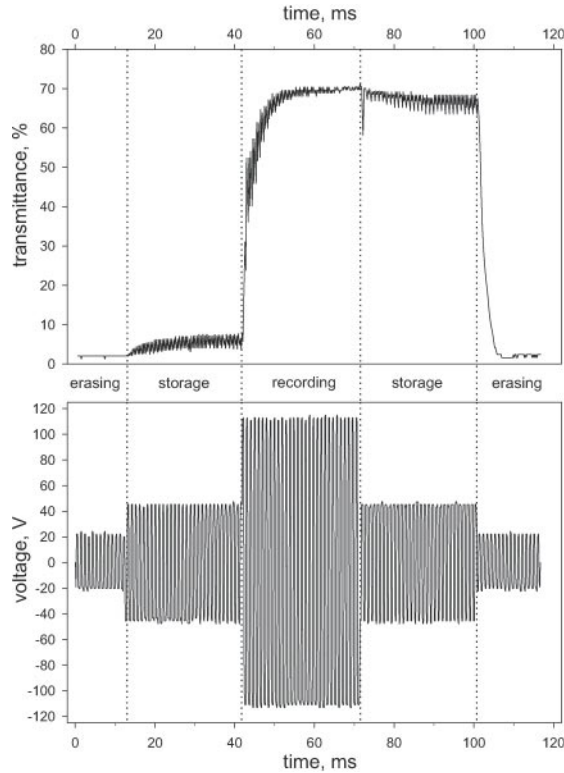


Figure 3. The voltage waveform at the single pixel for the sequence of regimes: recording, storage, erasing. The dynamics of optical response of PDChLC film at the signal is shown on top figure.

The amplitude of a row voltage must be so that the signals U_{col} and U_{row} in antiphase would provide the saturation level U_1 on the pixel. On the contrary, the inphase compensation of the above mentioned signals results in the switching off the operated voltage to the U_0 level. The image obtained at the row remains permanent under the action of the base voltage formed by column pulses regardless of variation of their phase during the subsequent switching off U_{row} and addressing of next matrix rows.

The hysteresis parameters of PDChLC films depend on the composition and preparation technique of material. In any cases, the given drive scheme allow us to select the values of operating voltage so that the resulting effective level of signal on the pixels has the required form.

In Fig. 3 the oscillograms of operating field and the optical response of the single matrix pixel are shown in step-by-step process “erasing-storage-recording-storage-erasing”. The enveloping curve of a resulting signal represents the sequence of 22, 45, 112, 45 and 22V levels with high-frequency filling. In storage regime two stable optical states of PDChLC film are holding

which approximately correspond to the transmittance values $T_0 = 5\%$ and $T_1 = 68\%$.

An optimization of the composition and preparation technique of PDChLC material allows to reduce the switching time to some milliseconds. The contrast ratio of the device is determined by the thickness of composite film, morphological parameters and the refractive indices of its components.

Acknowledgements

This work was supported, in part, by grants No 05-03-32852 of Russian Foundation for Basic Research; No 8.1, 2.10.2 and 18 of Russian Academy of Sciences.

References

1. I. Shiyonovskaya, A. Khan, S. Green, G. Magyar, J. W. Doane, Single substrate encapsulated cholesteric LCDs: coatable, drapable and foldable, SID 05 Digest, p.1556-1559 (2005).
2. Y.-R. Lin, S.-C. Jeng, L.-P. Hsin, J.-M. Ding, C.-C. Liao, Y.-H. Lien, J.-T. Shy, Electro-optical performance of bending ultra-flexible film-like display, SID 05 Digest, p.1565-1567 (2005).
3. T. Schneider, F. Nicholson, A. Khan, J. W. Doane, L.-C. Chien, Flexible encapsulated cholesteric LCDs by polymerization induced phase separation, SID 05 Digest, p.1568-1571 (2005).
4. D.K. Yang, L.C. Chien, and J.W. Doane, Cholesteric liquid crystal/polymer dispersion for haze-free light shutters, Appl. Phys. Lett., Vol.60 (25), p.3102-3104 (1992).
5. D.K. Yang, J.W. Doane, Cholesteric liquid crystal polymer gel dispersion: reflective display application, SID 92 Digest, Vol. 23, p.3102-3104 (1992).
6. H. Fujikake, K. Takizawa, H. Kikuchi, T. Fujii, Polymer-dispersed LCLVs with gray-scale memory, SID 93 Digest, Vol.24, p.873-876 (1993).
7. V.Ya.Zyryanov, S.L.Smorgon, V.A.Zhuikov, V.F.Shabanov, Memory effects in polymer-encapsulated cholesteric liquid crystals, JETP Lett., Vol.59, No8, p.547-550 (1994).
8. V.A.Zhuikov, S.L.Smorgon, V.Ya.Zyryanov, and V.F.Shabanov, Electrooptical bistability and thermoaddressed information recording in polymer dispersed cholesterics, Proceedings SPIE, Vol.2731, p.159-167 (1995).
9. A.V.Barannik, V.A.Zhuikov, V.Ya.Zyryanov, S.L.Smorgon, V.F.Shabanov, Grey-scale recording of information by thermal contact in polymer-dispersed cholesteric liquid crystal, Tech. Phys. (Rus), Vol.66, No5, p.177-179 (1996).
10. X.Y. Huang, D.K. Yang, P. Bos and J.W. Doane, Dynamic drive for bistable reflective cholesteric displays: A rapid addressing scheme, SID 95 Digest, p.347-350 (1995).
11. X.Y. Huang, M. Stefanov, High-performance Dynamic Drive Scheme for Bistable Reflective Cholesteric Displays, SID 96 Digest, p.359-362 (1996).

12. M. Zhu, D.K. Yang, High-Speed Dynamic Drive Scheme for Bistable Reflective Cholesteric Displays, SID 97 Digest, p.97-100 (1997).
13. V. Sorokin, Simple Driving Methods for Cholesteric Reflective LCDs, Proc. of the 18th International Display Research Conference Asia Display'98, p.749-752 (1998).
14. A. Rybalochka, V. Sorokin, S. Valyukh, A. Sorokin, V. Nazarenko, Dynamic Drive Scheme for Fast Addressing of Cholesteric Displays, SID 2000 Digest, p.818-821 (2000).
15. A. Rybalochka, V. Sorokin, S. Valyukh, A. Sorokin, Simple Drive Scheme for Bistable Cholesteric LCDs, SID 2001 Digest, p.882-885 (2001).
16. G.P.Crawford, S.Zumer. Liquid Crystals in Complex Geometries, Taylor and Francis Publ., 500 p. (1996).

FORMATION CONDITIONS OF POLARIZING STRUCTURE OF H- and L-TYPE POLARIZERS IN VIEW OF OPTICAL ANISOTROPY

N. Ivanova¹, V. Agabekov¹, S. Shahab,¹

¹Institute of Chemistry of New Materials of the National Academy of Sciences of Belarus, Minsk, E-mail:agabekov@ns.ichnm.ac.by

A. Tsaruk², V. Dlugunovich²

²B. I. Stepanov Institute of Physics of the National Academy of Sciences of Belarus, Minsk

Abstract

With Stoks-polarimetry method polarization properties of H- and L-types polarizer fabricated by two techniques usually used in practice for linearly polarizing structure formation: 1) by absorption of iodine (H-polarizer) or dichroic dye of group azobenzenenaphthalene (code M₁) (L-polarizer) from a solution into unpainted film of polyvinyl alcohol (PVA) – technique “in a bath” 2) by introduction of dichroic dye to initial composition for manufacturing of PVA-film – technique “in mass” are evaluated.

Introduction

Earlier with Stoks-polarimetry method we established that polarizing film received from preliminary painted PVA-composition by azodye M₁ have two kinds of optical anisotropy: amplitude and phase [1]. It was established that phase anisotropy as birefringence arises in orientated PVA-film during its stretching. It was shown that the undesirable display of this birefringence is eliminated by increase of dye concentration in film more than 1%. However main factor of the greatest optical transmission of received linear iodine H-polarizers is much lower [1, 2] than that one made in the Institute of Chemistry of New Materials of the National Academy of Sciences of Belarus, but on other technology. It worsens its consumer qualities and limits practical application area. At the same time technology of industrial manufacturing of highly effective N-polarizers given in extensive scientific and patent literature [5] is based on a coloring of a polymeric film in a solution.

In this connection the purpose of the given investigation consist in estimation of opportunities and efficiency of application of two above-stated methods for manufacturing of linearly polarizing structure of L-type polarizer with dichromofor M₁ by comparison of optical and polarizing parameters of polarizers determined by Stoks-polarimetry method.

Experimental

The technology description of manufacturing of H- and L-types polarizer and their spectral-polarizing characteristics measured with non-polarized light are given in works [2, 3].

In the given work with Stoks-polarimetry method using laser goniometric Stoks-polarimetr [6] were defined not only polarizing ability (q) and Q-factor (Q) of H- and L-types polarizer but also their main optical transmittance,

t_{\max} , t_{\min} - traditional characteristics, and also ellipticity (e) and birefringence (Δn) for the polarized He-Ne laser radiation at $\lambda = 0,63$ mm transmitted by polarizer.

In the beginning the maximum transmittance axis for radiation linearly polarized in the plane of incidence was determined. This axis was perpendicular to the film stretching axis. Then the measurements of Stoks parameters of radiation transmitted by polarizer at normal incidence of linearly polarized radiation with an azimuth of 0 , 90 and 45° according to maximum transmittance axis were carried out. By statistical treatment of six measurements of the polarizing characteristics under the formulas from work [7] the average meanings were determined:

$$\tau_{\max,\min} = \frac{I_{\parallel,\perp}}{I_o}; \quad q = \frac{\tau_{\max} - \tau_{\min}}{\tau_{\max} + \tau_{\min}}; \quad Q = \frac{\tau_{\max}}{\tau_{\min}}, \quad (1)$$

where I_o , I_{\parallel} , I_{\perp} - intensity of incident radiation (first Stoks parameter) and transmitted radiation, at azimuths of incident radiation 0° and 90° accordingly.

The absolute uncertainty of normalized Stoks parameters measurement did not exceed 0,03.

Effective birefringence parameter (Δn) corresponding to measured ellipticity of transmitted radiation and caused, on the one hand, by phase anisotropy appeared during PVA-film stretching for creation of entered dichromofor orientation effect, and on the other hand, by attenuation of absorption anisotropy was determined with use of expression (2) received by transformation of the formulas from [7]:

$$\Delta n = \frac{\lambda}{2\pi l} \arcsin \frac{2e}{(1+e^2) \sin 2\varphi}, \quad (2)$$

where λ - radiation wavelength, l - film thickness, φ - polarization azimuth of incident linearly polarized radiation, e - ellipticity of transmitted radiation.

The briefly above-stated method is in details described in [6]. According to this method the study of polarizing properties of H- and L-polarizers fabricated by coloring of a PVA-film with evolved iodine during film chemical processing [2] or by azodye M1 absorption from 0,05% solution [3] with subsequent orientation by stretching was carried out.

Results and discussion

The results of study of polarizing properties of H- and L-types polarizer fabricated by absorption of iodine or dichroic dye M1 from a solution into unpainted PVA-film and polarized characteristics of transmitted radiation are presented in tab 1.

It is seen that H-polarizer fabricated by exposure in solution during 1 minute characterized by high polarizing ability at maximal transmittance 0,82 0,03 close to transmittance of uncolored and not orientated PVA-film 0,89 0,02 (tab. 2). Radiation with azimuths 0, 45 and 90 concerning to the maximum transmittance axis transmitted polarizer characterized by ellipticity practically equal to zero. It is connected with very small optical transmission of radiation component with electric vector E, orientated along a film stretching direction. Practically complete absorption of this component lead to negligibility of effect of phase anisotropy arising during stretching original PVA-film on the polarizing characteristics of transmitted radiation. In more detail cause of occurrence of phase anisotropy of birefringence in

H-polarizer is set out in [5], and about negligibility of its influence on polarization characteristics of transmitted radiation - in [1].

L-type polarizers were fabricated by coloring in solution during 1 up to 9 minutes. It is seen (tab. 1) that the increase of exposure time in a solution leads to reduction of polarizer transmittance for orthogonally polarized components but simultaneously lead to increasing their polarizing ability and good quality. The influence of phase anisotropy presenting in investigated L-polarizers reduces to a minimum by their coloring in azodye M1 solution within nine minutes. Radiation transmitted through given polarizer is characterized by small ellipticity and also small effective birefringence parameter.

The results of investigation of polarizing properties of L-type polarizers fabricated by introduction of dye M1 "in mass" into a composition for manufacturing PVA-film, and parameters of transmitted radiation are submitted in tab. 2. Comparisons of results presented in the tables 1 and 2 shows that influence of phase anisotropy appeared as birefringence (the slow axis is parallel to direction of a PVA-film stretching) on the polarizing characteristics of transmitted radiation decreases with arising of its polarizing ability and Q-factor. The minimum of influence is achieved at such concentrations of dichromofor M1 in PVA-film fabricated as by "in bath" as by "in mass" technology when Q-factor and polarizing ability increase up to or more 100 and 0,998 accordingly. It is coordinated also to results obtained for H-type polarizers.

Thus given investigations show that during manufacturing of linear L-type polarizer by both techniques of introduction of dichromofor M1 into PVA-film undesirable influence of phase anisotropy, arising due to a PVA-film stretching is eliminated by comparable increase of absorption anisotropy. It confirms the mechanism and reasons underlying of technology of elimination of negative influence of a PVA- film stretching, technologically necessary for creation of polarizer at the directional M1 orientation [1]. In comparison with "in mass" polarizer fabricated technology, the "in bath" technology requires long processing within nine minutes or more that is necessary for elimination of negative influence of phase anisotropy on polarizer quality. In turn, the long film processing in a solution promotes increasing

of probability of occurrence of other reasons negatively influencing on a polarizer quality.

Conclusions

It was shown that in L-type polarizer with linearly polarization structure fabricated by absorption of M1 from uncolored PVA-film solution along with amplitude anisotropy there is phase anisotropy initiated by orientation PVA-film during its stretching. It was established that regardless of fabrication technology of given polarization structure the influence of phase anisotropy on polarizing properties of L-type polarizer decreases with increasing of absorption anisotropy. When Q-factor of polarizer increases up to 100 or more its phase anisotropy practically is eliminated.

Table 1 Parameters of H- and L-types polarizer fabricated by “in a bath” technique and polarized characteristics of transmitted radiation

Parameters	H-polarizer	L-polarizer		
	Exposure time in a solution, min			
	.1	1	6	9
τ_{max}	0,82±0,03	0,69±0,02	0,45±0,02	0,32±0,02
τ_{min}	0,0014±0,0002	0,0325±0,02	0,04±0,002	0,004±0,0002
Q	586±86	21±2	12,1±1	95±5
q	0,9966±0,0002	0,91±0,004	0,85±0,02	0,97±0,01
e	0,03±0,02	0,42±0,03	0,1±0,05	0,06±0,05
Δn	0,0003±0,0002	0,004±0,0002	0,001±0,0005	0,0006±0,0005

Table 2 Parameters of L-type polarizer fabricated by “in mass” technique and polarized characteristics of transmitted radiation

Parameters	PVA-FILM (uncolored and not stretched)	PVA-FILM (uncolored and stretched)	PVA-FILM with [M ₁]=0,5% (stretched)	PVA-FILM with [M ₁]=1% (stretched)
τ_{max}	0,89±0,02	0,89±0,02	0,56±0,05	0,28±0,02
τ_{min}	0,88±0,02	0,89±0,02	0,03±0,01	0,0014±0,0005
Q	1,01±0,03	1,0±0,03	18,6±5	200±5
q	0,005±0,002	0±0,002	0,9±0,002	0,99±0,002
e	0,02±0,05	0,5±0,2	0,15±0,06	0±0,05
Δn	0±0,0005	0,005±0,002	0,0015±0,0005	0±0,0005

References

1. *Ivanova N., Agabekov V., Shahab S., Tsaruk A., Dlugunovich V., Voschula I.* // Proceedings of the XIIIth International Symposium «Advanced display technologies», Raubichi, Belarus. 2004. P. 237 – 239.
2. *Kosmacheva T., Globa I., Ariko N., Agabekov V.* // Vesti NAN Belarus. Ser. chem. nauk. 2004. #1, P. 52 – 55.
3. *Kosmacheva T., Globa I., Ariko N., Agabekov V.* // Vesti NAN Belarus. Ser. chem. nauk. 2002. # 3, pp. 120 – 123.
4. *Ariko N., Agabekov V.* // Jour. Appl. Chem. 2003. V. 76, # 10. p. 1715 – 1719.
5. *Sherkliff U.* Polarized light. Moscow. 1965. 264 đ.
6. *Dlugunovich V., Snopko V., Tsaruk O.* // Jour. Appl. Spectros. 1999. V. 66, # 6, P. 869 – 874.
7. *Snopko V.* Polarization characteristics of optical radiation and methods of its measuring. Minsk. 1992. 336 p. (in Russian).

Displays for Green Earth

Shigeo Mikoshiba

The University of Electro-Communications, Chofu, Tokyo 182-8585, Japan

1. RoHS and WEEE Directives

The Restriction on Hazardous Substances (RoHS) was adopted by the European Union on January 27, 2003 [1]. The key provision of the RoHS directive is the following: "...from 1 July 2006, new electrical and electronic equipment put on the market [shall] not contain lead, mercury, cadmium, hexavalent chromium, polybrominated biphenyls (PBB) or polybrominated diphenyl ethers (PBDE)."

The companion legislation for RoHS, adopted at the same time, is the directive on Waste Electrical and Electronic Equipment (WEEE.) The main provision of WEEE is, "...by 13 August 2005, producers or third parties acting on their behalf, [must] set up systems to provide for the treatment of WEEE using best available treatment, recovery and recycling techniques". Recycling of 65% of the device materials is assessed. The time table of these legislations is shown in Fig. 1.



Fig. 1 Time schedule for RoHS and WEEE

Several governments, including Japan, China, California, and South Korea are preparing to enact similar WEEE and RoHS legislation. Companies are expected to move from mere compliance with these legislation to competitive advantage-oriented activities.

An addition of Pb lowers the melting point of glass, and adopted widely in both CCFLs for LCD backlights and PDPs. Pb-free glasses, using phosphates, phosphoric acids, boron oxide, and bismuth oxide have been investigated, but still issues remain, including cost. CCFLs utilize the Hg discharges. Although Hg can be replaced by Xe, power consumption increases by a factor two, assessing another environmental issue of CO₂ reduction in atmosphere, as will be discussed later.

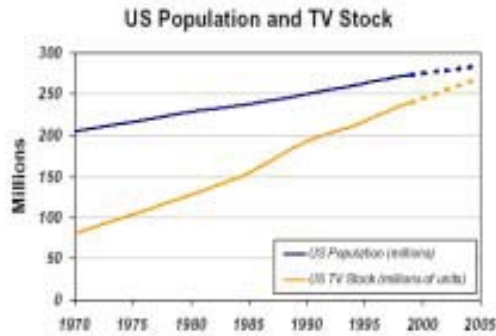


Fig. 2 Increase in TV sets in US

2. Annual Energy Consumption of TV Sets

Another issue for keeping the earth clean is to reduce the energy consumption of electronic devices. National Resources Defence Council of USA estimates that US televisions consumed over 46 billion KWh in 2004, or about 4% of national residential electricity use [2]. This number is to increase to over 70 billion KWh per year by 2009, an increase of over 50%. The magnitude of household energy use related to a home’s multiple TVs and some common associated peripherals such as DVDs and STBs amount to over 10% of the electric bill in a typical US household.

The number of installed TVs in the US will soon eclipse the country’s total population, with one TV for every US resident, Fig. 2. A proposed “EnergyGuide” label for TVs provides information on the amount of energy used to operate the TV annually, the cost to operate the TV annually, and also the range of annual energy consumption for other TVs of comparable size and resolution, as illustrated in Fig. 3.

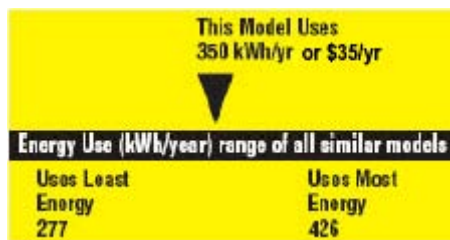


Fig. 3 Proposed EnergyGuide label for TV sets



Fig. 4

Japan Electronics & Information Technology Industries Association (JEITA) proposed four test patterns shown in Fig. 4 for measuring the power consumption, with an equation,

$$P_o = (1/6)P_w + (1/6)P_b + (1/3)P_c + (1/3)P_t.$$

The average picture level (APL) for the equation is 50%. The APL for TV programs, however, is typically 20% as found in Fig. 5 [3], requiring a proposal for an improved measurement method.

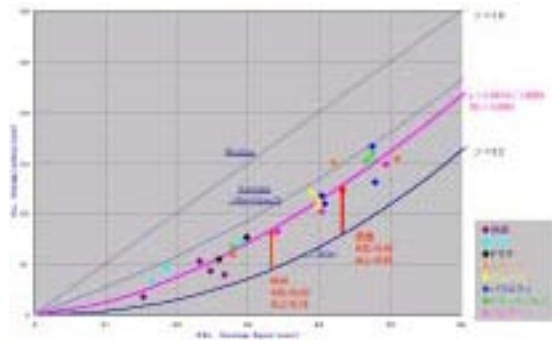


Fig. 5

3. Power consumption of LCD Backlights

Requirements for LCTV backlights include high luminance, high luminous flux, dimming capability, low power consumption, fast response, long life, and no environmental concern. The high luminance requirement arises from limited utilization of light from the backlight, due to polarizers, color filters, and small active matrix LCD aperture ratio of 20% - 30%. The high luminous flux becomes more important as the TV screen is enlarged.

The high luminance and flux can be realized by increasing the emitting area, i.e., by providing a flat discharge lamp such as that seen in Fig. 6 [4]. In terms of luminance and luminous efficacy, Hg glow discharge has excellent characteristics. Nevertheless, it has shortcomings of a high-voltage requirement of lamp ignition under low ambient temperatures. Also there is a strong temperature dependence of luminance and efficacy, as illustrated in Fig. 7.

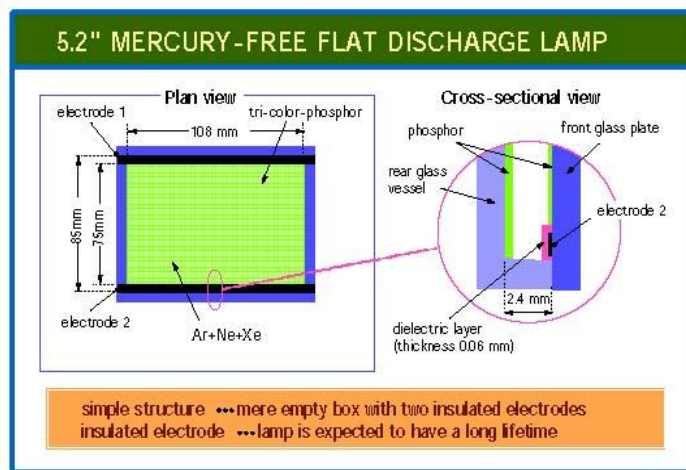


Fig. 6 Flat Fluorescent Lamp

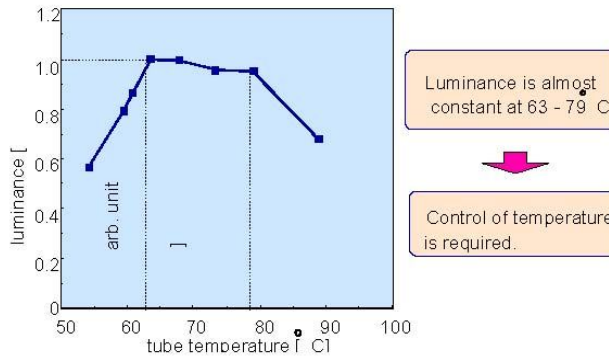


Fig. 7 Temperature dependence of luminance

Figures 8 and 9 compare the luminance and efficacy for Hg and Xe flat discharge lamps of Fig. 6. For Hg lamps, luminance and efficacy increase with drive voltage, but for Xe lamps, luminance increases while efficacy decreases with voltage. Namely the maximum luminance and maximum efficacy for the Xe lamps cannot be achieved simultaneously by varying the voltage. If we make two lamps having a similar size and luminance (e.g. 10,000 cd/m²) but one with Hg and the other with Xe, then the typical efficacies are 62 lm/W and 30 lm/W, respectively. Xe lamp efficacy is only half that of Hg.

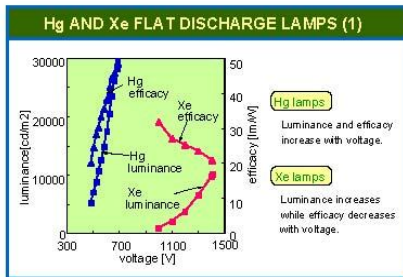


Fig. 8 Hg and Xe FFLs

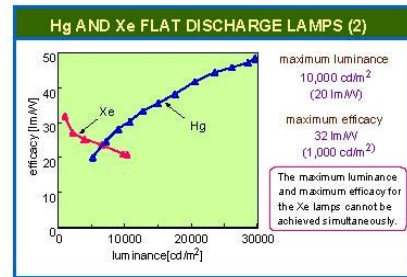


Fig. 9 Luminance vs. efficacy of Hg and Xe flat discharge lamps

The dimming capability of the lamps is necessary to improve gray scale expression in low luminance levels, and also to save power consumption. Figure 10 shows the experimental results of power reduction by using an adaptive dimming technique [5]. For a typical TV image having an APL of 25% (samples 2 and 3), the backlight power consumption is reduced to approximately 50%. It should be noted, however, that if the Hg lamps are used in the adaptive dimming mode, the lamp temperature lowers and efficiency decreases.

Power Consumption			
simple	1	2	3
picture content	garden	garden	sunrise
AFL	40%	28%	28%
without adaptive dimming	100%	100%	100%
with adaptive dimming without optical isolators	89%	56%	83%
with adaptive dimming with optical isolators	78%	54%	53%

Fig. 10 Power reduction with adaptive dimming technique

4. Power consumption of PDPs

Fabrication of PDPs is an energy consuming process. Figure 11 shows the temperature cycles required for the frit and baking processes. As can be found from the figure, the panel temperature is elevated to 450°C, cooled to room temperature, heated again to 350°C, and then cooled. Even before the frit/baking processes, there are drying and firing cycles for thick-film pastes.

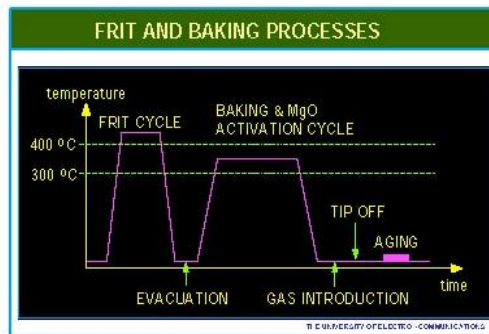


Fig. 11 Temperature profile for PDP production

Besides, the PDPs suffer from low luminous efficiency, typically 2 lm/W. This value is only 1/15 of the Xe fluorescent lamp of Figs. 8 and 9. One of the reasons of the efficiency difference between the PDPs and lamps is due to the discharge cell dimension. A rule of thumb is “efficiency is proportional to dimension.” This is because the smaller cells suffer from diffusion losses of charged particles, requiring larger power input to compensate for the loss. The barrier rib height should be higher to reduce the diffusion losses.

The target efficiency of PDPs is 5 lm/W, above which the power consumption of the drive electronics becomes dominant. The determining factors of efficiency related to the discharges are the secondary electron emission from MgO, diffusion/drift losses of charged particles, ionization and

excitation efficiencies, and saturation of output vacuum ultra-violet radiation with respect to discharge current.

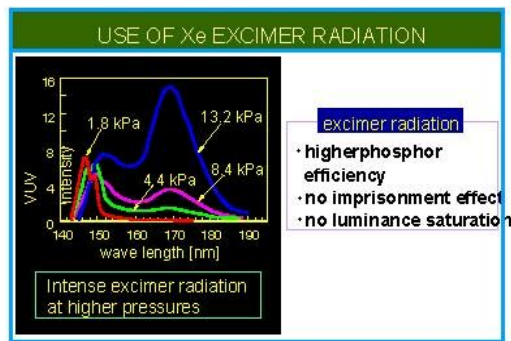


Fig. 12 Xe resonant and excimer radiations

The most recent researches on the efficiency improvement are oriented towards higher Xe content, with which 172nm excimer radiation is obtained in addition to 147nm resonance radiation, see Fig. 12. Improvement of efficacy is shown in Fig. 13 [6].

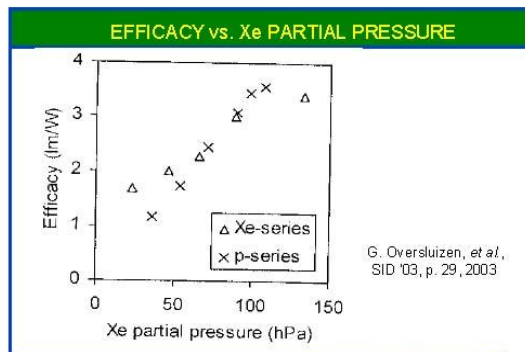


Fig. 13 Xe pressure vs. efficacy

A use of the high efficiency positive column discharge with long discharge gap, Fig. 14, is also suggested [7].

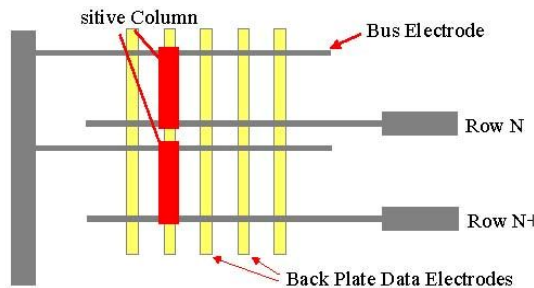


Fig. 14 PDP using positive column discharge (Positive Column AC PDP Electrode Structure)

In order to obtain high ionization and excitation efficiencies, lowering of electron temperature is essential. This can be done by superposing auxiliary pulses to the sustain pulses as shown in Fig. 15 [8].

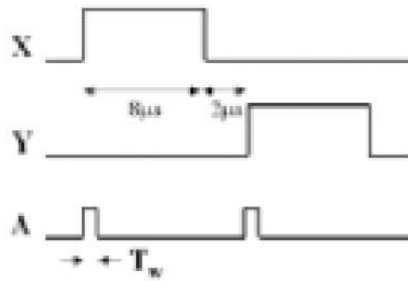


Fig. 15 High efficacy drive of PDPs

Variations of luminance and efficiency for experimental and production level PDPs are summarized in Fig. 16 [9]. An extrapolation predicts that 5 lm/W can be attained in 2007.

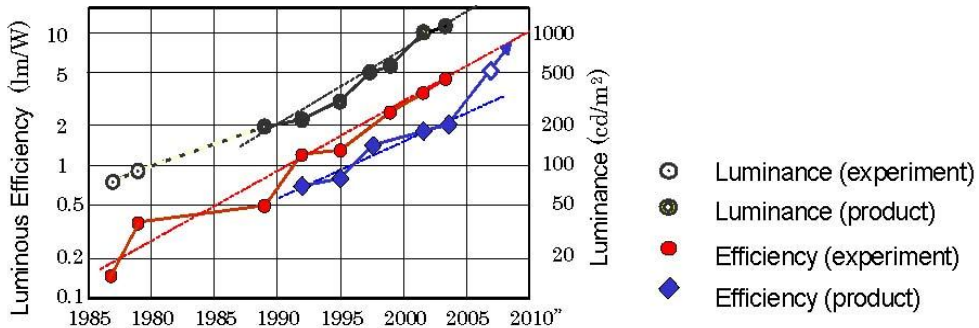


Fig. 16 PDP luminance and efficacy

References

- [1] <http://www.goodbyechain.com/index.html>
- [2] P. Ostendorp, *et al.*, "Television," NRDC Rept., Mar. 1995.
- [3] JEITA/OLED Report, 2004.
- [4] T. Shiga, *et al.*, Proc. 16th IDRC, pp. 233-236, 1996.
- [5] T. Shiga, *et al.*, SID 05 Digest, pp. 992-995, 2005.
- [6] G. Oversluizen, *et al.*, SID 03 Digest, pp. 29-32, 2003.
- [7] L. F. Weber, Conf. Rec. 23rd IDRC, pp.119-124, 2003.
- [8] K. -W. Whang, *et al.*, SID 05 Digest, pp. 1130-1133, 2005.
- [9] Y. Sato, PDP Tech. Mtg. Saga Forum 2003.